UNIVERSITY OF SÃO PAULO

INSTITUTE OF CHEMISTRY

Graduate Program in Chemistry

RAFAEL TRIVELLA PACHECO DA SILVA

Nanobiocatalysts: Nanozymes and Nanobioconjugates in Heterogeneous Catalysis and Electrocatalysis

Versão original da Tese defendida

São Paulo

Deposit date at SPG:

04/08/2022

UNIVERSIDADE DE SÃO PAULO

INSTITUTO DE QUÍMICA

Programa de Pós-Graduação em Química

RAFAEL TRIVELLA PACHECO DA SILVA

Nanobiocatalisadores: Nanozimas e Nanobioconjugados na Catálise Heterogênea e Eletrocatálise

Versão original da Tese defendida

São Paulo

Data de Depósito na SPG:

04/08/2022

RAFAEL TRIVELLA PACHECO DA SILVA

Nanobiocatalysts: Nanozymes and Nanobioconjugates in Heterogeneous Catalysis and Electrocatalysis

Thesis presented in the Institute of Chemistry
at the University of São Paulo to obtain
the Ph. D. degree in Science (Chemistry)

Advisor: Prof. Dr. Susana Inés Córdoba de Torresi

São Paulo

2022

Autorizo a reprodução e divulgação total ou parcial deste trabalho, por qualquer meio convencional ou eletronico, para fins de estudo e pesquisa, desde que citada a fonte.

Ficha Catalográfica elaborada eletronicamente pelo autor, utilizando o programa desenvolvido pela Seção Técnica de Informática do ICMC/USP e adaptado para a Divisão de Biblioteca e Documentação do Conjunto das Químicas da USP

Bibliotecária responsável pela orientação de catalogação da publicação:
Marlene Aparecida Vieira - CRB - 8/5562

da Silva , Rafael Trivella Pacheco
d586n Nanobiocatalysts: Nanozymes and nanobioconjugates in heterogeneous catalysis and electrocatalysis / Rafael Trivella Pacheco da Silva . - São Paulo, 2022.
134 p.

Tese (doutorado) - Instituto de Química da Universidade de São Paulo. Departamento de Química Fundamental.
Orientador: Cordoba de Torresi, Susana Ines

1. Nanobiocatalysis. 2. Nanobioconjugate. 3. Nanozyme. 4. Plasmonic catalysis. I. T. II. Cordoba de Torresi, Susana Ines , orientador.

FOLHA DE APROVAÇÃO

To those in my family and friends

whose love was the fuel that brought me here

Acknowledgements

This section is dedicated to all those who have contributed either directly or indirectly to the success of this work. First, I would like to thank my supervisor, Prof. Susana I. Cordoba de Torresi, who was always supportive, dedicated, and enthusiastic about my results. Her kindness and outspoken personality made me feel welcome and provided a cradle for new research ideas throughout my studies, even in difficult pandemic times. The financial and material support during my work time provided by Capes and FAPESP.

To Pedro H. C. Camargo, the catalyst that brought together bright minds to GrAND, where I began my doctoral work. To the fruitful (and fun) discussions during coffee breaks with Paulo, Helô, Maria, Thaylan, Eduardo, Carmine, Luanna, Jhon, Marcos, Ivo, and Vitor. In this context, I would also like to thank Gabi and Dri, the undergraduate students I had the pleasure of mentoring and bond with.

A special thanks goes to my former colleagues, whom I now consider lifelong friends: Paulo, Maria, Helô and Thiago. Paulo, who guided me as a friend and as a student with his brilliant brain that works in strange ways. Maria, who was always open-hearted in hearing my feelings and taught me about perseverance through methodical approaches. Helô, who is filled with a spirit of adventure and taught me how to bring it to research with enzymes. I will surely miss our evenings with wine and good food nights after the shift. Thiago, with whom I had the most profound conversations about society and the universe, after all, critical thinking is part of the scientific education.

Still within the Chemistry Institute, I thank the members of the LME with whom I have had the privilege of acquiring and sharing knowledge. I thank Prof. Marcia Temperini, who was my

supervisor in my first-year teaching assistantship program and with whom I stablished a great collaboration in my recent publications along with Rafaella.

Crossing the road to the Biosciences Institute, I would like to thank the young people who have supported me since 2019, when I had the not-so-sane idea to enroll in a Biology program during my graduation in Chemistry. Among others, a special thanks to Love, Shan, and Dio for bringing me back to the charm and freshness of pursuing a first degree, alongside the many opportunities that come with it. The intersection of the Biosciences and Chemistry Institutes belongs to Lucas, whose sense of humor (and apathy) could not be more like mine.

I would also like to thank those outside the Academy. First, my friends Luiza and Fernanda, who have grown alongside me for two decades and have played a big part in what I have become. This thesis is also dedicated to Bia and Mila, with whom I could share the perks and challenges of adulting as a Millennial. Mari and Maiassa, who turn peculiar into ordinary. Wilson, who (re)found me in the final months of my doctoral studies and was a loving support during such a difficult time.

Last but not least, my closest relatives, Marilia, Pacheco, Patty, Ro, and Bia, who were able to patiently understand the odd career choices of a young scientist. They have emotionally and materially provided the foundations from which I now stand. Hopefully, they are the ones who will be most proud of having a doctor (although not a medical one) in the family.

Rafael Trivella P. da Silva

Das Volumen des Festkörpers schuf Gott, ihre Oberfläche wurde vom Teufel gemacht.

“God made the bulk; the surfaces were invented by the Devil.”

Wolfgang Pauli

da Silva, R. T. P. **Nanobiocatalysts: Nanozymes and Nanobioconjugates in Heterogeneous Catalysis and Electrocatalysis**. 2022. 134 p. Tese - Programa de Pós-Graduação em Química. Instituto de Química, Universidade de São Paulo, São Paulo.

Resumo

O uso de nanomateriais metálicos para a biocatálise vem se consolidando devido ao seu grande poder catalítico, estabilidade frente a meios complexos e reciclabilidade. Além disso, a nanocatálise pode ser beneficiada por estímulos externos como a ressonância plasmônica localizada de superfície (LSPR), cujos efeitos óticos, eletrônicos e térmicos são capazes de intensificar ou até modificar os mecanismos catalíticos das reações originais. Essa tese se dedica em investigar: i) nanomateriais metálicos que podem atuar como enzimas, nas chamadas nanozimas e ii) nanomateriais metálicos como suportes de imobilização de proteínas em nanobioconjugados. Os materiais foram estudados sob o ponto de vista nanobiocatalítico e sob ação de estímulo LSPR.

Na primeira série de materiais, as nanozimas, nanopartículas de prata (AgNP) foram estudadas como agentes antimicrobianos contra *P. aeruginosa* multirresistente. Sob a ação de luz em LSPR, AgNP são capazes de causar morte celular a 100% das bactérias em apenas 1 h de tratamento. Essa eficiência se relaciona à maior produção de espécies reativas de oxigênio (EROs) na combinação de AgNP e luz, demonstrando o efeito do LSPR. Nanopartículas bimetálicas de AgAu também foram estudadas. Ligas bimetálicas de AgAu suportadas em SiO_2 foram sintetizadas mecanoquimicamente e utilizadas na hidrogenação da 2-nitroanilina. Nesse caso, observou-se um aumento de 4 vezes na constante de velocidade, bem como aumento da conversão catalítica em comparação aos metais isoladamente. Nanocascas bimetálicas de AgAu suportadas em óxido de grafeno (GO) e submicroesferas de SiO_2 foram sintetizadas por substituição galvânica em solução. As nanocascas foram testadas como peroxidases para a detecção eletroquímica de H_2O_2 por sua reação de redução (HPRR), havendo influência da composição e suporte, bem como da região de excitação do LSPR. Em comparação ao escuro, AgAu/GO apresentou aumento de 100% na sensibilidade sob estímulo de 405 ou 533 nm, enquanto AgAu/SiO2 levou a 120% de melhora sob estímulo de 650 nm.

No segundo tipo de materiais estudados, os nanobioconjugados, nanopartículas de ouro (AuNP) foram estudadas como suporte para imobilização de duas biomoléculas: Lipase de *Candida sp.* (CALB) e Citocromo C (CytC). CALB imobilizada demonstrou melhora na sua atividade catalítica sob estímulo LSPR de AuNP. A enzima foi investigada em termos das mudanças na estrutura secundária pela geração local de calor. Dicroísmo circular e Raman demostraram intensas mudanças, em especial nas α-hélices, após a imobilização, mas também sob a ação de temperatura e incidência de luz. Dinâmica molecular (MD) demonstra que esses estímulos podem levar a uma maior exposição da tríade catalítica Ser105-Asp187-His224 e, portanto, promoveriam uma maior atividade catalítica. Similarmente, quando CytC está imobilizada em AuNP, observou-se mudanças em sua estrutura secundária, em especial com uma perda significativa de α-hélice e ganho de folhas-β, além de considerável melhora na estabilidade térmica. Cataliticamente, o nanobioconjugado CytC@AuNP apresentou melhora de 68% na conversão catalítica. Sob LSPR, apenas o nanobioconjugado teve melhoria de desempenho em 12%. Com isso, esta tese demonstra vantagens do uso de nanopartículas metálicas em nanobiocatálise, seja através do emprego de

nanozimas ou de nanobioconjugados, ampliando também o que conhecemos da interação do LSPR e biomoléculas.

Palavras-chave: Catálise Plasmônica, LSPR, Nanobiocatálise, Nanobioconjugados, Nanozimas.

da Silva, R. T. P. **Nanobiocatalysts: Nanozymes and Nanobioconjugates in Heterogeneous Catalysis and Electrocatalysis**. 2022. 134 p. PhD Thesis – Graduate Program in Chemistry. Instituto de Química, Universidade de São Paulo, São Paulo.

Abstract

The use of metallic nanoparticles for biocatalysis has been steadily increasing due to their great catalytic potential, stability against complex media and recyclability. In addition, nanocatalysis can be benefited by external stimuli such as localized surface plasmon resonance (LSPR), whose optical, electronic and thermal effects are capable of intensifying or even modifying the catalytic mechanisms of the original reactions. This thesis is dedicated to investigating: i) metallic nanoparticles that can act as enzymes, in the so-called nanozymes and ii) metallic nanoparticles as supports for the immobilization of proteins in nanobioconjugates. The materials were studied from the nanobiocatalytic point of view and under the action of LSPR stimulus.

In the first series of materials, nanozymes, silver nanoparticles (AgNP) were studied as antimicrobial agents against multidrug-resistant *P. aeruginosa*. Under light stimulus on LSPR, AgNP are able to cause cell death to 100% of bacteria in just 1 h of treatment. This efficiency is related to the higher production of reactive oxygen species (ROS) in the combination of AgNP and light, demonstrating the effect of LSPR. Bimetallic AgAu nanoparticles were also studied. Bimetallic AgAu alloys supported on SiO_2 were synthesized mechanochemically and used in the hydrogenation of 2-nitroaniline. In this case, a 4-fold increase in the rate constant was observed, as well as an increase in catalytic conversion compared to the individual metals. Bimetallic AgAu nanoshells supported on graphene oxide (GO) and SiO_2 submicrospheres were synthesized by galvanic substitution in solution. The nanoshells were tested as peroxidases for the electrochemical detection of H_2O_2 by its reduction reaction (HPRR), with influence of the composition and support, as well as the excitation region of the LSPR. Compared to the dark, AgAu/GO showed a 100% increase in sensitivity under the stimuli of 405 or 533 nm, while AgAu/SiO2 led to a 120% improvement under the stimulus of 650 nm.

In the second type of materials studied, nanobioconjugates, gold nanoparticles (AuNP) were studied as support for immobilization of two biomolecules: Lipase from *Candida sp.* (CALB) and Cytochrome C (CytC). Immobilized CALB showed improvement in its catalytic activity under LSPR stimulation of AuNP. The enzyme was investigated in terms of secondary structure changes by local heat generation. Circular dichroism and Raman showed intense changes, especially in the α-helix, after immobilization, but also under the change of temperature and incidence of light. Molecular Dynamics (MD) demonstrates that these stimuli can lead to the exposure of the Ser105-Asp187-His224 catalytic triad and, therefore, would promote greater catalytic activity. Similarly, when CytC is immobilized in AuNP, changes in its secondary structure were observed, especially with a significant loss of α-helix and gain of β-sheets, in addition to a considerable improvement in thermal stability. Catalytically, the CytC@AuNP nanobioconjugate showed a 68% improvement in catalytic conversion. Under LSPR, only the nanobioconjugate had a performance improvement of 12%. Thus, this thesis demonstrates the advantages of using metallic nanoparticles in nanobiocatalysis, whether through the use of nanozymes or nanobioconjugates, also expanding what we know about the interaction of LSPR and biomolecules.

Keywords: LSPR, Nanobiocatalysis, Nanobioconjugates, Nanozymes, Plasmonic Catalysis.

List of Publications

This thesis is a compilation of published or submitted articles by Rafael Trivella Pacheco da Silva during the Doctoral work. All of them are going to be attached in section 3 and overviewed in a didactical order. They are listed here in chronological order:

1. **Rafael T. P. da Silva**, Marcos V. Petri, Estela Y. Valencia, Pedro H. C. Camargo, Susana I. Cordoba de Torresi, and Beny Spira. Visible light plasmon excitation of silver nanoparticles against antibiotic-resistant *Pseudomonas aeruginosa*. *Photodiagnosis Photodyn. Ther.*, **2020**, 31, p. 101908-13555. DOI: 10.1016/j.pdpdt.2020.101908
2. **Rafael T. P. da Silva**, Maria P. S. Rodrigues, Gabriela F. D. Davilla, Adriano M. R. P. da Silva, André H. B. Dourado, and Susana I. Cordoba de Torresi. AgAu Hollow Nanoshells on Layered Graphene Oxide and Silica Submicrospheres as Plasmonic Nanozymes for Light-Enhanced Electrochemical H_2O_2 Sensing. *ACS Appl. Nano Mater.*, **2021**, 4, 12062-12072. DOI: 10.1021/acsanm.1c02611
3. **Rafael T. P. da Silva**, Heloise R. de Barros, Daiana M. F. Sandrini, and Susana I. Cordoba de Torresi. Stimuli-Responsive Regulation of Biocatalysis through Metallic Nanoparticle Interaction. *Bioconjugate Chem.* **2022**, 33, 53-56. DOI: 10.1021/acs.bioconjchem.1c00515
4. **Rafael T. P. da Silva**, Susana I. Cordoba de Torresi, and Paulo F. M. de Oliveira. Mechanochemical Strategies for the Preparation of SiO2-Supported AgAu Nanoalloy Catalysts. *Front. Chem.* **2022**, 10:836597. DOI: 10.3389/fchem.2022.836597
5. **Rafael T. P. da Silva**, Heloise R. de Barros, Rafaella F. Fernandes, Marcia L. A. Temperini, and Susana I. Cordoba de Torresi. Cytochrome C with Peroxidase-like Activity Supported on Plasmonic AuNPs: Improved Stability and Enhanced Nanobioplasmonic Catalytic Conversion. **Submitted**. *ChemCatChem.* **2022**

6. **Rafael T. P. da Silva**, Heloise R. de Barros, Rafaella F. Fernandes, Jhoan Toro-Mendoza, Ivan Colluzza, Marcia L. A. Temperini, and Susana I. Cordoba de Torresi. Physicochemical insights into the LSPR-driven Enzymatic Activity of Lipase Adsorbed on Gold Nanoparticles. **Submitted**. *Angew. Chem.* **2022**

Summary

1. Introduction 16

2. Goals 18

3. Articles Overview 19

3.1 Nanozymes 19

3.1.1 Visible Light Plasmon Excitation of Silver Nanoparticles Against Antibiotic-Resistant *Pseudomonas aeruginosa* (Attachment 1) 19

3.1.2 Mechanochemical Strategies for the Preparation of SiO_2-Supported AgAu Nanoalloy Catalysts (Attachment 2) 29

3.1.3 AgAu Hollow Nanoshells on Layered Graphene Oxide and Silica Submicrospheres as Plasmonic Nanozymes for Light-Enhanced Electrochemical H_2O_2 Sensing (Attachment 3) 50

3.2 Nanobioconjugates 75

3.2.1 Stimuli-Responsive Regulation of Biocatalysis through Metallic Nanoparticle Interaction (Attachment 4) 75

3.2.2 Physicochemical insights into the LSPR-driven Enzymatic Activity of Lipase Adsorbed on Gold Nanoparticles (Attachment 5) 90

3.2.3 Cytochrome C with Peroxidase-like Activity Supported on Plasmonic AuNPs: Improved Stability and Enhanced Nanobioplasmonic Catalytic Conversion (Attachment 6) 105

4. Conclusions 118

5. References 121

6. Appendix 125

7. Curriculum Vitae 131

1. Introduction

In the last decades, the development of nanobiotechnology brought together scientists from different fields, such as chemists, molecular biologists, chemical engineers, biochemists, and materials scientists[1]. As nanotechnology made progress in its findings, polymeric, lipidic, and metallic nanostructures played a major role in the nanobiotechnological approaches[2]. Among this diversity, nanoparticles (NP) from noble metals present unique optical[3], electronic[4], and thermal[5] properties that differ from their bulk counterpart and have been broadly used in biotechnology. Metallic NPs display high surface area[6] and are relatively inert in complex environmental conditions[7]. Besides, their design is versatile in terms of size, shape, and composition[8], which includes the synergic combination of more than two metals in a single nanostructure[9]. Metallic NPs are liable to be smart materials, with a large variety of outcomes upon a range of external stimuli[10]. In the last years, the interaction of noble metal NPs with light has been explored due to the formation of localized surface plasmon resonance (LSPR), leading to physical events that benefit, among others, the fields of catalysis, spectroscopy, and photodynamic therapy[11].

Within nanobiotechnology, the research on novel nanobiocatalysts made from metallic NPs meets the high demand from the biocatalysis market, which is expected to reach U$10 billion by 2024[12]. Nanoparticles made of noble metals offer good platforms for biomolecule immobilization in hybrid systems called nanobioconjugates[13]. Often, nanobioconjugates improve the stability of biomolecules[14], as well as enhance their catalytic activity through the induction of changes in their secondary structure[15]. In a second strategy, the replacement of biomolecules by enzyme-like catalytic metallic nanoparticles has been gaining space with the development of nanozymes[16–18].

Nanozymes perform similarly to enzymes, although are promising for the replacement of these biomolecules, as they are less costly and usually more stable in a broader range of media.

In this thesis, we explored the design and application of nanozymes and nanobioconjugates based on silver, gold, and their nanoalloys (**Figure 1**). In Chapter 3.1, we approach nanozymes of AgNPs and AgAu nanoalloys. In Chapter 3.2, we investigate nanobioconjugates based on AuNPs. The systems were synthesized, characterized, and applied in heterogeneous catalysis and electrocatalytic reactions, such as hydrogenation, oxidation, and hydrolysis. In addition, nanobioconjugates were studied according to the biomolecule stability and changes in secondary structure upon adsorption and external stimuli application. LSPR-driven catalysis was investigated using the electromagnetic field as an external stimulus to improve catalytic activity and possible changes in catalytic mechanisms. This thesis enlightens the use of metal-based nanozymes and nanobioconjugates in nanobiocatalysis, demonstrating the benefits of the use of external stimuli, in special LSPR, to optimize the efficiency of worldwide used biocatalysts.

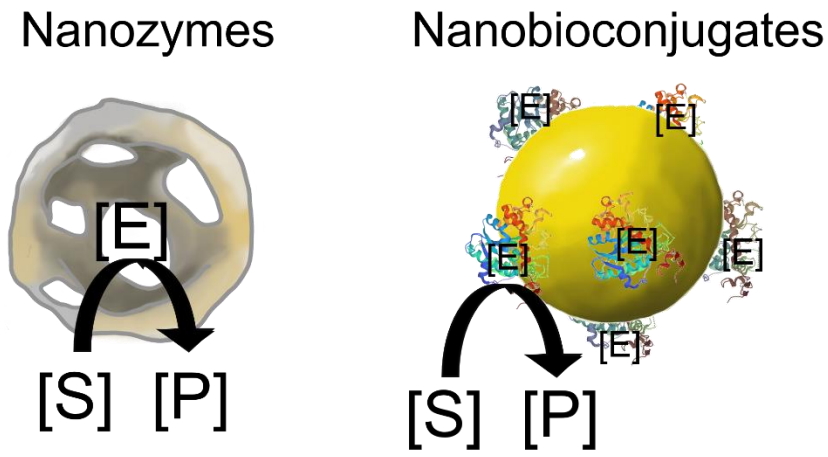


Figure 1 - General scheme of nanozymes and nanobioconjugates. [S] = substrates, [P] = products, [E] = enzyme/nanozyme.

2. Goals

- Evaluate the potential of nanozymes based on monometallic Ag nanoparticles and bimetallic AgAu nanoparticles toward catalytic and biocatalytic reactions, such as hydrogenation and oxidation;
- Design of nanobioconjugates through the immobilization of biomolecules on Au nanoparticles, in particular CALB and CytC, and evaluate the formation, structure and catalytic performance of the nanohybrids;
- Explore the mechanisms and outcomes of LSPR-driven nanobiocatalysis in nanozymes and nanobioconjugates.

3. Articles Overview

In this section, an overview of each article will be presented, showing the main goals and results obtained, followed by the article itself. The articles are presented in a didactical order and their connection is discussed in each overview. Their copyrights are in the Appendix section.

3.1 Nanozymes

3.1.1 Visible Light Plasmon Excitation of Silver Nanoparticles Against Antibiotic-Resistant *Pseudomonas aeruginosa* (Attachment 1)

Author Contribution: The author participated in conceiving the idea, designing the experiments, performing the assays, and writing the paper.

Multidrug-resistant pathogens are considered one of the top 10 global public health threats by the World Health Organization (WHO)[19]. Among the microorganisms considered on the priority list for research and development of new antibiotics to WHO, carbapenem-resistant *Pseudomonas aeruginosa* is in the critical level.

For thousands of years, silver is known for being an antibacterial and therapeutical agent[20]. With the development of nanotechnology, hundreds of commercial products have been created to prevent bacterial proliferation in clothes, toothbrushes, beauty products, etc[21]. Mechanistically, the antimicrobial activity of AgNP is still under debate. Most likely, it arises from a combination of parallel mechanisms: i) the high affinity of Ag^+ and AgNP to biomolecules such as proteins and nucleic acids and their deactivation; ii) Ag^+ and AgNP generating Reactive Oxygen Species (ROS)

that will further damage cell components leading to cell death[22]. In parallel, the development of light therapy against microorganisms has gained relevance in the last decades[23].

In this part of the work, we focus on the combination of both AgNP and light therapy as an antimicrobial strategy against antibiotic-resistant *P. aeruginosa*. For the first time, the interaction of AgNP with an external visible light source emitting mainly in the same wavelength as AgNP LSPR was investigated in terms of LSPR-driven outcomes to antimicrobial activity. Minimum Inhibitory Concentration (MIC) was determined for AgNP +light system as 5.0 μg/mL for *P. aeruginosa*, which was half the value found for AgNP in the dark. Kirby Bauer disk diffusion test showed that, on a solid medium, the inhibition halo for 10 μg/mL of AgNP + light had the same diameter presented for 40 μg/mL AgNP in dark conditions. These two tests indicated that a synergic effect could have taken place. Then, growth curves of *P. aeruginosa* for 2 h showed that light itself induces only a small decrease in the growth rate, analyzed by colony forming units (CFU/mL). On the contrary, in the presence AgNP in 1x MIC, *P. aeuginosa* had 1.1% of survival after 2 h of treatment. With LSPR stimulus, AgNP in 1x MIC showed complete cell death after 2 h of treatment. In twice the concentration of AgNP, 2x MIC, 2 h of treatment was enough to kill 100% of bacteria in the dark. However, it needed only 1 h of treatment to AgNP + light to achieve the same result. Mechanistically, it was proposed that ROS generation could be harvested from LSPR stimulus by hot carriers transfer on AgNP surface, which acted as an oxidase nanozyme. ROS levels were determined by flow cytometry. The treatment with AgNP + light had a 4.8-fold enhancement compared to the control, and 2.5-fold increase compared to AgNP in the dark. AgNP oxidation by Ostwald ripening was studied by Inductively Coupled Plasma Optical Emission Spectrometry (ICP-OES) in the presence and absence of light. Although there was an increase of

Ag^+ release observed upon light stimulus, it reached its maximum only after 6 h of treatment and corresponded to only 0.4 % (w/w) of AgNP under analysis, which indicates that the release of Ag^+ plays a secondary role in the antimicrobial mechanism of AgNP + light. This study is an inaugural work on LSPR-driven effects of AgNP as an antimicrobial agent and revealed an *in vitro* insight for a successful treatment against multidrug-resistant *P. aeruginosa*.

Photodiagnosis and Photodynamic Therapy 31 (2020) 101908

Contents lists available at ScienceDirect

Photodiagnosis and Photodynamic Therapy

journal homepage: www.elsevier.com/locate/pdpdt

Visible light plasmon excitation of silver nanoparticles against antibiotic-resistant *Pseudomonas aeruginosa*

Rafael T.P. da Silva[a,1], Marcos V. Petri[a,1], Estela Y. Valencia[b,1], Pedro H.C. Camargo[a], Susana I.C. de Torresi[a], Beny Spira[b,*]

[a] Department of Fundamental Chemistry, Institute of Chemistry, University of São Paulo, Brazil
[b] Department of Microbiology, Institute of Biomedical Sciences, University of São Paulo, Brazil

ARTICLE INFO

Keywords:
Silver nanoparticles
Surface plasmon resonance
Pseudomonas aeruginosa
Reactive oxygen species

ABSTRACT

The interaction of metallic nanoparticles with light excites a local surface plasmon resonance (LSPR). This phenomenon enables the transfer of hot electrons to substrates that release Reactive Oxygen Species (ROS). In this context, the present study aimed at enhancing the antibacterial effect of citrate-covered silver nanoparticles (AgNPs) by LSPR excitation with visible LED. AgNPs possess excellent antimicrobial properties against *Pseudomonas aeruginosa*, one of the most refractory organisms to antibiotic treatment. The Minimum Inhibitory Concentration (MIC) of the AgNPs was 10 μg/ml under dark conditions and 5 μg/ml under light conditions. The combination of light and AgNPs led to 100% cell death after 60 min. Flow cytometry quantification showed that bacteria treated with LSPR-stimulated AgNPs displayed 4.8 times more ROS. This significant increase in ROS possibly accounts for most of the antimicrobial effect of the AgNPs. In addition, light exposition caused a small release of silver ions (0.4%) suggesting that silver ions may play a secondary role in *P. aeruginosa* death. Overall, the results presented here show that LSPR stimulation of AgNPs by visible light enhances the antimicrobial activity of silver nanoparticles and can be an alternative for the treatment of topic infections caused by antibiotic-resistant bacteria such as *P. aeruginosa*.

1. Introduction

Metallic nanoparticles posses unique properties that can be used to treat microbial infections. They are easily synthesized and tweaked in their composition, structure, shape and scale. Electronic, optical and chemical properties of nanoparticles were set through synthetic techniques devised in the past decades [1]. Even small variations in one of the synthesis parameters may result in new properties that are absent in the analogous bulk material. Due to its high range of controllable features, metallic nanoparticles are now used in many processes, such as catalysis [2], SERS [3], electroanalytical sensors [4], plasmonics [5], photonics [6], photodynamic therapy [7,8] and others. The synthesis of silver nanoparticles (AgNPs) can be tightly controlled resulting in compounds with very different features ranging from small and simple spheroidal AgNPs [9] to more complex geometries [10,11] and even asymmetric shapes [12] with solid or hollow interiors [13]. Historically, silver has been extensively used as an antimicrobial agent. Many different commercial products relying on silver biocidal properties have been produced, most of them in the last 10 years. The wide variety of AgNPs as well as the intrinsic properties of metallic silver in relation to biological systems and biomolecules fostered the extensive use of AgNPs in medical applications, such as cancer treatment [14], drug delivery [15], imaging [16], antimicrobial treatment [17] and photodynamic inactivation [18]. *P. aeruginosa* is a ubiquitous Gram-negative γ-proteobacterium and an opportunistic pathogen associated with nosocomial infections. It also affects patients afflicted by chronic respiratory diseases such as cystic fibrosis [19]. The relatively large genome and genetic complexity of *P. aeruginosa* [20,21] provides insights into the basis of its versatility and ability to colonize the soil, water bodies, as well as plants and animal tissues [21]. *P. aeruginosa* infections are frequently refractory to quinolone, aminoglycosides and β-lactam antibiotics [22]. In fact, owe to its outer membrane low permeability, expression of efflux pumps, and biofilm formation, *P. aeruginosa* is one of the most antibiotic-resistant organisms that afflict humans. Skin infections caused by *P. aeruginosa* on burn victims are particularly problematic, in part due to the lack of appropriate treatment [23]. The World Health Organization (WHO) included carbapenem resistant *P. aeruginosa* in a list of critical bacteria to which the

* Corresponding author.
E-mail address: benys@usp.br (B. Spira).
[1] These authors contributed equally to this work.

https://doi.org/10.1016/j.pdpdt.2020.101908
Received 25 March 2020; Received in revised form 11 June 2020; Accepted 26 June 2020
Available online 05 July 2020
1572-1000/ © 2020 Elsevier B.V. All rights reserved.

research and development of new antibiotics and alternative treatments is of paramount urgency [24]. Anti-bacterial treatments with visible light, such as blue light therapy (BLT) have been emerging as non-invasive treatments of topic bacterial infections [25]. In a conducting medium, surface electrons of nanoparticles may oscillate in a resonant condition with a coupled electromagnetic field, resulting in a phenomenon called Local Surface Plasmon Resonance (LSPR), which confer on nanoparticles unique physical properties. Among them, local temperature increase, enhancement of optical near fields surrounding the particle and the generation of hot carriers can be highlighted [26]. The interaction of visible light with AgNPs in the range of LSPR and its possible antipseudomonal activity has not been thoroughly studied [25].

The antimicrobial efficacy of AgNPs has been evaluated in a broad range of microbes, including MDR (multi-drug resistant) and non-MDR bacterial strains, fungi, and viruses [27]. AgNPs exhibited antimicrobial property against ten different pathogenic bacteria, of which three are MDR strains (extended spectrum β-lactamase positive *Escherichia coli*, *Staphylococcus aureus* (MRSA) and teicoplanin resistant *Streptococcus Pneumoniae*) [28]. AgNPs have also been shown to reduce viability, growth yield and bacterial biofilms of both Gram-positive (*Staphylococcus epidermidis*, *Micrococcus luteus*, *Listeria monocytogenes*) and Gram-negative bacteria (*Proteus mirabilis*, *Escherichia coli*, *Acinetobacter baumannii*, *Klebsiella pneumoniae*, *Pseudomonas aeruginosa*, *Salmonella*, *Vibrio cholera*) [29]. Nevertheless, the extent of the bactericidal effect of AgNPs is not uniform across all bacterial species [30]. For instance, killing of *P. aeruginosa* and *S. aureus*, which are frequently multidrug resistant, often require higher concentrations of AgNPs [31–33,28].

Inspired by these findings, the present work describes the use of the concept of LSPR in order to enhance the antimicrobial properties of AgNPs against *P. aeruginosa* with the help of a white LED lamp. This strategy revealed a quicker and more effective treatment against *P. aeruginosa*, being a promising improvement in the fight against this pathogen.

2. Materials and methods

2.1. Materials

Silver nitrate ($AgNO_3$, Sigma–Aldrich, ≥99%), sodium citrate (Sigma–Aldrich, ≥99%), lysogeny broth (LB) medium (KASVI, Curitiba, Brazil), phosphate buffer saline (PBS, pH 7.4), bacteriological agar (KASVI, Curitiba, Brazil), Mueller-Hinton broth (BD Difco) and 2′,7′-dichlorofluorescin diacetate (DCFH-DA, ≥97%, Sigma–Aldrich) were of analytical grade. All solutions were prepared using deionized water (18.2 MΩ).

2.2. Synthesis of Silver Nanoparticles (AgNPs)

Preparation of AgNPs followed a slightly modified method described by Lee and Meisel [34]. Briefly, $AgNO_3$ (90 mg) was dissolved in 500 mL of distilled water. The solution was heated until boiling under magnetic stirring. 10 mL of a 34 mM sodium citrate solution were then added and the mixing proceeded for another 1 h. The suspension was transferred to an amber flask and stored at room temperature until further use.

2.3. Sample preparation for electron microscopy (SEM and TEM)

1 mL of the AgNPs suspension was washed three times by successive rounds of centrifugation at 17,000 rpm. The pellet containing the AgNPs was resuspended in 20 L or 300 L of water. For the SEM analysis, 1 L of the concentrated suspension was deposited onto a 1 cm^2 silicon wafer and let dry at room temperature. For the TEM analysis, 10 L of the suspension was transferred to a standard formvar coated copper TEM grid and dried at room temperature. Particles size were analyzed with the help of the ImageJ 2.0 software.

2.4. Media and bacterial growth conditions

Pseudomonas aeruginosa (strain PA14) was typically cultivated in LB medium at 37 °C for 16 h. The culture was then diluted 1/100 in 5 mL Mueller Hinton (MH) medium (MHA-DIFCO), and grown until the exponential growth phase (OD_{600} = 0.1). Bacterial growth rate was determined by growing cells under dark or light conditions in MH medium. At different time points samples were harvested, diluted and plated on MH or L-agar plates. The number of colony forming units (CFU/mL) was assessed following an overnight incubation.

2.5. Determination of the minimum inhibitory concentration (MIC)

MIC determination was performed by the broth microdilution technique (Clinical and Laboratory Standards Institute – CLSI, 2015). Briefly, 10^5 bacteria/ml were inoculated in 96-well plates containing MH medium and incubated in the presence of increasing concentrations of AgNPs (0 to 80 μg/mL). One plate was covered with aluminium foil (dark conditions) and the other was placed on the top of it (light conditions). The plate on the top was positioned 10 cm away from a LED floodlight (50 W). Both plates were incubated overnight at 30 °C. On the next day the turbidity of the cultures was measured at 600 nm in an EpochTM Microplate Spectrophotometer (BioTek).

2.6. Antimicrobial activity of AgNPs (disc diffusion method)

The antimicrobial activity of AgNPs in solid medium was evaluated through the Kirby-Bauer disc diffusion method according to standard guidelines (Clinical and Laboratory Standards Institute – CLSI, 2015). MH agar plates were evenly swabbed with 100 L of a PA14 culture (OD_{600} = 0.1). Sterile filter paper discs (6 mm diameter, Oxoid) were uniformly placed on the plate surface and 10 L of different concentrations of AgNPs were dropped onto each disc. As a negative control sodium citrate was used. Plates were incubated overnight at 30 °C and the halos formed by the antibiotic activity were measured with the help of the ImageJ 2.0 software.

2.7. Kinetics of AgNPs antibacterial effect

Each well of two 24-well plates were filled with 1.5 mL of MH medium containing different concentrations of AgNPs. A final concentration of exponentially-growing 10^5 cells/mL was added to each well. One of the plates was covered with aluminum foil (dark conditions) and the other one was placed on its top (light conditions). Both plates were statically incubated at 30 °C, while the plate on the top was 10 cm away from the LED floodlight (50 W). Aliquots of 100 L were withdrawn at 0, 15, 30 and 60 min from both plates and subsequently diluted in 0.9% NaCl, plated on L-Agar and incubated for 24 h at 37 °C. The number of colony forming units (CFU/mL) was determined. This experiment was performed with twelve biological replicates.

2.8. Intracellular ROS assay

Three independent overnight cultures of *P. aeruginosa* were diluted 1:100 in fresh MH medium, incubated under agitation until reaching the concentration of 10^8 cells/mL. Different concentrations of AgNPs and 20 M DCFH-DA were then added. The cultures were incubated at 30 °C for 1 h in the presence and absence of light exposition. Then, 1 mL of each culture was withdrawn and centrifuged at 8000 rpm for 5 min. The pellets were washed with 1 mL of PBS and suspended again in 100 L PBS. The fluorescence emitted by the intracellular oxidation of the dye was determined using the BD AccuriTM C6 flow cytometer at the excitation wavelength of 488 nm and at an emission wavelength of 535 nm.

2.9. Quantification of released Ag^+

Six dialysis membranes each filled with 20 mL AgNPs were placed in 800 mL beakers filled with 500 mL distilled water under magnetic stirring. Three of them were placed 10 cm away from the floodlight, while the other three were covered in aluminum foil. After 1, 2, 4, 6 and 24 h, 5 mL aliquots of water from each beaker were withdrawn and stored for further analysis. Silver ions were detected by iCAPTM 7000 Plus Series ICP-OES (Thermo ScientificTM).

2.10. Statistical analyses

Statistical significance was calculated by ANOVA followed by Tukey pairwise comparison. Values of $p < 0.05$ were considered statistically significant.

3. Results and discussion

3.1. AgNPs synthesis

Citrate-covered AgNPs with a diameter of 20 ± 3 nm were synthesized (Fig. 1a). Citrate has the ability to reduce silver ions to metallic silver [35]. It interacts with the 111 facets of Ag ensuring sufficient capping of the nanoparticle surface, reducing its surface energy and allowing stabilization at the nanometric size [36]. In addition, *P. aeruginosa* is able to ferment and utilize citrate as a carbon source. Thus it is not supposed to negatively affect bacterial growth or viability in any fashion.

The extinction spectrum of the nanoparticles displayed a full width at half maximum (FWHM) of 131 nm and a maximum at 436 nm, the LSPR wavelength of the AgNPs (Fig. 1b). This wavelength matches the maximum emission from the LED floodlight used in this study, suggesting that the LSPR stimulus would be optimal when this light source is applied. The extinction band is broadened due to a standard deviation in particle size distribution, which represents ca. 15% of the average nanoparticle diameter. This is a typical spectrum for AgNPs synthesized by the citrate method [37,38]. To take advantage of LSPR, AgNPs were excited by an external radiation source in the region of their maximum absorption. To avoid possible mutagenic and carcinogenic effects of UV radiation, a light source that did not emit in the UV region was chosen.

3.2. Bactericidal effect of AgNPs on P. aeruginosa

Preliminary assays showed that the synthesized AgNPs displayed strong antimicrobial activity against *P. aeruginosa*. The minimal inhibitory concentration (MIC) of the AgNPs was 10 g/mL, which is comparable to values reported by similar studies in this bacterial species [33,32,39]. When the AgNPs were exposed to light the MIC dropped to 5 g/mL. The minimal bactericidal concentrations (MBC) were 20 g/mL and 10 g/mL under dark and light conditions, respectively. For the MIC analysis 12 independent cultures for each AgNP concentration (from 0.2 to 80 g/mL) were performed under each condition – light and dark. It should be mentioned that to avoid shadows and edge effects bacteria were seeded and grown only in wells located in the central portion of the 96-well plate. To rule out any differential effect of light exposure on the temperature of the growth media both light-treated and dark-treated plates were positioned under the light source, only that the dark-treated plates were covered with aluminum foil. In addition to the MIC assay in liquid medium, a Kirby-Bauer disc diffusion assay using filters containing different concentrations of AgNPs was performed in the presence and absence of light (Fig. 2). In the absence of light an inhibition halo became apparent with AgNPs concentrations higher than 15 g/mL and larger halos were observed with increasing AgNPs concentrations. In contrast, when the AgNPs were exposed to light, 10 g/mL sufficed to produce a halo similar to that observed when the bacteria were treated with 40 g/mL AgNPs in the dark, indicating that light considerably enhanced the bactericidal effect of the silver nanoparticles.

It is worth noticing that upon light exposition, there is a decrease in the intensity of the green color of *P. aeruginosa* colonies (not shown). The green color is caused by the pigments pyoverdine and pyocyanin, which are well-known virulence factors of *P. aeruginosa* and legitimate targets for the screening of antimicrobial compounds [40–42]. Accordingly, some studies have shown that light reduces the concentration of pyocyanin in *P. aeruginosa* and that this effect was dependent on light intensity and wavelength [43]. It has also been shown that high doses of blue light treatment inhibited the activity of pyocyanin, staphylolysin, pseudolysin and other proteases [23,25]. Furthermore, it has been demonstrated that pyocyanin confers on *P. aeruginosa* resistance to ionic silver [44]. It is thus possible that pyocyanin inhibition by LED floodlight contributes to the antipseudomonal effect of AgNPs and to the reduced virulence of the surviving bacteria.

To further explore the effect of light exposition on *P. aeruginosa*, bacteria were grown for 60 min in MH medium without AgNPs in the presence or absence of light (Fig. 6). The calculated growth rates were 1.26 h^{-1} and 1.04 h^{-1} under dark and light conditions, respectively. This 17.5% reduction in growth rate suggests that light exposition mildly interferes with bacterial growth. We also measured the effect of AgNPs on cell viability at different time intervals. Bacteria treated for 15, 30, 60 and 120 min with 10 g/mL AgNPs showed a survival rate of 12.8%, 4.4%, 1.6% and 1.1% in the dark and 4.5%, 0.7%, 0.2% and 0.0% under light conditions, respectively (Fig. 3a), while bacteria treated with 20 g/mL showed a survival rate of 20.6%, 6.4%, 2.2% and 0.0% (dark conditons) and 3.6%, 0.4%, 0.0% and 0.0% (light conditions) at 15, 30, 60 and 120 min, respectively (Fig. 3b). Therefore, an 1 h treatment with 10 g/mL AgNPs under light exposition (2× MIC)

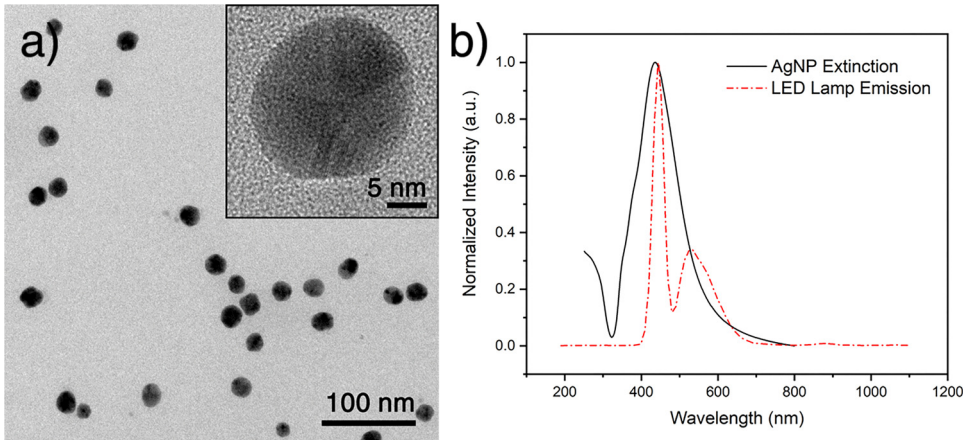


Fig. 1. Characterization of AgNPs. (a) Representative TEM and HRTEM (inset) micrographs of citrate-coated AgNPs with an average diameter of 20 ± 3 nm. (b) Extinction spectrum of AgNPs showing the SPR peak at 436 nm superposed with the LED floodlight emission spectrum. The floodlight emission has a maximum intensity at 448 nm, with no measurable emission from 190 to 406 nm.

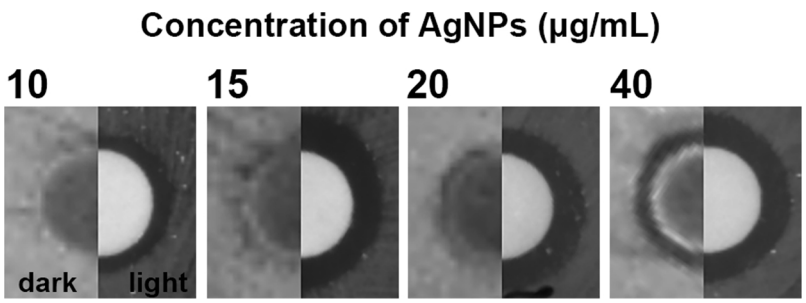


Fig. 2. Effect of AgNPs on *P. aeruginosa* viability assayed by disc diffusion assay. Paper discs each containing 10 L of 10, 15, 20 or 40 g/mL AgNPs were placed on MH plates previously spread to confluency with *P. aeruginosa* cells. Each plate was incubated overnight under dark or light conditions. The pictures on the left show the halos produced by the respective AgNP concentration in plates incubated in the dark, while those at the right show the halos of plates incubated under light.

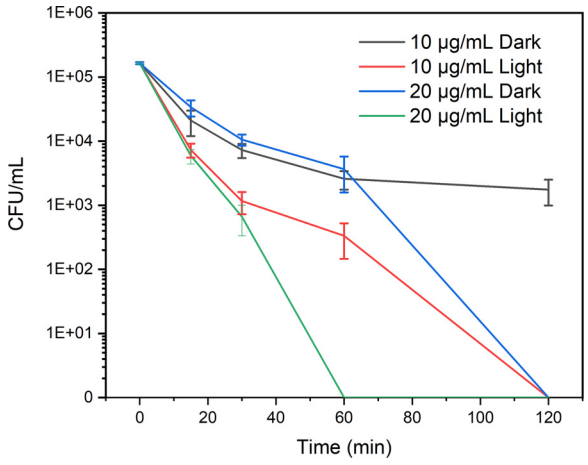


Fig. 3. Combined effect of light and AgNPs on bacterial viability. Bacteria were grown in MH medium containing 10 g/mL AgNPs (a), or 20 g/mL AgNPs (b), in the absence (black) or presence (white) of light. Aliquots of 100 L were withdrawn at 0, 15, 30 and 60 min to determine bacterial survival. The initial number of cells in all experiments was $1.64 \cdot 10^5$ CFU/mL. Each bar represents the mean ± SD of 12 independent cultures. *$p < 0.05$.

suffices to kill all $1.64 \cdot 10^5$ bacteria present in the sample. These results indicate that AgNPs display a bactericidal effect on *P. aeruginosa* and that the ability to kill this bacterium is enhanced upon exposition of AgNPs to white light.

It has previously been reported that the dimensions of silver nanoparticles affect the antimicrobial activity of colloidal AgNPs [32]. The MICs of AgNPs against *P. aeruginosa* thus far reported in the literature are: 8 g/mL for AgNPs of 8 nm (*P. aeruginosa* PAO1) [33]; 16 g/mL for particles of 64 nm (*P. aeruginosa* ATCC 10145) [39]; AgNPs of 9 nm and 14 nm resulted in MICs of 14 g/mL and 29 g/mL, respectively, in *P. aeruginosa* strain CCM 3955 [32]. The aforementioned reports tested the effect on AgNPs in the absence of light excitation. However, there is one study in which the effect of AgNPs (15–20 nm) on the viablity of a clinical isolate of *P. aeruginosa* was tested. The reported MIC was 8 mg/ml, three-orders of magnitude above the MIC reported in our manuscript [45]. In contrast, the data presented here showed that our 20 nm AgNPs displayed a MIC of 10 g/ml which was further reduced to 5 g/ml under white light exposition. This is a tremendous improvement when compared to the above mentioned study.

3.3. Effect of light and AgNPs on ROS generation

The antimicrobial mechanism of action of AgNPs is still not fully understood mainly due to the difficulty in evaluating the individual contributions of nanosized metallic silver and silver ions that are released by the former [46,47]. While some studies support the idea that silver ions play the main role in cellular damage [48], others claim that the strong antibacterial activity of AgNPs is associated with the introduction of nicks in the cytoplasmic membrane which ultimately lead to cell death [49]. Previous studies showed that AgNPs promote the induction of reactive oxygen species (ROS) [50,51] and enhance the expression of superoxide dismutase, catalase and peroxidase [51]. These authors concluded that the main mechanism of antimicrobial action of AgNPs involves the disequilibrium of oxidation and anti-oxidation processes and the inability to eliminate ROS. High concentration of ROS in the bacterium lead to oxidative stress with the consequent damage of the cell cytoskeleton, proteins and nucleic acids oxidation, which potentially lead to chromosomal aberrations and cell demise.

To test whether our AgNPs cause oxidative stress, the intracellular level of ROS in *P. aeruginosa* was evaluated. Bacteria were treated with 10 g/mL AgNPs under light or dark conditions followed by exposure to 2′,7′-Dichlorofluorescin diacetate (DCFH-DA). This compound diffuses into the cell where it is hydrolyzed by intracellular esterases (DCFH), resulting in the production of 2′,7′-dichlorofluorescein (DCF), which fluoresces upon oxidation. The intracellular ROS level thus correlates with the level of fluorescence emitted by DCF in the presence of ROS such as H_2O_2, ROO^- and $ONOO^-$ [52]. Fig. 4 shows that after 1 h in the presence of AgNPs, the level of ROS increased by 2.5-fold (dark) and 4.8-fold (light) when compared to the respective controls.

LSPR confer on nanoparticles unique physical properties, such as local increase in temperature, enhancement of optical near fields surrounding the particle and the generation of hot carriers [26]. This last property received a special attention in the field of catalysis due to the possibility of electronic or vibrational activation of substrates or reaction intermediates. Interestingly, recent studies have demonstrated the formation of ROS at the surface of metallic nanoparticles [53–55]. For example, LSPR-based antibacterial treatment with gold nanoparticles has been reported [56–58]. Likewise, the AgNPs antipseudomonal

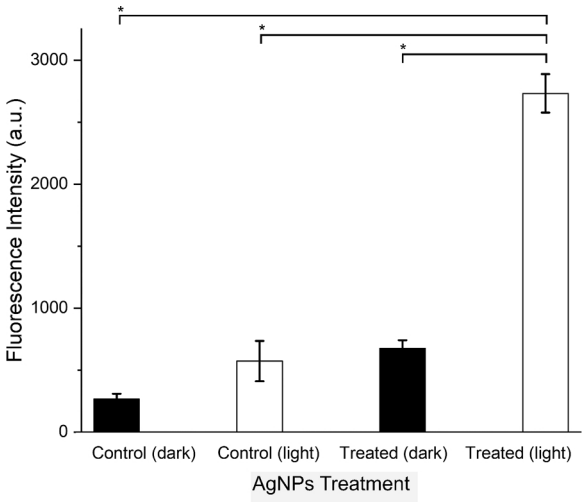


Fig. 4. Light increases intracellular ROS generation in *P. aeruginosa* treated with AgNPs. Bacteria were exposed for 1 h to 10 g/mL AgNPs in the absence or presence of light. Fluorescence intensities of DCFH-DA were measured by flow cytometry. Each point represents the mean ± SD of 3 independent cultures. *Denotes statistical significance with $p < 0.05$.

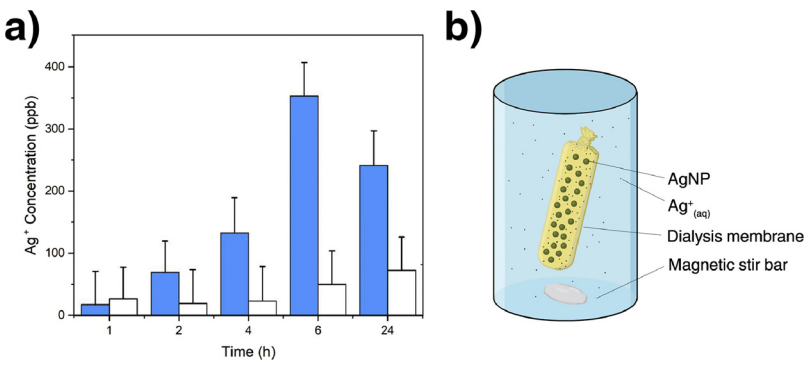


Fig. 5. Concentration of silver ions released by AgNPs through a dialysis membrane over time in the presence (blue color) or absence of light (white color), respectively. A known amount of AgNPs was added to a tightly closed dialysis membrane and the system was submerged in distilled water under magnetic stirring. (a) Analysis of Ag^+ content by ICP-OES. (b) Schematic representation of the dialysis method used to quantify silver ions. (For interpretation of the references to color in this figure legend, the reader is referred to the web version of this article.)

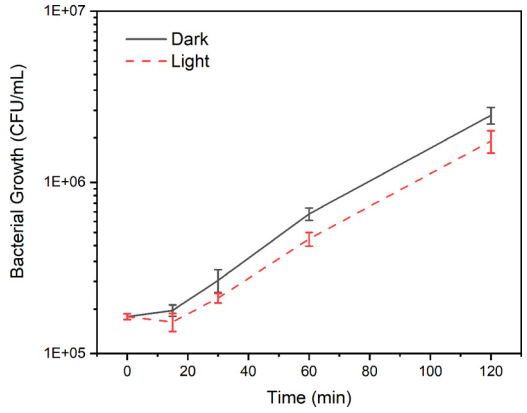


Fig. 6. Effect of light on bacteria growing in MH medium. Bacterial growth rate was determined by growing cells under dark or light conditions in liquid MH medium and measuring the number of colony forming units (CFU/mL) at different time points.

effect reported here was likeley to be enhanced by the formation of ROS at the surface of the nanoparticles via LSPR.

It has also been suggested that the formation of ROS by AgNPs occurs either at the particle surface or it is indirectly caused by Ag^+ ions released from aging nanoparticles [59,60]. To test whether exposition to light affects the production of Ag^+ from AgNPs by an aging process, a closed dialysis membrane filled with an AgNPs suspension was submerged in distilled water and the concentration of released Ag^+ in the solution was followed during 24 h (Fig. 5). At 0 h the concentration of silver ions was below the limit of detection by ICP-OES. The highest concentration of Ag^+ under dark conditions was four times lower than that observed under light exposition. Although the concentration of Ag^+ increased with light treatment, the highest observed Ag^+ concentration (at 6 h, under light exposition) represented only 0.4% (w/w) of the total amount of silver in the sample. Moreover, the release of Ag^+ occurred several hours after AgNPs have already killed the bacteria (see Fig. 3). At the time in which the bactericidal effect and ROS were evaluated (1 h), no significant difference in the concentration of Ag^+ under light or dark conditions was detected. Therefore, the release of Ag^+ by the nanoparticles is unlikely to play a role in the mechanism through which AgNPs cause bacterial death.

3.4. Conclusion

The AgNPs synthesized in this study proved to be effective against *P. aeruginosa*. The bactericidal effect of AgNPs were intensified upon irradiation by white light, indicating that the combination of light and AgNPs ensures a quick and more effective treatment against this pathogen. A treatment period of one hour was sufficient to kill all the bacteria present in the suspension. The bactericidal effect of AgNPs was associated with the upsurge of intracellular ROS, which was in part generated by the hot carrier transfer of LSPR on the AgNPs surface. In conclusion, the data presented here support the use of a viable treatment that combines two pre-existing strategies: AgNPs application and light exposition, that synergistically enhance the treatment of *P. aeruginosa* topical infections.

Conflicts of interest

None declared.

Acknowledgements

This work was supported by FAPESP (grant number 2018/16219-5). E.Y.V was funded by a postdoctoral fellowship from PNPD/CAPES (grant < /GN2 > 1680341 < /GN2 >). R.T.P.S was funded by a PhD fellowship from CAPES (grant 88882.328241/2019-01). BS is a recipient of a CNPq productivity scholarship.

References

[1] Y. Sun, Shape-controlled synthesis of gold and silver nanoparticles, Science 298 (5601) (2002) 2176–2179, https://doi.org/10.1126/science.1077229.
[2] J. Wang, E.C. Barbosa, Z. Fang, A.L. Parussulo, F.V. Reis, R.A. Ando, K. Araki, H.E. Toma, P.H. Camargo, On the effect of TiO nanocrystallites over the plasmonic photodegradation by nanoparticles, J. Raman Spectrosc. 49 (12) (2018) 1953–1960, https://doi.org/10.1002/jrs.5492.
[3] R. Haldavnekar, K. Venkatakrishnan, B. Tan, Non plasmonic semiconductor quantum SERS probe as a pathway for in vitro cancer detection, Nat. Commun. 9 (1) (2018) 3065, https://doi.org/10.1038/s41467-018-05237-x.
[4] A.H. Dourado, A.G. da Silva, F.A. Pastri, R.L. Munhos, A.P. de Lima Batista, A.G. de Oliveira-Filho, J. Quiroz, D.C. de Oliveira, P.H. Camargo, S.I. Córdoba de Torresi, In situ FTIR insights into the electrooxidation mechanism of glucose as a function of the surface facets of Cu2O-based electrocatalytic sensors, J. Catal. 375 (2019) 95–103, https://doi.org/10.1016/j.jcat.2019.05.032.
[5] R.S. Geonmonond, A.G.M. da Silva, T.S. Rodrigues, I.C. de Freitas, R.A. Ando, T.V. Alves, P.H.C. Camargo, Addressing the effects of size-dependent absorption, scattering, and near-field enhancements in plasmonic catalysis, ChemCatChem 10 (16) (2018) 3447–3452, https://doi.org/10.1002/cctc.201800691.
[6] L. Sun, H. Lin, K.L. Kohlstedt, G.C. Schatz, C.A. Mirkin, Design principles for photonic crystals based on plasmonic nanoparticle superlattices, Proc. Natl. Acad. Sci. USA 115 (28) (2018) 7242–7247, https://doi.org/10.1073/pnas.1800106115.
[7] J. Depciuch, M. Stec, B. Klebowski, A. Maximenko, E. Drzymala, J. Baran, M. Parlinska-Wojtan, Size effect of platinum nanoparticles in simulated anticancer photothermal therapy, Photodiagn. Photodyn. Ther. 29 (2020) 101594, https://doi.org/10.1016/j.pdpdt.2019.101594.
[8] J. Krajczewski, K. Rucinska, H.E. Townley, A. Kudelski, Role of various nanoparticles in photodynamic therapy and detection methods of singlet oxygen, Photodiagn. Photodyn. Ther. 26 (2019) 162–178, https://doi.org/10.1016/j.pdpdt.2019.03.016.
[9] N.G. Bastús, F. Merkoçi, J. Piella, V. Puntes, Synthesis of highly monodisperse citrate-stabilized silver nanoparticles of up to 200 nm: kinetic control and catalytic properties, Chem. Mater. 26 (9) (2014) 2836–2846, https://doi.org/10.1021/cm500316k.
[10] Y. Wang, D. Wan, S. Xie, X. Xia, C.Z. Huang, Y. Xia, Synthesis of silver octahedra with controlled sizes and optical properties via seed-mediated growth, ACS Nano 7 (5) (2013) 4586–4594, https://doi.org/10.1021/nn401363e.
[11] H.J. Han, T. Yu, W.-S. Kim, S.H. Im, Highly reproducible polyol synthesis for silver nanocubes, J. Cryst. Growth (September) (2016), https://doi.org/10.1016/j.jcrysgro.2016.09.038.
[12] A.G.M. da Silva, T.S. Rodrigues, J. Wang, L.K. Yamada, T.V. Alves, F.R. Ornellas, R.A. Ando, P.H.C. Camargo, The fault in their shapes: investigating the surface-

plasmon-resonance-mediated catalytic activities of silver quasi-spheres, cubes, triangular prisms, and wires, Langmuir 31 (37) (2015) 10272–10278, https://doi.org/10.1021/acs.langmuir.5b02838.
[13] M.V. Petri, R.A. Ando, P.H. Camargo, Tailoring the structure, composition, optical properties and catalytic activity of Ag-Au nanoparticles by the galvanic replacement reaction, Chem. Phys. Lett. 531 (2012) 188–192, https://doi.org/10.1016/j.cplett.2012.02.039.
[14] H. Chugh, D. Sood, I. Chandra, V. Tomar, G. Dhawan, R. Chandra, Role of gold and silver nanoparticles in cancer nano-medicine, Artif. Cells Nanomed. Biotech. 46 (sup1) (2018) 1210–1220, https://doi.org/10.1080/21691401.2018.1449118.
[15] M. Arif, Q.-J. Dong, M.A. Raja, S. Zeenat, Z. Chi, C.-G. Liu, Development of novel pH-sensitive thiolated chitosan/PMLA nanoparticles for amoxicillin delivery to treat *Helicobacter pylori*, Mater. Sci. Eng. C 83 (2018) 17–24, https://doi.org/10.1016/j.msec.2017.08.038.
[16] M. Ardini, J.-A. Huang, C.S. Sánchez, M.Z. Mousavi, V. Caprettini, N. Maccaferri, G. Melle, G. Bruno, L. Pasquale, D. Garoli, F. De Angelis, Live intracellular biorthogonal imaging by surface enhanced Raman spectroscopy using Alkyne-Silver nanoparticles clusters, Sci. Rep. 8 (1) (2018) 12652, https://doi.org/10.1038/s41598-018-31165-3.
[17] P. Prasher, M. Singh, H. Mudila, Silver nanoparticles as antimicrobial therapeutics: current perspectives and future challenges, 3 Biotech 8 (10) (2018) 411, https://doi.org/10.1007/s13205-018-1436-3.
[18] M.S. Ribeiro, L.S.A. de Melo, S. Farooq, A. Baptista, I.T. Kato, S.C. Núñez, R.E. de Araujo, Photodynamic inactivation assisted by localized surface plasmon resonance of silver nanoparticles: in vitro evaluation on escherichia coli and streptococcus mutans, Photodiagn. Photodyn. Therapy 22 (2018) 191–196, https://doi.org/10.1016/j.pdpdt.2018.04.007.
[19] J.B. Lyczak, C.L. Cannon, G.B. Pier, Lung infections associated with cystic fibrosis, Clin. Microbiol. Rev. 15 (2) (2002) 194–222, https://doi.org/10.1128/CMR.15.2.194-222.2002.
[20] D.G. Lee, J.M. Urbach, G. Wu, N.T. Liberati, R.L. Feinbaum, S. Miyata, L.T. Diggins, J. He, M. Saucier, E. Déziel, L. Friedman, L. Li, G. Grills, K. Montgomery, R. Kucherlapati, L.G. Rahme, F.M. Ausubel, Genomic analysis reveals that *Pseudomonas aeruginosa* virulence is combinatorial, Genome Biol. 7 (10) (2006) R90, https://doi.org/10.1186/gb-2006-7-10-r90.
[21] C.K. Stover, X.Q. Pham, A.L. Erwin, S.D. Mizoguchi, P. Warrener, M.J. Hickey, F.S. Brinkman, W.O. Hufnagle, D.J. Kowalik, M. Lagrou, R.L. Garber, L. Goltry, E. Tolentino, S. Westbrock-Wadman, Y. Yuan, L.L. Brody, S.N. Coulter, K.R. Folger, A. Kas, K. Larbig, R. Lim, K. Smith, D. Spencer, G.K. Wong, Z. Wu, I.T. Paulsen, J. Reizer, M.H. Saier, R.E. Hancock, S. Lory, M.V. Olson, Complete genome sequence of *Pseudomonas aeruginosa* PAO1, an opportunistic pathogen, Nature 406 (6799) (2000) 959–964, https://doi.org/10.1038/35023079.
[22] P.D. Lister, D.J. Wolter, N.D. Hanson, Antibacterial-resistant *Pseudomonas aeruginosa*: clinical impact and complex regulation of chromosomally encoded resistance mechanisms, Clin. Microbiol. Rev. 22 (4) (2009) 582–610, https://doi.org/10.1128/CMR.00040-09.
[23] B. Jugmohan, J. Loveland, L. Doedens, R.L. Moore, A. Welthagen, C.J. Westgarth-Taylor, Mortality in paediatric burns victims: a retrospective review from 2009 to 2012 in a single centre, S. Afr. Med. J. 106 (2) (2016) 189, https://doi.org/10.7196/SAMJ.2016.v106i2.8942.
[24] E. Tacconelli, E. Carrara, A. Savoldi, S. Harbarth, M. Mendelson, D.L. Monnet, C. Pulcini, G. Kahlmeter, J. Kluytmans, Y. Carmeli, M. Ouellette, K. Outterson, J. Patel, M. Cavaleri, E.M. Cox, C.R. Houchens, M.L. Grayson, P. Hansen, N. Singh, U. Theuretzbacher, N. Magrini, A.O. Aboderin, S.S. Al-Abri, N. Awang Jalil, N. Benzonana, S. Bhattacharya, A.J. Brink, F.R. Burkert, O. Cars, G. Cornaglia, O.J. Dyar, A.W. Friedrich, A.C. Gales, S. Gandra, C.G. Giske, D.A. Goff, H. Goossens, T. Gottlieb, M. Guzman Blanco, W. Hryniewicz, D. Kattula, T. Jinks, S.S. Kanj, L. Kerr, M.-P. Kieny, Y.S. Kim, R.S. Kozlov, J. Labarca, R. Laxminarayan, K. Leder, L. Leibovici, G. Levy-Hara, J. Littman, S. Malhotra-Kumar, V. Manchanda, L. Moja, B. Ndoye, A. Pan, D.L. Paterson, M. Paul, H. Qiu, P. Ramon-Pardo, J. Rodríguez-Bano, M. Sanguinetti, S. Sengupta, M. Sharland, M. Si-Mehand, L.L. Silver, W. Song, M. Steinbakk, J. Thomsen, G.E. Thwaites, J.W. van der Meer, N. Van Kinh, S. Vega, M.V. Villegas, A. Wechsler-Fördös, H.F.L. Wertheim, E. Wesangula, N. Woodford, F.O. Yilmaz, A. Zorzet, Discovery, research, and development of new antibiotics: the WHO priority list of antibiotic-resistant bacteria and tuberculosis, Lancet Infect. Dis. 18 (3) (2018) 318–327., https://doi.org/10.1016/S1473-3099(17)30753-3.
[25] G. Fila, A. Kawiak, M.S. Grinholc, Blue light treatment of *Pseudomonas aeruginosa*: strong bactericidal activity, synergism with antibiotics and inactivation of virulence factors, Virulence 8 (6) (2017) 938–958, https://doi.org/10.1080/21505594.2016.1250995.
[26] G. Baffou, R. Quidant, Nanoplasmonics for chemistry, Chem. Soc. Rev. 43 (11) (2014) 3898., https://doi.org/10.1039/c3cs60364d.
[27] T.C. Dakal, A. Kumar, R.S. Majumdar, V. Yadav, Mechanistic basis of antimicrobial actions of silver nanoparticles, Front. Microbiol. 7 (2016) 1831, https://doi.org/10.3389/fmicb.2016.01831.
[28] R. Thapa, C. Bhagat, P. Shrestha, S. Awal, P. Dudhagara, Enzyme-mediated formulation of stable elliptical silver nanoparticles tested against clinical pathogens and mdr bacteria and development of antimicrobial surgical thread, Ann. Clin. Microbiol. Antimicrob. 16 (2017) 39, https://doi.org/10.1186/s12941-017-0216-y.
[29] G. Franci, A. Falanga, S. Galdiero, L. Palomba, M. Rai, G. Morelli, M. Galdiero, Silver nanoparticles as potential antibacterial agents, Molecules (Basel, Switzerland) 20 (2015) 8856–8874, https://doi.org/10.3390/molecules20058856.
[30] S. Chernousova, M. Epple, Silver as antibacterial agent: ion, nanoparticle, and metal, Angew. Chem. Int. Ed. 52 (6) (2013) 1636–1653.
[31] M. Zhang, K. Zhang, B. De Gusseme, W. Verstraete, R. Field, The antibacterial and anti-biofouling performance of biogenic silver nanoparticles by *Lactobacillus fermentum*, Biofouling 30 (2014) 347–357, https://doi.org/10.1080/08927014.2013.873419.
[32] M. Guzman, J. Dille, S. Godet, Synthesis and antibacterial activity of silver nanoparticles against gram-positive and gram-negative bacteria, Nanomed. Nanotechnol. Biol. Med. 8 (1) (2012) 37–45, https://doi.org/10.1016/j.nano.2011.05.007.
[33] M. Radzig, V. Nadtochenko, O. Koksharova, J. Kiwi, V. Lipasova, I. Khmel, Antibacterial effects of silver nanoparticles on gram-negative bacteria: influence on the growth and biofilms formation, mechanisms of action, Colloids Surf. B 102 (2013) 300–306, https://doi.org/10.1016/j.colsurfb.2012.07.039.
[34] P.C. Lee, D. Meisel, Adsorption and surface-enhanced Raman of dyes on silver and gold sols, J. Phys. Chem. 86 (17) (1982) 3391–3395, https://doi.org/10.1021/j100214a025.
[35] Y. Xia, Y. Xiong, B. Lim, S.E. Skrabalak, Shape-controlled synthesis of metal nanocrystals: simple chemistry meets complex physics? Angew. Chem. Int. Ed. 48 (1) (2009) 60–103, https://doi.org/10.1002/anie.200802248.
[36] D.S. Kilin, O.V. Prezhdo, Y. Xia, Shape-controlled synthesis of silver nanoparticles: Ab initio study of preferential surface coordination with citric acid, Chem. Phys. Lett. 458 (1–3) (2008) 113–116.
[37] A.M. Atta, H.A. Allohedan, G.A. El-Mahdy, A.-R.O. Ezzat, Application of stabilized silver nanoparticles as thin films as corrosion inhibitors for carbon steel alloy in 1 M hydrochloric acid, J. Nanomater. 2013 (2013) 1–8, https://doi.org/10.1155/2013/580607.
[38] D. Acharya, K.M. Singha, P. Pandey, B. Mohanta, J. Rajkumari, L.P. Singha, Shape dependent physical mutilation and lethal effects of silver nanoparticles on bacteria, Sci. Rep. 8 (1) (2018) 201, https://doi.org/10.1038/s41598-017-18590-6.
[39] M. Wypij, J. Czarnecka, M. Świecimska, H. Dahm, M. Rai, P. Golinska, Synthesis, characterization and evaluation of antimicrobial and cytotoxic activities of biogenic silver nanoparticles synthesized from Streptomyces xinghaiensis OF1 strain, World, J. Microbiol. Biotechnol. 34 (2) (2018) 23, https://doi.org/10.1007/s11274-017-2406-3.
[40] A. Sandri, A. Ortombina, F. Boschi, E. Cremonini, M. Boaretti, C. Sorio, P. Melotti, G. Bergamini, M. Lleo, Inhibition of *Pseudomonas aeruginosa* secreted virulence factors reduces lung inflammation in CF mice, Virulence 9 (1) (2018) 1008–1018, https://doi.org/10.1080/21505594.2018.1489198.
[41] P. Rathinam, H.S. Vijay Kumar, P. Viswanathan, Eugenol exhibits anti-virulence properties by competitively binding to quorum sensing receptors, Biofouling 33 (8) (2017) 624–639, https://doi.org/10.1080/08927014.2017.1350655.
[42] A. Thomann, A.G.G. de Mello Martins, C. Brengel, M. Empting, R.W. Hartmann, Application of dual inhibition concept within looped autoregulatory systems toward antivirulence agents against *Pseudomonas aeruginosa* infections, ACS Chem. Biol. 11 (5) (2016) 1279–1286, https://doi.org/10.1021/acschembio.6b00117.
[43] C. PROPST, L. LUBIN, Light-mediated changes in pigmentation of *Pseudomonas aeruginosa* cultures, J. Gen. Microbiol. 113 (2) (1979) 261–266, https://doi.org/10.1099/00221287-113-2-261.
[44] M. Muller, N.D. Merrett, Pyocyanin production by *Pseudomonas aeruginosa* confers resistance to ionic silver, Antimicrob. Agents Chemother. 58 (9) (2014) 5492–5499, https://doi.org/10.1128/AAC.03069-14.
[45] M. Mohamed El-Azizi, S. Nour El Din, T. El-Tayeb, K. Abou Aisha, In vitro and in vivo antimicrobial activity of combined therapy of silver nanoparticles and visible blue light against *Pseudomonas aeruginosa*, Int. J. Nanomed. (2016) 1749, https://doi.org/10.2147/IJN.S102398.
[46] P. Chairuangkitti, S. Lawanprasert, S. Roytrakul, S. Aueviriyavit, D. Phummiratch, K. Kulthong, P. Chanvorachote, R. Maniratanachote, Silver nanoparticles induce toxicity in A549 cells via ROS-dependent and ROS-independent pathways, Toxicol. Vitro 27 (1) (2013) 330–338, https://doi.org/10.1016/j.tiv.2012.08.021.
[47] D. McShan, P.C. Ray, H. Yu, Molecular toxicity mechanism of nanosilver, J. Food Drug Anal. 22 (1) (2014) 116–127, https://doi.org/10.1016/j.jfda.2014.01.010.
[48] C. Beer, R. Foldbjerg, Y. Hayashi, D.S. Sutherland, H. Autrup, Toxicity of silver nanoparticles-Nanoparticle or silver ion? Toxicol. Lett. 208 (3) (2012) 286–292, https://doi.org/10.1016/j.toxlet.2011.11.002.
[49] O. Choi, K.K. Deng, N.-J. Kim, L. Ross, R.Y. Surampalli, Z. Hu, The inhibitory effects of silver nanoparticles, silver ions, and silver chloride colloids on microbial growth, Water Res. 42 (12) (2008) 3066–3074, https://doi.org/10.1016/j.watres.2008.02.021.
[50] Y.-G. Yuan, Q.-L. Peng, S. Gurunathan, Effects of silver nanoparticles on multiple drug-resistant strains of *Staphylococcus aureus* and *Pseudomonas aeruginosa* from Mastitis-infected goats: an alternative approach for antimicrobial therapy, Int. J. Mol. Sci. 18 (3) (2017) 569, https://doi.org/10.3390/ijms18030569.
[51] S. Liao, Y. Zhang, X. Pan, F. Zhu, C. Jiang, Q. Liu, Z. Cheng, G. Dai, G. Wu, L. Wang, L. Chen, Antibacterial activity and mechanism of silver nanoparticles against multidrug-resistant *Pseudomonas aeruginosa*, Int. J. Nanomed. 14 (2019) 1469–1487, https://doi.org/10.2147/IJN.S191340.
[52] D.J. Dwyer, P.A. Belenky, J.H. Yang, I.C. MacDonald, J.D. Martell, N. Takahashi, C.T.Y. Chan, M.A. Lobritz, D. Braff, E.G. Schwarz, J.D. Ye, M. Pati, M. Vercruysse, P.S. Ralifo, K.R. Allison, A.S. Khalil, A.Y. Ting, G.C. Walker, J.J. Collins, Antibiotics induce redox-related physiological alterations as part of their lethality, Proc. Natl. Acad. Sci. USA 111 (20) (2014) E2100–E2109, https://doi.org/10.1073/pnas.1401876111.
[53] D. Zhang, J. Wang, In situ photoactivated plasmonic Ag3PO4@silver as a stable catalyst with enhanced photocatalytic activity under visible light, Mater. Res. 20 (3) (2017) 702–711, https://doi.org/10.1590/1980-5373-mr-2016-0800.
[54] L. Gao, R. Liu, F. Gao, Y. Wang, X. Jiang, X. Gao, Plasmon-mediated generation of reactive oxygen species from near-infrared light excited gold nanocages for photodynamic therapy in vitro, ACS Nano 8 (7) (2014) 7260–7271, https://doi.org/10.1021/nn502325j.

[55] A.G.M. da Silva, T.S. Rodrigues, V.G. Correia, T.V. Alves, R.S. Alves, R.A. Ando, F.R. Ornellas, J. Wang, L.H. Andrade, P.H.C. Camargo, Plasmonic nanorattles as next-generation catalysts for surface Plasmon resonance-mediated oxidations promoted by activated oxygen, Angew. Chem. Int. Ed. 128 (25) (2016) 7227–7231, https://doi.org/10.1002/ange.201601740.

[56] I. de Miguel, I. Prieto, A. Albornoz, V. Sanz, C. Weis, P. Turon, R. Quidant, Plasmon-based biofilm inhibition on surgical implants, Nano Lett. 19 (4) (2019) 2524–2529, https://doi.org/10.1021/acs.nanolett.9b00187.

[57] V.P. Zharov, K.E. Mercer, E.N. Galitovskaya, M.S. Smeltzer, Photothermal nanotherapeutics and nanodiagnostics for selective killing of bacteria targeted with gold nanoparticles, Biophys. J. 90 (2) (2006) 619–627, https://doi.org/10.1529/biophysj.105.061895.

[58] M. Pihl, E. Bruzell, M. Andersson, Bacterial biofilm elimination using gold nanorod localised surface plasmon resonance generated heat, Mater. Sci. Eng. C 80 (2017) 54–58, https://doi.org/10.1016/j.msec.2017.05.067.

[59] D. He, A.M. Jones, S. Garg, A.N. Pham, T.D. Waite, Silver nanoparticle-reactive oxygen species interactions: application of a charging-discharging model, J. Phys. Chem. C 115 (13) (2011) 5461–5468, https://doi.org/10.1021/jp111275a.

[60] D. He, S. Garg, T.D. Waite, H2O2-mediated oxidation of zero-valent silver and resultant interactions among silver nanoparticles, silver ions, and reactive oxygen species, Langmuir 28 (27) (2012) 10266–10275, https://doi.org/10.1021/la300929g.

3.1.2 Mechanochemical Strategies for the Preparation of SiO_2-Supported AgAu Nanoalloy Catalysts (Attachment 2)

Author Contribution: The author participated in conceiving the idea, designing the experiments, performing the catalytic assays, and writing the paper.

In 2021, IUPAC considered mechanochemistry as one of the top ten emerging technologies in Chemistry, as an alternative to solvent-based protocols[24]. However, most mechanochemical syntheses of NPs developed so far follow top-down approaches, which lead to a poorly controlled distribution of size and shape when compared to solution-based synthesis[25]. To circumvent this matter, bottom-up mechanochemical strategies have been able to produce finely tuned nanoparticles in shape, size, and composition[26]. In the solution-based modern rational design of NPs, the synthesis of bimetallic nanostructures play a big role[27]. The synergy between two metals in a single nanostructure significantly affects the catalytic properties of the individual counterparts[28].

In this work, we report two mechanochemical strategies to prepare AgAu nanoalloys supported on SiO_2 in a bottom-up approach, alongside their characterization, and application as hydrogenase-like nanozymes toward the reduction of 2-nitroaniline (2-NA). The first strategy employed was through the galvanic replacement reaction (GRR), where a previously prepared Ag/SiO_2 was submitted to ball milling with Au^{3+}. The differences in electrochemical potentials are able to oxidize Ag atoms to Ag^+ and reduce Au^{3+} to Au atoms in the nanostructure. The second strategy was the one-pot correduction of both metallic precursors at once. Scanning Transmission Electron Microscopy (STEM) and X-ray Photoelectron Spectroscopy (XPS) proved that both

strategies were able to successfully produce bimetallic nanostructures of 6.1 nm (galvanic) and 4.0 nm (one-pot). 2-NA is an environmental pollutant and a byproduct of several anthropogenic chemical processes[29]. Therefore, hydrogenation of 2-NA to o-phenylenediamine (o-PDA) was performed in the presence of $NaBH_4$ and the nanoalloys as nanozymes. Both samples had improved performances compared to the individual AgNP and AuNP supported on SiO_2. Galvanically-prepared nanostructures presented a 2-fold increase in the catalytic rate constant, whereas one-pot showed a 4-fold increase. The difference in their performances may be explained either by the difference in metallic arrangement on the NPs surface or in the NPs size. In summary, this study was able to propose two different strategies for bottom-up approaches in the mechanochemical synthesis of bimetallic nanoparticles. Moreover, it reinforces the effects of the synergy between two metals on nanocatalysis.

frontiers in Chemistry

ORIGINAL RESEARCH
published: 02 February 2022
doi: 10.3389/fchem.2022.836597

Mechanochemical Strategies for the Preparation of SiO_2-Supported AgAu Nanoalloy Catalysts

*Rafael T. P. da Silva, Susana I. Córdoba De Torresi and Paulo F. M. de Oliveira**

Institute of Chemistry, University of São Paulo - USP, São Paulo, Brazil

Silver-gold nanoalloys were prepared from their metal salts precursors through bottom-up mechanochemical synthesis, using one-pot or galvanic replacement reaction strategies. The nanostructures were prepared over amorphous SiO_2 as an inert supporting material, facilitating their stabilization without the use of any stabilizing agent. The nanomaterials were extensively characterized, confirming the formation of the bimetallic nanostructures. The nanoalloys were tested as catalysts in the hydrogenation of 2-nitroaniline and exhibited up to 4-fold the rate constant and up to 37% increased conversion compared to the respective single metal nanoparticles. Our approach is advantageous to produce nanoparticles with clean surfaces with available catalytic sites, directly in the solid-state and in an environmentally friendly manner.

Keywords: mechanochemical synthesis, bottom-up approach, ball-milling, bimetallic nanoparticle, nanoalloys, nanocatalysis, galvanic replacement reaction, nitrobenzene reduction

OPEN ACCESS

Edited by:
Elena Vladimirovna Boldyreva, Novosibirsk State University, Russia

Reviewed by:
Matej Baláž, Slovak Academy of Sciences, Slovakia
Vasile-Dan Hodoroaba, Federal Institute for Materials Research and Testing (BAM), Germany

****Correspondence:***
Paulo F. M. de Oliveira
paulofmo@usp.br

Specialty section:
This article was submitted to Solid State Chemistry, a section of the journal Frontiers in Chemistry

Received: *15 December 2021*
Accepted: *05 January 2022*
Published: *02 February 2022*

Citation:
da Silva RTP, Córdoba De Torresi SI and de Oliveira PFM (2022) Mechanochemical Strategies for the Preparation of SiO_2-Supported AgAu Nanoalloy Catalysts. Front. Chem. 10:836597. doi: 10.3389/fchem.2022.836597

1 INTRODUCTION

The interest in designing metal nanoparticles (NPs) is in constant increase, resulting from the exceptional properties of the nanostructures, which are relevant in catalysis (Araujo et al., 2019), energy (Califano et al., 2021), biomedicine (Li et al., 2017), and sensing (Jeon et al., 2016; Ma et al., 2020). Many advances have been made in tuning the properties of single metal NPs by controlling their size and shape. Nonetheless, a material containing a single element hardly satisfies all the requirements for a certain application. In catalysis field, for example, an ideal material should be highly active, selective, chemically, and structurally stable. Additionally, for industrial purposes the material should also be available at scale. These technological demands can be accomplished by the association of two or more elements into the final nanostructure. The combination of different metals in a single nanostructure is an opportunity to integrate the properties emerging from all individual contributors in a synergistic fashion (Gilroy et al., 2016).

Solution-based and thermal-annealing protocols have succeeded in the preparation of multimetallic structures containing two, eventually three elements (da Silva et al., 2016; Bhunia et al., 2018; Quiroz et al., 2018; Rodrigues et al., 2021). The solution-based techniques are, however, considerably sensitive to the reaction conditions, and are solvent- and/or energy-intensive. In addition, classical routes still face challenges for the preparation of nanostructures at larger scales (Paliwal et al., 2014). In the past decades, environmentally friendly syntheses have been developed in order to overcome these issues, including the use of bio-based reducing agents and alternative energy inputs (Iravani, 2011; Baláž et al., 2017; Ahmad et al., 2019; Jorge de Souza et al., 2019). In such contexts, mechanochemistry and mechanically-induced transformations in the solid-state (Boldyrev, 2006; Boldyreva, 2013) have gained prominence as an alternative to solvent-based protocols in the preparation of a diversity of

chemicals (James et al., 2012) and materials (Xu et al., 2015; Muñoz-Batista et al., 2018). In fact, the use of mechanical energy to induce transformations in multimetallic systems through milling, the so-called mechanical alloying (Suryanarayana, 2001), is one of the its most explored applications. The early works were mostly dedicated to investigate the alloying of non-noble transition metals via top-down approaches, i.e., by milling the elemental powders (Suryanarayana, 2001).

More recently, noble metal nanoparticles have been more investigated under mechanochemical conditions, however, similarly to previous works, the studies have used the top-down methodology with elements such as Au, Ag and Pd to produce the final multicomponent nanomaterials (Delogu, 2008; Danielis et al., 2018; Schreyer et al., 2019; De Bellis et al., 2021). The greatest advantage offered by the technique is related to the simplicity of the treatment, dismissing any post-synthetic workup. On the other hand, top-down approaches are limited in terms of size and shape control. The alternative is to start from the metal salt precursors and construct the nanostructure by the chemical reduction or decomposition, known as bottom-up approach (Moores, 2018; de Oliveira et al., 2020b). The reduction or decomposition processes enable the control of reaction rate, nucleation and generation of growing species, leading to nanoparticles with tunable sizes and shape. Previous works have demonstrated that mechanochemical synthesis in ball milling devices is a promising strategy for the preparation of catalytically relevant noble single metal nanoparticles from their metal precursors (Debnath et al., 2009; Rak et al., 2014; De Oliveira et al., 2019; de Oliveira et al., 2020a; Baláž et al., 2021; Jin et al., 2021; Quiroz et al., 2021). On the other hand, few works associate more than one metal in the final structure totally through bottom-up mechanochemical synthesis. The examples include Pd-Ag nanoalloys (Ruiz-Ruiz et al., 2018, 2022), and Ag-Au nanoclusters (Murugadoss et al., 2012).

In the present report, we describe different approaches for the bottom-up mechanochemical synthesis of noble metal AgAu nanoalloys. Ag and Au were chosen due to their high miscibility and the possibility of a galvanic replacement according to the standard redox potentials of Ag and Au species. Additionally, Ag and Au NPs displays their localized surface plasmon resonance (LSPR) in the visible range, making the alloyed NPs suitable candidates for further studies as plasmonic materials (Liu et al., 2018). For the preparation of the nanoalloys, we adopted two strategies; 1) one-pot/co-reduction of Ag and Au metallic precursors and, 2) two-step galvanic replacement reaction (GRR), using Ag NPs as templates. The use of amorphous SiO_2 as solid support enabled the stabilization of the nanoalloys in sizes smaller than 10 nm without using any surfactant or capping agent. The clean surfaces are an advantage for catalytic applications. Thus, the final nanoalloys were tested in the catalytic reduction of 2-nitroaniline (2-NA) to *o*-phenylenediamine (*o*-PDA), and exhibited superior activities compared to their monometallic Ag and Au NPs counterparts.

2 MATERIALS AND METHODS

2.1 Chemicals

Flash silica (high-purity grade, Sigma-Aldrich), $HAuCl_4.3H_2O$ (hydrogen tetrachloroaurate trihydrate, 48% in gold, Sigma-Aldrich), $AgNO_3$ (silver nitrate, ≥99%, Sigma-Aldrich), $C_6H_6N_2O_2$ (2-nitroaniline, 98%, Sigma-Aldrich), $C_6H_8N_2$ (o-phenylenediamine, ≥99%, Sigma-Aldrich), $NaBH_4$ (sodium borohydride, powder, ≥98%, Sigma-Aldrich). All chemicals were analytical grade reagents. Deionized water (18.2 MΩ) was used throughout the experiments.

2.2 Instrumentation

Transmission electron microscopy (TEM) and high-resolution TEM (HRTEM) images were obtained using a JEOL JEM 2100 operated at 200 kV. A Talos F200S microscope (Thermo Scientific) operating at 200 kV was used for high-angle annular dark-field imaging scanning transmission electron microscopy (HAADF-STEM) and STEM-energy dispersive x-ray analysis (STEM-EDX). Samples were prepared by drop casting 5 μL from a well dispersed isopropanol suspension of each sample on a Formvar/Carbon Film coated, 200 Mesh, copper grid. UV-VIS and diffusive reflectance spectra (DRS) of the solid samples were obtained using a Shimadzu UV-2600 UV-VIS spectrophotometer. For catalytic experiments in water a quartz cuvette with an optical path of 1 cm was used. Powder X-ray diffraction (XRD) patterns were recorded in Shimadzu 7,000 Maxima diffractometer with Cu Kα radiation ($\lambda_{CuK\alpha}$ = 1.5418 Å for combined $K\alpha_1$ and $K\alpha_2$) in a Bragg-Brentano geometry. XPS analyses were performed with a UNI-SPECS UHV at pressure below $5{\cdot}10^{-7}$ Pa ($Mg_{K\alpha}$ hν = 1,253.6 eV). A carbon tape was used as substrate to fix the samples. To determine the metal composition in the samples, inductively coupled plasma–optical emission spectrometry (ICP-OES) Spectro Arcos equipment was used. Aqua regia or HNO_3 was used for the digestion of the samples. Then, a 10-fold dilution with distilled water was performed before each measurement. Further details can be found in the Supplementary Material.

2.3 Bottom-Up Mechanochemical Synthesis of Supported Metal Nanoparticles

2.3.1 Silver Nanoparticles–Ag/SiO_2

Typically, Ag NPs/SiO_2 were synthesized using $AgNO_3$ (19.6 mg) as precursor and $NaBH_4$ (19.6 mg) as reducing agent in presence on SiO_2 (250 mg). The reactants and the support were placed in a PMMA jar containing one single ZrO_2 milling ball (ø = 10 mm, m = 3.14 g) and milled at 50 Hz for 60 min in a vibratory ball-mill Pulversitte 23 Fritsch®. After the milling period the powder underwent several cycles of redispersion in water and centrifugation to eliminate the byproducts formed.

2.3.2 Gold Nanoparticles–Au/SiO_2

Au/SiO_2 nanoparticles were prepared similarly to Ag/SiO_2. $HAuCl_4.3H_2O$ (25 mg) was used as gold precursor and $NaBH_4$

(25 mg) as reducing agent. SiO_2 (250 mg) was utilized as solid support.

2.3.3 AgAu Nanoalloy - Galvanic Replacement Reaction

$HAuCl_4.3H_2O$ (7.5 mg) and cleaned and dried $AgNPs/SiO_2$ (250 mg) were added to the milling jar and milled for 60 min at 50 Hz. Note that no reducing agent was used and the Au^{3+} reduction to metallic gold was induced only by the galvanic replacement of Ag^0 according to **Eq. 1**. To eliminate the byproduct, i.e., AgCl, the powder was dispersed in a supersaturated NaCl solution, to generate $(AgCl_x)^{-(x-1)}$ (x > 1) soluble species, and centrifuged. A final washing cycle was performed with water.

$$AuCl_4^- + Ag^0 \rightarrow 3Ag^+ + Au^0 + 4Cl^- \quad \varepsilon^0 = 0.2\,V \qquad (1)$$

2.3.4 AgAu Nanoalloy - One-Pot Synthesis

The one-pot synthesis of AgAu NAs was performed by the simultaneously addition of $AgNO_3$ (9.8 mg). $HAuCl_4.3H_2O$ (12.5 mg) (Ag: Au ratio 1:1 m/m) and $NaBH_4$ (22.3 mg) into the milling jar containing SiO_2 (250 mg).

2.4 CATALYTIC REDUCTION OF 2-NITROANILINE

Hydrogenation of 2-nitroaniline (0.75 μmol) were performed with $NaBH_4$ (0.26 μmol) in triplicates in a quartz cuvette and monitored using a UV-Vis spectrophotometer ranging from 500 to 250 nm. The total load of metal used was 1.6 *wt*%, considering the catalyst/substrate ratio. (Details in the Supplementary Material).

3 RESULTS AND DISCUSSION

3.1 Materials Synthesis and Characterization

The specific combination of Ag and Au as noble metals in bimetallic systems offers the opportunity to minimize the cost of Au catalysts and, at the same time, enhance the material catalytic performance through use synergistic effects (Slater et al., 2014). Typically, Ag and Au are combined either in core-shell or in alloys to applications in biosensors (Jia et al., 2014), SERS (Chen et al., 2013; Girão et al., 2017), catalysis (Wang et al., 2014; Kisukuri et al., 2016; Rodrigues et al., 2016) or electrocatalysis (Nazir et al., 2017; Balasubramanian et al., 2020; da Silva et al., 2021). They may be either blended in nanocrystals comprised of the individual elements or in an alloyed or intermetallic atomic ordering (Gilroy et al., 2016). Most of the experimental protocols requires capping agents to keep the colloidal nanoparticle dispersion stable. Capping agents, however, usually act as a physical barrier hindering the catalytic surface of nanoparticles from the access of reactants. In addition, they can act poisoning the catalytic sites (Niu and Li, 2014).

In the present work, two different approaches were used to synthesize AgAu bimetallic alloys supported over amorphous SiO_2, without any addition of capping agents, as depicted in **Figure 1**. The first (**Figure 1A**) is a two-step reaction, where the first step led to the reduction of Ag NPs on amorphous SiO_2 through the addition of Ag precursor and $NaBH_4$ as the reducing agent, leading to Ag/SiO_2. After washing steps to remove remaining $NaBH_4$ and other byproducts, the Ag NPs acted as templates for the mechanochemical GRR. In this second step, due to the difference in the reduction potential of $AuCl_4^-$ and Ag^0 (**Eq. (1)**), the Ag atoms quickly oxidize with the addition of Au precursor salt, driving the formation of the nanoalloys, also supported on SiO_2, named $AgAu/SiO_2$ galvanic. The second strategy (**Figure 1B**) was based in a one-pot co-reduction, where both Ag and Au precursors salts were added simultaneously with $NaBH_4$ as a reducing agent with SiO_2 in a ball mill, leading to $AgAu/SiO_2$ one-pot. Besides, monometallic Ag/SiO_2 and Au/SiO_2 nanostructures were prepared for the subsequent comparison of the catalytic activity. The metal content of the final materials was determined by ICP-OES (**Supplementary Table S1**) and the reaction yield for each metal for 1-h milling is given on **Supplementary Table S2**.

TEM micrographs of the synthesized samples are depicted in **Figures 2A–D**. TEM images show an even distribution of rounded nanoparticles throughout the supporting material. Particle-size distribution for each sample was determined through averaging the diameter of at least 150 nanoparticles, measured one-by-one (**Supplementary Figure S1**). Single metal Ag/SiO_2 (**Figure 2A**) and Au/SiO_2 (**Figure 2B**) present relatively polydisperse particle sizes of 5.9 ± 1.7 nm and 6.4 ± 3.3 nm, respectively. On the other hand, the generated bimetallic nanoalloys displayed a relatively narrow size distribution of 6.1 ± 1.7 nm for $AgAu/SiO_2$ galvanic (**Figure 2C**) and 4.0 ± 1.0 nm for $AgAu/SiO_2$ one-pot samples (**Figure 2B**). When comparing the size of the Ag NPs templates for GRR (5.9 nm) and the final bimettalic nanoalloys (6.1 nm), we see no significant difference, which suggests a constant rate of Ag^0 oxidation and Au^0 deposition. Interestingly, the one-pot route generated smaller nanoparticles (4.0 nm). We believe that this is probably due to the concurrent reactions that could take place: reduction of Ag^+, reduction of $AuCl_4^-$, GRR of Ag^0 by Au^{3+} and redeposition/reduction of displaced Ag^+. Each one of these reactions can occur in different rates but, at the end, there are a number of nucleation events that hampers further particle growth. It was already demonstrated the bottom-up mechanochemical synthesis of NP may not follow the yet known solution chemistry for the construction of similar architectures, making difficult further discussions over the mechanism of formation of the bimetallic systems at this stage (de Oliveira et al., 2020a).

The insets of **Figures 2A–D** show HRTEM and the lattice spacing of the nanocrystals. All distances found were 2.35 Å (Ag/SiO_2), 2.39 Å (Au/SiO_2), 2.34 Å ($AgAu/SiO_2$ galvanic) and 2.24 Å ($AgAu/SiO_2$ one-pot), which are consistent with the (111) facet of metallic fcc Ag and Au (ICSD 44382 and 44362). STEM of Ag and Au in $AgAu/SiO_2$ galvanic and $AgAu/SiO_2$ one-pot are displayed in **Figures 2E–H** and **Figures 2I–L**, respectively. The images show the colocalization of Ag and Au in both nanostructures.



FIGURE 1 | Scheme of the bottom-up mechanochemical synthesis routes for the preparation of AgAu/SiO_2 galvanic **(A)** and AgAu/SiO_2 one-pot **(B)** nanoalloys. The symbols over the arrows follow the recommendation of ref. (Michalchuk et al., 2021).

This pattern is plausible due to the high miscibility among the two metals (Guisbiers et al., 2016). **Supplementary Figure S2** shows HAADF-STEM of Ag, Au, Si and O for AgAu/SiO_2 galvanic and AgAu/SiO_2 one-pot.

UV-VIS diffusive reflectance spectra (DRS) spectra after Kubelka-Munk function of the synthesized materials are presented in **Figure 3A**. Both monometallic materials present a narrower localized surface plasmon resonance (LSPR) peak in comparison to the bimetallic alloys. LSPR peak referent to Ag/SiO_2 has its maximum at 422 nm, whereas the maximum of Au/SiO_2 is at 528 nm, corresponding to the values previously reported for mechanochemical syntheses of these metallic nanoparticles (De Oliveira et al., 2019; Baláž et al., 2021). The bimetallic samples present broader LSPR spectra, composed by overlapped LSPR contributions of shifted Ag and Au NPs and are liable to deconvolution. AgAu/SiO_2 galvanic LSPR maximum is comprehended at 512 nm and a shoulder peak can be seen at 450 nm. For AgAu/SiO_2 one-pot, these values are 452 and 501 nm, respectively. This indicates that although there is the formation of alloy through both GRR and one-pot strategies indicated by the redshift in both samples, some remaining monometallic particles could have been formed, as well as regions of higher density of single element within the bimetallic nanostructure. Accordingly, in solution-based synthesis alloyed AgAu nanoparticles present a LSPR broadening and a redshift, varying their maxima starting from the AgNP used as templates to the near infrared (Vongsavat et al., 2011; Gilroy et al., 2016; da Silva et al., 2021).

Regarding the PXRD data presented in **Figure 3B**, we see that all the samples are crystalline, however displaying a broad diffraction pattern, which indicates the presence of nanoparticles. No significant shifts in the PXRD reflections for the nanoalloys are noteworthy relative to the monometallic Ag/SiO_2 and Au/SiO_2 sanples. For example, the reflections relative to (111) crystalline planes represented in 2θ ($\lambda_{CuK\alpha}$) for single Ag/SiO_2 and Au/SiO_2 are 2θ = 38.15° and 38.24°, respectively. Similarly, for bimetallic AgAu/SiO_2 galvanic and AgAu/SiO_2 one-pot samples this occurs at 2θ = 38.24° and 38.20°. This is because, both Ag and Au have the same fcc crystal structure and similar lattices constants (a_{gold} = 4.079 Å; a_{silver} = 4.086 Å) (da Silva et al., 2017). Actually, these parametric similarities facilitate the high miscibility of these metals at nanoscale and promote the formation of uniform AgAu alloys.

To gain further insights in the structure and surface composition of the supported nanoparticles, the samples were also characterized by XPS (**Figures 3C–F** and **Supplementary Figure S3**). In the case of single metal Ag/SiO_2 composite, the XPS spectrum shows two intense photoelectron peaks with binding energies (BE) at the maxima in 368.1 and 374.1 eV, ascribed to Ag $3d_{5/2}$ and $3d_{3/2}$ doublet, respectively (**Supplementary Figure S3**) (Liu et al., 1994). These BE values and the splitting value between them (6.0 eV) are characteristics of metallic Ag, indicating the efficiency of the mechanochemical route in the reduction of the Ag^+, and that the final material is stable on the support, not undergoing any oxidation when stored in room conditions. Similarly, the XPS spectrum of single metal Au/SiO_2 demonstrates the formation of metallic Au according to the Au $4f_{7/2}$ and $4f_{5/2}$ doublet with BE of 84.1 and 87.6 eV, respectively and a splitting value of 3.5 eV (**Supplementary Figure S3**) (Mansour, 1994).

Concerning the XPS spectra of the nanoalloys (**Figures 3C–F**), they demonstrate the metallic character of both metals present in the sample. However, small shifts in the BE can be considered when compared to the respective single metal NPs. In the XPS spectra of AgAu/SiO_2 galvanic sample (**Figure 3C**), the peaks related to the Ag $3d_{5/2}$ and $3d_{3/2}$ spin orbit coupling doublet, shifts in −0.4 eV while for AgAu/SiO_2 one-pot sample (**Figure 3E**) this shift is around −0.3 eV. The shifted BE to lower values is consistent with the formation of a Ag alloyed structure which is, in the present case, with Au (Tyson et al., 1992; Sun et al., 2018). For the BE values of Au $4f_{7/2}$ and $4f_{5/2}$ doublet in the samples of alloyed NPs (**Figures 3D,F**), the shifts compared to Au in the Au/SiO2 sample are meaningless considering the precision of ±0.1 eV in determining the BE.

3.2 Catalytic Reduction of 2-Nitroaniline

The successful mechanochemical preparation of bimetallic AgAu nanoalloys, without using any stabilizing surface agent, make them suitable materials for catalytic applications. We employed the catalytic reduction of 2-nitroaniline (2-NA) to probe the catalytic activity of the nanostructures. Nitrobenzenes' reductions

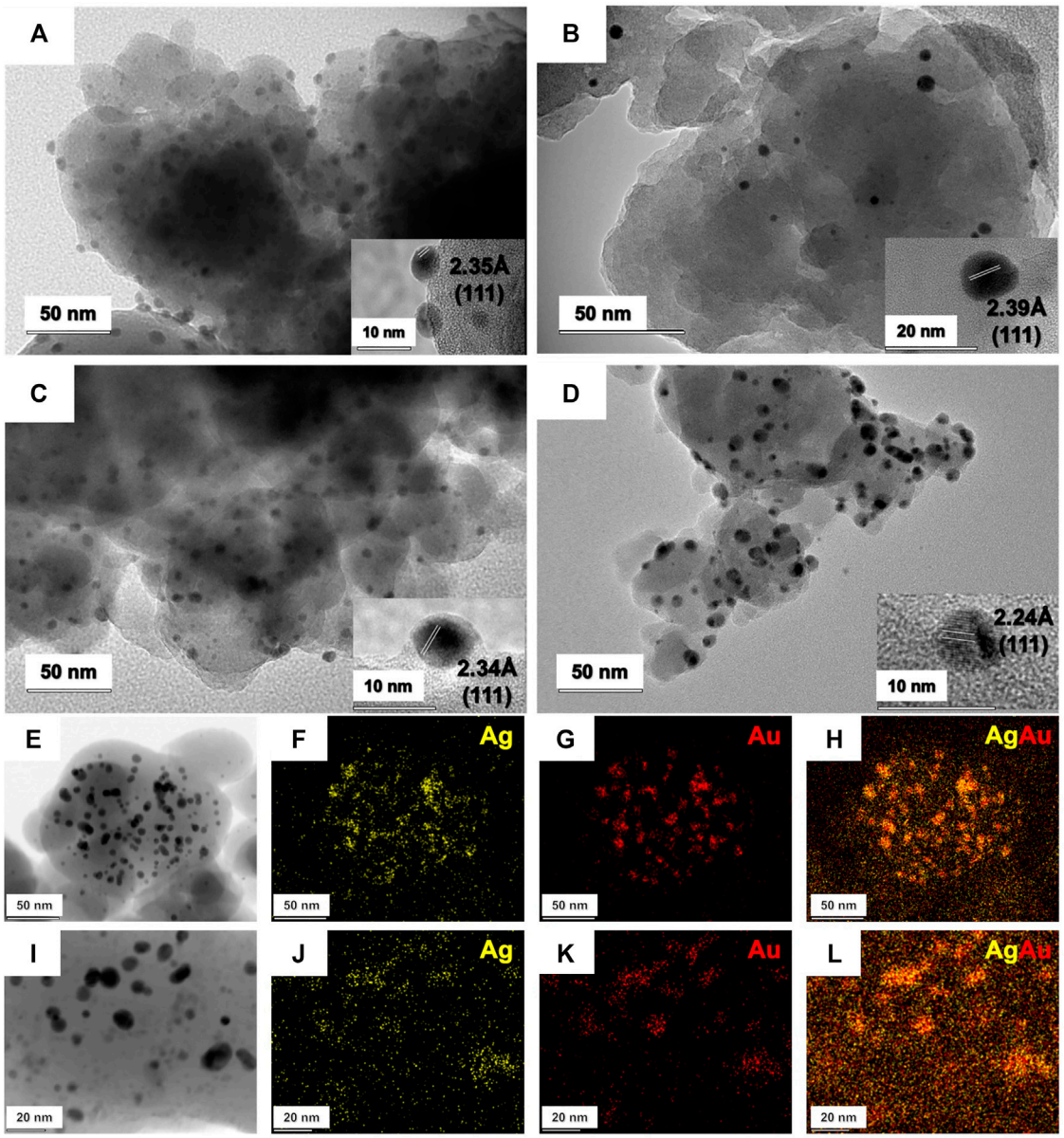


FIGURE 2 | TEM, HRTEM and STEM of the mechanochemically prepared nanoparticles. TEM and HRTEM of AgNP **(A)**, AuNP **(B)**, AgAu/SiO_2 galvanic **(C)** and AgAu/SiO_2 one-pot **(D)**. STEM of AgAu/SiO_2 galvanic **(E–H)** and AgAu/SiO_2 one-pot **(I–L)**.

are largely investigated in order to assess the catalytic activity of noble metal nanomaterials due to the simplicity in extracting kinetic data from spectroscopic measurements (Le et al., 2014; Hajfathalian et al., 2015; Menumerov et al., 2016; Naseem et al., 2017; Saire-Saire et al., 2019). In our case, we used 2-NA, which is an environmental pollutant and is the by-product of several anthropogenic chemical processes, such as the production of dyes, explosives and pharmaceutical products (Naseem et al., 2017). The product of its catalytic reduction is the ortho-phenylenediamine (o-PDA), a precursor for the synthesis of antioxidants, polymers, surfactants, and for products of food and fine chemistry industries. Therefore, the conversion of 2-NA into o-PDA is an environmental solution and a chemical opportunity.

The scheme of the catalytic reduction of 2-NA by BH_4^- is illustrated in **Figure 4A**. The same amount of total metal load was used in each catalytic run of the different materials. The metal load was determined by ICP-OES (**Supplementary Table S1**). The conversion of 2-NA was followed by UV-VIS spectroscopy through the decay of 412 nm band, as demonstrated by **Supplementary Figure S4**. A shift in the 283—288 nm range was also observed throughout the catalytic reaction, and it is assigned to the formation of o-PDA (**Supplementary Figure S5**). As the catalytic reaction

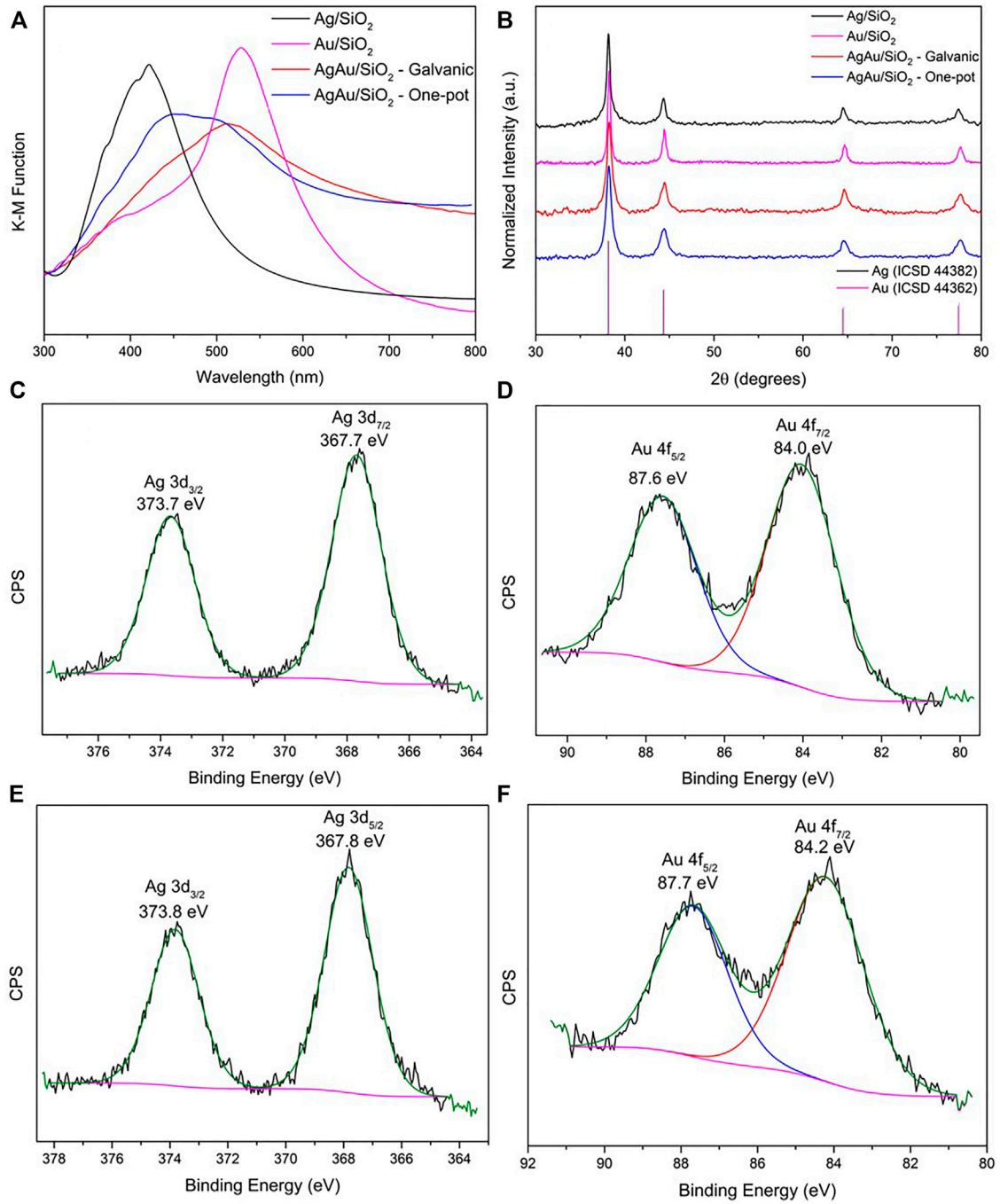


FIGURE 3 | Characterization of the nanoparticles supported on SiO_2. UV-VIS DRS spectra **(A)**, XRD patterns **(B)** and XPS spectra of AgAu/SiO_2 galvanic **(C,D)** and AgAu/SiO_2 one-pot **(E,F)** for the Ag 3d and Au 4f core levels.

progresses, the yellowish starting solution characteristic of 2-NA becomes transparent with its conversion to o-PDA. **Figure 4B** show the triplicate of conversion curves for the different mechanochemically synthesized catalytic materials. The first points of these curves represent the induction period necessary for restructuring the surface of the catalyst with the substrate, just as observed for others nitrobenzenes (Hervés et al., 2012). This induction period plays a major role for Ag/SiO_2, slowing up the 412 nm band decay for this material in the first minutes, whereas Au/SiO_2 and both alloys show a shorter induction period. For the same period of reaction (~25 min), the conversions were around 60% for both Ag/SiO_2 and Au/SiO_2. These values are much lower in comparison to the nanoalloys, which reached 2-NA conversions of 87 and

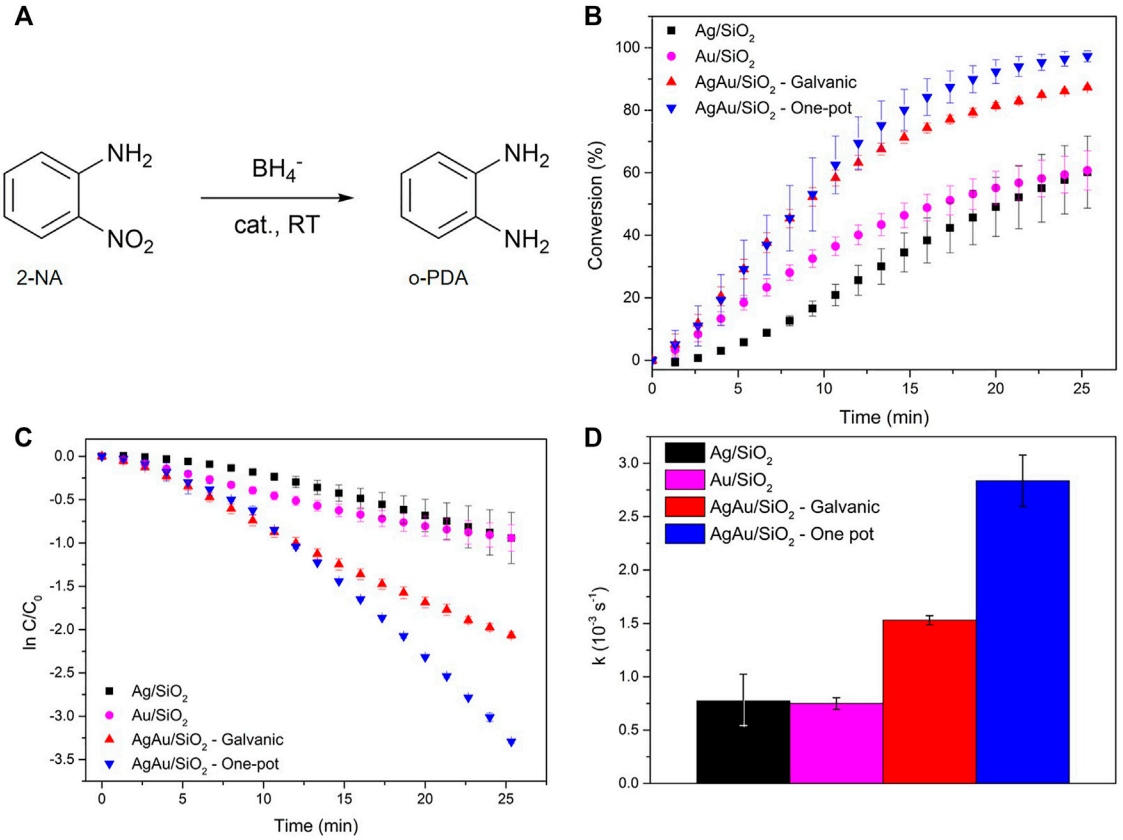


FIGURE 4 | Catalytic reduction of 2-NA. Reaction scheme of 2-NA reduction to o-PDA **(A)**. Reduction of 2-NA analyzed by the decay of 412 nm band **(B)**. Linearization considering a pseudo first-order reaction **(C)**. Reaction pseudo first-order rate constant values obtained from C **(D)**.

97%, for $AgAu/SiO_2$ galvanic and $AgAu/SiO_2$ one-pot, respectively.

The apparent reaction rate constants (k) were obtained after linearization of the conversion data as presented in **Figure 4C**, considering a typical pseudo-first order reaction (high excess of $NaBH_4$) (**Figure 4D**). The induction periods were not considered for this calculation since they do not follow a linear trend. Similar apparent rate constants were shown by Ag/SiO_2 ($k_{Ag} = 7.75\ 10^{-4}\ s^{-1}$) and Au/SiO_2 ($k_{Au} = 7.50\ 10^{-4}\ s^{-1}$), values that are consistent with previously reported studies for monometallic Ag and Au nanomaterials in the catalytic reduction of 2-NA (Nalawade et al., 2013; Dong et al., 2014). However, $AgAu/SiO_2$ galvanic and $AgAu/SiO_2$ one-pot showed twice and four-fold the rate constant values of $k_{Galvanic} = 1.53\ 10^{-3}\ s^{-1}$ and $k_{one\text{-}pot} = 2.84\ 10^{-3}\ s^{-1}$, respectively.

It is worth discussing the better performance shown by the $AgAu/SiO_2$ one-pot material. One can suggest that the composition, i.e., the Ag/Au ratio, can affect the catalytic activity. The metal content determined by ICP-OES (**Supplementary Table S1**) indicates that $AgAu/SiO_2$ galvanic is composed by 58 *wt*% of Ag and 42 *wt*% of Au, whereas the one-pot sample consists of 36 *wt*% of Ag and 64 *wt*% of Au. However, the similar activities for single metal NPs indicate no significant effect of the metal in our experimental conditions. Another possibility for such difference of the catalytic activity between the nanoalloys could be the surface composition, as the studied catalytic reaction strongly depends on the surface chemistry. The surface composition estimated by XPS (**Supplementary Table S3**) shows the same fraction of Ag (62 *wt* %) and Au (38 *wt*%) for both galvanic and one-pot prepared nanostructures. Thus, this possibility solely can also be dismissed. A final aspect that must be considered is simply the difference of particle size. $AgAu/SiO_2$ one-pot material presents smaller particles (4.0 nm) compared to the material prepared by the galvanic route (6.1 nm). It is of wide knowledge that smaller sizes are related to higher specific surface areas, which can be available for catalysis, and consequently increase the reaction rate.

Conversion, induction period and reaction rate constant strongly suggest that the bimetallic nanoalloys benefit from the synergy between silver and gold, just as previously reported (Wang et al., 2014; Kisukuri et al., 2016; da Silva et al., 2021). Although many examples of enhanced catalytic properties of bimetallic systems have been reported, the synergistic effect between metals in these systems is yet to be fully comprehended. Among reaction conditions such as pH, temperature and diffusion rates, catalytic rate constants are related to adsorption energy of reactants on active sites. In its turn, adsorption energy is dependent on the crystallite size, facets and composition, properties that are susceptible of changes by the formation of alloys in bimetallic systems. Besides, the rearranged

atomic ordering admitted by alloys may change the surface electronic structure of the nanoparticles and, thus, affect their catalytic properties (Sha et al., 2019).

4 CONCLUSION

Bimetallic nanoparticles offer the possibility to combine the different properties in a single structure. We demonstrated different possibilities to prepare crystalline AgAu nanoalloys through bottom-up mechanochemical synthesis. Both galvanic and one-pot/co-reduction strategies led to the formation of nanoalloys with diameters of 6.1 ± 1.7 nm and 4.0 ± 1.0 nm, respectively. STEM-EDX images and XPS confirmed the formation of these alloys. The LSPR in the UV-VIS DRS, however, demonstrated that some monometallic NPs or regions of higher density of a single element can also be formed. This shows that further investigation into elementary steps of the nanostructure formation is necessary if one aims an effective control of the final materials, and therefore, their properties. Our results reinforces that we need to understand the specific rules for solid-state mechanochemical synthesis of nanomaterial from their respective precursors. This includes the different rates of reactions, and therefore, the nucleation and the formation of feeding species to the growing sites.

Additionally, in our work, the mechanochemical route was able to generate materials with efficient distribution over the support. Besides, the direct synthesis over SiO_2 dismisses the use of capping agents and eliminate impregnation steps. The catalytic activity of our $AgAu/SiO_2$ nanoalloys were tested in the reduction of 2-NA. The alloyed nanoparticles displayed higher catalytic activity in terms of reaction rate constants ($k_{Galvanic}$ = 1.53 10^{-3} s^{-1} and $k_{one\text{-}pot}$ = 2.84 10^{-3} s^{-1}) and conversion (87 and 97%, respectively) when compared to the single metal NPs (k_{Ag} = 7.75 10^{-4} s^{-1} and k_{Au} = 7.50 10^{-4} s^{-1} with 60% conversion for both materials). The higher reaction rate and conversion were obtained for the $AgAu/SiO_2$ one-pot material, showing the dominant effect of the particle size. It still worth mentioning that the LSPR displayed by the nanoalloys are very interesting for further studies on light-enhanced plasmonic catalysis.

The mechanochemical route for the preparation of multicomponent catalysts with active surfaces is highly envisioned to improve catalytic activity and minimize costly processes. This also includes the possibility of scaling up the process to meet industrial requirements, in addition of being a powerful tool for a sustainable design of new materials.

DATA AVAILABILITY STATEMENT

The raw data supporting the conclusion of this article will be made available by the authors, without undue reservation.

AUTHOR CONTRIBUTIONS

RTPS and PFMO conceived the project. RTPS performed the catalytic assays and wrote the manuscript. PFMO developed the synthetic approaches, synthesized the materials, and wrote the manuscript. PFMO and SICT supervised the work.

FUNDING

This work was supported by FAPESP (Grants 2015/26308–7 and 2018/16219–5). RTPS was funded by a PhD fellowship from CAPES (Grant 88882.328241/2019–01). PFMO thanks FAPESP for the Grants 2020/14955-6 and 2021/12899-4.

ACKNOWLEDGMENTS

The authors thank the work of C. Prinz, M. Heilmann and F. Emmerling from the Federal Institute for Materials Research and Testing (BAM–Berlin) for HRTEM and STEM images and Peter Hammer from LEFE, Physical Chemistry department, IQ-UNESP for XPS data and analysis.

SUPPLEMENTARY MATERIAL

The Supplementary Material for this article can be found online at: https://www.frontiersin.org/articles/10.3389/fchem.2022.836597/full#supplementary-material

REFERENCES

Ahmad, S., Munir, S., Zeb, N., Ullah, A., Khan, B., Ali, J., et al. (2019). Green Nanotechnology: a Review on green Synthesis of Silver Nanoparticles - an Ecofriendly Approach. *Ijn* 14, 5087–5107. doi:10.2147/IJN.S200254

Araujo, T. P., Quiroz, J., Barbosa, E. C. M., and Camargo, P. H. C. (2019). Understanding Plasmonic Catalysis with Controlled Nanomaterials Based on Catalytic and Plasmonic Metals. *Curr. Opin. Colloid Interf. Sci.* 39, 110–122. doi:10.1016/j.cocis.2019.01.014

Balasubramanian, P., He, S.-B., Jansirani, A., Peng, H.-P., Huang, L.-L., Deng, H.-H., et al. (2020). Bimetallic AgAu Decorated MWCNTs Enable Robust Nonenzyme Electrochemical Sensors for *In-Situ* Quantification of Dopamine and H2O2 Biomarkers Expelled from PC-12 Cells. *J. Electroanalytical Chem.* 878, 114554. doi:10.1016/j.jelechem.2020.114554

Baláž, M., Bedlovičová, Z., Daneu, N., Siksa, P., Sokoli, L., Tkáčiková, Ľ., et al. (2021). Mechanochemistry as an Alternative Method of green Synthesis of Silver Nanoparticles with Antibacterial Activity: A Comparative Study. *Nanomaterials* 11, 1139. doi:10.3390/nano11051139

Baláž, M., Daneu, N., Balážová, Ľ., Dutková, E., Tkáčiková, Ľ., Briančin, J., et al. (2017). Bio-mechanochemical Synthesis of Silver Nanoparticles with Antibacterial Activity. *Adv. Powder Technol.* 28, 3307–3312. doi:10.1016/j.apt.2017.09.028

Banin, U., Waiskopf, N., Hammarström, L., Boschloo, G., Freitag, M., Johansson, E. M. J., et al. (2021). Nanotechnology for Catalysis and Solar Energy Conversion. *Nanotechnology* 32 (4), 042003. doi:10.1088/1361-6528/abbce8

Bhunia, K., Khilari, S., and Pradhan, D. (2018). Monodispersed PtPdNi Trimetallic Nanoparticles-Integrated Reduced Graphene Oxide Hybrid Platform for Direct Alcohol Fuel Cell. *ACS Sustain. Chem. Eng.* 6, 7769–7778. doi:10.1021/acssuschemeng.8b00721

Boldyrev, V. V. (2006). Mechanochemistry and Mechanical Activation of Solids. *Russ. Chem. Rev.* 75, 177–189. doi:10.1070/RC2006v075n03ABEH001205

Boldyreva, E. (2013). Mechanochemistry of Inorganic and Organic Systems: what Is Similar, what Is Different? *Chem. Soc. Rev.* 42, 7719–7738. doi:10.1039/c3cs60052a

Chen, L., Chabu, J. M., and Liu, Y. (2013). Bimetallic AgM (M = Pt, Pd, Au) Nanostructures: Synthesis and Applications for Surface-Enhanced Raman Scattering. *RSC Adv.* 3, 4391–4399. doi:10.1039/c3ra23137b

da Silva, A. G. M., Rodrigues, T. S., Haigh, S. J., and Camargo, P. H. C. (2017). Galvanic Replacement Reaction: Recent Developments for Engineering Metal Nanostructures towards Catalytic Applications. *Chem. Commun.* 53, 7135–7148. doi:10.1039/C7CC02352A

da Silva, R. T. P., de Souza Rodrigues, M. P., Davilla, G. F. B., da Silva, A. M. R. P., Dourado, A. H. B., and Córdoba de Torresi, S. I. (2021). AgAu Hollow Nanoshells on Layered Graphene Oxide and Silica Submicrospheres as Plasmonic Nanozymes for Light-Enhanced Electrochemical H2O2 Sensing. *ACS Appl. Nano Mater.* 4, 12062–12072. doi:10.1021/acsanm.1c02611

Danielis, M., Colussi, S., de Leitenburg, C., Soler, L., Llorca, J., and Trovarelli, A. (2018). Outstanding Methane Oxidation Performance of Palladium-Embedded Ceria Catalysts Prepared by a One-step Dry Ball-Milling Method. *Angew. Chem. Int. Ed.* 57, 10212–10216. doi:10.1002/anie.201805929

da Silva, A. G. M., Rodrigues, T. S., Correia, V. G., Alves, T. V., Alves, R. S., Ando, R. A., et al. (2016). Plasmonic Nanorattles as Next-Generation Catalysts for Surface Plasmon Resonance-Mediated Oxidations Promoted by Activated Oxygen. *Angew. Chem. Int. Ed.* 55, 7111–7115. doi:10.1002/anie.201601740

De Bellis, J., Felderhoff, M., and Schüth, F. (2021). Mechanochemical Synthesis of Supported Bimetallic Catalysts. *Chem. Mater.* 33, 2037–2045. doi:10.1021/acs.chemmater.0c04134

de Oliveira, P. F. M., Michalchuk, A. A. L., Marquardt, J., Feiler, T., Prinz, C., Torresi, R. M., et al. (2020a). Investigating the Role of Reducing Agents on Mechanosynthesis of Au Nanoparticles. *CrystEngComm* 22, 6261–6267. doi:10.1039/D0CE00826E

De Oliveira, P. F. M., Quiroz, J., De Oliveira, D. C., and Camargo, P. H. C. (2019). A Mechano-Colloidal Approach for the Controlled Synthesis of Metal Nanoparticles. *Chem. Commun.* 55, 14267–14270. doi:10.1039/c9cc06199a

de Oliveira, P. F. M., Torresi, R. M., Emmerling, F., and Camargo, P. H. C. (2020b). Challenges and Opportunities in the Bottom-Up Mechanochemical Synthesis of noble Metal Nanoparticles. *J. Mater. Chem. A.* 8, 16114–16141. doi:10.1039/D0TA05183G

Debnath, D., Kim, S. H., and Geckeler, K. E. (2009). The First Solid-phase Route to Fabricate and Size-Tune Gold Nanoparticles at Room Temperature. *J. Mater. Chem.* 19, 8810. doi:10.1039/b905260g

Delogu, F. (2008). A Mechanistic Study of Ag50Cu50 Solid Solution Formation by Mechanical Alloying. *Acta Materialia* 56, 2344–2352. doi:10.1016/j.actamat.2008.01.024

Dong, Z., Le, X., Li, X., Zhang, W., Dong, C., and Ma, J. (2014). Silver Nanoparticles Immobilized on Fibrous Nano-Silica as Highly Efficient and Recyclable Heterogeneous Catalyst for Reduction of 4-nitrophenol and 2-nitroaniline. *Appl. Catal. B: Environ.* 158-159, 129–135. doi:10.1016/j.apcatb.2014.04.015

Gilroy, K. D., Ruditskiy, A., Peng, H.-C., Qin, D., and Xia, Y. (2016). Bimetallic Nanocrystals: Syntheses, Properties, and Applications. *Chem. Rev.* 116, 10414–10472. doi:10.1021/acs.chemrev.6b00211

Girão, A. V., Pinheiro, P. C., Ferro, M., and Trindade, T. (2017). Tailoring Gold and Silver Colloidal Bimetallic Nanoalloys towards SERS Detection of Rhodamine 6G. *RSC Adv.* 7, 15944–15951. doi:10.1039/c7ra00685c

Guisbiers, G., Mendoza-Cruz, R., Bazán-Díaz, L., Velázquez-Salazar, J. J., Mendoza-Perez, R., Robledo-Torres, J. A., et al. (2016). Electrum, the Gold-Silver alloy, from the Bulk Scale to the Nanoscale: Synthesis, Properties, and Segregation Rules. *ACS Nano* 10, 188–198. doi:10.1021/acsnano.5b05755

Hajfathalian, M., Gilroy, K. D., Yaghoubzade, A., Sundar, A., Tan, T., Hughes, R. A., et al. (2015). Photocatalytic Enhancements to the Reduction of 4-Nitrophenol by Resonantly Excited Triangular Gold-Copper Nanostructures. *J. Phys. Chem. C* 119, 17308–17315. doi:10.1021/acs.jpcc.5b04618

Hervés, P., Pérez-Lorenzo, M., Liz-Marzán, L. M., Dzubiella, J., Lu, Y., and Ballauff, M. (2012). Catalysis by Metallic Nanoparticles in Aqueous Solution: Model Reactions. *Chem. Soc. Rev.* 41, 5577–5587. doi:10.1039/c2cs35029g

Iravani, S. (2011). Green Synthesis of Metal Nanoparticles Using Plants. *Green. Chem.* 13, 2638–2650. doi:10.1039/c1gc15386b

James, S. L., Adams, C. J., Bolm, C., Braga, D., Collier, P., Friščić, T., et al. (2012). Mechanochemistry: Opportunities for New and Cleaner Synthesis. *Chem. Soc. Rev.* 41, 413–447. doi:10.1039/C1CS15171A

Jeon, T. Y., Kim, D. J., Park, S.-G., Kim, S.-H., and Kim, D.-H. (2016). Nanostructured Plasmonic Substrates for Use as SERS Sensors. *Nano Convergence* 3. doi:10.1186/s40580-016-0078-6

Jia, K., Khaywah, M. Y., Li, Y., Bijeon, J. L., Adam, P. M., Déturche, R., et al. (2014). Strong Improvements of Localized Surface Plasmon Resonance Sensitivity by Using Au/Ag Bimetallic Nanostructures Modified with Polydopamine Films. *ACS Appl. Mater. Inter.* 6, 219–227. doi:10.1021/am403943q

Jin, T., Liu, X., Su, Y.-Q., Pan, F., Han, X., Zhu, H., et al. (2021). Mesoporous Carbon-Supported Ultrasmall Metal Nanoparticles via a Mechanochemical-Driven Redox Reaction: A "Two-In-One" Strategy. *Appl. Catal. B: Environ.* 294, 120232. doi:10.1016/j.apcatb.2021.120232

Jorge de Souza, T. A., Rosa Souza, L. R., and Franchi, L. P. (2019). Silver Nanoparticles: An Integrated View of green Synthesis Methods, Transformation in the Environment, and Toxicity. *Ecotoxicology Environ. Saf.* 171, 691–700. doi:10.1016/j.ecoenv.2018.12.095

Kisukuri, C. M., Palmeira, D. J., Rodrigues, T. S., Camargo, P. H. C., and Andrade, L. H. (2016). Bimetallic Nanoshells as Platforms for Metallo- and Biometallo-Catalytic Applications. *ChemCatChem* 8, 171–179. doi:10.1002/cctc.201500812

Le, X., Dong, Z., Zhang, W., Li, X., and Ma, J. (2014). Fibrous Nano-Silica Containing Immobilized Ni@Au Core-Shell Nanoparticles: A Highly Active and Reusable Catalyst for the Reduction of 4-nitrophenol and 2-nitroaniline. *J. Mol. Catal. A: Chem.* 395, 58–65. doi:10.1016/j.molcata.2014.08.002

Li, F., Lu, J., Kong, X., Hyeon, T., and Ling, D. (2017). Dynamic Nanoparticle Assemblies for Biomedical Applications. *Adv. Mater.* 29, 1605897. doi:10.1002/adma.201605897

Liu, J., He, H., Xiao, D., Yin, S., Ji, W., Jiang, S., et al. (2018). Recent Advances of Plasmonic Nanoparticles and Their Applications. *Materials* 11, 1833. doi:10.3390/ma11101833

Liu, Y., Jordan, R. G., and Qiu, S. L. (1994). Electronic Structures of Ordered Ag-Mg Alloys. *Phys. Rev. B* 49, 4478–4484. doi:10.1103/PhysRevB.49.4478

Ma, J., Liu, X., Wang, R., Zhang, J., Jiang, P., Wang, Y., et al. (2020). Bimetallic Core-Shell Nanostars with Tunable Surface Plasmon Resonance for Surface-Enhanced Raman Scattering. *ACS Appl. Nano Mater.* 3, 10885–10894. doi:10.1021/acsanm.0c02144

Mansour, A. N. (1994). Gold Mg Kα XPS Spectra from the Physical Electronics Model 5400 Spectrometer. *Surf. Sci. Spectra* 3, 197–201. doi:10.1116/1.1247747

Menumerov, E., Hughes, R. A., and Neretina, S. (2016). Catalytic Reduction of 4-Nitrophenol: A Quantitative Assessment of the Role of Dissolved Oxygen in Determining the Induction Time. *Nano Lett.* 16, 7791–7797. doi:10.1021/acs.nanolett.6b03991

Michalchuk, A. A. L., Boldyreva, E. V., Belenguer, A. M., Emmerling, F., and Boldyrev, V. V. (2021). Tribochemistry, Mechanical Alloying, Mechanochemistry: What Is in a Name? *Front. Chem.* 9, 1–29. doi:10.3389/fchem.2021.685789

Moores, A. (2018). Bottom up, Solid-phase Syntheses of Inorganic Nanomaterials by Mechanochemistry and Aging. *Curr. Opin. Green Sustain. Chem.* 12, 33–37. doi:10.1016/j.cogsc.2018.05.004

Muñoz-Batista, M. J., Rodriguez-Padron, D., Puente-Santiago, A. R., and Luque, R. (2018). Mechanochemistry: Toward Sustainable Design of Advanced Nanomaterials for Electrochemical Energy Storage and Catalytic Applications. *ACS Sustain. Chem. Eng.* 6, 9530–9544. doi:10.1021/acssuschemeng.8b01716

Murugadoss, A., Kai, N., and Sakurai, H. (2012). Synthesis of Bimetallic Gold-Silver alloy Nanoclusters by Simple Mortar Grinding. *Nanoscale* 4, 1280. doi:10.1039/c2nr11727d

Nalawade, P., Mukherjee, T., and Kapoor, S. (2013). Green Synthesis of Gold Nanoparticles Using Glycerol as a Reducing Agent. *Anp* 02, 78–86. doi:10.4236/anp.2013.22014

Naseem, K., Begum, R., and Farooqi, Z. H. (2017). Catalytic Reduction of 2-nitroaniline: a Review. *Environ. Sci. Pollut. Res.* 24, 6446–6460. doi:10.1007/s11356-016-8317-2

Nazir, R., Fageria, P., Basu, M., and Pande, S. (2017). Decoration of Carbon Nitride Surface with Bimetallic Nanoparticles (Ag/Pt, Ag/Pd, and Ag/Au) via Galvanic Exchange for Hydrogen Evolution Reaction. *J. Phys. Chem. C* 121, 19548–19558. doi:10.1021/acs.jpcc.7b04595

Niu, Z., and Li, Y. (2014). Removal and Utilization of Capping Agents in Nanocatalysis. *Chem. Mater.* 26, 72–83. doi:10.1021/cm4022479

Paliwal, R., Babu, R. J., and Palakurthi, S. (2014). Nanomedicine Scale-Up Technologies: Feasibilities and Challenges. *AAPS PharmSciTech* 15, 1527–1534. doi:10.1208/s12249-014-0177-9

Quiroz, J., Barbosa, E. C. M., Araujo, T. P., Fiorio, J. L., Wang, Y.-C., Zou, Y.-C., et al. (2018). Controlling Reaction Selectivity over Hybrid Plasmonic Nanocatalysts. *Nano Lett.* 18, 7289–7297. doi:10.1021/acs.nanolett.8b03499

Quiroz, J., de Oliveira, P. F. M., Shetty, S., Oropeza, F. E., de la Peña O'Shea, V. A., Rodrigues, L. C. V., et al. (2021). Bringing Earth-Abundant Plasmonic Catalysis to Light: Gram-Scale Mechanochemical Synthesis and Tuning of Activity by Dual Excitation of Antenna and Reactor Sites. *ACS Sustain. Chem. Eng.* 9, 9750–9760. doi:10.1021/acssuschemeng.1c02063

Rak, M. J., Friščić, T., and Moores, A. (2014). Mechanochemical Synthesis of Au, Pd, Ru and Re Nanoparticles with Lignin as a Bio-Based Reducing Agent and Stabilizing Matrix. *Faraday Discuss.* 170, 155–167. doi:10.1039/C4FD00053F

Rodrigues, M. P. d. S., Dourado, A. H. B., Cutolo, L. d. O., Parreira, L. S., Alves, T. V., Slater, T. J. A., et al. (2021). Gold-Rhodium Nanoflowers for the Plasmon-Enhanced Hydrogen Evolution Reaction under Visible Light. *ACS Catal.* 11, 13543–13555. doi:10.1021/acscatal.1c02938

Rodrigues, T. S., da Silva, A. G. M., de Moura, A. B. L., Freitas, I. G., and Camargo, P. H. C. (2016). Rational Design of Plasmonic Catalysts: Matching the Surface Plasmon Resonance with Lamp Emission Spectra for Improved Performance in AgAu Nanorings. *RSC Adv.* 6, 62286–62290. doi:10.1039/C6RA11362A

Ruiz-Ruiz, V.-F., Betancourt, I., Zumeta-Dubé, I., Díaz-Pardo, R., and Díaz, D. (2022). Magnetic Properties of Pd-Ag Nanoalloys Obtained by Liquid-Assisted Mechanochemical Pathway. *J. Phys. Chem. Sol.* 161, 110427. doi:10.1016/j.jpcs.2021.110427

Ruiz-Ruiz, V.-F., González-Olvera, R., Díaz-Pardo, R., Betancourt, I., Zumeta-Dubé, I., Díaz, D., et al. (2018). Mechanochemically Obtained Pd-Ag Nanoalloys. Structural Considerations and Catalytic Activity. *Materialia* 4, 166–174. doi:10.1016/j.mtla.2018.09.031

Saire-Saire, S., Barbosa, E. C. M., Garcia, D., Andrade, L. H., Garcia-Segura, S., Camargo, P. H. C., et al. (2019). Green Synthesis of Au Decorated CoFe2O4 Nanoparticles for Catalytic Reduction of 4-nitrophenol and Dimethylphenylsilane Oxidation. *RSC Adv.* 9, 22116–22123. doi:10.1039/C9RA04222A

Schreyer, H., Eckert, R., Immohr, S., de Bellis, J., Felderhoff, M., and Schüth, F. (2019). Milling Down to Nanometers: A General Process for the Direct Dry Synthesis of Supported Metal Catalysts. *Angew. Chem. Int. Ed.* 58, 11262–11265. doi:10.1002/anie.201903545

Sha, J., Paul, S., Dumeignil, F., and Wojcieszak, R. (2019). Au-based Bimetallic Catalysts: How the Synergy between Two Metals Affects Their Catalytic Activity. *RSC Adv.* 9, 29888–29901. doi:10.1039/c9ra06001d

Slater, T. J. A., Macedo, A., Schroeder, S. L. M., Burke, M. G., O'Brien, P., Camargo, P. H. C., et al. (2014). Correlating Catalytic Activity of Ag-Au Nanoparticles with 3D Compositional Variations. *Nano Lett.* 14, 1921–1926. doi:10.1021/nl4047448

Sun, L., Lv, P., Li, H., Wang, F., Su, W., and Zhang, L. (2018). One-step Synthesis of Au-Ag alloy Nanoparticles Using Soluble Starch and Their Photocatalytic Performance for 4-nitrophenol Degradation. *J. Mater. Sci.* 53, 15895–15906. doi:10.1007/s10853-018-2763-9

Suryanarayana, C. (2001). Mechanical Alloying and Milling. *Prog. Mater. Sci.* 46, 1–184. doi:10.1016/S0079-6425(99)00010-9

Tyson, C. C., Bzowski, A., Kristof, P., Kuhn, M., Sammynaiken, R., and Sham, T. K. (1992). Charge Redistribution in Au-Ag Alloys from a Local Perspective. *Phys. Rev. B* 45, 8924–8928. doi:10.1103/PhysRevB.45.8924

Vongsavat, V., Vittur, B. M., Bryan, W. W., Kim, J.-H., and Lee, T. R. (2011). Ultrasmall Hollow Gold-Silver Nanoshells with Extinctions Strongly Red-Shifted to the Near-Infrared. *ACS Appl. Mater. Inter.* 3, 3616–3624. doi:10.1021/am2008322

Wang, J. L., Ando, R. A., and Camargo, P. H. C. (2014). Investigating the Plasmon-Mediated Catalytic Activity of AgAu Nanoparticles as a Function of Composition: Are Two Metals Better Than One? *ACS Catal.* 4, 3815–3819. doi:10.1021/cs501189m

Xu, C., De, S., Balu, A. M., Ojeda, M., and Luque, R. (2015). Mechanochemical Synthesis of Advanced Nanomaterials for Catalytic Applications. *Chem. Commun.* 51, 6698–6713. doi:10.1039/C4CC09876E

Conflict of Interest: The authors declare that the research was conducted in the absence of any commercial or financial relationships that could be construed as a potential conflict of interest.

Publisher's Note: All claims expressed in this article are solely those of the authors and do not necessarily represent those of their affiliated organizations, or those of the publisher, the editors and the reviewers. Any product that may be evaluated in this article, or claim that may be made by its manufacturer, is not guaranteed or endorsed by the publisher.

Copyright © 2022 da Silva, Córdoba De Torresi and de Oliveira. This is an open-access article distributed under the terms of the Creative Commons Attribution License (CC BY). The use, distribution or reproduction in other forums is permitted, provided the original author(s) and the copyright owner(s) are credited and that the original publication in this journal is cited, in accordance with accepted academic practice. No use, distribution or reproduction is permitted which does not comply with these terms.

frontiers

Supplementary Material

Mechanochemical Strategies for the Preparation of SiO_2 – Supported AgAu Nanoalloy Catalysts

Rafael T. P. da Silva[1], Susana I. Córdoba de Torresi[1], Paulo F. M. de Oliveira[1*]

[1]Institute of Chemistry, University of São Paulo - Brazil

*** Correspondence:**

Paulo F. M. de Oliveira
paulofmo@usp.br

Catalytic Reduction of 2-Nitroaniline S2

XPS Data Acquisition and Analysis S2

Supplementary Figure S1 – Particle size distribution of the the metallic nanoparticles S3

Supplementary Figure S2 – HAADF-STEM and STEM-EDX characterization of the bimetallic materials. S4

Supplementary Table S1 - ICP-OES analysis S4

Supplementary Table S2 - Reaction yield for one-hour milling……..S5

Supplementary Figure S3 - XPS spectra of the mechanochemically prepared samples. S6

Supplementary Table S3 – XPS elemental analysis S7

Supplementary Figure S4 – Catalytic reduction of 2-NA to o-PDA. S8

Supplementary Figure S5 – Band shift in the range of 280 nm throughout the catalytic reduction of 2-NA S9

Catalytic Reduction of 2-Nitroaniline

A 1 mg·mL^{-1} aqueous stock solution of each catalyst was prepared. In a cuvette, 2.8 mL of water, 120 µL of 2-NA (6.25 mM), 130 µL of $NaBH_4$ (2 mM) and, at last, the volume correspondent to 1.6 % (m/m) of metal/2-NA of each catalyst was added. The spectra were collected every 80 seconds. The determination of the reaction rate constant followed the pseudo first-order,

$$A = A_0 e^{-\frac{k}{t}} \quad \text{(S1)}$$

in which A = A_{412}-A_{500}, A_0 = initial absorbance at 412 nm, k is the reaction rate constant and t is time. Each reaction was repeated three times. Between catalytic runs, the cuvette was washed with aqua regia and several times with water to eliminate any deposition of metals.

The conversion (%) was calculated by:

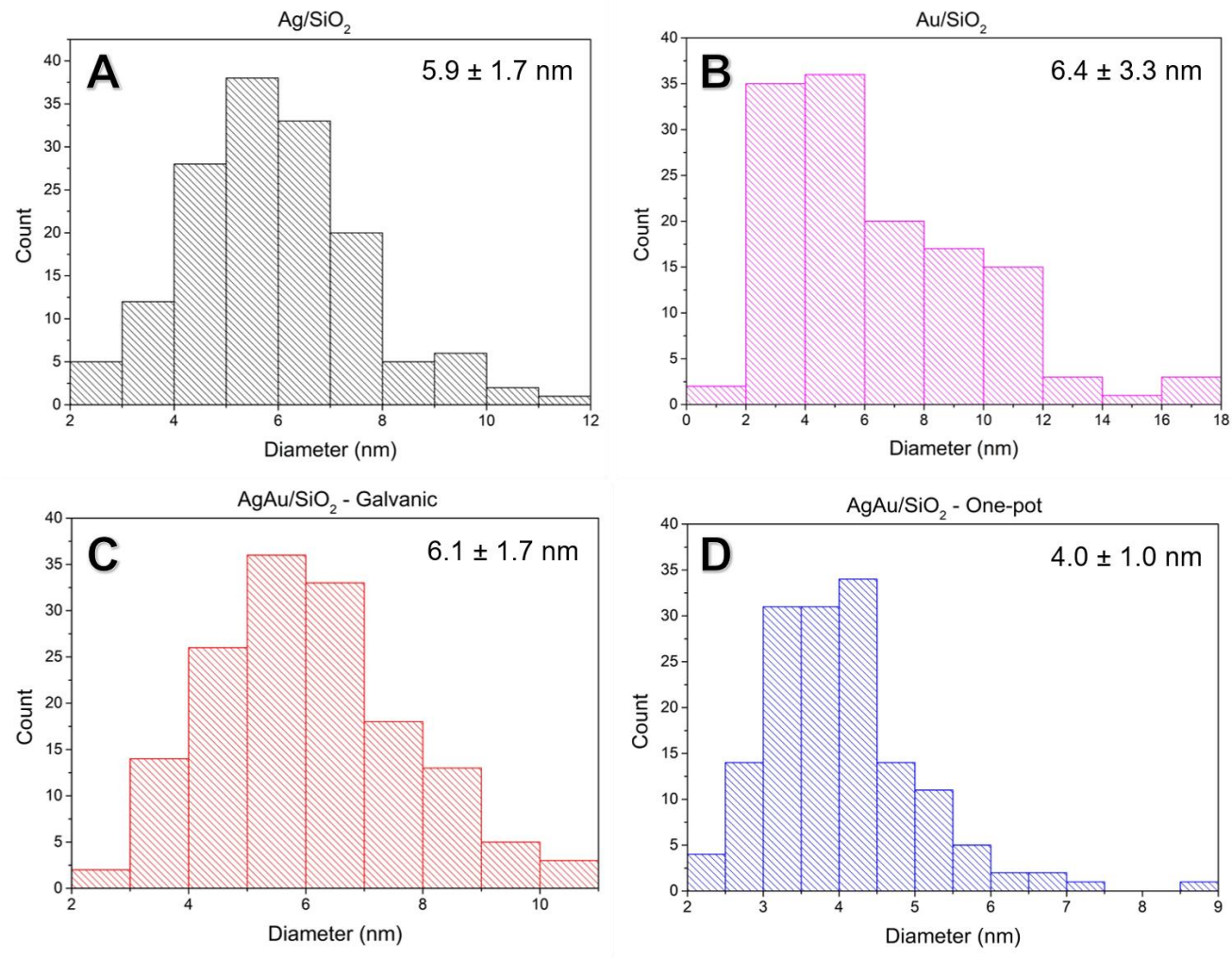
$$Conversion\ (\%) = \frac{A_0 - A}{A_0} \times 100 \quad \text{(S2)}$$

Considering Equation S1 and a pseudo-first order reaction, the linearization of the conversion curves followed:

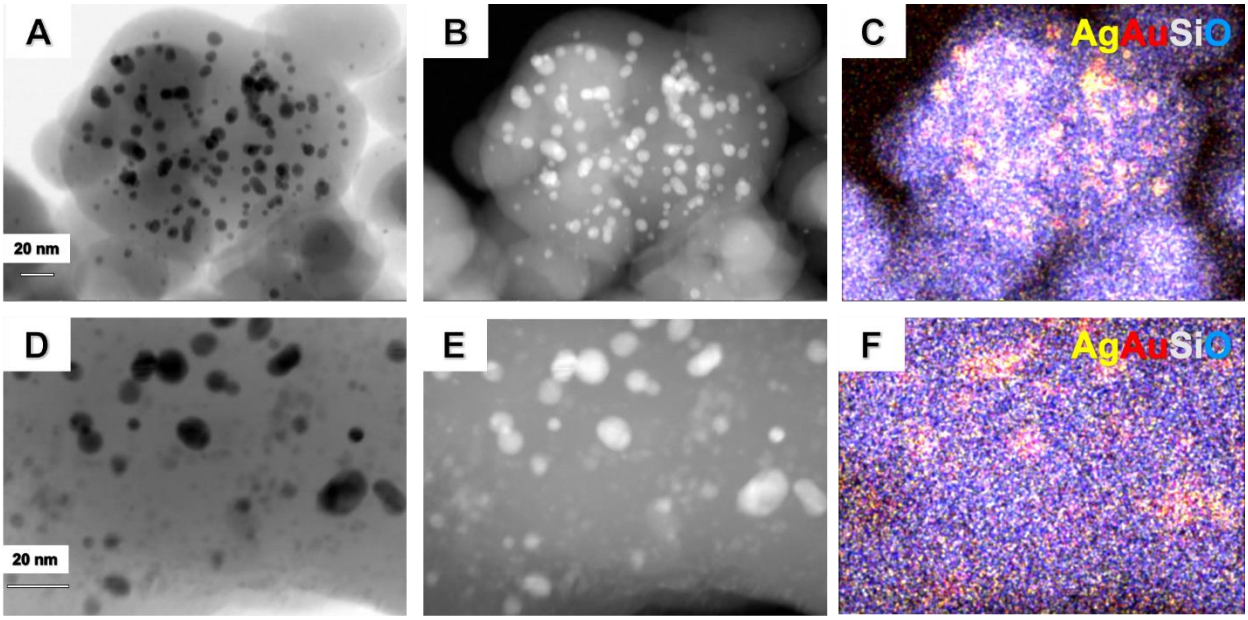
$$\ln\left(\frac{C}{C_0}\right) = ln\left(\frac{A}{A_0}\right) = -kt \quad \text{(S3)}$$

XPS Data Acquisition and Analysis

XPS spectra were collected using Mg Kα line as a source of ionization (hν = 1256.6 eV) and the pass energy was adjusted to 15 eV. The inelastic scattering of XPS of Ag 3d and Au 4f were subtracted using Shirley's method. Composition of the surface (<5 nm) was determined by the relative proportional areas of the peaks corrected by the Scofield atomic sensitivity factor with a precision of ±5%. Binding energy were corrected using the hydrocarbon components (C-H) set at 284.9 eV. Spectra were deconvoluted using a Voigtian function with a convolution of Gaussian (70%) and Lorentzian (30%) functions. FWHM varied between 1.2 and 2.1 eV and the peak positions were determined with a precision of ± 0.1 eV.



Supplementary Figure S1 – Particle size distribution of the the metallic nanoparticles on the synthesized materials. Ag/SiO_2 **(A)**, Au/SiO_2 **(B)**, $AgAu/SiO_2$ galvanic **(C)**, $AgAu/SiO_2$ one-pot **(D)**. For particle size distribution at least 150 individual particles were considered.



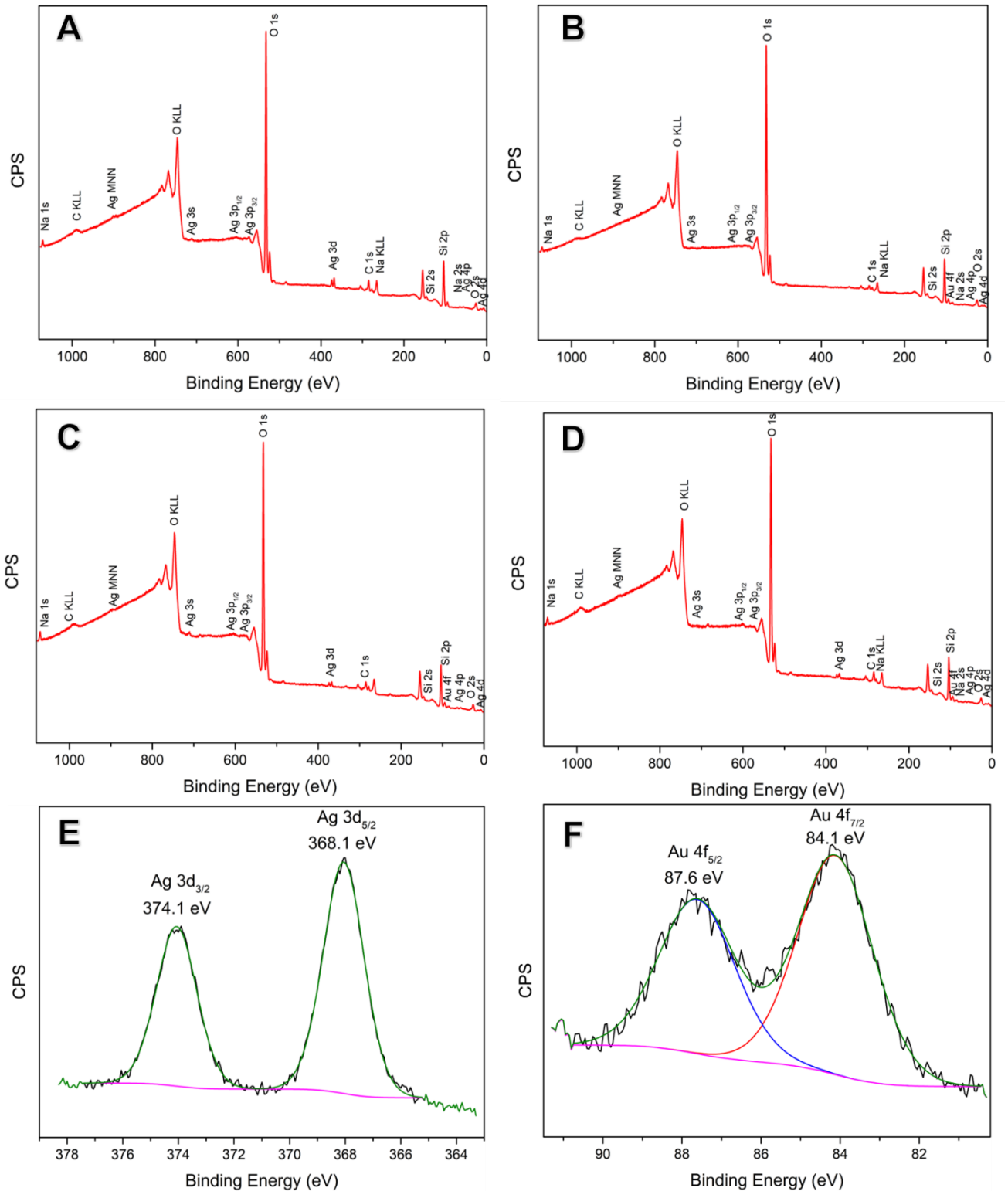
Supplementary Figure S2 – HAADF-STEM and STEM-EDX characterization of the bimetallic materials. AgAu/SiO_2 galvanic **(A-C)**, AgAu/SiO_2 one-pot **(D-F)**.

Supplementary Table S1 - ICP-OES analysis

Sample	Total metal in sample (mass %)	Ag (mass %)	Au (mass %)
Ag/SiO_2	2.50	100	-
Au/SiO_2	2.84	-	100
AgAu/SiO_2 galvanic	3.10	58	42
AgAu/SiO_2 one-pot	2.73	36	64

Supplementary Table S2 – Reaction yield for 1h-milling calculated from ICP-OES and metal salt added.

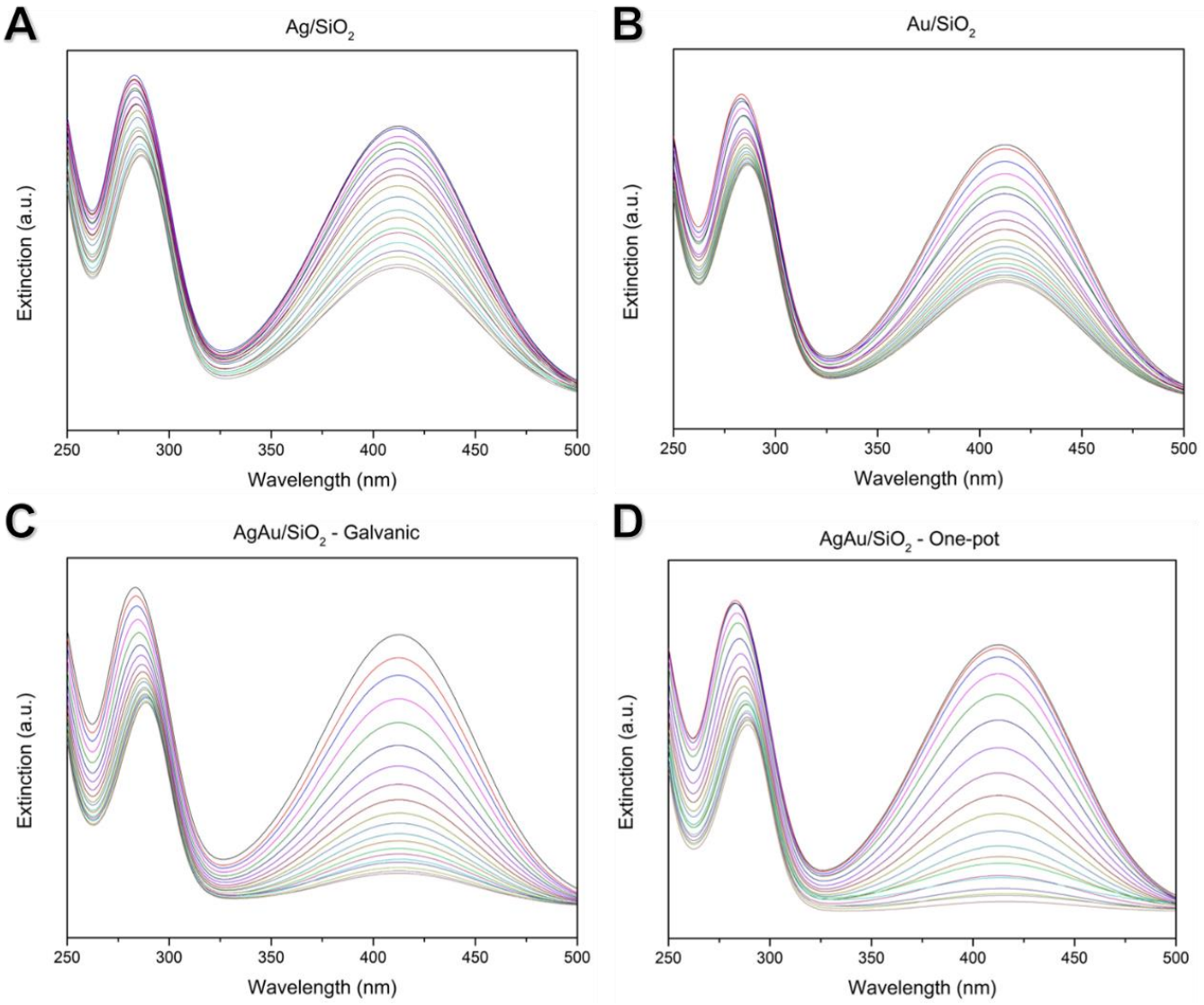
Sample	Initial amount of Ag (mass %)	Initial amount of Au (mass %)	Obtained amount of Ag (mass %)	Obtained amount of Au (mass %)	Yield Ag (%)	Yield Au (%)
Ag/SiO_2	4.41	-	2.50	-	56.7	-
Au/SiO_2	-	4.60	-	2.84	-	61.7
$AgAu/SiO_2$ galvanic	2.50	1.60	1.80	1.29	72.0	80.6
$AgAu/SiO_2$ one-pot	2.11	2.34	0.99	1.75	46.9	74.8



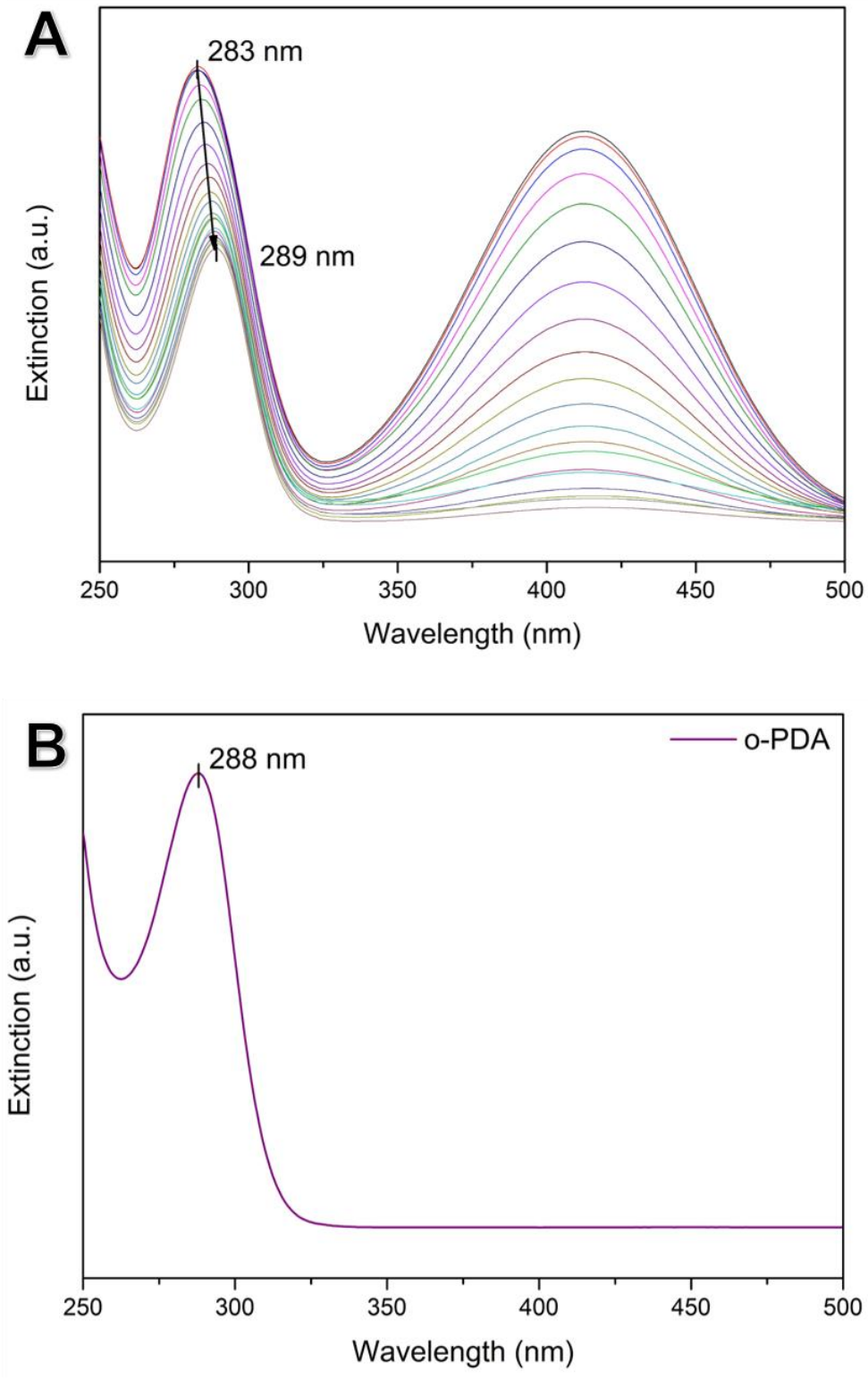
Supplementary Figure S3 - XPS spectra of the mechanochemically prepared samples. Survey spectra of Ag/SiO_2 **(A)**, Au/SiO_2 **(B)**, $AgAu/SiO_2$ Galvanic **(C)**, $AgAu/SiO_2$ one-pot **(D)**. HR-XPS for Ag 3d of Ag/SiO_2 **(E)** and Au 4f of Au/SiO_2 **(F)** regions.

Supplementary Table S3 – XPS elemental analysis

Sample	Ag (mass %)	Au (mass %)
Ag/SiO_2	100	-
Au/SiO_2	-	100
$AgAu/SiO_2$ galvanic	62	38
$AgAu/SiO_2$ one-pot	62	38



Supplementary Figure S4 – Catalytic reduction of 2-NA to o-PDA with $NaBH_4$ catalyzed by Ag/SiO_2 **(A)**, Au/SiO_2 **(B)**, $AgAu/SiO_2$ galvanic **(C)** and $AgAu/SiO_2$ one-pot **(D)**.



Supplementary Figure S5 – Band shift in the range of 280 nm throughout the catalytic reduction of 2-NA **(A)** represents the formation of o-PDA **(B).**

3.1.3 AgAu Hollow Nanoshells on Layered Graphene Oxide and Silica Submicrospheres as Plasmonic Nanozymes for Light-Enhanced Electrochemical H_2O_2 Sensing (Attachment 3)

Author Contribution: The author participated in conceiving the idea, designing the experiments, performing the assays, and writing the paper.

In the recent years, the development of nanozymes as electrochemical sensors has been emerging as a promising alternative to natural enzymes[30]. The use of metallic nanozymes as sensors is a cost-effective strategy that benefits from features such as nanozymes stability and their ease of storage. In addition, with the recent advances in nanotechnology, nanozymes can be remotely controlled by different external stimuli, such as heat, magnetic field, ultrasound, and light[31]. In this sense, the rational control over metallic ratio in bimetallic materials is a promising strategy to finely tune a set of properties, including the position of the LSPR band in the UV-Vis spectrum[32]. In this sense, LSPR-driven catalysis plays an important role in metallic nanozymes responsive to light, enhancing their performance as electrochemical sensors.

Herein, we present a novel synthesis strategy of controlled AgAu nanoshells supported on graphene oxide (GO) and SiO_2 submicrospheres. Differently from what was presented in **Attachment 2**, we present a solution-based process, using water as medium for the Galvanic Replacement Reaction (GRR) process to occur on supports with previously supported AgNP. Due to morphological differences between GO and SiO_2, different metallic ratios are obtained from each support, $Ag_{79}Au_{21}$/GO and $Ag_{50}Au_{50}/SiO_2$. Consequently, LSPR bands from each system are placed in different regions from UV-Vis spectrum. These two synthesized structures were used as

peroxidase-like nanozymes stimulated in LSPR in the electrochemical detection of H_2O_2 through hydrogen peroxide reduction reaction (HPRR). To this end, three different light sources (405, 533, and 650 nm) were used to irradiate the working electrode. Compared to dark conditions, $Ag_{79}Au_{21}$/GO showed an increase in sensitivity of 122% upon 533 nm and 105% upon 405 nm, both wavelengths matching the nanostructure LSPR. $Ag_{50}Au_{50}/SiO_2$ presented a 119% increase upon 650 nm, wavelength that matched its LSPR. In both cases, wavelengths that did not match the LSPR presented negligible improvements when compared to dark, suggesting LSPR-driven sensing is the main mechanism behind this stimulus. In the basic medium of analysis, the main mechanism of LSPR is the faster electron transfer from the nanostructure to dioxidanide, leading to H_2O_2 reduction to hydroxyl ions. The systems were also analyzed by Michaelis-Menten enzyme kinetics approach, which showed higher I_{max} and a lowering in apparent Michaelis constant (K_M^{app}) in the best-performing systems, suggesting increased substrate affinity in comparison to previously reported values for enzymatic and nonenzymatic biosensors for H_2O_2.

ACS APPLIED NANO MATERIALS

www.acsanm.org Article

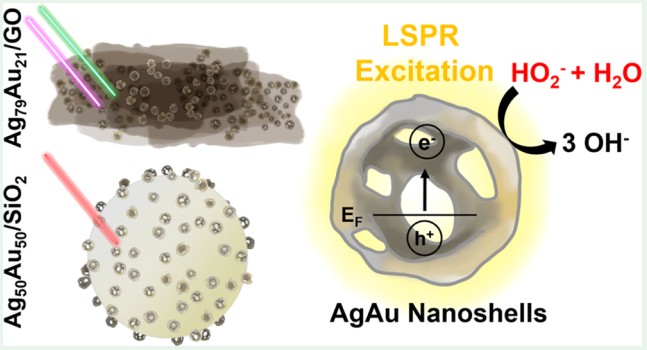
AgAu Hollow Nanoshells on Layered Graphene Oxide and Silica Submicrospheres as Plasmonic Nanozymes for Light-Enhanced Electrochemical H_2O_2 Sensing

Rafael T. P. da Silva, Maria Paula de Souza Rodrigues, Gabriela F. B. Davilla, Adriano M. R. P. da Silva, André H. B. Dourado, and Susana I. Córdoba de Torresi*

Cite This: *ACS Appl. Nano Mater.* 2021, 4, 12062−12072 Read Online

ACCESS | Metrics & More | Article Recommendations | Supporting Information

ABSTRACT: Localized surface plasmon resonance (LSPR) is a phenomenon derived from the interaction between light and nanostructures, and its outcomes have been explored mainly for applications in surface-enhanced Raman spectroscopy (SERS), phototherapy, and catalysis. Bimetallic nanostructures are able to synergically combine the properties of two different metals to create a tuned response to LSPR according to their composition, shape, and morphology. In this study, an in situ synthesis of AgAu bimetallic hollow nanoshells (NS) over layered graphene oxide (GO) and silica submicrospheres (SiO_2) is presented. The synthesized structures acted as peroxidase-like nanozymes in the plasmon-enhanced electrochemical sensing of H_2O_2. The nanozymes were submitted to 405, 533, and 650 nm laser irradiation while performing the hydrogen peroxide reduction reaction (HPRR) with a fast response speed (4 s), exhibiting enhancements in sensitivity of 122% (for $Ag_{79}Au_{21}$/GO at 533 nm, 787 μA mM^{-1} cm^{-2}), 105% (for $Ag_{79}Au_{21}$/GO at 405 nm, 725 μA mM^{-1} cm^{-2}), and 119% (for $Ag_{50}Au_{50}/SiO_2$ at 650 nm, 885 μA mM^{-1} cm^{-2}) compared to the dark conditions when matching the LSPR band maximum for each synthesized structure. When laser stimuli did not match LSPR band maximum, lower enhancements were achieved in both cases. According to Michaelis−Menten enzyme kinetics, the nanozymes I_{max} followed the same LSPR bias and K_m^{app} was lowered after LSPR stimuli, showing the smallest values upon 405 nm irradiation (0.599 mM for $Ag_{79}Au_{21}$/GO and 0.228 mM for $Ag_{50}Au_{50}/SiO_2$) demonstrating increased substrate affinity in comparison to values previously reported in enzymatic and nonenzymatic biosensors of H_2O_2. Thus, we propose that LSPR is the main mechanism involved in the faster electron transfer rates and the consequent enhancement of electrochemical H_2O_2 sensitivities, I_{max}, and K_m^{app} by the bimetallic nanozymes synthesized by this approach.



KEYWORDS: *nanoplasmonics, nanozymes, electrochemical sensors, LSPR, bimetallic nanoparticles*

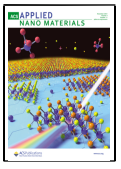
Downloaded via UNIV OF SAO PAULO on July 30, 2022 at 20:39:13 (UTC).
See https://pubs.acs.org/sharingguidelines for options on how to legitimately share published articles.

INTRODUCTION

Hydrogen peroxide (H_2O_2) is an important analyte, and its determination plays a key role in different fields, such as biology, biomedicine, the food industry, and pharmaceutical, biochemical, and environmental analyses.[1,2] Moreover, it is involved in several biological processes, and its excess can affect the proper functioning of cells; thus, its accurate determination is valuable.[3] Over the years, different techniques have been explored for its determination, such as titrimetry,[4] chromatography,[5] spectrophotometry,[6] colorimetry,[7] fluorescence,[8] and electrochemistry.[9] However, electrochemical methods are preferred due to their rapid development, good accuracy, lower detection limits, easy miniaturization, biocompatibility, low cost, simple instrumentation, high selectivity, and fast response.[10−14]

Enzymatic and nonenzymatic electrochemical sensors are of great interest due to their high activities and selectivity. Nonetheless, enzymatic sensors have some disadvantages, such as poor stability, critical operating conditions, immobilization procedures, and limited lifetimes.[9,15] To overcome these challenges, nonenzymatic sensors using metallic nanoparticles (NPs) have been explored as an alternative for H_2O_2 sensing, acting as peroxidase-like catalysts.[13] Nanoparticles that

Received: August 21, 2021
Accepted: October 13, 2021
Published: October 26, 2021



ACS Publications © 2021 American Chemical Society

perform biocatalytic reactions in the replacement of enzymes have been called nanozymes in recent years.[16]

Metallic nanoparticles are of great interest in several areas due to their high surface area, quantum confinement effects, and localized surface plasmon resonance (LSPR) effects, which are not observed in their bulk counterparts.[17,18] The LSPR is a phenomenon that occurs mainly when the interaction between plasmonic metal nanostructures and irradiated light takes place. When the frequency of the light is resonant with the normal oscillation frequency of free electrons in these nanostructures, three major outcomes are reported: the formation of electron−hole pairs at the nanostructure surface, the local heat generated through the recombination of these pairs, and the near-field enhancement.[19] These effects have been extensively explored, including for catalysis,[20] photothermic therapy,[21] and surface-enhanced Raman spectroscopy (SERS).[22,23] Recently, the enhancement of electrochemical sensor sensitivity and responses through LSPR stimuli has been demonstrated to be an effective tool to improve sensitivity using a renewable source of energy.[24,25]

In particular, gold and silver have been extensively used as plasmonic sensors since they are noble metals with intense LSPR activity in the visible spectrum, mainly due to their dielectric functions in combination with the surrounding medium.[26] Silver nanoparticles (AgNPs) are advantageous as a result of their low rate of intrinsic energy loss with a high oscillator strength.[27] Although gold nanoparticles are more stable and inert than silver, they present higher rates of intrinsic energy loss, mainly in the short-wavelength regions, where interband transitions occur.[28]

The combination of more than one metal in bimetallic nanomaterials has attracted attention, as there is an opportunity not only to combine individual properties from the elements but also to achieve some unexpected properties arising from the synergy among them.[29−34] Typically, nanosized silver and gold are combined as core−shell or alloyed bimetallic nanoshells (NS).[29,30] Bimetallic hollow NS formed by the galvanic replacement reaction (GRR) have a considerable improvement in the ratio between the surface area and volume, minimizing the amount of metals.[35] Hollow nanostructures enhance plasmonic effects by forming plasmon hybridization between the cavity and sphere plasmon modes, inducing a more stable hybridized mode with improved charge separation on the structure.[36] In addition, the GRR between gold and silver progressively presents a redshift of the LSPR band depending on the corrosion level, which requires fewer energetic photons for plasmonic excitation than their individual metal counterparts.[37,38] There are still a few studies in the literature exploring AgAu hollow nanostructures to enhance electrochemical reactions, although none of them were found to use LSPR stimulus outcomes.[39−42]

Oxide supports have been used to stabilize the nanoparticles, preventing their aggregation through adhesion energy between the metals and the oxide surfaces.[43] In our study, we anchor metallic nanoparticles over layered graphene oxide (GO) and submicrospheres of silicon dioxide (SiO_2). Although GO-based nanocomposites present an insulating nature, they have been receiving attention in electrochemical sensing.[44,45] This is due to the fact that they offer a hydrophilic biocompatible microenvironment with an increased surface area that facilitates immobilization of electroactive species.[46] A second insulator, SiO_2 submicrosphere, was chosen in terms of comparison because it displays an assemble with increased exposition of nanoparticles. Besides, SiO_2 has been used in many fields such as biomedicine and catalysis as an inert host matrix of simple surface modification.[47−49]

In this work, we present an innovative in situ GRR between Au precursor and Ag templates anchored over GO and SiO_2 submicrospheres. The formed AgAu NS were evaluated as nanozymes in terms of their plasmonic catalytic activity toward the HPRR for H_2O_2 sensing to assess the aspects of LSPR with stimulation at specific wavelengths.

EXPERIMENTAL METHODS

Chemicals. Hydrogen tetrachloroaurate trihydrate ($HAuCl_4 \cdot 3H_2O$, 48% in gold, Sigma-Aldrich), silver nitrate ($AgNO_3$, ≥99%, Sigma-Aldrich), tetraethyl orthosilicate (TEOS, 98%, Sigma-Aldrich), ammonium hydroxide (NH_4OH, 27%, Synth), 3-aminopropylethoxysilane (APTES, ≥98%, Sigma-Aldrich), poly(vinylpyrrolidone) (PVP, Sigma-Aldrich, MW 55 000 and 10 000 g mol^{-1}), ethylene glycol ($C_2H_6O_2$, 99.5%, Synth), acetone (C_3H_6O, 99.5%, Synth), ethanol (C_2H_6O, 95%, Synth), toluene (C_7H_8, 100%, Synth), sulfuric acid (H_2SO_4, 98%, Synth), nitric acid (HNO_3, 65%, Synth), hydrochloric acid (HCl, 37%, Synth), phosphoric acid (H_3PO_4, 85%, Synth), potassium permanganate ($KMnO_4$, 100%, Synth), hydrogen peroxide (H_2O_2, 29%, Synth), potassium hydroxide (KOH, 90%, Sigma-Aldrich), graphite flakes (+100 mesh, Sigma-Aldrich), Carbon Vulcan (XC-72R), Nafion 5% ($C_7HF_{13}O_5S \cdot C_2F_4$, 15−20%, Sigma-Aldrich). All chemicals were analytical-grade reagents. Deionized water (18.2 MΩ) was used throughout the experiments.

Instrumentation. Scanning electron microscopy (SEM) images were obtained using a JEOL FEG-SEM JSM 6330F microscope operated at 5 kV. Samples were prepared by drop-casting an aqueous suspension of the particles on a Si wafer, followed by drying under ambient conditions. Transmission electron microscopy (TEM) images were obtained using a Tecnai FEI G20 operated at 200 kV. Samples were prepared by drop-casting 5 μL from an aqueous suspension of each sample in a lacey-carbon copper grid. UV−vis spectra were obtained using a Shimadzu UV-2600 UV−vis spectrophotometer and quartz cuvette with an optical path of 1 cm. For each measurement, the cuvette was washed three times with acetone and once with water. To determine the metal composition in the samples, ICP-OES Spectro Arcos equipment was used. The digestion of the samples occurred by aqua regia in a 1:1 ratio. Then, a 10-fold dilution with distilled water was performed before each measurement. The X-ray diffraction (XRD) data were obtained using Rigaku-Miniflex equipment and Cu Kα radiation. The diffraction pattern was measured in the 2θ range of 10−70° with a 1° min^{-1} angular speed scan. X-ray photoelectron spectroscopy (XPS) was performed in a Specs FlexPS system equipped with a Phoibos 150 2D CCD detector and using an XR50 X-ray source with a nonmonochromatized Al Kα (1486.61 eV) source. The catalyst ink was drop-cast over a Si substrate, covering properly the Si surface, as no Si signal (main transition for SiO_2 is Si 2p at 103.3 eV)[50] was detected. All spectra were registered in a high-vacuum chamber at pressures below 10^{-9} mbar and were corrected by the C 1s signal (284.5 eV).[50,51]

Silver Nanoparticle (AgNP) Synthesis via the Ethylene Glycol Method. As previously described, 5.0 g of PVP with an MW of 10 000 was dissolved in 37.5 mL of ethylene glycol at room temperature.[52] Then, 200 mg of $AgNO_3$ was solubilized with assistance from an ultrasonic bath. The system was heated by a heating plate with magnetic stirring at a 1 °C min^{-1} rate until 120 °C and left reacting for 90 min. After cooling, the product was diluted with distilled water to 125 mL.

AgAu Nanoshell (AgAu NS) Synthesis. Inspired by a previously described procedure,[35] a solution of PVP with an MW of 55 000 (50 mL, 1 mg mL^{-1}) was heated to ebullition by a heating plate with a magnetic stirrer, and 2.78 mL of AgNPs was added. After 10 min, 5, 10, 20, or 30 mL of $HAuCl_4 \cdot 3H_2O$ (0.2 mmol L^{-1}) was added dropwise for the galvanic replacement reaction to take place. Then, the reaction was stirred for 10 min to be completed. The amount of

https://doi.org/10.1021/acsanm.1c02611
ACS Appl. Nano Mater. 2021, 4, 12062−12072

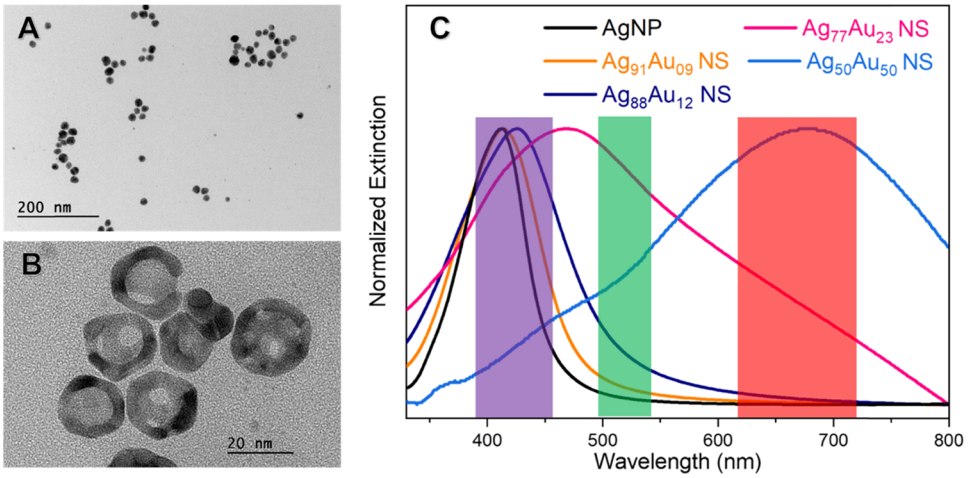


Figure 1. Characterization of AgAu NS synthesis. TEM micrographs for AgNPs (A) employed as templates for the synthesis of $Ag_{50}Au_{50}$ NS with hollow interiors (B). UV−Vis spectra for AgNPs and different degrees of galvanization of AgAu NS, represented by the metal ratio in the subscript (C). The subscription in the caption represents the molar ratio between the metals, and the colored stripes represent the absorbed colors corresponding to that spectral region.

$HAuCl_4 \cdot 3H_2O$ (0.2 mmol L^{-1}) dictated the degree of corrosion of the structure, as depicted by the structural characterization.

Graphene Oxide (GO) Synthesis. A modified Hummer's method was used as previously described in the literature.[53] Therefore, a mixture of 360 mL of H_2SO_4 and 40 mL of H_3PO_4 was prepared. To this mixture, a solid mixture of 18.0 g of $KMnO_4$ in six equally divided portions and 3.0 g of graphite was added to an ice-cold bath. The resulting solution was stirred for 12 h at 50 °C on a stirring hot plate. Then, 3 mL of H_2O_2 (30 v/v) and 400 mL of frozen distilled water were added. The product was vacuum-filtered and washed with a mixture of 1020 mL of distilled water, 180 mL of HCl, and 600 mL of ethanol. The resulting material was left to dry at 70 °C for 12 h.

Amine-Functionalized Submicrospheres of Silicon Dioxide (SiO_2) Synthesis. A modified Stöber method was used for the synthesis of SiO_2-NH_2.[47] A mixture containing 35 mL of NH_4OH, 75 mL of ethanol, and 15 mL of distilled water was added to 25 mL of a solution of TEOS in ethanol (26% v/v) and stirred for 2 h. The submicrospheres were separated by centrifugation (7000 rpm, 10 min) and washed twice with distilled water and once with ethanol. The sample was dried at 100 °C and calcinated at 600 °C for 2 h. The amine functionalization procedure was performed with some adjustments from that previously described.[54] Surface functionalization promoted an optimized anchoring platform to metallic nanoparticles compared to nonfunctionalized synthesis. Therefore, 1 g of SiO_2 submicrospheres was added to 150 mL of dried toluene and sonicated for 30 min. Then, 1.5 mL of 3-aminopropylethoxysilane (APTES) was added dropwise to the mixture under stirring at room temperature and kept under stirring for 2 h. Finally, SiO_2-NH_2 was separated by centrifugation, washed once with toluene and twice with acetone, and dried at 80 °C for 20 h.

Synthesis of AgNP/GO and AgNP/SiO_2. To decorate GO and SiO_2 with AgNPs, a dry impregnation method was used. Therefore, 10 mL of the as-synthesized AgNPs was washed three times in a mixture of 10% water and 90% acetone for 15 min at 15 000 rpm. Some droplets of water were used to disperse the pellet, and 10 mL of acetone was further added to remove the excess PVP used in the AgNP synthesis. This procedure was performed three times. The final redispersion was performed with 1 mL from a 1:1 mixture of water and ethanol. Then, 200 mg of solid GO or SiO_2-NH_2 was spread onto a petri dish over a heating plate set at 60 °C. Aliquots of 70 μL were sequentially dropped with a micropipette onto the solid, and with the help of a spatula, the solid was homogenized until completely dried. This process was repeated until the concentrated 1 mL was entirely consumed.

Synthesis of AgAu/GO and AgAu/SiO_2. The galvanic replacement reaction proceeded for the in situ formation of AgAu NS. Therefore, 10 mg of AgNP/GO or AgNP/SiO_2 was added to 8.4 mL of an aqueous solution of PVP with an MW of 55 000 (1 mg mL^{-1}) brought to boil on a heating plate with magnetic stirring. After complete suspension, 1 mL of $HAuCl_4 \cdot 3H_2O$ (0.2 mmol L^{-1}) was added dropwise. Then, the reaction was stirred for an additional 10 min for completion.

Ink Preparation. For further electrochemical application, the catalysts were deposited on Carbon Vulcan by wet impregnation. Five milliliters of each catalyst and 5 mg of Carbon Vulcan were dispersed in water. The mixture was sonicated for 1 h and stored for further experiments.

Electrochemical Methods. A three-electrode electrochemical cell was used for the electrochemical experiments, with Ag/AgCl (KCl saturated) as a reference electrode and Pt wire as the auxiliary electrode. The working electrode was a glassy carbon rotating-disk electrode (GCE, d = 1.5 mm) modified by drop-casting 10 μL of the previously prepared catalyst ink and 5 μL of Nafion 0.05%. Moreover, 70 mL of 1.0 mol L^{-1} KOH solution was used as the electrolyte. The cell was N_2-saturated to avoid reactive oxygen species formation. Hydrodynamic conditions (1600 rpm, controlled by a Pine AFMSRCE RDE) were used to keep the analyte concentration (H_2O_2) homogeneous in the electrochemical cell.

Triangular and current step perturbations were controlled and executed by a PGSTAT302N Autolab potentiostat/galvanostat to investigate the catalyst H_2O_2 sensing performance. All perturbation programs are depicted in the figures. For the current step perturbation investigation, a fixed potential of −0.3 $V_{Ag/AgCl}$ was applied for 5 min, followed by 20 additions of 50 μmol L^{-1} H_2O_2 and 5 additions of 100 μmol L^{-1} H_2O_2. The additions were made every 20 s.

For the light experiments, 200 mW modular lasers of 405, 533, and 650 nm were positioned 7 cm from the working electrode. The laser was turned on at least 5 min before the measurements, avoiding possible fluctuations in power. The triangular and step perturbations were performed as described previously for the light experiments. All measurements were normalized by the electrochemically active surface area (ECSA), which was estimated from the double-layer capacitance (C_{dl}) of each catalyst divided by the C_{dl} of bare Carbon Vulcan.

RESULTS AND DISCUSSION

Synthesis of AgAu Nanoshells (AgAu NS). The synthesis of AgAu NS was proceeded by the galvanic replacement reaction (GRR), a strategy that has been used

https://doi.org/10.1021/acsanm.1c02611
ACS Appl. Nano Mater. 2021, 4, 12062−12072

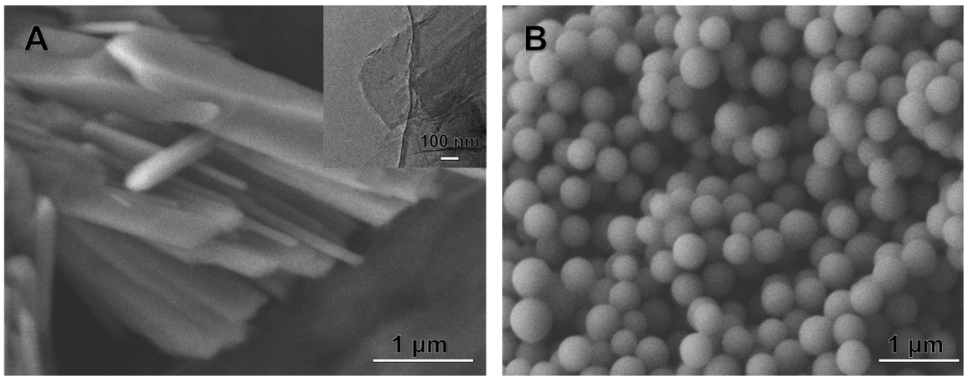


Figure 2. Micrographs of the supports. SEM micrograph of GO with a TEM micrograph as the inset (A) and SEM micrograph of SiO_2 submicrospheres (B).

in the field of nanoparticles design to create hollow nanostructures with tunable and well-controlled physical and chemical properties.[55,56] In this study, AgNPs were synthesized by the ethylene glycol method as templates and $HAuCl_4$ as the gold precursor. Different degrees of galvanization were achieved by varying the amount of gold precursor added from 5 to 30 mL of $HAuCl_4 \cdot 3H_2O$ (0.2 mmol L^{-1}). The molar ratio among the two metals was determined by ICP-OES and is represented as a subscript in the "AgAu NS" notation: $Ag_{91}Au_{09}$, $Ag_{88}Au_{12}$, $Ag_{77}Au_{23}$, and $Ag_{50}Au_{50}$ NS. TEM micrographs from the templates and the resultant $Ag_{50}Au_{50}$ NS after GRR are presented in Figure 1A,B, respectively. The size distribution before and after GRR for this sample is represented in Figure S1. The AgNP templates presented a spherical shape of 16 ± 3 nm in diameter, whereas after the GRR, the $Ag_{50}Au_{50}$ NS followed a spherical shape with hollow interiors with a diameter of 20 ± 4 nm and a shell thickness of ~4 nm. Both samples were relatively monodispersed in terms of size and morphology. TEM images of $Ag_{91}Au_{09}$ and $Ag_{77}Au_{23}$ are demonstrated in Figure S2, where a progressive corrosion degree is noticeable, starting from a bulky nanostructure with some defects (Figure S2A, $Ag_{91}Au_{09}$) toward a thicker shell structure presented by $Ag_{77}Au_{23}$ (Figure S2B). Figure S3 shows HRTEM images of $Ag_{50}Au_{50}$ NS, confirming the presence of 0.234 nm (111) lattice spacing after averaging the distance of 15 fringes. This can be assigned to the presence of fcc of either Ag or Au (ICSD 98-004-4362 and 98-004-4387). The center of the particle focused in HRTEM shows no fringes, indicating the hollow interior of the formed nanostructure. Energy-dispersive spectroscopy (TEM-EDS) was performed over the same particle, indicating the coexistent presence of both Ag and Au. Figure 1C shows the UV−Vis absorption spectra of the different materials and reveals that while the AgNP templates had their maximum at 413 nm, represented by a narrow LSPR band, bimetallic AgAu NS samples varied their maximum and presented band broadening. The bands were centered at 413 nm for $Ag_{91}Au_{09}$ NS, 425 nm for $Ag_{88}Au_{12}$ NS, 469 nm for $Ag_{77}Au_{23}$ NS, and 678 nm for $Ag_{50}Au_{50}$ NS with a progressive LSPR band redshift and broadening. The colored stripes on the UV−Vis extinction spectra represent the absorbed colors corresponding to that spectral region.

Both the redshift and broadening of the LSPR band are in agreement with the increase in the Au ratio in the alloy and the expected degree of corrosion resulting from the sequence of GRR.[32,38,57] The red-shifted LSPR band toward the near-infrared (NIR) region has been demonstrated by previous studies to be an interesting property concerning biological applications related to maximized penetration in tissue, such as photodynamic therapy.[58,59] Moreover, the LSPR excitation of the red-shifted alloy requires lower-energy photons than the pure silver or gold nanoparticle counterparts with higher-energy LSPR bands. In addition, band broadening provides the opportunity to work with wider spectrum sources, such as the solar light spectrum, with higher efficiency yields concerning plasmonic outcome effects.[60]

In Situ Synthesis of AgAu NS over Graphene Oxide and SiO_2 Submicrospheres (AgAu/GO and AgAu/SiO_2). Two supports were chosen for the in situ synthesis of AgAu NS. The first is graphene oxide (GO), a layered organization of carbon functionalized with hydroxyl groups, and the second is SiO_2, a submicrometric material with a spherical shape functionalized with amine groups. The synthesis of GO followed an improved Hummer's method, where the flake graphite is exfoliated by a strong oxidizing mixture up to its conversion to graphene oxide.[53] In turn, submicrospheres of SiO_2 were synthesized by a slightly modified Stöber's method with post-functionalization with APTES, with an amine terminal group that improves the anchoring of further synthesized metallic nanoparticles.[61] Micrographs of the supports are shown in Figure 2. GO presented a layered structure, and its Raman spectrum analysis suggests Raman modes D (1353 cm^{-1}), 2D (2670 cm^{-1}), and G (1595 cm^{-1}), as indicated in Figure S4. X-ray diffraction (XRD) patterns of both supports are demonstrated in Figure S5. SiO_2 submicrospheres show a typical amorphous peak, whereas graphene oxide shows a typical main peak at $2\theta = 9.3°$, indicating (001) planes with 0.95 nm interlayer spacing, according to Bragg's law.[62] The weak peaks at 2θ = 23.0 and 42.6° may indicate incomplete oxidation of graphite.[63,64] Concerning the particle size distribution, SiO_2 submicrospheres have a relatively monodisperse distribution of 367 ± 39 nm in diameter, as indicated by the histogram in Figure S1.

To perform the in situ GRR, the supports were impregnated with AgNPs in a first step, as shown by the TEM micrographs in Figure 3A,B. The AgNPs maintained their original spherical shape after the impregnation process, and their distribution along the sample was homogeneous, apart from some clusters over the SiO_2 microspheres, especially between the particles. The opacity of AgNPs in GO sheets may indicate either an uneven surface of GO or an overlap of graphene sheets in the preparation of TEM grid, since AgNP probably would not be

https://doi.org/10.1021/acsanm.1c02611
ACS Appl. Nano Mater. 2021, 4, 12062−12072

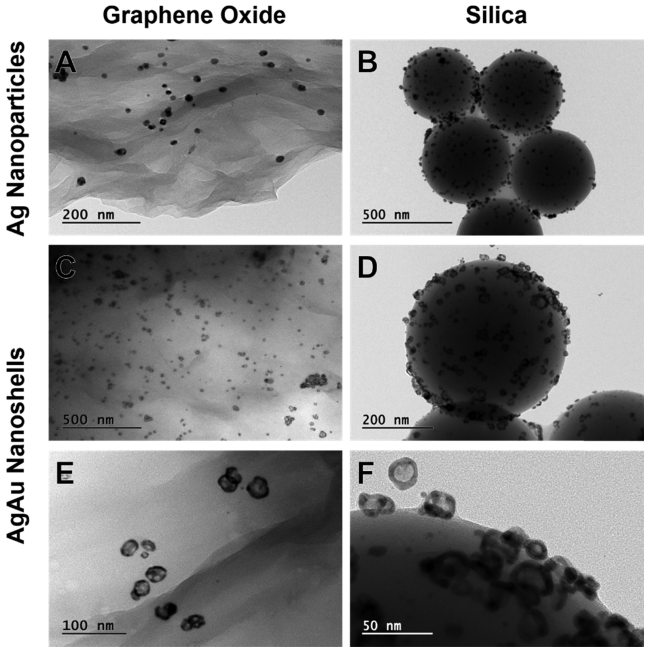


Figure 3. TEM characterization of the in situ synthesis of AgAu NS. TEM micrographs of AgNPs over GO (A) and over SiO_2 submicrospheres (B). After an in situ galvanic replacement reaction, TEM micrograph of $Ag_{79}Au_{21}$/GO, (C), also represented by the micrograph of higher magnification (E) and $Ag_{50}Au_{50}/SiO_2$ (D), with the respective micrograph of higher magnification (F) were obtained.

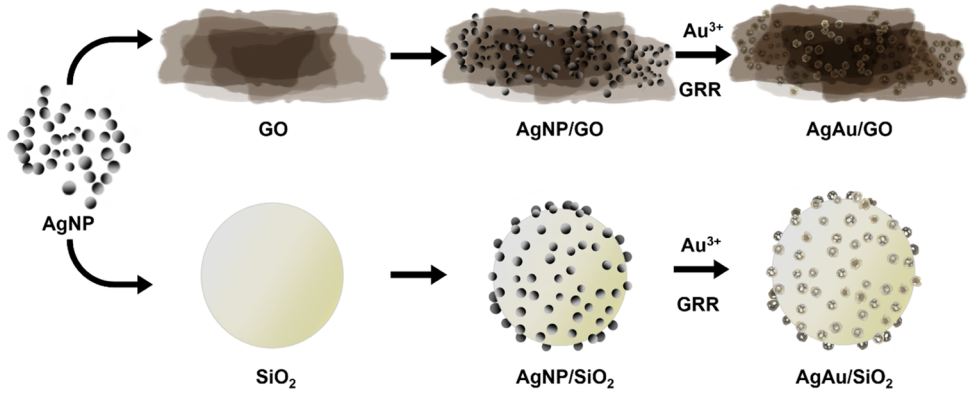
able to interpenetrate GO layers. The GRR took place in situ, that is, between Ag^0, from the supported AgNPs, and Au^{3+}, from the gold precursor added. The AgAu NS in GO and SiO_2 are shown in Figure 3C,D, respectively. Higher magnifications of the formed structures are represented in Figure 3E,F. Concerning the formation of the AgAu NS, both materials presented a similar morphology compared with the free $Ag_{50}Au_{50}$ NS (Figure 1), that is, a hollow interior of a perforated metallic nanoshell. Nonetheless, as determined by ICP-OES, the NS showed different compositions on each support, $Ag_{79}Au_{21}$/GO and $Ag_{50}Au_{50}/SiO_2$. In comparison, the shells of $Ag_{79}Au_{21}$/GO presented better monodispersion and uniformity throughout the sample, whereas some larger NS and agglomerates resided on $Ag_{50}Au_{50}/SiO_2$. Anchored on the supports, AgAu NS show a considerable improvement in the sample stability, since after a couple of days free AgAu nanoshells lost their original grayish color and a precipitated was observed in the bottom of the conical centrifuge tubes, whereas no significant difference was observed after at least 1 month in the TEM images of supported samples on GO and/or SiO_2, although mixing was required due to sedimentation. Figure S1 shows the histograms of the formed AgAu NS on each support. Although a composition discrepancy was found between the two samples, there was no evident difference in corrosion levels in the TEM images. This result indicates that although the same amount of precursor was added in the synthesis, GRR occurred in higher yields in the $Ag_{50}Au_{50}/SiO_2$ sample, possibly due to the limited access of precursor between the GO layers or the adsorption of Au^{3+} on the high surface area of GO layers. Moreover, a distinct plasmonic behavior toward the plasmon-enhanced HPRR is expected in each case, as different corrosion levels lead to distinct LSPR band shapes and positions, as demonstrated in Figure 1C. Scheme 1 summarizes the routes used for the in situ production of AgAu/GO and AgAu/SiO_2.

These materials were also analyzed by XPS (Figure S6). The Au and Ag signals in the survey measurements are much lower than the ones observed for the other elements, which is related to the low amount of these elements in the catalyst ink composition. The Ag signals related to the Ag_{3d} transition were observed at 367.7 and 373.5 eV for the GO supported material, and 366.8 and 372.2 eV for the SiO_2. The distance between these peaks is always close to 6 eV, being 5.8 and 5.4 eV for GO and SiO_2, respectively. With these relations, it is possible to assign these signals to the presence of Ag^0 in the material.[50] In both cases, the signal located at lower binding energies is always broader than that located at higher binding energies. This can indicate the presence of Ag^+, to some extent, but due to the low signal-to-noise ratio observed, a deconvolution could not be performed.[65,66]

For the Au_{4f} signals, the intensity was very low and the proximity to the Si 2p signals made the analysis more difficult. In this case, we decided to discuss just the Au $4f_{7/2}$, since the signals which should be related to Au $4f_{5/2}$ were too broad to be distinguished from the baseline in the case of the SiO_2 supported material. In both cases, GO and SiO_2 supported materials, the signal was found to be centered at 82.8 eV. This signal is lower than the 84.0 eV expected for Au^0.[50] This difference can be related to the cluster-sized material, which already lead to works reporting Au^0-related signals between 82.6 and 83.1 eV.[65,67,68]

Electrochemical Characterization. After material synthesis and characterization, we focused on their application as

Scheme 1. Schematic Representation of the Routes for In Situ GRR Leading to the Formation of AgAu/GO and AgAu/SiO_2



https://doi.org/10.1021/acsanm.1c02611
ACS Appl. Nano Mater. 2021, 4, 12062−12072

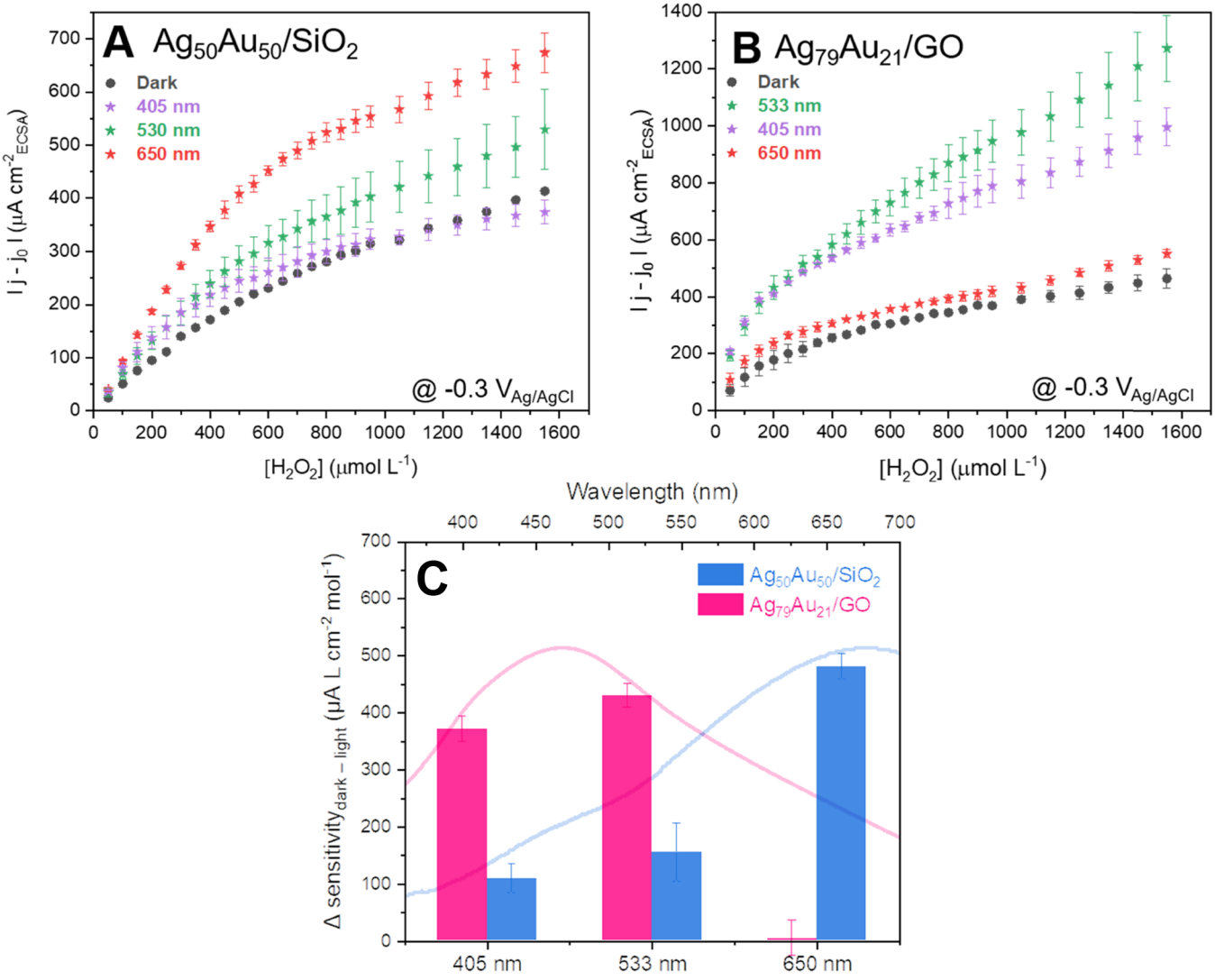


Figure 4. Calibration curve for the HPRR by $Ag_{50}Au_{50}/SiO_2$ (A) and $Ag_{79}Au_{21}$/GO (B) under irradiation by a set of lasers. UV−vis spectra of $Ag_{50}Au_{50}/SiO_2$ and $Ag_{79}Au_{21}$/GO and the difference in sensitivity bar graph with and without each laser source incidence (C). All measurements were performed at −0.3 $V_{Ag/AgCl}$ in KOH 1.0 mol L^{-1}.

nanozymes for plasmon-enhanced H_2O_2 electroreduction and sensing. We are interested in evaluating the differences in the plasmonic properties of $Ag_{50}Au_{50}/SiO_2$ and $Ag_{79}Au_{21}$/GO toward the enhancement of the HPRR under different wavelengths within the visible light spectrum. We started by performing triangular potential sweeps at 100 mV s^{-1} from 0.3 to −0.4 $V_{Ag/AgCl}$, which is the potential range for H_2O_2 reduction in alkaline media.[69,70] They were performed before and after H_2O_2 addition for the bare supports before and after AgAu NS formation (Figure S7). It is noteworthy that the bare supports only show current due to impregnation in Carbon Vulcan, as both GO and SiO_2 present insulant behavior.

Bare SiO_2 (Figure S7A) showed no oxidation and/or reduction peaks in the cyclic voltammetry. On the other hand, SiO_2 modified with AgAu NS presented an increase in current, indicating a higher conductivity due to metallic loading. After H_2O_2 addition to $Ag_{50}Au_{50}/SiO_2$, the catalyst showed an increase in current density, starting at −0.20 $V_{Ag/AgCl}$, typical from the HPRR.[71,72] Bare GO and $Ag_{79}Au_{21}$/GO showed no characteristic peaks in the cyclic voltammetry (Figure S7B). Nonetheless, the addition of the analyte $Ag_{79}Au_{21}$/GO improved the current density toward HPRR. Thus, in both cases, for SiO_2 and GO, the supports presented a low contribution toward the HPRR and required a catalytic counterpart to perform this reaction.

Although both materials showed improved activity, $Ag_{79}Au_{21}$/GO presented a more capacitive electrochemical profile and lower current density than $Ag_{50}Au_{50}/SiO_2$. To assess this subject, electrochemical impedance spectroscopy (EIS) experiments were performed with bare SiO_2 and GO (Figure S8). The charge transfer resistance (R_{ct}) was obtained from the diameter of the semicircle in the Nyquist plot.[73,74] A lower R_{ct} indicates a higher rate of electron transfer kinetics and, consequently, a higher activity.[75−77] Neither of the measured Nyquist plots presented a closed semicircle, meaning that both materials present expressive isolation properties and low faradaic activity at the applied potential.[78] However, GO signal seems to present not only a tendency to close the semicircle at higher real values (R_{ct}) but also higher $-Z''$ values, which can indicate higher capacitive behavior, if a capacitor in parallel to a resistor (double-layer capacitance and R_{ct}, respectively) is assumed as an electrochemical equivalent circuit.

https://doi.org/10.1021/acsanm.1c02611
ACS Appl. Nano Mater. 2021, 4, 12062−12072

Plasmon-enhanced sensing for H_2O_2 detection was investigated by monitoring the catalyst chronoamperometric response at −0.3 $V_{Ag/AgCl}$ with and without light incidence (Figure S9). We worked with modular lasers as a proof of concept to evaluate the LSPR outcome effects, as this is a wavelength-dependent property. Three wavelengths were chosen, according to the maximum LSPR absorption of each AgAu stoichiometric ratio as depicted in Figure 1C: 405 and 533 nm, located in the maximum LSPR absorption from a free structure close to $Ag_{79}Au_{21}$/GO composition, and 650 nm, matching the maximum intensity of the free $Ag_{50}Au_{50}$ LSPR band. The chronoamperometric response was recorded for the clean GCE, bare SiO_2 and GO, and AgAu NS-modified supports.

Before analyte addition, the current reached a steady state, and as hydrogen peroxide solution was added, the current increased proportionally. The calibration curves were derived from the linear step perturbation (Figure S9) and are shown in Figure 4. Negligible activity toward hydrogen peroxide reduction was observed for the GCE, GO, and SiO_2 electrodes, even under light irradiation, as shown in Figure S10. Nonetheless, the supports modified with AgAu NS increased the activity sharply with light, indicated by the rapid increase in current density.

Both the $Ag_{50}Au_{50}/SiO_2$ and $Ag_{79}Au_{21}$/GO electrodes showed a fast response to each H_2O_2 addition, achieving a steady-state current within 4 s after each aliquot. A fast response indicates rapid diffusion, which can be facilitated by hydrodynamic conditions.[24] The $Ag_{50}Au_{50}/SiO_2$ analytic curve showed two linear ranges (Figure 4A), the first from 0 to 600 μmol L^{-1} H_2O_2 and the second from 600 μmol L^{-1} onward. $Ag_{79}Au_{21}$/GO calibration curves (Figure 4B) also showed two linear ranges, the first from 0 to 300 μmol L^{-1} and the second from 300 μmol L^{-1} onward. $Ag_{50}Au_{50}/SiO_2$ and $Ag_{79}Au_{21}$/GO showed similar responses under dark conditions, with sensitivities of 404 and 353 μA mM^{-1} cm^{-2}, respectively. The similar sensitivity under dark conditions and the poor response of the bare supports (Figure S10) indicate that NS are primarily responsible for the observed electrocatalytic reaction, acting as nanozymes in the HPRR.

$Ag_{50}Au_{50}/SiO_2$ achieved the highest sensitivity, considering both the first and second linear ranges, under 650 nm laser incidence. The slope concerning the first range indicates a sensitivity of 885 μA mM^{-1} cm^{-2}, with a 119% increase with respect to the dark condition (Figure 4C). Both 405 and 533 nm lasers showed similar and worse responses, with increases of 27 and 38% in sensitivity relative to the condition without light, respectively. This result agrees with the NS LPSR band, as both 405 and 533 nm are on the tail of the LSPR band for the structure with equal metal ratios ($Ag_{50}Au_{50}$ NS) and present only suboptimal improved activity. On the other hand, 650 nm is located at the maximum of the LSPR extinction band, leading to an optimal response (Figure 1C). $Ag_{79}Au_{21}$/GO calibration curves showed its highest response under 533 nm laser irradiation, 787 μA mM^{-1} cm^{-2}, representing a 122% increase under light incidence, followed by a 105% increase with a 405 nm laser. As seen in the LSPR spectra of $Ag_{77}Au_{23}$ NS, the sample with the closest composition to $Ag_{79}Au_{21}$/GO, at both 405 and 533 nm, shows similar LSPR intensities, explaining the observed behavior. The 650 nm laser showed the poorest improvement with light irradiation (1.08%) for these electrodes. Sensitivities for each material and experiment are summarized in Table 1.

Table 1. Linear Fit from the First Slope of Calibration Curves and Kinetic Parameters according to Michaelis−Menten Enzyme Kinetics for the Nanozymes

catalyst	light source	linear fit	I_{max} (μA cm^{-2})	K_m^{app} (mM)
$Ag_{50}Au_{50}/SiO_2$	dark	$y = 0.404x + 6.41$, $R^2 = 0.997$	743.1	1.327
	405 nm	$y = 0.513x + 13.0$, $R^2 = 0.980$	521.7	0.599
	533 nm	$y = 0.559x + 12.0$, $R^2 = 0.993$	898.0	1.147
	650 nm	$y = 0.885x + 3.93$, $R^2 = 0.995$	1177	1.021
$Ag_{79}Au_{21}$/GO	dark	$y = 0.353x + 108$, $R^2 = 0.986$	568.7	0.506
	405 nm	$y = 0.725x + 303$, $R^2 = 0.981$	864.7	0.228
	533 nm	$y = 0.787x + 269$, $R^2 = 0.995$	1405	0.506
	650 nm	$y = 0.350x + 164$, $R^2 = 0.976$	541.4	0.324

In both cases, the enhancement in sensitivity is wavelength-dependent, with the maximum increase with light following the trends observed in the LSPR extinction spectra for NS with the corresponding composition. Thus, for $Ag_{50}Au_{50}/SiO_2$ and $Ag_{79}Au_{21}$/GO, the plasmonic effect led to an improvement toward the HPRR. The sensitivities found for our synthesized nanozymes under dark conditions are in agreement with the best materials performing the same reaction in previous studies.[79] However, with an enhancement of ∼120% under light exposure, our sensor demonstrated excellent performance in comparison to previously reported nanozymes.

The enzyme-like activity of nanozymes are usually carried out through Michaelis−Menten enzyme kinetics.[16,80] In our study, this strategy was used to determine the maximum response current (I_{max}) and the apparent Michaelis constant (K_m^{app}) of the designed nanozymes as demonstrated in Table 1. The hyperbolic response of peroxide concentration and the amperometric signals are in agreement with the Michaelis−Menten kinetics and can be described according to the hyperbolic function $y = ax/(b + x)$, where a corresponds to I_{max} and b to K_m^{app}.[81,82] I_{max} values followed the sensitivity rank, where the highest obtained sensitivities (650 nm to $Ag_{50}Au_{50}/SiO_2$ and 533/405 nm to $Ag_{79}Au_{21}$/GO) presented higher I_{max} values. K_m^{app} showed lower values for the experiments conducted with LSPR stimuli in comparison to dark conditions, indicating that LSPR could play a role in increasing the substrate affinity to the nanozymes. For both materials, K_m^{app} presented lower values for the experiments conducted with 405 nm. However, interestingly, I_{max} obtained at 405 nm for $Ag_{50}Au_{50}/SiO_2$ was 30% lower in comparison to the experiment performance with no LSPR stimulus. Following a similar bias, even though similar high sensitivities were found for 405 and 533 nm for $Ag_{79}Au_{21}$/GO, I_{max} showed a 40% lower value under 405 nm stimulus in comparison to the 533 nm. This result suggests that a laser source of higher energy may be the one to most interfere either in the reaction mechanism or stability of the system components.

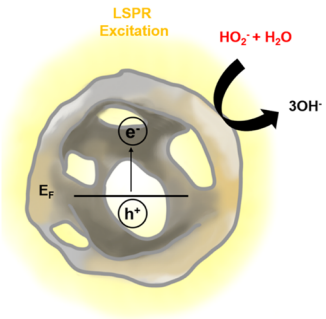
The values found for sensitivity for both $Ag_{50}Au_{50}/SiO_2$ and $Ag_{79}Au_{21}$/GO are among the range described in the literature. Zhao et al. reported a summarized table of sensitivity values from different metal-containing composites for electrochemical H_2O_2 sensing, showing a range that, in general, varies from 22.27 to 396.7 μA mM^{-1} cm^{-2}.[79] Among 13 references

https://doi.org/10.1021/acsanm.1c02611
ACS Appl. Nano Mater. 2021, 4, 12062−12072

brought in the survey, a single exception of PtNi supported on multiwalled carbon nanotubes showed a sensitivity of 2123.1 μA mM^{-1} cm^{-2}, being the only one to perform better than our best results after LSPR stimulus for both of our materials. Soto et al. developed an iron nanomaterial coated with graphene layers and supported on multiwalled carbon nanotubes, further deposited on a catalase functionalized electrode acting as a peroxidase for H_2O_2 sensing.[83] For this material, a sensitivity of 59 μA mM^{-1} cm^{-2} and a K_m^{app} value of 17.9 mM were found. Huang et al. determined a K_m^{app} of 2.81 mM for catalase in a gold NP-graphene composite.[84] Even the K_m^{app} of free catalase was determined to be 34.07 mM, demonstrating a much lower substrate affinity compared to our study with peroxidase-like nanozymes.[85] This outcome indicates that nanozymes have a vast potential to perform better than enzyme-based materials, with increased sensitivity and substrate affinity under Michaelis–Menten enzyme kinetics approach. Moreover, these parameters can be optimized after LSPR stimulus with the use of plasmonic nanoparticles.

Based on these results and the reported literature for the HPRR in alkaline media,[86−88] Scheme 2 suggests a mechanism

Scheme 2. Schematic Representation of the Hydrogen Peroxide Reduction Reaction in AgAu NS Under Light Irradiation in Alkaline Medium[a]



[a]The hot electrons generated flow to adsorbed HO_2^- ions, leading to its reduction and OH^- production.

for the plasmon-enhanced HPRR in AgAu NS supported on GO or SiO_2. As the support showed no catalytic contribution to the reaction, it was not considered in the scheme. As has been reported in the literature, the plasmon-enhanced HPRR leads to a kinetic improvement,[89−91] which has also been described for other plasmon-enhanced reactions. After hydrogen peroxide is added to the electrolyte, it is transformed into HO_2^- and dioxidanide, as its pKa (11.7) is lower than the pH of the electrolyte (pH = 13), as shown in eq 1.[86,87] Then, HO_2^- is adsorbed on the surface of the AgAu NS.[88] The dioxidanide is then reduced, leading to hydroxide ions. Under light irradiation, 533 or 650 nm for $Ag_{50}Au_{50}/SiO_2$ and $Ag_{79}Au_{21}$/GO, respectively, hot electrons and holes are generated from the LSPR of the AgAu NS and are injected into the dioxidanide, accelerating the electron transfer kinetics.[90]

The hot electrons are then transferred to dioxidanide, leading to the overall reduction of hydrogen peroxide (eq 2).

$$H_2O_2 + OH^- \rightleftharpoons HO_2^- + H_2O \quad (1)$$

$$HO_2^- + 2e^- + H_2O \rightleftharpoons 3OH^- \quad (2)$$

CONCLUSIONS

In summary, we have successfully developed an innovative synthesis in situ of AgAu bimetallic hollow nanostructures onto two different supports, GO and SiO_2. These structures presented different metallic ratios and, consequently, optical properties concerning the LSPR band shape and maximum. They were used as peroxidase-like nanozymes in the plasmon-enhanced HPRR for H_2O_2 electrochemical detection, in which their optimized performance regarding sensitivity was reached using laser matching of the wavelength at the maximum LSPR extinction of these structures. For $Ag_{79}Au_{21}$/GO, the sensitivity was improved by 122% at 533 nm and 105% at 405 nm compared to dark conditions, although almost no improvement (1.08%) was observed for the laser not matching the LSPR (650 nm). For $Ag_{50}Au_{50}/SiO_2$, the sensitivity was improved by 118% with exposure to the LSPR matching laser (650 nm) compared to dark conditions, although worse enhancements of 27% and 38% were obtained for the lasers not matching LSPR (405 and 533 nm, respectively). The materials presented high sensitivity values in comparison to previously reported nanozymes under dark conditions, which were optimized after LSPR stimulus. Under the Michaelis–Menten enzyme kinetics approach, I_{max} values for all experiments in both materials followed the same bias as sensitivity, reaching the highest values of 1177 μA cm^{-2} for $Ag_{50}Au_{50}/SiO_2$ upon 650 nm stimulus and 1405 μA cm^{-2} for $Ag_{79}Au_{21}$/GO upon 533 nm radiation. Both nanozymes presented lower K_m^{app} values in comparison to free catalase under dark conditions, indicating a high substrate affinity. These values were lowered after LSPR stimulus, especially upon 405 nm radiation, indicating better affinity than previously described enzymatic and nonenzymatic composites. The noticeable enhancement in the sensitivity, I_{max}, and K_m^{app} of sensors promoted by nanozymes suggests the efficacy of LSPR stimulus as an opportunity for the improvement of electrocatalytic reactions.

ASSOCIATED CONTENT

Supporting Information

The Supporting Information is available free of charge at https://pubs.acs.org/doi/10.1021/acsanm.1c02611.

Size distribution of AgNPs, AgAu NS, Ag in Ag/SiO_2 and Ag/GO, AgAu NS in $Ag_{50}Au_{50}/SiO_2$ and $Ag_{79}Au_{21}$/GO, and SiO_2 submicrospheres; TEM images of $Ag_{91}Au_{09}$ NS, $Ag_{77}Au_{23}$ NS, and $Ag_{50}Au_{50}$ NS; HRTEM and TEM-EDS characterization of AgAu NS; Raman spectrum of GO; XRD patterns of SiO_2 submicrospheres and GO; XPS data of $Ag_{50}Au_{50}/SiO_2$ and $Ag_{79}Au_{21}$/GO; cyclic voltammograms of SiO_2, GO, $Ag_{50}Au_{50}/SiO_2$, and $Ag_{79}Au_{21}$/GO; Nyquist plots for GO and SiO_2; chronoamperograms of $Ag_{50}Au_{50}/SiO_2$ and $Ag_{79}Au_{21}$/GO with and without light stimulus; and sensitivity bar graphs for GCE, GO, and SiO_2 (PDF)

AUTHOR INFORMATION

Corresponding Author

Susana I. Córdoba de Torresi − *Departamento de Química Fundamental, Instituto de Química, Universidade de São Paulo, São Paulo 05508-000, Brazil;* orcid.org/0000-0003-3290-172X; Email: storresi@iq.usp.br

Authors

Rafael T. P. da Silva − *Departamento de Química Fundamental, Instituto de Química, Universidade de São Paulo, São Paulo 05508-000, Brazil;* orcid.org/0000-0002-1762-793X

Maria Paula de Souza Rodrigues − *Departamento de Química Fundamental, Instituto de Química, Universidade de São Paulo, São Paulo 05508-000, Brazil;* orcid.org/0000-0002-3731-2644

Gabriela F. B. Davilla − *Departamento de Química Fundamental, Instituto de Química, Universidade de São Paulo, São Paulo 05508-000, Brazil;* orcid.org/0000-0002-7545-2875

Adriano M. R. P. da Silva − *Departamento de Química Fundamental, Instituto de Química, Universidade de São Paulo, São Paulo 05508-000, Brazil;* orcid.org/0000-0002-9955-2571

André H. B. Dourado − *Nonequilibrium Chemical Physics, Department of Physics, Technische Universität München, 85748 Garching, Germany;* orcid.org/0000-0001-8354-6444

Complete contact information is available at: https://pubs.acs.org/10.1021/acsanm.1c02611

Author Contributions

R.T.P.S. and M.P.S.R. contributed equally. R.T.P.S., M.P.S.R., and S.I.C.T. conceived the project. R.T.P.S., G.F.B.D., and A.M.R.P.S. developed the AgAu/GO and AgAu/SiO_2 in situ synthesis and performed the material characterization. R.T.P.S. and M.P.S.R. developed and performed the plasmon-enhanced electrochemical assays and wrote the manuscript. A.H.B.D. performed and analyzed XPS data. S.I.C.T. supervised the work.

Notes

The authors declare no competing financial interest.

■ ACKNOWLEDGMENTS

This work was supported by CNPq (#302173/2016-1) and the São Paulo Research Foundation FAPESP (Grant Numbers 2015/26308-7 and 2018/16219-5). R.T.P.S. was funded by a PhD fellowship from CAPES (Grant 88882.328241/2019-01). M.P.S.R. was funded by a PhD fellowship from FAPESP (Grant Number 2018/16846-0).

■ ABBREVIATIONS

APTES, 3-aminopropylethoxysilane
ECSA, electrochemically active surface area
EDS, energy-dispersive spectroscopy
EIS, electrochemical impedance spectroscopy
GCE, glassy carbon electrode
GO, layered graphene oxide
GRR, galvanic replacement reaction
HPRR, hydrogen peroxide reduction reaction
LSPR, localized surface plasmon resonance
NIR, near-infrared
NP, nanoparticle
NS, nanoshell
SEM, scanning electron microscopy
SERS, surface-enhanced Raman spectroscopy
TEM, transmission electron microscopy
TEOS, tetraethyl orthosilicate
XPS, X-ray photoelectron spectroscopy
XRD, X-ray diffraction

■ REFERENCES

(1) Chen, S.; Yuan, R.; Chai, Y.; Hu, F. Electrochemical Sensing of Hydrogen Peroxide Using Metal Nanoparticles: A Review. *Microchim. Acta* **2013**, *180*, 15−32.

(2) Lu, W.; Luo, Y.; Chang, G.; Sun, X. Synthesis of Functional SiO2-Coated Graphene Oxide Nanosheets Decorated with Ag Nanoparticles for H2O2 and Glucose Detection. *Biosens. Bioelectron.* **2011**, *26*, 4791−4797.

(3) Sun, X.; Guo, S.; Liu, Y.; Sun, S. Dumbbell-like PtPd-Fe3O4 Nanoparticles for Enhanced Electrochemical Detection of H2O2. *Nano Lett.* **2012**, *12*, 4859−4863.

(4) Putt, K. S.; Pugh, R. B. A High-Throughput Microtiter Plate Based Method for the Determination of Peracetic Acid and Hydrogen Peroxide. *PLoS One* **2013**, *8*, No. e79218.

(5) Song, M.; Wang, J.; Chen, B.; Wang, L. A Facile, Nonreactive Hydrogen Peroxide (H2O2) Detection Method Enabled by Ion Chromatography with UV Detector. *Anal. Chem.* **2017**, *89*, 11537−11544.

(6) Hagen, C. L.; Sanders, S. T. Investigation of Multi-Species (H2O2 and H2O) Sensing and Thermometry in an HCCI Engine by Wavelength-Agile Absorption Spectroscopy. *Meas. Sci. Technol.* **2007**, *18*, 1992−1998.

(7) Teodoro, K. B. R.; Migliorini, F. L.; Christinelli, W. A.; Correa, D. S. Detection of Hydrogen Peroxide (H2O2) Using a Colorimetric Sensor Based on Cellulose Nanowhiskers and Silver Nanoparticles. *Carbohydr. Polym.* **2019**, *212*, 235−241.

(8) Wu, H.; Nißler, R.; Morris, V.; Herrmann, N.; Hu, P.; Jeon, S. J.; Kruss, S.; Giraldo, J. P. Monitoring Plant Health with Near-Infrared Fluorescent H2O2 Nanosensors. *Nano Lett.* **2020**, *20*, 2432−2442.

(9) Han, Y.; Zheng, J.; Dong, S. A Novel Nonenzymatic Hydrogen Peroxide Sensor Based on Ag-MnO2-MWCNTs Nanocomposites. *Electrochim. Acta* **2013**, *90*, 35−43.

(10) Chakraborty, S.; Retna Raj, C. Pt Nanoparticle-Based Highly Sensitive Platform for the Enzyme-Free Amperometric Sensing of H2O2. *Biosens. Bioelectron.* **2009**, *24*, 3264−3268.

(11) Thatikayala, D.; Ponnamma, D.; Sadasivuni, K. K.; Cabibihan, J.-J.; Al-Ali, A. K.; Malik, R. A.; Min, B. Progress of Advanced Nanomaterials in the Non-Enzymatic Electrochemical Sensing of Glucose and H2O2. *Biosensors* **2020**, *10*, No. 151.

(12) Chen, W.; Cai, S.; Ren, Q.-Q.; Wen, W.; Zhao, Y.-D. Recent Advances in Electrochemical Sensing for Hydrogen Peroxide: A Review. *Analyst* **2012**, *137*, 49−58.

(13) Dhara, K.; Mahapatra, D. R. Recent Advances in Electrochemical Nonenzymatic Hydrogen Peroxide Sensors Based on Nanomaterials: A Review. *J. Mater. Sci.* **2019**, *54*, 12319−12357.

(14) Pundir, C. S.; Deswal, R.; Narwal, V. Quantitative Analysis of Hydrogen Peroxide with Special Emphasis on Biosensors. *Bioprocess Biosyst. Eng.* **2018**, *41*, 313−329.

(15) Xu, F.; Sun, Y.; Zhang, Y.; Shi, Y.; Wen, Z.; Li, Z. Graphene-Pt Nanocomposite for Nonenzymatic Detection of Hydrogen Peroxide with Enhanced Sensitivity. *Electrochem. Commun.* **2011**, *13*, 1131−1134.

(16) Liang, M.; Yan, X. Nanozymes: From New Concepts, Mechanisms, and Standards to Applications. *Acc. Chem. Res.* **2019**, *52*, 2190−2200.

(17) Wang, H.; Gu, X.-K.; Zheng, X.; Pan, H.; Zhu, J.; Chen, S.; Cao, L.; Li, W.-X.; Lu, J. Disentangling the Size-Dependent Geometric and Electronic Effects of Palladium Nanocatalysts beyond Selectivity. *Sci. Adv.* **2019**, *5*, No. eaat6413.

(18) Roduner, E. Size Matters: Why Nanomaterials Are Different. *Chem. Soc. Rev.* **2006**, *35*, 583−592.

(19) Baffou, G.; Quidant, R. Nanoplasmonics for Chemistry. *Chem. Soc. Rev.* **2014**, *43*, 3898.

(20) Araujo, T. P.; Quiroz, J.; Barbosa, E. C. M.; Camargo, P. H. C. Understanding Plasmonic Catalysis with Controlled Nanomaterials Based on Catalytic and Plasmonic Metals. *Curr. Opin. Colloid Interface Sci.* **2019**, *39*, 110−122.

(21) Huang, X.; Jain, P. K.; El-Sayed, I. H.; El-Sayed, M. A. Plasmonic Photothermal Therapy (PPTT) Using Gold Nanoparticles. *Lasers Med. Sci.* **2008**, *23*, 217−228.
(22) Jeon, T. Y.; Kim, D. H. J.; Park, S. G.; Kim, S. H.; Kim, D. H. J. Nanostructured Plasmonic Substrates for Use as SERS Sensors. *Nano Convergence* **2016**, *3*, No. 18.
(23) Ma, J.; Liu, X.; Wang, R.; Zhang, J.; Jiang, P.; Wang, Y.; Tu, G. Bimetallic Core-Shell Nanostars with Tunable Surface Plasmon Resonance for Surface-Enhanced Raman Scattering. *ACS Appl. Nano Mater.* **2020**, *3*, 10885−10894.
(24) Maji, S. K. Plasmon-Enhanced Electrochemical Biosensing of Hydrogen Peroxide from Cancer Cells by Gold Nanorods. *ACS Appl. Nano Mater.* **2019**, *2*, 7162−7169.
(25) Liu, W.; Wu, X.; Li, X. Gold Nanorods on Three-Dimensional Nickel Foam: A Non-Enzymatic Glucose Sensor with Enhanced Electro-Catalytic Performance. *RSC Adv.* **2017**, *7*, 36744−36749.
(26) Kabashin, A. V.; Evans, P.; Pastkovsky, S.; Hendren, W.; Wurtz, G. A.; Atkinson, R.; Pollard, R.; Podolskiy, V. A.; Zayats, A. V. Plasmonic Nanorod Metamaterials for Biosensing. *Nat. Mater.* **2009**, *8*, 867−871.
(27) Rycenga, M.; Cobley, C. M.; Zeng, J.; Li, W.; Moran, C. H.; Zhang, Q.; Qin, D.; Xia, Y. Controlling the Synthesis and Assembly of Silver Nanostructures for Plasmonic Applications. *Chem. Rev.* **2011**, *111*, 3669−3712.
(28) Achermann, M. Exciton-Plasmon Interactions in Metal-Semiconductor Nanostructures. *J. Phys. Chem. Lett.* **2010**, *1*, 2837−2843.
(29) Kisukuri, C. M.; Palmeira, D. J.; Rodrigues, T. S.; Camargo, P. H. C.; Andrade, L. H. Bimetallic Nanoshells as Platforms for Metallo- and Biometallo-Catalytic Applications. *ChemCatChem* **2016**, *8*, 171−179.
(30) Wang, J. L.; Ando, R. A.; Camargo, P. H. C. Investigating the Plasmon-Mediated Catalytic Activity of Agau Nanoparticles as a Function of Composition: Are Two Metals Better than One? *ACS Catal.* **2014**, *4*, 3815−3819.
(31) da Silva, A. G. M.; Rodrigues, T. S.; Correia, V. G.; Alves, T. V.; Alves, R. S.; Ando, R. A.; Ornellas, F. R.; Wang, J.; Andrade, L. H.; Camargo, P. H. C. Plasmonic Nanorattles as Next-Generation Catalysts for Surface Plasmon Resonance-Mediated Oxidations Promoted by Activated Oxygen. *Angew. Chem., Int. Ed.* **2016**, *55*, 7111−7115.
(32) Rodrigues, T. S.; da Silva, A. G. M.; de Moura, A. B. L.; Freitas, I. G.; Camargo, P. H. C. C. Rational Design of Plasmonic Catalysts: Matching the Surface Plasmon Resonance with Lamp Emission Spectra for Improved Performance in AgAu Nanorings. *RSC Adv.* **2016**, *6*, 62286−62290.
(33) Wang, N.; Cao, P.; Sun, S.; Ma, H.; Ma, H. Hollow Multiple Noble Metallic Nanoalloys by Mercury-Assisted Galvanic Replacement Reaction for Hydrogen Evolution. *Inorg. Chem.* **2021**, *60*, 3471−3478.
(34) Wang, H.; Zhao, W.; Zhao, Y.; Xu, C. H.; Xu, J. J.; Chen, H. Y. Real-Time Tracking the Electrochemical Synthesis of Au@Metal Core-Shell Nanoparticles toward Photo Enhanced Methanol Oxidation. *Anal. Chem.* **2020**, *92*, 14006−14011.
(35) Kisukuri, C. M.; Macedo, A.; Oliveira, C. C. S.; Camargo, P. H. C.; Andrade, L. H.; Prof, A.; Prestes, L.; Sa, S. P. Investigating the Influence of the Interface in Thiol-Functionalized Silver − Gold Nanoshells over Lipase Activity. *Langmuir* **2013**, *29*, 15974−15980.
(36) Genç, A.; Patarroyo, J.; Sancho-Parramon, J.; Bastús, N. G.; Puntes, V.; Arbiol, J. Hollow Metal Nanostructures for Enhanced Plasmonics: Synthesis, Local Plasmonic Properties and Applications. *Nanophotonics* **2017**, *6*, 193−213.
(37) Russo, L.; Merkoçi, F.; Patarroyo, J.; Piella, J.; Merkoçi, A.; Bastús, N. G.; Puntes, V. Time- and Size-Resolved Plasmonic Evolution with Nm Resolution of Galvanic Replacement Reaction in AuAg Nanoshells Synthesis. *Chem. Mater.* **2018**, *30*, 5098−5107.
(38) Vongsavat, V.; Vittur, B. M.; Bryan, W. W.; Kim, J. H.; Lee, T. R. Ultrasmall Hollow Gold-Silver Nanoshells with Extinctions Strongly Red-Shifted to the near-Infrared. *ACS Appl. Mater. Interfaces* **2011**, *3*, 3616−3624.
(39) Yan, X.; Yu, S.; Tang, Y.; Sun, D.; Xu, L.; Xue, C. Triangular AgAu@Pt Core−Shell Nanoframes with a Dendritic Pt Shell and Enhanced Electrocatalytic Performance toward the Methanol Oxidation Reaction. *Nanoscale* **2018**, *10*, 2231−2235.
(40) Saw, E. N.; Grasmik, V.; Rurainsky, C.; Epple, M.; Tschulik, K. Electrochemistry at Single Bimetallic Nanoparticles - Using Nano Impacts for Sizing and Compositional Analysis of Individual AgAu Alloy Nanoparticles. *Faraday Discuss.* **2016**, *193*, 327−338.
(41) Balasubramanian, P.; He, S.-B.; Jansirani, A.; Peng, H.-P.; Huang, L.-L.; Deng, H.-H.; Chen, W. Bimetallic AgAu Decorated MWCNTs Enable Robust Nonenzyme Electrochemical Sensors for In-Situ Quantification of Dopamine and H2O2 Biomarkers Expelled from PC-12 Cells. *J. Electroanal. Chem.* **2020**, *878*, No. 114554.
(42) Nazir, R.; Fageria, P.; Basu, M.; Pande, S. Decoration of Carbon Nitride Surface with Bimetallic Nanoparticles (Ag/Pt, Ag/Pd, and Ag/Au) via Galvanic Exchange for Hydrogen Evolution Reaction. *J. Phys. Chem. C* **2017**, *121*, 19548−19558.
(43) Hemmingson, S. L.; Campbell, C. T. Trends in Adhesion Energies of Metal Nanoparticles on Oxide Surfaces: Understanding Support Effects in Catalysis and Nanotechnology. *ACS Nano* **2017**, *11*, 1196−1203.
(44) Baek, S. H.; Roh, J.; Park, C. Y.; Kim, M. W.; Shi, R.; Kailasa, S. K.; Park, T. J. Cu-Nanoflower Decorated Gold Nanoparticles-Graphene Oxide Nanofiber as Electrochemical Biosensor for Glucose Detection. *Mater. Sci. Eng. C* **2020**, *107*, No. 110273.
(45) Shetti, N. P.; Malode, S. J.; Nayak, D. S.; Bagihalli, G. B.; Reddy, K. R.; Ravindranadh, K.; Reddy, C. V. A Novel Biosensor Based on Graphene Oxide-Nanoclay Hybrid Electrode for the Detection of Theophylline for Healthcare Applications. *Microchem. J.* **2019**, *149*, No. 103985.
(46) Dinesh, B.; Mani, V.; Saraswathi, R.; Chen, S. M. Direct Electrochemistry of Cytochrome c Immobilized on a Graphene Oxide-Carbon Nanotube Composite for Picomolar Detection of Hydrogen Peroxide. *RSC Adv.* **2014**, *4*, 28229−28237.
(47) Rossi, L. M.; Shi, L.; Quina, F. H.; Rosenzweig, Z. Stöber Synthesis of Monodispersed Luminescent Silica Nanoparticles for Bioanalytical Assays. *Langmuir* **2005**, *21*, 4277−4280.
(48) Liberman, A.; Mendez, N.; Trogler, W. C.; Kummel, A. C. Synthesis and Surface Functionalization of Silica Nanoparticles for Nanomedicine. *Surf. Sci. Rep.* **2014**, *69*, 132−158.
(49) Jeelani, P. G.; Mulay, P.; Venkat, R.; Ramalingam, C. Multifaceted Application of Silica Nanoparticles. A Review. *Silicon* **2020**, *12*, 1337−1354.
(50) Chastian, J. *Handbook of X-Ray Photoelectron Spectroscopy*; In Muilenberg, G. E., Ed.; Perkin Elmer Corporation: Eden Prairie, 1992.
(51) Yumitori, S. Correlation of C1s Chemical State Intensities with the O1s Intensity in the XPS Analysis of Anodically Oxidized Glass-like Carbon Samples. *J. Mater. Sci.* **2000**, *35*, 139−146.
(52) Papa, L.; de Freitas, I. C.; Geonmonond, R. S.; de Aquino, C. B.; Pieretti, J. C.; Domingues, S. H.; Ando, R. A.; Camargo, P. H. C. C. Supports Matter: Unraveling the Role of Charge Transfer in the Plasmonic Catalytic Activity of Silver Nanoparticles. *J. Mater. Chem. A* **2017**, *5*, 11720−11729.
(53) Marcano, D. C.; Kosynkin, D. V.; Berlin, J. M.; Sinitskii, A.; Sun, Z.; Slesarev, A.; Alemany, L. B.; Lu, W.; Tour, J. M. Improved Synthesis of Graphene Oxide. *ACS Nano* **2010**, *4*, 4806−4814.
(54) Jacinto, M. J.; Kiyohara, P. K.; Masunaga, S. H.; Jardim, R. F.; Rossi, L. M. Recoverable Rhodium Nanoparticles: Synthesis, Characterization and Catalytic Performance in Hydrogenation Reactions. *Appl. Catal., A* **2008**, *338*, 52−57.
(55) Xia, X.; Wang, Y.; Ruditskiy, A.; Xia, Y. 25th Anniversary Article: Galvanic Replacement: A Simple and Versatile Route to Hollow Nanostructures with Tunable and Well-Controlled Properties. *Adv. Mater.* **2013**, *25*, 6313−6333.
(56) Wang, Y.; Wan, D.; Xie, S.; Xia, X.; Huang, C. Z.; Xia, Y. Synthesis of Silver Octahedra with Controlled Sizes and Optical

https://doi.org/10.1021/acsanm.1c02611
ACS Appl. Nano Mater. 2021, 4, 12062−12072

Properties via Seed-Mediated Growth. *ACS Nano* **2013**, *7*, 4586−4594.
(57) Gilroy, K. D.; Ruditskiy, A.; Peng, H. C.; Qin, D.; Xia, Y. Bimetallic Nanocrystals: Syntheses, Properties, and Applications. *Chem. Rev.* **2016**, *116*, 10414−10472.
(58) Pansare, V. J.; Hejazi, S.; Faenza, W. J.; Prud'homme, R. K. Review of Long-Wavelength Optical and NIR Imaging Materials: Contrast Agents, Fluorophores, and Multifunctional Nano Carriers. *Chem. Mater.* **2012**, *24*, 812−827.
(59) Gao, L.; Liu, R.; Gao, F.; Wang, Y.; Jiang, X.; Gao, X. Plasmon-Mediated Generation of Reactive Oxygen Species from near-Infrared Light Excited Gold Nanocages for Photodynamic Therapy in Vitro. *ACS Nano* **2014**, *8*, 7260−7271.
(60) Enrichi, F.; Quandt, A.; Righini, G. C. Plasmonic Enhanced Solar Cells: Summary of Possible Strategies and Recent Results. *Renewable Sustainable Energy Rev.* **2018**, *82*, 2433−2439.
(61) Rao, X.; Tatoulian, M.; Guyon, C.; Ognier, S.; Chu, C.; Hassan, A. A. A Comparison Study of Functional Groups (Amine vs. Thiol) for Immobilizing AuNPs on Zeolite Surface. *Nanomaterials* **2019**, *9*, No. 1034.
(62) Sarkar, S. K.; Raul, K. K.; Pradhan, S. S.; Basu, S.; Nayak, A. Magnetic Properties of Graphite Oxide and Reduced Graphene Oxide. *Physica E* **2014**, *64*, 78−82.
(63) Siburian, R.; Sihotang, H.; Lumban Raja, S.; Supeno, M.; Simanjuntak, C. New Route to Synthesize of Graphene Nano Sheets. *Orient. J. Chem.* **2018**, *34*, 182−187.
(64) Johra, F. T.; Lee, J. W.; Jung, W. G. Facile and Safe Graphene Preparation on Solution Based Platform. *J. Ind. Eng. Chem.* **2014**, *20*, 2883−2887.
(65) Zhidkov, I. S.; Kurmaev, E. Z.; Condorelli, M.; Cholakh, S. O.; Boyarchenkov, A. S.; Fazio, E.; D'urso, L. X-Ray Photoelectron Spectra of Ag-Au Colloidal Nanoparticles after Interaction with Linear Carbon Chains. *Appl. Sci.* **2021**, *11*, No. 685.
(66) Jeon, T. H.; Monllor−Satoca, D.; Moon, G. −H.; Kim, W.; Kim, H. −I.; Bahnemann, D. W.; Park, H.; Choi, W. Ag(I) Ions Working as a Hole-Transfer Mediator in Photoelectrocatalytic Water Oxidation on WO3 Film. *Nat. Commun.* **2020**, *11*, No. 967.
(67) Sankar, M.; He, Q.; Morad, M.; Pritchard, J.; Freakley, S. J.; Edwards, J. K.; Taylor, S. H.; Morgan, D. J.; Carley, A. F.; Knight, D. W.; Kiely, C. J.; Hutchings, G. J. Synthesis of Stable Ligand-Free Gold-Palladium Nanoparticles Using a Simple Excess Anion Method. *ACS Nano* **2012**, *6*, 6600−6613.
(68) Radnik, J.; Mohr, C.; Claus, P. On the Origin of Binding Energy Shifts of Core Levels of Supported Gold Nanoparticles and Dependence of Pretreatment and Material Synthesis. *Phys. Chem. Chem. Phys.* **2003**, *5*, 172−177.
(69) Ding, R.; Qi, L.; Jia, M.; Wang, H. Simple Hydrothermal Synthesis of Mesoporous Spinel NiCo2O4 Nanoparticles and Their Catalytic Behavior in CH3OH Electro-Oxidation and H2O2 Electro-Reduction. *Catal. Sci. Technol.* **2013**, *3*, 3207−3215.
(70) Li, Y.; Cao, D.; Liu, Y.; Liu, R.; Yang, F.; Yin, J.; Wang, G. CuO Nanosheets Grown on Cupper Foil as the Catalyst for H 2O 2 Electroreduction in Alkaline Medium. *Int. J. Hydrogen Energy* **2012**, *37*, 13611−13615.
(71) Ensafi, A. A.; Zandi-Atashbar, N.; Rezaei, B.; Ghiaci, M.; Taghizadeh, M. Silver Nanoparticles Decorated Carboxylate Functionalized SiO2, New Nanocomposites for Non-Enzymatic Detection of Glucose and Hydrogen Peroxide. *Electrochim. Acta* **2016**, *214*, 208−216.
(72) Yin, J.; Qi, X.; Yang, L.; Hao, G.; Li, J.; Zhong, J. A Hydrogen Peroxide Electrochemical Sensor Based on Silver Nanoparticles Decorated Silicon Nanowire Arrays. *Electrochim. Acta* **2011**, *56*, 3884−3889.
(73) Chang, B. Y.; Park, S. M. Electrochemical Impedance Spectroscopy. *Annu. Rev. Anal. Chem.* **2010**, *3*, 207−229.
(74) Lasia, A. Electrochemical Impedance Spectroscopy and Its Applications. In *Modern Aspects of Electrochemistry*; Springer: Boston, MA, 2002; Vol. 32, pp 143−248.
(75) Wu, Z. L.; Li, C. K.; Yu, J. G.; Chen, X. Q. MnO2/Reduced Graphene Oxide Nanoribbons: Facile Hydrothermal Preparation and Their Application in Amperometric Detection of Hydrogen Peroxide. *Sens. Actuators, B* **2017**, *239*, 544−552.
(76) Pan, Y.; Hou, Z.; Yi, W.; Zhu, W.; Zeng, F.; Liu, Y. N. Hierarchical Hybrid Film of MnO2 Nanoparticles/Multi-Walled Fullerene Nanotubes-Graphene for Highly Selective Sensing of Hydrogen Peroxide. *Talanta* **2015**, *141*, 86−91.
(77) Munawar, K.; Mansoor, M. A.; Olmstead, M. M.; Zaharinie, T.; Mohd Zubir, M. N.; Haniffa, M.; Basirun, W. J.; Mazhar, M. Fabrication of Ag-ZnO Composite Thin Films for Plasmonic Enhanced Water Splitting. *Mater. Chem. Phys.* **2020**, *255*, No. 123220.
(78) Yang, C.; Cattelan, M.; Fox, N.; Huang, Y.; Golden, M. S.; Schwarzacher, W. Electrochemical Modification and Characterization of Topological Insulator Single Crystals. *Langmuir* **2019**, *35*, 2983−2988.
(79) Zhao, W.; Jin, J.; Wu, H.; Wang, S.; Fneg, C.; Yang, S.; Ding, Y. Electrochemical Hydrogen Peroxide Sensor Based on Carbon Supported Cu@Pt Core-Shell Nanoparticles. *Mater. Sci. Eng. C* **2017**, *78*, 185−190.
(80) Jiang, B.; Duan, D.; Gao, L.; Zhou, M.; Fan, K.; Tang, Y.; Xi, J.; Bi, Y.; Tong, Z.; Gao, G. F.; Xie, N.; Tang, A.; Nie, G.; Liang, M.; Yan, X. Standardized Assays for Determining the Catalytic Activity and Kinetics of Peroxidase-like Nanozymes. *Nat. Protoc.* **2018**, *13*, 1506−1520.
(81) Anusha, J. R.; Raj, C. J.; Cho, B. B.; Fleming, A. T.; Yu, K. H.; Kim, B. C. Amperometric Glucose Biosensor Based on Glucose Oxidase Immobilized over Chitosan Nanoparticles from Gladius of Uroteuthis Duvauceli. *Sens. Actuators, B* **2015**, *215*, 536−543.
(82) Ramanavičius, A.; Kaušaite, A.; Ramanavičiene, A. Polypyrrole-Coated Glucose Oxidase Nanoparticles for Biosensor Design. *Sens. Actuators, B* **2005**, *111*−*112*, 532−539.
(83) Soto, D.; Alzate, M.; Gallego, J.; Orozco, J. Hybrid Nanomaterial/Catalase-Modified Electrode for Hydrogen Peroxide Sensing. *J. Electroanal. Chem.* **2021**, *880*, No. 114826.
(84) Huang, K. J.; Niu, D. J.; Liu, X.; Wu, Z. W.; Fan, Y.; Chang, Y. F.; Wu, Y. Y. Direct Electrochemistry of Catalase at Amine-Functionalized Graphene/Gold Nanoparticles Composite Film for Hydrogen Peroxide Sensor. *Electrochim. Acta* **2011**, *56*, 2947−2953.
(85) Prakash, P. A.; Yogeswaran, U.; Chen, S. M. A Review on Direct Electrochemistry of Catalase for Electrochemical Sensors. *Sensors* **2009**, *9*, 1821−1844.
(86) Poux, T.; Bonnefont, A.; Ryabova, A.; Kéranguéven, G.; Tsirlina, G. A.; Savinova, E. R. Electrocatalysis of Hydrogen Peroxide Reactions on Perovskite Oxides: Experiment versus Kinetic Modeling. *Phys. Chem. Chem. Phys.* **2014**, *16*, 13595−13600.
(87) Cai, X.; Tanner, E. E. L.; Lin, C.; Ngamchuea, K.; Foord, J. S.; Compton, R. G. The Mechanism of Electrochemical Reduction of Hydrogen Peroxide on Silver Nanoparticles. *Phys. Chem. Chem. Phys.* **2018**, *20*, 1608−1614.
(88) Strbac, S. The Effect of PH on Oxygen and Hydrogen Peroxide Reduction on Polycrystalline Pt Electrode. *Electrochim. Acta* **2011**, *56*, 1597−1604.
(89) Zhao, X.; Deng, Z.; Zhao, W.; Feng, B.; Wang, M.; Huang, M.; Liu, L.; Zou, G.; Shao, Y.; Zhu, H. Nanoporous Silver Using Pulsed Laser Deposition for High-Performance Oxygen Reduction Reaction and Hydrogen Peroxide Sensing. *Nanoscale* **2020**, *12*, 19413−19419.
(90) Maduraiveeran, G.; et al. Electrochemical Detection of Hydrogen Peroxide Based on Silver Nanoparticles via Amplified Electron Transfer Process. *J. Mater. Sci.* **2018**, *53*, 8328−8338.
(91) Silva, C. G.; Juárez, R.; et al. Influence of Excitation Wavelength (UV or Visible Light) on the Photocatalytic Activity of Titania Containing Gold Nanoparticles for the Generation of Hydrogen or Oxygen. *J. Am. Chem. Soc.* **2011**, *22*, 595−602.

https://doi.org/10.1021/acsanm.1c02611
ACS Appl. Nano Mater. 2021, 4, 12062−12072

Supporting Information

AgAu Hollow Nanoshells on Layered Graphene Oxide and Silica Submicrospheres as Plasmonic Nanozymes for Light-Enhanced Electrochemical H_2O_2 Sensing

Rafael T. P. da Silva ‡[a], *Maria Paula de S. Rodrigues*‡[a], *Gabriela F. B. Davilla*[a], *Adriano M. R. P. da Silva*[a], *André H. B. Dourado*[b], *Susana I. Córdoba de Torresi**[a]

[a] Departamento de Química Fundamental, Instituto de Química, Universidade de São Paulo, São Paulo (SP), 05508-000, Brazil.

[b] Nonequilibrium Chemical Physics, Department of Physics Technische Universität München, James-Franck-Strasse 1, 85748, Garching, Germany

*Corresponding Author

Email: storresi@iq.usp.br

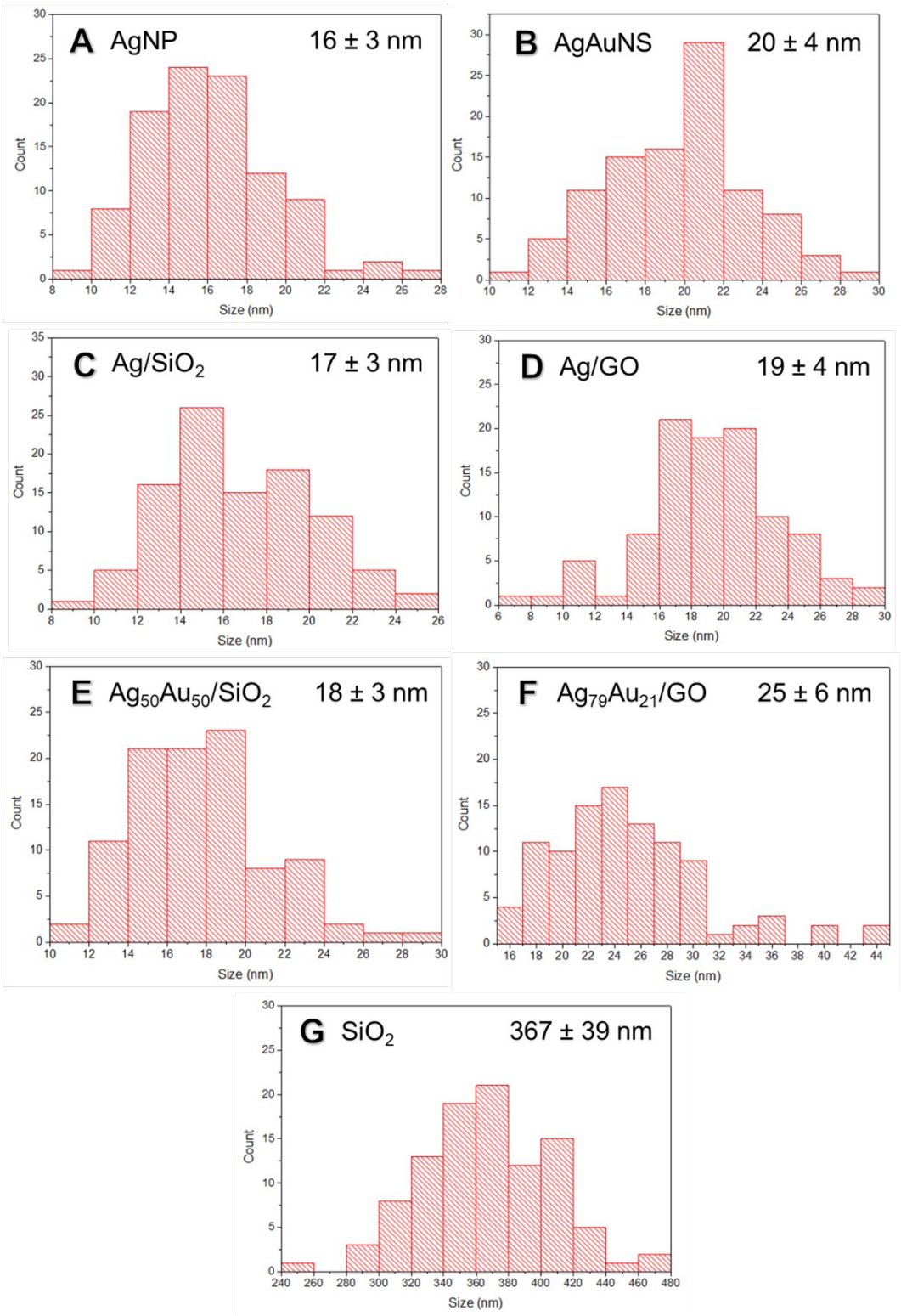


Figure S1. Size distribution histograms for AgNPs (A), AgAu NSs (B), Ag in Ag/SiO_2 (C), Ag in Ag/GO (D), AgAu NSs in $Ag_{50}Au_{50}/SiO_2$ (E), AgAu NSs in $Ag_{79}Au_{21}$/GO and (F) SiO_2 submicrospheres (G).

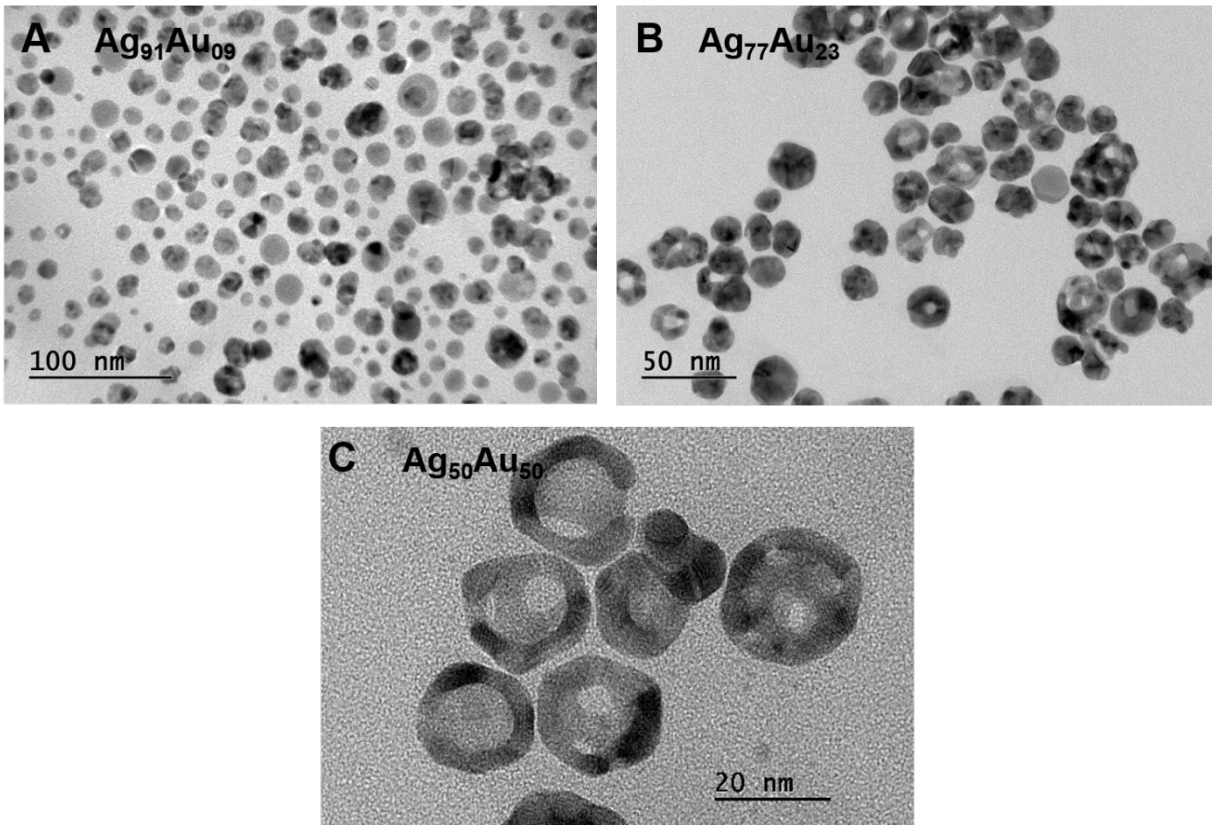


Figure S2. TEM of different corrosion degrees of GRR between Ag^0 and Au^{3+} in AgAu NS samples. $Ag_{91}Au_{09}$ NS (A), $Ag_{77}Au_{23}$ NSs (B), $Ag_{50}Au_{50}$ NS (C).

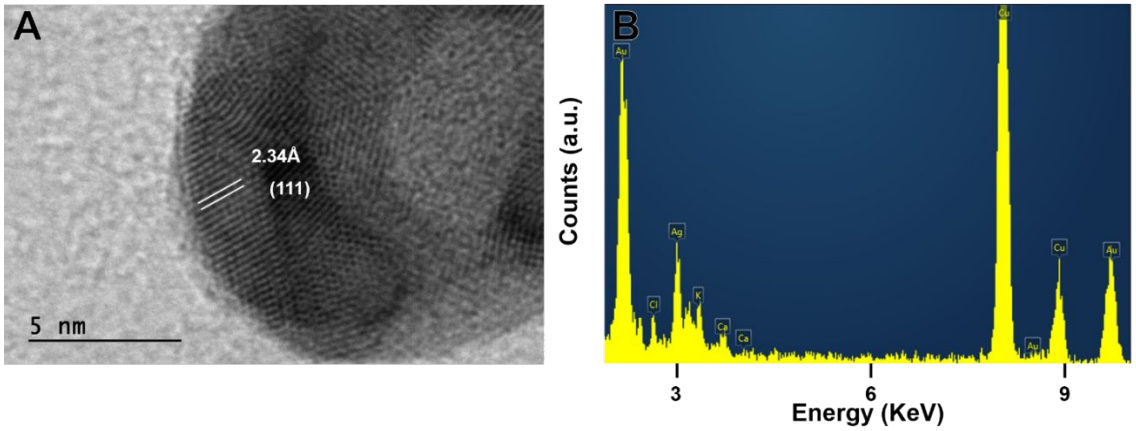


Figure S3. HRTEM characterization of AgAu NS. Plane of 2.34 Å (111) lattice spacing after averaging 15 fringes (A). TEM-EDS of the same particle, indicating the simultaneous presence of Ag and Au (B).

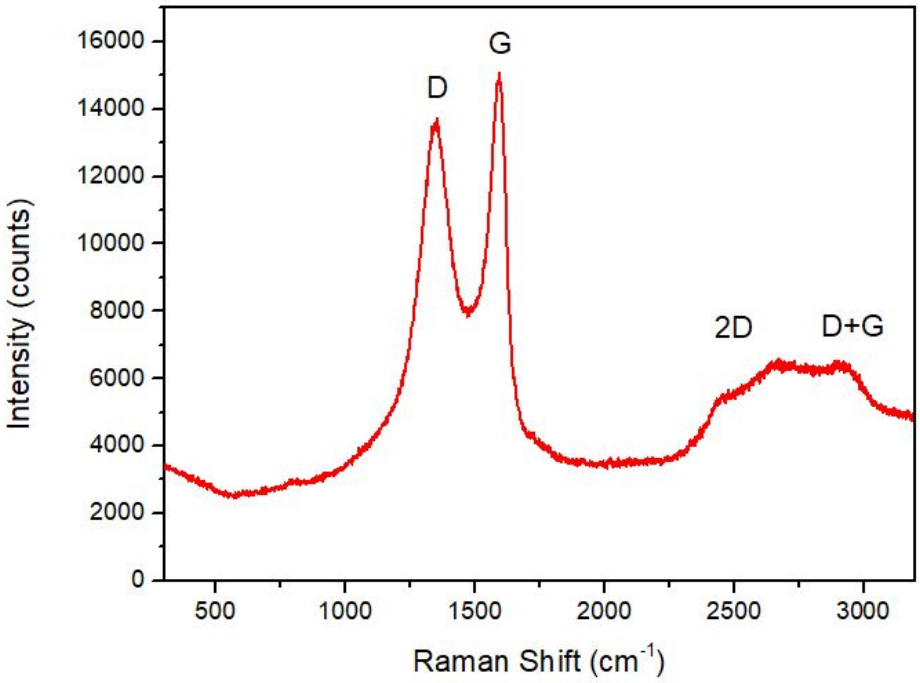


Figure S4. Raman spectra of GO, indicating the corresponding Raman modes in the vibrational bands.

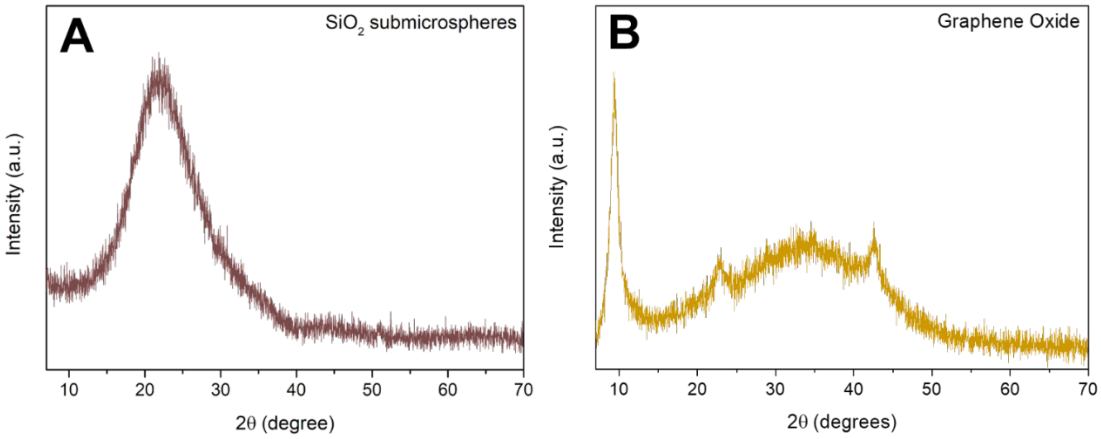


Figure S5. XRD patterns of supports. SiO_2 submicrospheres (A) and GO (B).

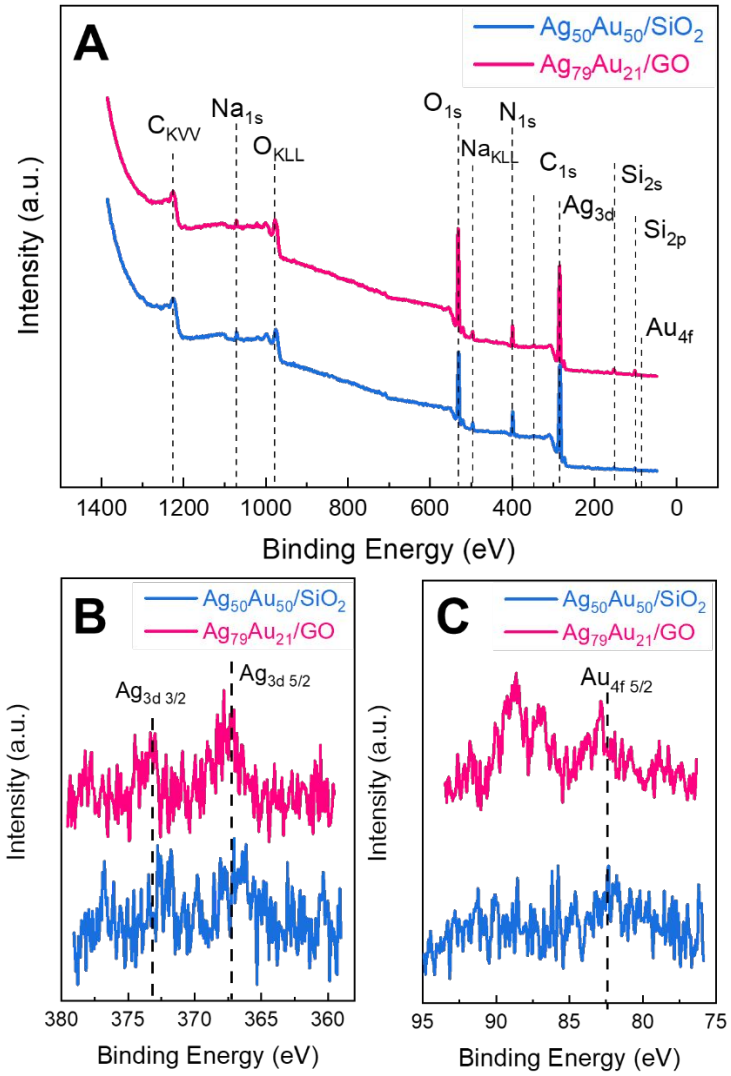


Figure S6. XPS of $Ag_{50}Au_{50}/SiO_2$ and $Ag_{79}Au_{21}$/GO. SiO_2 submicrospheres. Survey XPS data (A). The peaks observed were related to C at 1225.9 and 284.8 eV (KVV and 1s transitions[1], in order, being the former the signal used to correct the whole measurements), Na at 1071.2 and 497.1 eV (1s and KLL transitions[1]), being this element probably due to the presence of Na^+ in some of the chemicals used during the synthesis. O was observed at 978.0 and 531.3 eV (KLL and 1s[1]), N_{1s} was observed at 399.5 eV in both materials, suggesting that the same chemical species is the responsible for this signal. In this case, it was interpreted that PVP is the mains reason for this signal.[2] Si was observed at 151.7 and 100.1 eV (2s and 2p, in order[1]). Since the substrate used for the material deposition was already made of Si, this signal was not considered for deeper analysis. Ag_{3d} and Au_{4f}, the main transitions for the respective elements, were expected to be at 368.3 and 84.0 eV, in order. However, the amount of these materials in the ink is so low that they were not possible to be observed in the survey spectra. HR-XPS for Ag_{3d} (B) and Au_{4f} (C) regions. Due to the low signal/noise ratio, the deconvolutions of these peaks were not possible. The discussion of these data can be found in the main text.

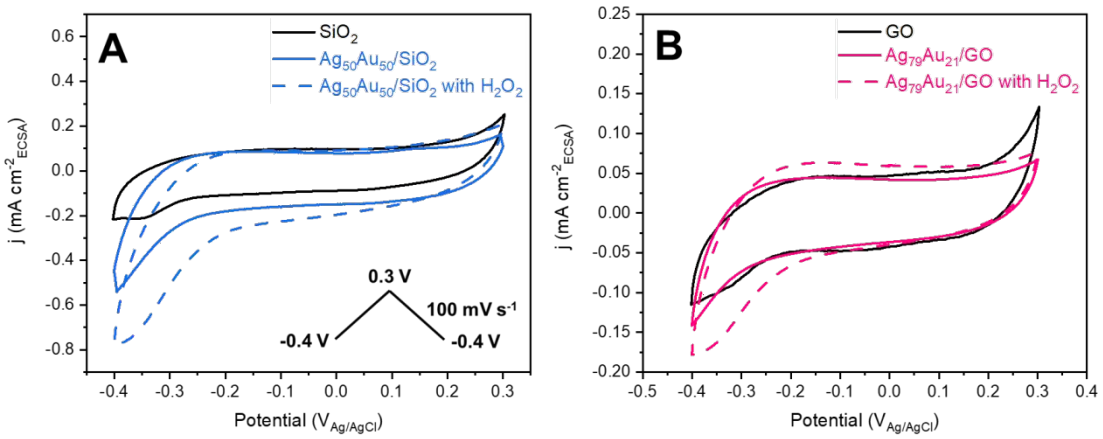


Figure S7. Cyclic voltammograms from -0.4 to 0.3 $V_{Ag/AgCl}$ at 100 mV s^{-1} in 1.0 mol L^{-1} KOH of SiO_2 and $Ag_{50}Au_{50}/SiO_2$ (A) and GO and $Ag_{79}Au_{21}$/GO (B) before and after H_2O_2 addition (1.6 mmol L^{-1}). The perturbation program is in the inset.

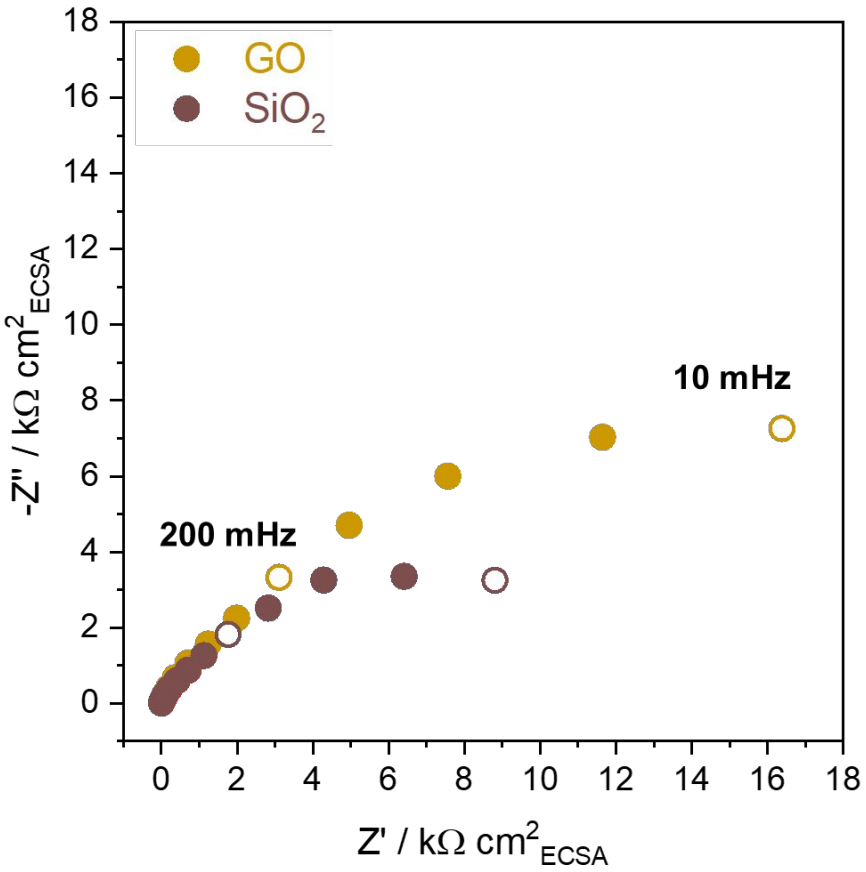


Figure S8. Nyquist plot (frequencies indicated with hollow circles) at -0.3 $V_{Ag/AgCl}$ for bare GO and SiO_2 in N_2-saturated KOH 1.0 mol L^{-1}.

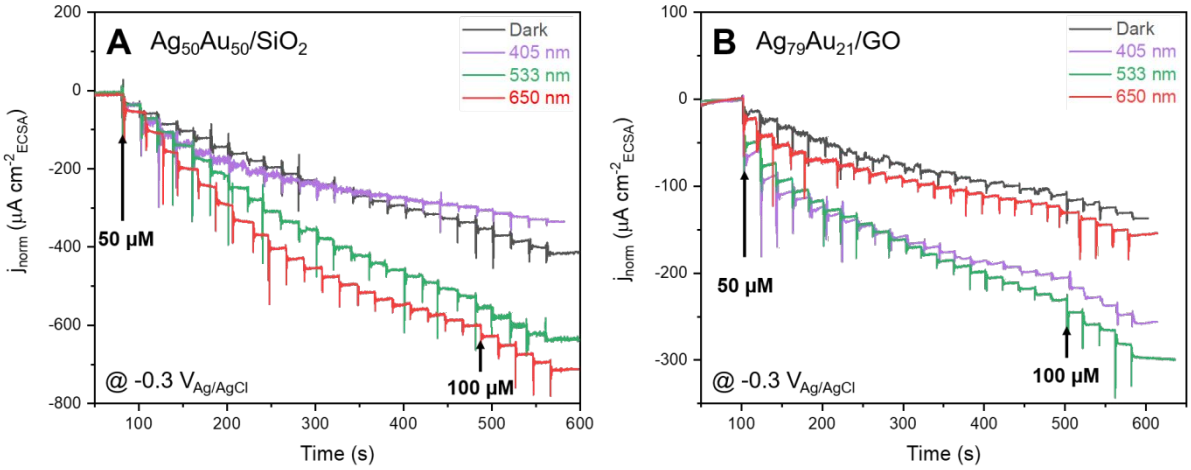


Figure S9. Chronoamperograms obtained for $Ag_{50}Au_{50}/SiO_2$ (A) and $Ag_{79}Au_{21}$ (B) with 20 additions of 50 µmol L^{-1} and 5 additions of 100 µmol L^{-1} H_2O_2 with and without light stimulus at -0.3 $V_{Ag/AgCl}$ in N_2-saturated KOH 1.0 mol L^{-1}.

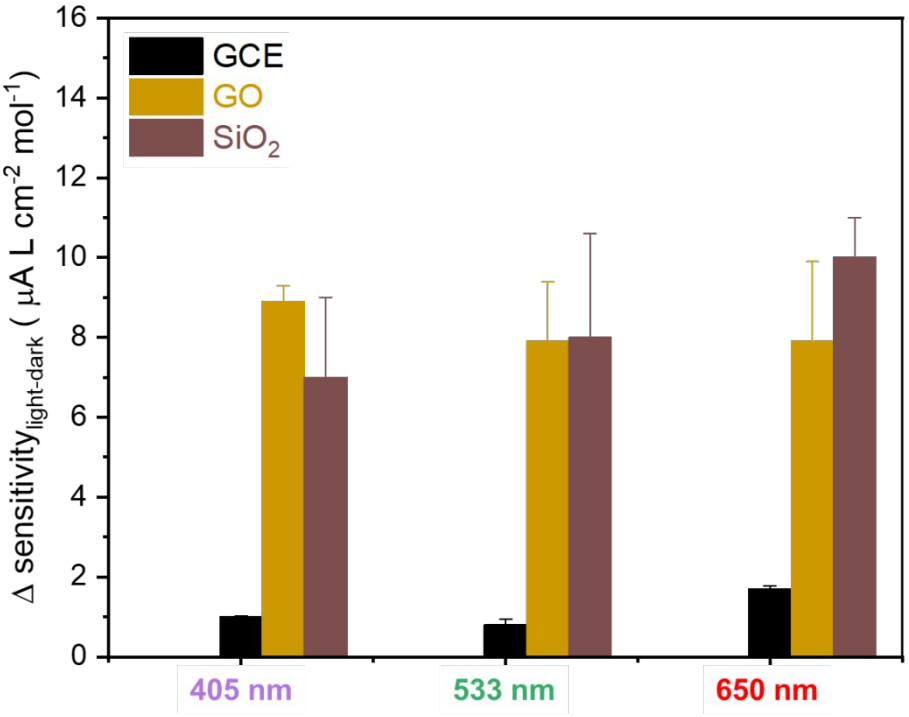


Figure S10. H_2O_2 sensitivity bar graph for GCE, GO and SiO_2 summarizing all catalysts with and without light incidence at -0.3 $V_{Ag/AgCl}$ and in N_2-saturated KOH 1.0 mol L^{-1}.

REFERENCES

[1] Wagner, C.; Riggs, W.; Davis, L.; Moulder, J. *Handbook of X-Ray Photoelectron Spectroscopy*; Muilenberg, G. E., Ed.; Perkin Elmer Corporation: Eden Prairie, 1979.

[2] Safo, I. A.; Werheid, M.; Dosche, C.; Oezaslan, M. The Role of Polyvinylpyrrolidone (PVP) as a Capping and Structure-Directing Agent in the Formation of Pt Nanocubes. *Nanoscale Adv.* **2019**, *1* (8), 3095–3106.

3.2 Nanobioconjugates

3.2.1 Stimuli-Responsive Regulation of Biocatalysis through Metallic Nanoparticle Interaction (Attachment 4)

Author Contribution: The author participated in conceiving the idea, leading the writing step, revising, and writing the paper.

Nanobioconjugates are comprised of nanostructures that act as supports for the immobilization of biomolecules. As previously discussed in **Attachment 1** and **Attachment 3**, metallic nanoparticles are liable to a series of external stimuli that induce electric, thermal, optical, and magnetic changes in the surrounding environments. In this review, we explore different aspects of stimuli-responsive nanobioconjugates for catalytic applications taking into account the modifications promoted by external stimuli in the biomolecules. State of the art on the application of external stimuli such as electricity, temperature, light, and magnetism on nanobioconjugates are presented and the outcoming effects are debated. A final section of this review outlines promising opportunities in this field that may instigate further researchers in the near future.

Bioconjugate Chemistry

pubs.acs.org/bc

Review

Stimuli-Responsive Regulation of Biocatalysis through Metallic Nanoparticle Interaction

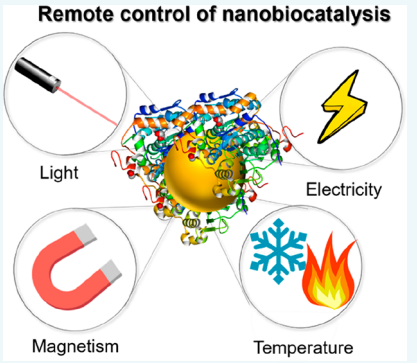
Rafael T. P. da Silva, Heloise Ribeiro de Barros, Daiana M. Furlan Sandrini, and Susana I. Córdoba de Torresi*

Cite This: *Bioconjugate Chem.* 2022, 33, 53−66

Read Online

ACCESS | Metrics & More | Article Recommendations

ABSTRACT: The remote control of biocatalytic processes in an extracellular medium is an exciting idea to deliver innovative solutions in the biocatalysis field. With this purpose, metallic nanoparticles (NPs) are great candidates, as their inherent thermal, electric, magnetic, and plasmonic properties can readily be manipulated upon external stimuli. Exploring the unique NP properties beyond an anchoring platform for enzymes brings up the opportunity to extend the efficiency of biocatalysts and modulate their activity through triggered events. In this review, we discuss a set of external stimuli, such as light, electricity, magnetism, and temperature, as tools for the regulation of nanobiocatalysis, including the challenges and perspectives regarding their use. In addition, we elaborate on the use of combined stimuli that create a more refined framework in terms of a multiresponsive system. Finally, we envision this review might instigate researchers in this field of study with a set of promising opportunities in the near future.



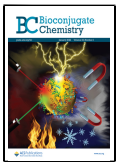
INTRODUCTION

The control of biocatalytic processes in an extracellular medium is highly attractive for a variety of nanobiotechnological applications. In particular, enzymatic activity regulation by external stimuli is an interesting strategy that can simulate cellular processes and interactions at the molecular level. These processes can occur dynamically *in vivo*, including cell signaling, adhesion, metabolism, drug delivery, biosynthesis, or *in situ* self-assembly. Regarding the reactivity of the enzyme and substrate pairs, they are either spontaneous or driven by forces already found in biological systems, such as temperature changes and electric potentials of lower magnitudes. However, there are still underexplored outcome effects in biocatalysis caused by some nonbiological external stimuli, such as magnetism and light. Additionally, the regulation of enzyme activity in real time by remote stimuli offers possibilities to combine several enzymes in cascade reactions, maximizing the specificity and efficiency in terms of rates and yields of biosynthetic pathways.

The interaction of enzymes with the surface of metallic nanoparticles (NPs) represents a promising alternative to achieve an optimized response toward biocatalysis. The large surface area of NPs allows the loading of large amounts of proteins per unit of mass on the surface and facilitates the development of specific interactions with the enzyme.[1−3] The bioconjugation of the enzyme to metallic nanoparticles may either preserve or induce the active conformation of the enzyme by creating a stable interaction between the protein and the metallic substrate with the due exposition of the active site to substrate molecules.[4,5] In addition to the structural and operational stability of enzymes, the orientation and density of proteins grafted onto the solid support surface are other important factors that can contribute to regulating the activity of conjugated enzymes.[6] Enzyme preparation associated with metallic supports is already well-known for presenting considerable stability to reaction conditions that negatively affect the catalytic performance of the free enzyme, resulting in higher tolerance to pH, temperature,[4,7,8] organic solvents,[4,9] or other denaturant agents.[10] Apart from their robustness and thermal and electrical conductivity, metallic NPs may exhibit unique properties, such as superparamagnetism and localized plasmonic resonance, depending on their size, morphology, and composition.[11] These unique properties of NPs can be used to design intelligent hybrids with programmed responses upon external triggers, such as magnetic fields, electric fields, light, and temperature.[12]

This review highlights the use and progress of metallic NPs as controllable and adjustable nanomodulators for enzyme activity. In this context, an overview of how external stimuli, in particular light, electricity, magnetic field, and temperature, can be used to trigger responses in nanostructures and responsive

Received: November 3, 2021
Revised: November 27, 2021
Published: December 16, 2021



Downloaded via UNIV OF SAO PAULO on July 30, 2022 at 20:40:31 (UTC).
See https://pubs.acs.org/sharingguidelines for options on how to legitimately share published articles.

ACS Publications

© 2021 American Chemical Society

https://doi.org/10.1021/acs.bioconjchem.1c00515
Bioconjugate Chem. 2022, 33, 53−66

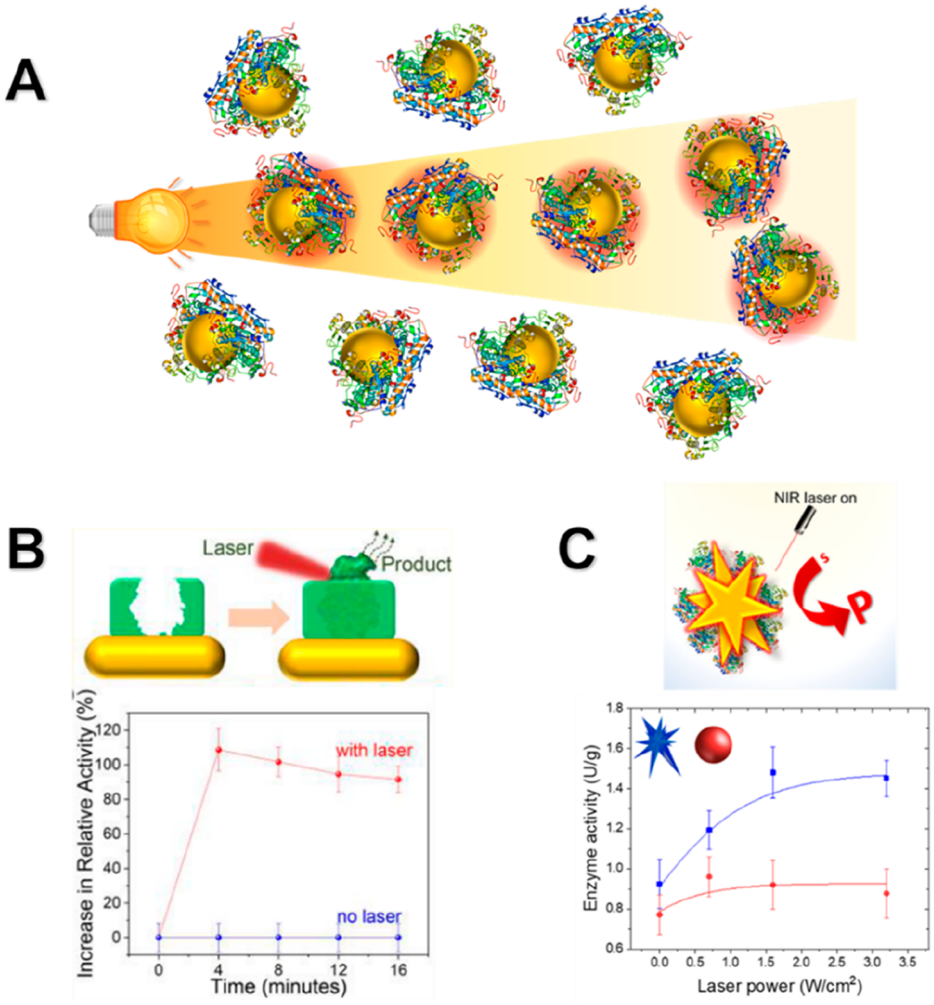


Figure 1. Light as an external stimulus to regulate nanobiocatalysis (A). Polymer-encapsulated HRP conjugated on Au nanorods (B). Adapted with permission from ref 28. Copyright 2017 American Chemical Society. Enzyme activity is enhanced upon 808 nm laser exposure (red line) in comparison to dark conditions (blue line). Enhancement of CALB activity immobilized on Au nanostars (blue line) and Au NPs (red line) regulated by an NIR laser (C). Adapted with permission from ref 31. Copyright 2021 American Chemical Society.

systems with the goal of regulating the properties of enzymes immobilized on NPs for various applications, including biosensors, phototherapy, photocatalysis, and catalysis, is proposed. Moreover, the most recent possibilities in multi-responsive control systems for enzymatic catalysis will be presented. Finally, future perspectives regarding the potential applications of controllable nanobiocatalysts will be highlighted, as well as a brief discussion about the challenges inherent to research and future applications in this innovative field of study.

LIGHT

The use of light as an external stimulus to regulate enzyme properties is fascinating because it represents an opportunity to develop a remote and instantaneous controlling tool. Moreover, the use of light is an attractive approach because it is a noninvasive and sustainable feature that is appealing for green chemistry solutions in the field of biocatalysis.[13] Few classes of enzymes can be naturally light-responsive due to photoswitchable moieties in their structure. These moieties can either undergo conformational changes that may affect the accessibility of the substrate or change metallic redox states upon light irradiation.[14,15] However, even though the promising changes induced by light are fairly interesting for the external regulation of enzymes, the limitation to a few classes of enzyme and biocatalytic processes is certainly a drawback.

In this regard, exploring metallic NPs for the immobilization of enzymes is an attractive strategy for the remote light regulation of biocatalysis. In recent years, the use of metallic NPs as an alternative tool for the light regulation of enzymes has gained significant relevance.[16] This arises mainly from the remarkable thermal and optical properties of metallic NPs, through which they offer unique light-stimulus-responsive properties. Upon light irradiation, metallic NPs provide ready heating and cooling rates for biocatalytic processes[17−19] (Figure 1A). For instance, the transference of heat to molecules close to the surface of Au nanorods covalently grafted onto the surface of proteinosomes took just 1 min when the system was irradiated by a near-infrared (NIR) laser, which certainly can lead to prompt "on/off systems" toward remote light regulation of biocatalysis.[20]

Regarding the remarkable optical properties, metallic NPs with absorption in the UV, visible, and IR spectrum are particularly interesting, and this phenomenon occurs in metals with conductive free electrons in their structure.[21] The

https://doi.org/10.1021/acs.bioconjchem.1c00515
Bioconjugate Chem. 2022, 33, 53−66

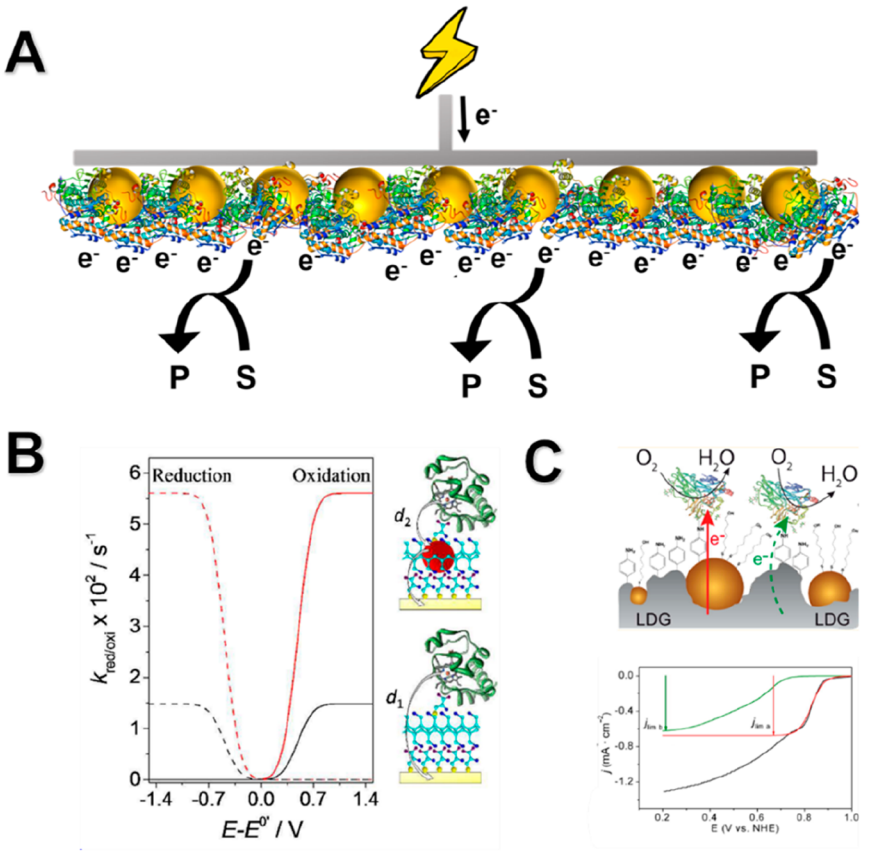


Figure 2. Electricity as an external stimulus to regulate nanobiocatalysis (A). Electron transfer rate constants between the cytochrome c redox center and the electrode surface mediated by Au NPs (red line) and without Au NPs (black line) (B). Used with permission of RSC, from ref 54; permission conveyed through Copyright Clearance Center, Inc. Electron transfer rate calculated from O_2 electroreduction catalytic waves of a low-density graphite (LDG) system containing Au NP-laccase. The process mediated by Au NPs (red line) occurs at high electron rate constants, whereas the process without Au NP mediation (green line) is rate limited with a distribution of electron transfer rate constants (C). Adapted with permission from ref 55. Copyright 2012 American Chemical Society.

coherent collective oscillation of the conductive electrons of such NPs generates a localized surface plasmon resonance (LSPR) excitation signal.[21,22] The excitation of the LSPR through light at a similar frequency in the spectrum can trigger chemical transformations close to the NP surface. In particular, plasmonic nanoparticles (such as Au and Ag NPs) show remarkable optical properties toward chemical transformations upon light irradiation. LSPR excitation generates photothermal heating or photoelectronic (e.g., excited charge carriers, such as hotspots and hot electrons) effects that may deliver at least one of these energetic processes into the enzyme located on the NP surface.[23] Moreover, the response of the light interaction is relatively simple to tune through the intrinsic properties of the NPs, such as their size and morphology. As a result, the broad variation of responses enables a myriad of possibilities for biocatalytic transformations with fine spatial and temporal control.

Pioneering studies have reported the photothermal heating effects of metallic NPs to manipulate biomolecule properties, such as protein degradation, peptide assembly, and DNA melting.[18,24,25] In particular, controlling the properties of enzyme activity by metallic NPs upon light irradiation was reported for the first time by Simon and co-workers.[17] In this study, they described the photothermal deactivation of horseradish peroxidase adsorbed on Au NPs upon laser irradiation. Although these results showed a decrease in enzyme activity under light irradiation, this study elicited many novel opportunities for future studies. For example, an interesting study was conducted to regulate the reversibility of laccase deactivation with Au NPs by controlling the time of laser irradiation.[26] In this hybrid system assembly, laccase acted as both a reducing and stabilizing agent. Subsequently, a significant advance in the topic was carried out: the biocatalytic reaction rate of a thermophilic enzyme (*Aeropyrum pernix* glucokinase (Glk)) thiol-conjugated on Au nanorods and embedded in a calcium alginate matrix was increased by 60%.[27] The matrix was employed to retain the photothermal heat generated by the Au nanorods and to stabilize the enzyme with the goal of increasing the biocatalytic activity. Similar strategies making use of a matrix were further employed to enhance the biocatalytic activity of conventional enzymes, in which horseradish peroxidase (HRP) adsorbed on Au nanorods was encapsulated through *in situ* polymerization and by a metal–organic framework (MOF) (Figure 1B).[28,29] Recently, photothermal enhancement of biocatalytic yield was successfully carried out without the use of a matrix by employing enzymes with different optimal temperatures (meso, thermo, and hyperthermophilic) functionalized on Au nanorods via self-assembly, in which the hyperthermophilic enzyme showed higher activity upon light irradiation, as expected.[30] The photothermal enhancement of biocatalytic activity using a conventional enzyme (lipase from *Candida antarctica* fraction

https://doi.org/10.1021/acs.bioconjchem.1c00515
Bioconjugate Chem. 2022, 33, 53−66

B (CALB)) without the need for a matrix was very recently reported through their adsorption on Au nanostars and upon light irradiation (Figure 1C).[31] In this way, the evolution of these studies reveals rapid progress in the field and promising studies to come in the foreseeable future.

Although most studies with light have focused on Au NPs, there is still room to study the regulation by this stimulus with other plasmonic NPs or metallic nanoparticles. Iron oxide nanoparticles supported on reduced graphene oxide were able to enhance the reaction rates of lipase, glucose oxidase, and organophosphorus hydrolase covalently linked with polydopamine by the local heating promoted upon NIR exposure.[32]

The studies presented here elicit examples of photothermal heating generated from metallic NPs upon light irradiation to regulate biocatalytic processes. Moreover, as previously described, different energetic processes from the metallic NPs upon light irradiation can also take place, such as generation of hot spots or hot electrons. These processes are fairly known in light-driven catalysis for metallic NPs (in particular for plasmonic catalysis). However, they are still challenging to exploit in light-driven catalysis by metallic NPs involving enzymatic reactions in terms of mechanisms and assignments of multiple effects at the nanoscale. In this scenario, there are many opportunities to explore the light regulation of biocatalysis through either photothermal heating or photoelectronic effects of metallic NPs toward the development of more sophisticated systems and biocatalytic processes.

■ ELECTRICITY

Redox biomolecules, such as certain enzymes, were first immobilized on electrode surfaces almost six decades ago, aiming mainly for biosensor applications.[33] Despite the growth of the biosensor field as a hot topic,[34−37] bioelectrochemistry currently presents a more diverse range of applications, such as biofuel cells,[38−41] biosupercapacitors,[42−44] and bioreactors.[45−47] The development of nanotechnology and, hence, its application in surface-modified electrodes has been demonstrated to be a versatile tool. In particular, a conjugated system of metallic nanoparticles and enzymes is able to provide increased surface area, which bears the immobilization of higher loads of enzyme, and thus, higher current densities can be reached in electrochemical assays.[48] Therefore, nanoparticles allow electrochemical device miniaturization and enlighten interesting physicochemical properties that differ from their bulk counterparts, such as high reactivity due to increased surface energy.[49]

The use of electrochemistry is envisioned, since, in terms of thermodynamics, the electrical potential is directly related to the Gibbs free energy.[50] Thus, electrical stimulation may be able to regulate and induce redox reactions (Figure 2A). However, the Nernst equation relates the electrical potential with the yield given by the equilibrium constant under nonstandard conditions.

As with any other external stimulus, electrochemical methods should also take into consideration enzyme conformation. Immobilization techniques on the electrode must keep the enzymatic active site unblocked and must maintain enzyme molecular geometry concerning catalytic purposes.[51] Regarding enzymes as biocatalysts, the most commonly used class of enzymes in bioelectrochemical applications is oxireductases, also called redox enzymes. Their use is prioritized due to the high electron mobility in the active site combined with the high specificity to substrates already assessed in classical biocatalysis.[52]

The immobilization of enzymes onto Au NPs—the most classical NPs used for this purpose—can either assume a favored conformation or facilitate electron transfer between the electrode surface and the prosthetic groups of the enzyme.[53] Luz and Crespilho studied the optimization of electron transfer between cytochrome c immobilized on Au NPs and the electrode.[54] According to the authors, self-assembly with Au NPs, cysteine, and poly(allylamine hydrochloride) led to changes in the microenvironment from the redox center of this protein, as reflected by the shift in its Soret band. A significant increase in the faradaic current from the Fe^{III}/Fe^{II} redox couple was observed in the presence of Au NPs, indicating higher rates of this redox reaction. To assess the reasons for this, the authors investigated the effective distance between the redox center of cytochrome c and the electrode surface through theoretical models for heterogeneous systems. The electron transfer rate constant for the sample containing Au NPs was approximately 4-fold higher, which may suggest an electron hopping mechanism (Figure 2B). The electron transfer rate constants for low-density graphite (LDG)-containing laccase, a copper metalloenzyme, and covalently immobilized via 1-(3-dimethylamino-propyl)-3-ethylcarbodiimide (EDC) and *N*-hydroxysuccinimide (NHS) on Au NPs were determined for O_2 electroreduction.[55] The deconvoluted electrocatalytic wave presented an electron rate transfer rate value of 400 s^{-1} at lower overpotentials that was assigned to the enzyme molecules efficiently wired to Au NPs. In contrast, the least efficiently wired sample presented a rate-limited reaction with a distribution of electron transfer rate values (Figure 2C). Since then, some other studies have observed an enhancement in electron transfer to the enzyme redox center using Au NPs assembled with horseradish peroxidase,[56] sulfite oxidase,[57,58] formate dehydrogenase,[41] and hydrogenase.[59]

Wang et al. studied the interaction of adsorbed cytochrome c with hematite nanowire (NW) array electrodes.[60] Upon electrochemical stimulation, the electron transfer rates were related to two different cytochrome c conformations, namely, the native and partially unfolded forms. The concentration ratios of these two protein forms and amount absorbed by the NWs were strongly affected by the pH of the medium and electrical potential applied. The authors observed that the change in conformation was induced by the interaction between the protein and the hematite. Regarding the electron transfer rate constants, the authors claim that the unfolded protein presented approximately 37% faster rates than the native form.

Redox enzymes are able to either accept or donate electrons from or to electrodes directly or via redox mediators.[61] Electrochemical techniques meet this need by providing an electrical environment to favor these reactions. When the electron transfer mechanism occurs directly between the enzymatic catalytic site and the electrode, it is called direct electron transfer (DET), whereas mediated electron transfer (MET) is the type of reaction that needs a mediator to take place. It is possible to find organic and inorganic molecules that may act as redox mediators, such as methylene blue, Prussian blue, thionin, toluidine blue, quinone derivates, ferrocene and its derivates, and inorganic redox ions, such as ferri/ferrocyanide.[62] In nature, electron mediators are often cofactors, such as nicotinamide adenine dinucleotide (NAD^+) and flavin adenine nucleotide (FAD), as well as ascorbic acid,

https://doi.org/10.1021/acs.bioconjchem.1c00515
Bioconjugate Chem. 2022, 33, 53−66

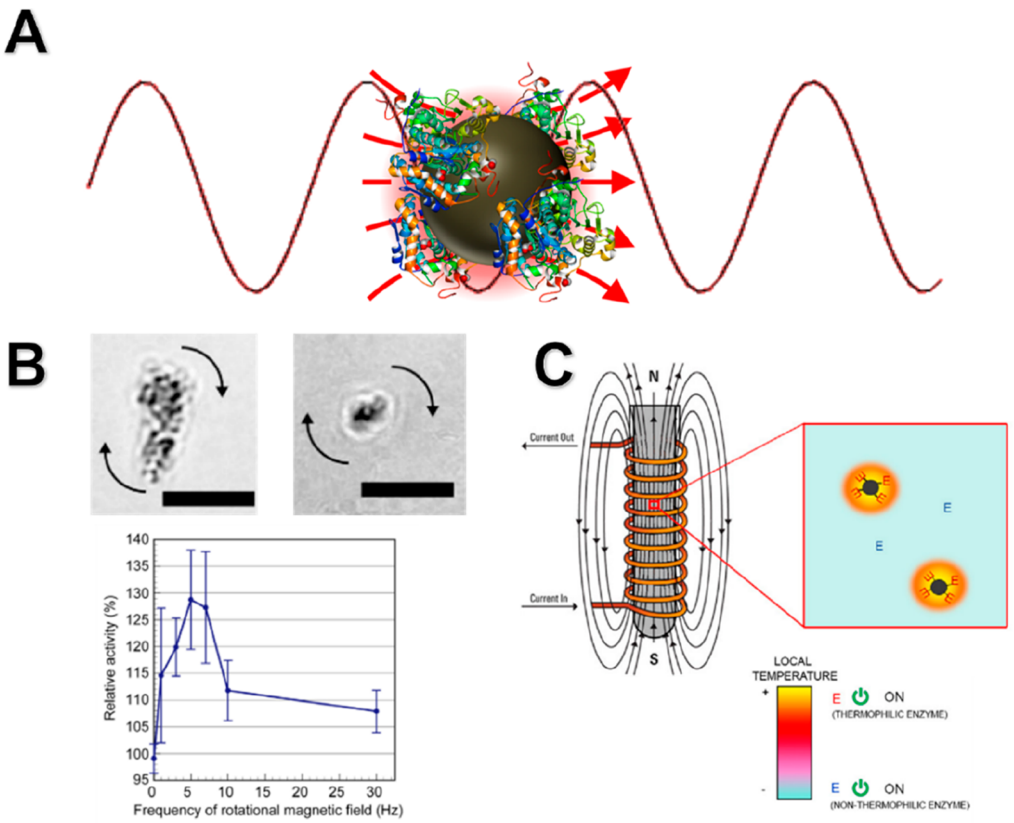


Figure 3. Magnetism as an external stimulus to regulate nanobiocatalysis (A). The activity of α-amylase increases in a rotational magnetic field, reaching its maximum at 5 Hz (B). Reprinted with permission from ref 81. Copyright 2010 Elsevier. Alternating magnetic fields induce heat generation on superparamagnetic nanoparticle surfaces. An increase in the local temperature activates thermophilic enzymes, whereas nearly no increase in the bulk solution preserves the activity of nonthermophilic enzymes (C). Reprinted with permission from ref 85. Copyright 2019 Elsevier.

flavin mononucleotide, and inorganic cofactors, such as metallic ions (Mg^{2+}, Cu^{+}, Mn^{2+}). Although the reported number of DET systems has recently increased, fewer enzymes present this mechanism. This is because DET only occurs when the enzyme catalytic sites are within an electron-tunneling distance from the electrode and there is no residence of electrons at any in-between entity.[63] The main advantage of DET is the elimination of redox mediators and their associated overpotential losses, which makes MET less ideal for use in real applications.[61,64]

To overcome the challenges of energy loss by MET, electrochemical cofactor regeneration is a strategy widely explored by some groups by the coimmobilization of cofactors and enzymes at regions surrounding the electrode surface.[65,66] In addition, high regenerative yields prevent the further addition of these expensive redox mediators and indicate long-lasting reactions. However, some issues concerning the stability and assessment of global kinetic parameters are still challenges faced with coimmobilized systems.[67] Usually, metallic nanoparticles are good catalysts for this conversion, and thus, system enzyme nanoparticles are advantageous.

Using Cu NPs as supports, Song et al. reported an electron-mediator-free system with the coimmobilization of the cofactor NAD^{+} with formate dehydrogenase (FDH). The results revealed one of the best faradaic efficiencies and molar productivity based on the enzyme loading already reported for CO_2 electroreduction by FDH.[66] In this study, the FDH–NAD^{+} conjugate was cross-linked into a polyethylene glycol (PEG) swing arm that could reach the surface of a Cu-NP-modified electrode, which was capable of both regenerating NAD^{+} and immobilizing enzymes through Cu–S bonds with cysteine residues from FDH. The regeneration yield was over 90% with −1.0 V (vs Ag/AgCl) applied over the Cu NPs. Si NWs were used for NADH regeneration by Lee et al. in the presence of visible light irradiation and −0.8 V (vs Ag/AgCl), reaching greater than 40% regeneration in Si NWs of optimal length.[68] When decorated with platinum NWs (Pt–Si NWs), the material reached 1.54-fold higher NADH regeneration under the same conditions when compared to the bare Si NWs. More recently, Ali et al. developed a system of multiwalled carbon nanotubes decorated with nickel nanoparticles (Ni-MWCNTs) in which the regeneration percentage of NADH reached 98% at −1.1 V (vs Ag/AgCl).[69] The same authors had already previously developed two materials, namely, platinum and nickel nanoparticles, on glassy carbon electrodes.[70] Both reached 100% NADH recovery, although the first needed a higher potential of −1.1 V than the second at −1.0 V vs Ag/AgCl.

Although there have been few studies exploring cofactor regeneration with either nanocatalytic or enzymatic pathways, there is still room for projects that associate cofactor regeneration with bioelectrocatalysis. This strategy could improve both the lifetime and sustainability of bioelectrochemical devices.

In summary, the electrochemical performance of metallic nanoparticle–enzyme systems is deeply related to the

https://doi.org/10.1021/acs.bioconjchem.1c00515
Bioconjugate Chem. 2022, 33, 53−66

interactions that occur between these two components and the electrode surface.[71] To understand these interactions, advanced multidisciplinary approaches have been developed, such as a quartz crystal microbalance with dissipation (QCM-D) and spectroscopic techniques, such as infrared and Raman techniques.[72] QCM-D provides information relative to enzyme loading, relative orientation, clustering, and denaturation of enzymes at the electrode surface.[73] Spectroscopic techniques are able to assess information on secondary and tertiary structures and the redox state of cofactors or active sites.[74] In the next years, a further development of these characterization techniques regarding robustness and resolution could be promising for this field. Alongside the results of remote electrical stimulation control, these characterization techniques are a key factor to elucidate the complexity and to improve the processes involving electron transfer within nanobiocatalysts.

MAGNETISM

As enzymes are a relatively expensive class of compounds, their recovery from the solvent medium in catalytic applications is highly desired. Traditional methods of separation, such as chemical separation and ultrafiltration, may lead to denaturation and inactivation of enzymes, hindering their successful recycling.[75] Immobilization in magnetic nanoparticles—especially those made of iron oxide—has been used as an alternative to provide recovery and reusability in catalytic cycles through magnetic separation without damaging the protein structures. Additional features of these nanoparticles with tunable size and morphology are their low toxicity, high rates of charge transfer, high enzyme loading capacity, and ease of surface modification.[76] Although only a limited number of materials are responsive to magnetism,[77] several surface modifications are able to enhance their stability under acidic conditions, delay oxidation, and prevent agglomeration and are usually performed with silica, carbohydrates, polymers, composites, or amino-containing molecules.[78]

Apart from magnetic separation, the magnetic stimulus applied with an alternating magnetic field (AMF) has been demonstrated to generate a set of effects that are able to enhance the catalytic efficiency of enzymes. When the magnetic moment from the nanoparticles aligns to the external magnetic field in a continuously alternated fashion, microscopic motions are observed and make the nanoparticles behave as a microscopic stirrer, which increases the collisions at a molecular scale (Figure 3A).[79] Zheng et al. demonstrated in a systematic study that the reaction rate of a bienzyme system composed of glutamate dehydrogenase and glucose dehydrogenase coimmobilized through γ-glycidoxypropyl trimethoxysilane with the cofactor onto magnetic nanoparticles was 2.3 higher when AMF was applied, depending on its strength and frequency.[80] Mizuki et al. also explored the use of low-frequency AMF to improve the motion of adsorbed enzyme−nanoparticle conjugated systems, leading to increased collisions between the substrates and catalysts.[81] In their system, α-amylases supported on Fe_3O_4 superparamagnetic nanoparticles reached ca. 130% catalytic activity at a frequency of 5 Hz, which is an optimal frequency for clusters composed of several hundred particles. This effect was not seen if the motion was induced by the conventional stirrer and shaker. They showed that there was no conformational effect on the enzyme active site after immobilization onto superparamagnetic nanoparticles, suggesting that α-amylase activity was not tuned by any possible conformational change (Figure 3B).

In addition to the increased motion induced by AMF, recent studies have demonstrated that heat can be generated at the surface of magnetic nanoparticles under AMF without affecting the bulk temperature of the solution.[82−85] In small nanoparticles, magnetic heating can occur due to hysteresis losses and/or eddy currents.[86] Along with the dependence on the nanoparticle size and composition, magnetic heating is influenced by magnetic anisotropy and interparticle magnetic interactions. In larger nanoparticles, the Joule effect should also be considered.[87] Xiong et al. developed a ferromagnetic nanoring−enzyme hybrid catalyst through the EDC/NHS coupling that enables the regulation of enzyme activity upon AMF.[82] The authors claimed that β-galactosidase (β-gal), *Klebsiella pneumoniae* carbapenemase, and glucose oxidase activities were enhanced upon exposure to an AMF due to local heat generation on the surface of the nanoring. To prove the local heat produced by AMF, fluoresceinamine was immobilized on the nanoring using a thermolabile azo linker. Its cleavage was followed by the liberation of a fluorescent dye that could be monitored by fluorescence spectroscopy. In addition, it was demonstrated that the enzymatic activity could be enhanced up to 180% when enzymes were conjugated to the nanoring under an AMF, and no influence was observed on the activity of free enzymes surrounding the nanoparticles. Even though an increase in temperature in the bulk solution showed a similar increase in enzyme activity, this process took at least 3 min, whereas AMF experiments showed an elevated activity response almost instantly.

Since heat generation from magnetic nanoparticles under AMF does not induce a rise in the bulk temperature of the solution, a multienzymatic system composed of thermophilic enzymes and thermolabile enzymes, substrates, and products could be designed for a system to operate in a simultaneous fashion.[82,83,85] In this way, thermophilic enzymes could be activated by temperature when conjugated to a magnetic nanoparticle, and free thermolabile components in the solution would not be influenced by heat locally generated from the nanoparticles, as suggested by Armenia et al.[85] The authors explored heat generation from iron oxide superparamagnetic nanoparticles using an AMF to activate thermophilic enzymes (L-aspartate oxidase and α-amylase) in a remote-controlled way. Three covalent immobilization strategies were used starting from the aminated superparamagnetic nanoparticles. The first approach used EDC/NHS, a second through bis(sulfosuccinimidyl)suberate, and the third modified the surface molecules into thiol-reactive species by the addition of sulfosuccinimidyl 4-(*N*-maleimidomethyl)cyclohexane-1-carboxylate). Since they observed nearly no increase in the bulk solution temperature but only at the nanoparticle surface, it is possible to create two environments within the same system. Thermophilic enzymes are influenced by the surface heat of the nanoparticles, whereas dispersed nonthermophilic enzymes have preserved activity under an overall solution temperature in a multienzyme system (Figure 3C). The nanoparticle size of superparamagnetic iron oxide allows the magnetic and thermal outcomes to be switched off as soon as the external magnetic stimulus is removed. The reduction in the size of the nanoparticles is important to preserve their superparamagnetic properties, such as high magnetic moments under the effect of an external magnetic field, as well as no coercivity and no remanence.[88] These properties imply demagnetization of the system with spontaneous recovery of the initial zero net magnetic moment with the removal of the external magnetic

https://doi.org/10.1021/acs.bioconjchem.1c00515
Bioconjugate Chem. 2022, 33, 53−66

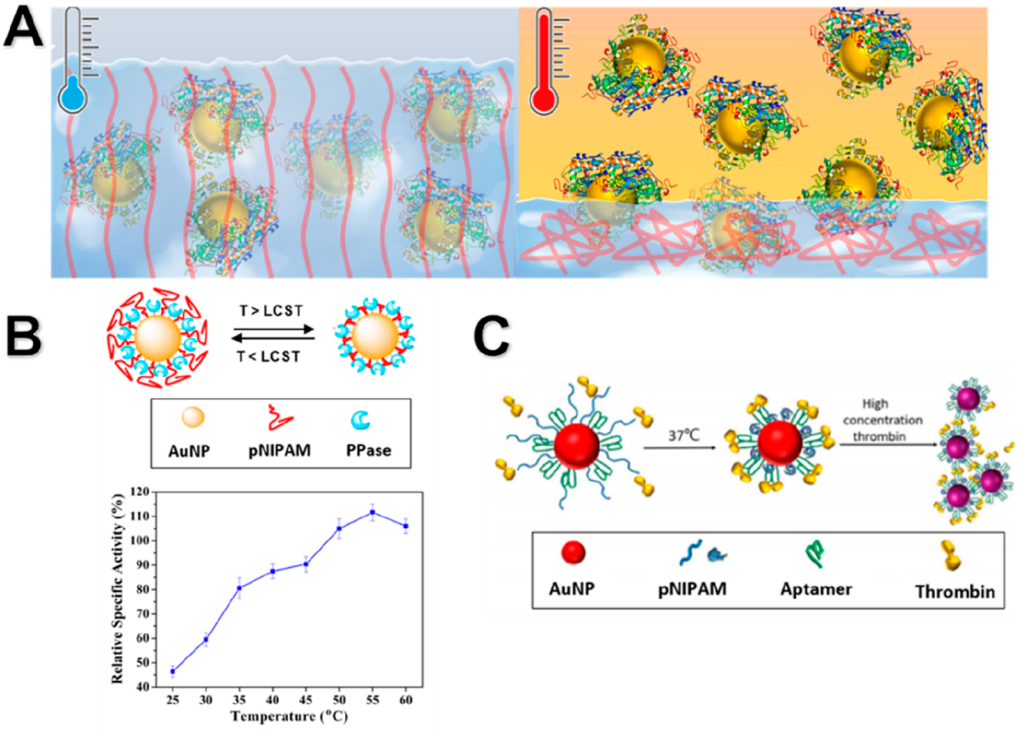


Figure 4. Temperature as an external stimulus to regulate nanobiocatalysis through the collapse of thermoresponsive polymers (A). *E. coli* PPase and pNIPAM fabricated onto Au NPs to regulate PPase activity. Temperatures above the LCST expose PPase (B). Adapted with permission from ref 6. Copyright 2015 American Chemical Society. Grafting pNIPAM and an aptamer on the surface of Au NPs to regulate thrombin activity. At low temperatures, pNIPAM chains are extended, and the aptamer is prevented from capturing thrombin (C). Reprinted with permission from ref 103. Copyright 2016 Elsevier.

field. Armenia et al. also demonstrated that the optimal temperature of the enzymes can be tuned by the enzyme orientation on the nanoparticles. This factor directly influences the enzymatic activity at a given temperature and affects the thermostability of the conjugated enzyme. In another study designed by Suzuki et al., DNA ligase was immobilized by electrostatic forces onto ferromagnetic iron nanoparticles.[83,84] They reported an increase in the efficiency of DNA ligase heated by a magnetic field together with a low influence of nanoparticle heat dissipation on DNA annealing performance. The immobilized DNA ligase presented a slightly lower activity than its free counterpart. However, in the presence of an AMF, the ligation efficiency increased almost 190% compared to that in the absence of the magnetic field.

In addition to thermal effects caused by AMF, conformational changes can be triggered when applying a nonheating low-frequency magnetic field (LF MF), offering a distinct effect of controlling enzyme activity.[89−92] The realignment of the magnetic moment (μ) of magnetic nanoparticles under a LF MF generates deformations, such as stretching, contraction, compression, and twisting, on the conjugated enzymes.[89,92,93] In this context, enzyme activity can be modulated by magnetomechanical effects, which involve the oscillation of magnetic nanoparticles due to the remote response to the LF MF. In a study with α-chymotrypsin conjugated to gold-coated magnetic nanoparticles, Efremova et al. observed a decrease in enzyme catalytic activity, assuming that the hybrid system formed a dimer structure, where the enzyme was attached via adsorption to both nanoparticles.[92] In the proposed system, the reorientation of the magnetic nanoparticles under a LF MF induced conformational changes that hindered the access of the substrate to the catalytic site of the enzyme. Through FTIR analysis of the α-chymotrypsin secondary structure, the enzyme exhibited a reduction in β-sheets and β-turns from 42% to 19% and a slight increase in the α-helix from 22% to 27% before and after LF MF exposure, respectively. Computer simulations revealed that these conformational changes and rearrangements did not alter the position of the catalytic triad or the folding of the protein chain but rather caused local deformation in the area surrounding the active site, which led to a decrease in substrate binding and consequent loss in catalytic activity. A similar result was obtained by Guo et al., where horseradish peroxidase immobilized on superparamagnetic beads by 3-aminopropyltriethoxysilane was magneto-mechanically deformed using magnetic tweezers.[94] They reported a loss in substrate binding when pulling forces from magnetic tweezers were applied, indicating that the conformation of the active site plays a crucial role in modulating enzyme activity.

Although a conformational change depicted by the surface interaction of the enzymes with the magnetic nanoparticle should be expected, the effects of an AMF and a LF MF together with the recovery rates provided by the magnetic stimulus are the most important features for enzymatic catalysis. By understanding these phenomena and their particularities according to the set of enzyme and nanoparticle features, one should be able to modulate the best conditions for catalysis improvement under a magnetic field. Alongside refined studies of magnetic stimulus toward biocatalysis, finding alternatives that improve costs, complexity, and robustness of experimental setups are still imperative to its large-scale applications.[95]

https://doi.org/10.1021/acs.bioconjchem.1c00515
Bioconjugate Chem. 2022, 33, 53−66

Table 1. Advantages and Limitations of Individual Stimuli-Responsive Systems for the Regulation of Enzymatic Biocatalysis

external stimuli	advantages	limitations
light	noninvasive and environmentally benign feature[13]	few classes of enzymes are responsive to light[14,15]
	high spatiotemporal control of local heating and cooling[17−20,32]	restricted number of metallic nanoparticles which can effectively absorb light and convert it into chemical energy[23]
	easily tunable tool to achieve programmed responses in biocatalysis[20,26−32,108,110]	strategies for preserving the activity of mesophilic enzymes in remote control systems by light are little explored[16]
	efficient source for photothermal generation that tunes properties of biomolecules[17,18,24,25]	
electricity	versatility in applications, such as biosensors,[33−37] biofuel cells,[38−41] biosupercapacitors,[42−44] and bioreactors[45−47]	methods are mainly focused on redox enzymes[52]
	possibility of device miniaturization[49]	few redox enzymes are able to perform DET[63]
	efficient and instantaneous energy transfer yield through DET[47,57,61,71]	coimmobilization with redox mediators lacks stability and assessment of kinetic parameters[67]
magnetism	possibility to recover and recycle enzymes[75]	limited number of materials are responsive to magnetism[77]
	ease of nanoparticle surface modification[76,78]	costly and challenging experimental setups[95]
	increase of reaction collisions through AMF without the need of denaturing agents[79−81]	
	high spatiotemporal control of local heating and cooling[82−87]	
	changes in enzyme conformation through LF MF modulate biocatalysis[89−94]	
temperature	readily accessible feature[14,99,100]	enzyme-integrated thermoresponsive structures are needed to precisely regulate biocatalysis[6,102,103,106]
	required temperatures are close to ambient[12]	low spatiotemporal control of bulk heating and cooling and high energy loss[102,103,107]

TEMPERATURE

Temperature as an external stimulus is usually related to enhancing the kinetic energy of the mixture components. However, the functionalization of enzyme−metal nanoparticle conjugates with thermoresponsive structures enables the use of temperature as an effective external stimulus to regulate the enzymatic activity in these conjugates (Figure 4A). The most explored polymers to thermally regulate enzymatic function exhibit a lower critical solution temperature (LCST) behavior, in which their solubility is reduced when above this temperature.[14] The thermosponsive polymer poly(*N*-isopropylacrylamide) (pNIPAM) is widely used because its LCST is not far from room temperature and, moreover, is close to human body temperature.[96−98] The change in the solubility of pNIPAM is a consequence of the conformational change in the chemical structure of the polymer, which can either be collapsed or extended, as a function of the change in the temperature of the medium.[98]

As a readily accessible stimulus, temperature has been shown to be a promising and effective tool that can be used noninvasively to dynamically control enzyme activity by increasing and decreasing it successively.[14,99,100] To obtain refined control over the activity of inorganic pyrophosphatase (PPase) from *Escherichia coli*, Liu et al. developed a thermocontrollable system in which the PPase enzyme and pNIPAM were coimmobilized onto the surface of Au NPs via adsorption and EDC/NHS coupling reaction, respectively (Figure 4B).[6] The pNIPAM molecules acted as a "cap" on the surface of the Au NPs, sterically blocking part of the enzyme catalytic sites at temperatures below the LCST. When the medium was heated above the LCST, dehydration of the pNIPAM chains followed by their collapse exposed the enzyme catalytic sites and made them accessible to the substrate, which increased the activity of the conjugate up to 270%. The reversible adjustment of biocatalytic performance in thermoresponsive systems is mainly driven by the change in the properties of responsive structures, such as conformation and solubility, due to the direct heating of the reaction medium.[12] Importantly, when changing conformation in response to temperature, responsive polymers protect the immobilized enzyme from the external environment with no changes in its functional stability. This characteristic is of great importance because it allows the use of biocatalysts under adverse reaction conditions and for repeated operational cycles without requiring their replacement.[101] Moreover, the authors reported that the presence of pNIPAM in the conjugated enzymes increased the resistance to digestion by proteases. After 90 min of trypsin digestion at 45 °C, the free enzyme lost 70% of its activity.[6] In contrast, the conjugated PPase lost only 30% of its activity.

Au NPs as a support for the coimmobilization of biomolecules and pNIPAM have become the focus of research on the controlled "on−off" switching of biomolecule activity by temperature induction. Zhang et al. modified the Au NP interface by covalent attachment of thiol-terminated thermosensitive pNIPAM and thiol-terminated single-stranded DNA in order to create a dynamic and reversible nanoparticle assembled system responsive to temperature.[102] Above the LCST, DNA-recognition-induced assembly was observed due to the exposure of DNA−Au NPs from the polymer surface to complementary DNA bases. The cooling of the solution below the LCST was responsible for the extension of the pNIPAM chains, which blocked access to the DNA−Au NPs and prohibited their recognition. Thermoresponsive platforms on Au NPs can also be used to set up "on−off" systems for reverse regulation of biomolecule activity. An example was the system developed by Yu et al., in which thrombin binding aptamer and pNIPAM, both thiolated, were covalently attached on the surface of Au NPs and promoted the reversibility of thrombin inhibition through the interaction with aptamers mediated by temperature change (Figure 4C).[103] At 25 °C, thrombin was prevented from binding to the aptamer, thus catalyzing the release of the chromophoric *p*-nitroaniline group, resulting in high absorbance at 405 nm. However, at 37 °C, the collapsed pNIPAM state exposed aptamers on Au NPs for binding to thrombin, and their capture of the reaction medium resulted in

https://doi.org/10.1021/acs.bioconjchem.1c00515
Bioconjugate Chem. 2022, 33, 53−66

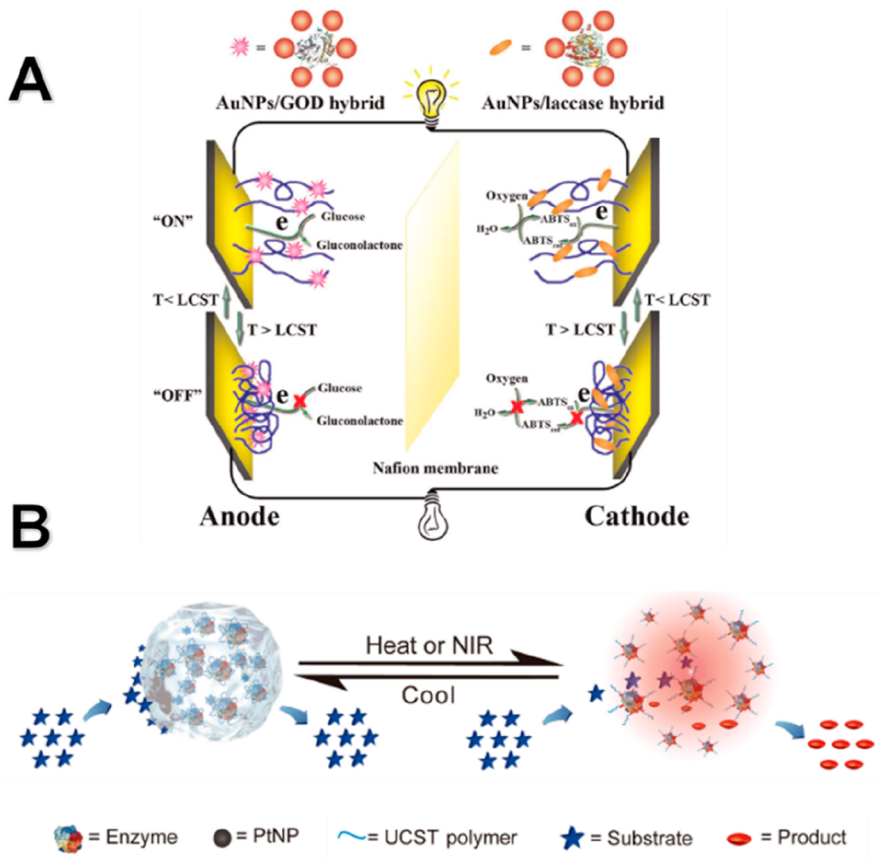


Figure 5. Combined stimuli regulating nanobiocatalysis. "On−off" switch on enzyme activity dependent on heat or NIR. A switchable EBFC is heated to turn the electrochemical system on whenever the temperature is below the LCST of pNIPAM (A). Reprinted with permission from ref 106. Copyright 2015 Elsevier. The interaction of Pt NPs with NIR induces a photothermal effect in the NPs that act as a secondary local heat source to expand the UCST polymer chains (B).[108]

inhibition of activity with low absorbance at 405 nm. Although thrombin−aptamer systems have been extensively explored in previous studies, this was the first report of a temperature-responsive inhibitor for the remote control of thrombin catalysis.

Considering enzymatic activity's strong dependence on temperature, the studies reported reinforce the importance of integrating thermosponsive structures with enzymatic systems to precisely regulate biocatalysis by simple and practical local temperature changes. The limited number of studies that use temperature as a primary external stimulus to modulate the catalytic activity of enzymes may represent opportunities and challenges to explore new strategies for temperature regulation as well as new thermocontrollable biocatalytic systems. In this context, the search for new thermoresponsive platforms, which include responsive polymers as well as underexplored metallic or bimetallic NPs as solid matrixes, can be promising candidates to this end.

■ COMBINED STIMULI

So far, this review has addressed the studies concerning individual stimuli-responsive systems for the regulation of enzymatic biocatalysis, whose advantages and limitations are summarized in Table 1. Given the independent contribution of each stimulus within their particularities, a system that is able to combine a set of stimuli can be envisioned as a smart multiresponsive material. By understanding their individual effects, the synergy of two or more stimuli in a single system will lead to enhanced outcomes and promote more refined control over nanobiocatalysis.

The secondary generation of heat is commonly attributed to magnetic, electric, and light stimuli and is widely explored. Usually, heat release is associated with the direct enhancement of the reaction rates from a particular structure. As an example, the photothermal effect has been strategically used mainly as a platform for drug delivery or cancer treatment.[104] For the purpose of this systematic review, we considered this phenomenon as a single external stimulus, whereas, when the generated heat was able to trigger a secondary "on−off" response, it was considered a combined stimulus.

Among the possible combinations, the design of a system responsive to combined magnetic and thermal stimuli was studied by Knecht et al.[105] In this study, the use of a magnetic stimulus via an AMF on Fe_3O_4 nanoparticles as a heat generator was explored to increase the activity of hydrogel-entrapped thermophilic dehalogenase at an optimal temperature of 70 °C. Treatment with an AMF was able to reach a local temperature matching the optimal temperature of the enzyme, which presented a 2-fold increase in activity in comparison to the system externally heated by a water bath. This indicates that the secondary enhancement of the local temperature by the AMF was essential rather than the limited diffusive heat from an external bath.

Concerning a thermal "on−off" switch combined with an electrochemical application, Chen et al. immobilized via adsorption GOD and laccase onto Au NPs and later trapped

https://doi.org/10.1021/acs.bioconjchem.1c00515
Bioconjugate Chem. 2022, 33, 53−66

this system in pNIPAM chains to catalyze glucose oxidation and O_2 reduction, respectively, in a switchable enzyme biofuel cell (EBFC).[106] The study demonstrated that the repeatable on−off behavior of biocatalysis was achieved in a few minutes whenever the temperature in the EBFC changed from 20 to 45 °C. Above the LCST of this specific pNIPAM (45 °C), the collapsed chains achieved hydrophobicity, the enzyme active sites were hindered, and the reactions were impeded. In addition, when operated continuously for 40 days in the "on" state, EBCF maintained 92% of the maximum open circuit voltage (E_{cell}^{ocv}) (Figure 5A). These results strongly suggest that Au NPs together with pNIPAM provided an adequate microenvironment to maintain the structural and functional stability of enzymes in bioelectrodes.

Depicting the combination between light and electrical stimuli, Sánchez-Iglesias et al. studied plasmonic substrates under visible light stimulus for the electrochemical regeneration of NADH.[107] Light irradiation over platinum-covered Au nanocubes, nanorods, and nanostars resulted in hot electron generation from the structure. This was further confirmed with the help of theoretical calculations. As a result, platinum-covered gold nanostars were the most effective material for NADH regeneration. According to the authors, the branched structure was the best to harvest light, and this result was confirmed by the higher photocurrent values and the less scattered light obtained for this structure, as studied by the surface integral equation-method of moments formulation (SIE-MoM).

A combined stimulus of light and temperature was developed by Zhang et al., where near-infrared radiation induced the phase transition of a polymer that exhibits an upper critical solution temperature (UCST).[108] This polymer is composed of a nanohybrid embedding ultrasmall platinum NPs synthesized by borohydride reduction *in situ* on different enzymes, such as glucoamylase, proteinase K, and deoxyribonuclease I. The photothermal effect is able to cause a phase transition of the polymer and unblock the approach of macromolecular substrates to the enzymatic sites (Figure 5B). The enzymatic activities increased up to 61-fold upon laser irradiation. Interestingly, alternative approaches have been reported to indirectly harness the photothermal heating of metallic NPs upon light irradiation to trigger biocatalytic processes. As examples, Au nanocages covered by a thermoresponsive polymer were employed to encapsulate enzymes toward controlled release upon light irradiation.[109,110] The photothermal heating generated by the Au nanocages enabled the expansion or collapse of the thermoresponsive polymer for the controlled release of lysozyme to the media, where biocatalysis takes place.[109] Moreover, more complex systems can be designed by using two different laser sources. For example, different enzymes and their substrates were encapsulated in different Au nanocages that respond to specific LSPR signals.[110] In this way, the specific release of both enzyme and substrate for biocatalysis occurs by photothermal heating when the wavelength of the incident laser matches the LSPR of each Au nanocage. These systems are envisioned for biomedical applications for the release of specific enzymes at target areas of organisms to trigger selected biocatalytic transformations.

The creation of multiresponsive smart materials demands refined knowledge of all sets of external stimuli within their potentialities and limitations. The establishment of an assemblage of triggers in the same system is able to diversify the range of applications, enhance enzyme activity, and provide more tuned spatial-time control over the outcome effects of nanobiocatalysis.

CHALLENGES AND PERSPECTIVES

The union of the intrinsic properties of metallic NPs with enzymes provides a myriad of opportunities for the remote control of biocatalytic processes. The examples discussed in this review demonstrate how the control of specific properties of enzymes interfaced with metallic NPs has provided outstanding results for the development of innovative methods relevant across all facets of the biocatalysis field. As long as external stimuli can be precisely controlled at the nanoscale, more oriented and improved biocatalytic properties can be exploited. In this context, we envision that the use of metallic NPs enables a path forward for mimicking events triggered in nature through sophisticated responsive systems, which increases selectivity and expands their use in applications that require more precise control.

We herein addressed the more commonly used external stimuli via metallic NPs to date (light, electricity, magnetism, temperature, and the combination of different stimuli). However, undoubtedly, it will not take long for scientists to identify many other stimuli that have not yet been discussed. As a potential example, pH stimulus is harnessed through photoacid generators upon irradiation, by which free enzymes can be activated or deactivated by changing the pH of the solution.[14,111−113] Moreover, variations in pH have been demonstrated to impact the orientation of antibodies adsorbed onto Au NPs.[114] Presumably, in combination with metallic NPs, in particular plasmonic NPs, this environmental design may improve the transfer process of irradiation energy into the biocatalytic environment, leading to higher yields of laser-induced pH-jump processes. Additionally, further stimuli that promote a response directly on the selectivity for the accessibility of the substrate into the active site are envisioned for potential remote-controlled application via metallic NPs. We also predict more complex systems created by combining different enzymes on a more diverse range of metallic NP systems toward selective multistep and cascade reactions, in which each step can work independently by controlling the remote stimuli applied at different triggers, hence conferring high spatial-time control. In this regard, Claaßen et al. envisioned the development of methods to control orthogonally different free enzymes in multistep reactions,[14] which in fact can be extended to systems combined with metallic NPs to guide the required orthogonal control. Finally, technological advances toward engineering enzymes to design very specific characteristics are a step forward for remote-controlled biocatalysts.[115] Along with all of these examples, effective integration of computational simulations and experimental tools allows major breakthroughs in the area.

Biocatalysts in nature are fantastic: they operate exactly where and when they must act. The specific control of biocatalyst properties as well as self-controlled regulation have been a great desire for scientists. Understanding how to mimic biocatalytic processes in nature may be helpful to combat diseases or to improve biocatalytic events in the areas of biomedicine,[83,85,104] biosensors,[34−37] industry,[30] and energy,[38−44] among many others. Over the past few years, major progress has been made to develop remote regulation of enzymes, and the use of metallic NPs certainly offers a great opportunity in this direction. Notwithstanding, it is evident

https://doi.org/10.1021/acs.bioconjchem.1c00515
Bioconjugate Chem. 2022, 33, 53−66

that much remains to be known about the events involved in this new field. As an example, mechanistic and kinetics studies of such events are still scarcely explored. Based on the recent studies reported in this review, we foresee that much more can be developed, which makes it a promising field that can continue to develop and innovate. Surely, we understand that the knowledge behind the development of the field will also depend on the advances of technological devices to assess these systems, such as techniques that allow identifying the origin and nature of the phenomena at the nanoscale, monitoring real-time evolution, and visualization of the events in 2D and 3D by high-resolution techniques, to name a few, along with workable systems to develop straightforward approaches.[116] We finally encourage researchers in the field to envision further discoveries, in which the limitations will be the imagination in the use of "invisible hands" to control enzyme properties on metallic NPs.

AUTHOR INFORMATION

Corresponding Author

Susana I. Córdoba de Torresi − *Instituto de Química, Universidade de São Paulo, São Paulo, SP 05508-000, Brazil;* orcid.org/0000-0003-3290-172X; Email: storresi@iq.usp.br

Authors

Rafael T. P. da Silva − *Instituto de Química, Universidade de São Paulo, São Paulo, SP 05508-000, Brazil;* orcid.org/0000-0002-1762-793X

Heloise Ribeiro de Barros − *Instituto de Química, Universidade de São Paulo, São Paulo, SP 05508-000, Brazil;* orcid.org/0000-0003-2700-7803

Daiana M. Furlan Sandrini − *Instituto de Química, Universidade de São Paulo, São Paulo, SP 05508-000, Brazil;* orcid.org/0000-0002-1844-5353

Complete contact information is available at: https://pubs.acs.org/10.1021/acs.bioconjchem.1c00515

Notes

The authors declare no competing financial interest.

ACKNOWLEDGMENTS

This work was supported by CNPq (#302173/2016-1) and the São Paulo Research Foundation FAPESP (grant nos. 2015/26308-7 and 2018/16219-5). R.T.P.d.S. was funded by a Ph.D. fellowship from CAPES (grant 88882.328241/2019-01). H.R.d.B. was funded by a postdoc fellowship from FAPESP (grant no. 2017/20892-4). D.M.F.S. was funded by a Ph.D. fellowship from CAPES (grant 8887.580710/2020-00).

ABBREVIATIONS

β-gal, *β*-galactosidase; AMF, alternating magnetic field; CALB, lipase from *Candida antarctica* fraction B; DET, direct electron transfer; EBFC, enzyme biofuel cell; EDC, 1-(3-dimethylamino- propyl)-3-ethylcarbodiimide; FAD, flavin adenine nucleotide; FDH, formate dehydrogenase; Glk, *Aeropyrum pernix* glucokinase; HRP, horseradish peroxidase; LCST, lower critical solution temperature; LDG, low-density graphite; LF MF, low-frequency magnetic field; LSPR, localized surface plasmon resonance; MET, mediated electron transfer; MOF, metal−organic framework; MWCNTs, multiwalled carbon nanotubes; NAD, nicotinamide adenine dinucleotide; NHS, *N*- hydroxysuccinimide; NIR, near-infrared; NPs, nanoparticles; NWs, nanowires; PEG, polyethylene glycol; pNIPAM, poly(*N*-isopropylacrylamide); PPase, pyrophosphatase; QCM-D, quartz crystal microbalance with dissipation; UCST, upper critical solution temperature; SIE-MoM, surface integral equation-method of moments formulation

REFERENCES

(1) Venditti, I.; Palocci, C.; Chronopoulou, L.; Fratoddi, I.; Fontana, L.; Diociaiuti, M.; Russo, M. V. Candida Rugosa Lipase Immobilization on Hydrophilic Charged Gold Nanoparticles as Promising Biocatalysts: Activity and Stability Investigations. *Colloids Surf., B* **2015**, *131*, 93−101.

(2) Cherian, E.; Dharmendirakumar, M.; Baskar, G. Immobilization of Cellulase onto MnO2 Nanoparticles for Bioethanol Production by Enhanced Hydrolysis of Agricultural Waste. *Cuihua Xuebao/Chin. J. Catal.* **2015**, *36* (8), 1223−1229.

(3) Orfanakis, G.; Patila, M.; Catzikonstantinou, A. V.; Lyra, K. M.; Kouloumpis, A.; Spyrou, K.; Katapodis, P.; Paipetis, A.; Rudolf, P.; Gournis, D.; et al. Hybrid Nanomaterials of Magnetic Iron Nanoparticles and Graphene Oxide as Matrices for the Immobilization of *β*-Glucosidase: Synthesis, Characterization, and Biocatalytic Properties. *Front. Mater.* **2018**, *5* (April), 1−11.

(4) Meryam Sardar, R. A. Enzyme Immobilization: An Overview on Nanoparticles as Immobilization Matrix. *Biochem. Anal. Biochem.* **2015**, *4* (2), 1000178.

(5) Das, R.; Talat, M.; Srivastava, O. N.; Kayastha, A. M. Covalent Immobilization of Peanut *β*-Amylase for Producing Industrial Nano-Biocatalysts: A Comparative Study of Kinetics, Stability and Reusability of the Immobilized Enzyme. *Food Chem.* **2018**, *245*, 488−499.

(6) Liu, F.; Cui, Y.; Wang, L.; Wang, H.; Yuan, Y.; Pan, J.; Chen, H.; Yuan, L. Temperature-Responsive Poly(N -Isopropylacrylamide) Modified Gold Nanoparticle-Protein Conjugates for Bioactivity Modulation. *ACS Appl. Mater. Interfaces* **2015**, *7* (21), 11547−11554.

(7) Reis, C.; Sousa, E.; Serpa, J.; Oliveira, R.; Oliveira, R.; Santos, J. DESIGN OF IMMOBILIZED ENZYME BIOCATALYSTS: DRAWBACKS AND OPPORTUNITIES. *Quim. Nova* **2019**, *X* (00), 1−16.

(8) Diyanat, S.; Homaei, A.; Mosaddegh, E. Immobilization of Penaeus Vannamei Protease on ZnO Nanoparticles for Long-Term Use. *Int. J. Biol. Macromol.* **2018**, *118*, 92−98.

(9) Liu, D. M.; Dong, C. Recent Advances in Nano-Carrier Immobilized Enzymes and Their Applications. *Process Biochem.* **2020**, *92*, 464−475.

(10) Długosz, O.; Matysik, J.; Matyjasik, W.; Banach, M. Catalytic and Antimicrobial Properties of *α*-Amylase Immobilised on the Surface of Metal Oxide Nanoparticles. *J. Cluster Sci.* **2021**, *32*, 1609.

(11) Grzelczak, M.; Liz-Marzán, L. M.; Klajn, R. Stimuli-Responsive Self-Assembly of Nanoparticles. *Chem. Soc. Rev.* **2019**, *48* (5), 1342−1361.

(12) Li, F.; Lu, J.; Kong, X.; Hyeon, T.; Ling, D. Dynamic Nanoparticle Assemblies for Biomedical Applications. *Adv. Mater.* **2017**, *29* (14), 1605897.

(13) Özgen, F. F.; Runda, M. E.; Schmidt, S. Photo-Biocatalytic Cascades: Combining Chemical and Enzymatic Transformations Fueled by Light. *ChemBioChem* **2021**, *22* (5), 790−806.

(14) Claaßen, C.; Gerlach, T.; Rother, D. Stimulus-Responsive Regulation of Enzyme Activity for One-Step and Multi-Step Syntheses. *Adv. Synth. Catal.* **2019**, *361* (11), 2387−2401.

(15) Schmermund, L.; Jurkaš, V.; Özgen, F. F.; Barone, G. D.; Büchsenschütz, H. C.; Winkler, C. K.; Schmidt, S.; Kourist, R.; Kroutil, W. Photo-Biocatalysis: Biotransformations in the Presence of Light. *ACS Catal.* **2019**, *9* (5), 4115−4144.

(16) de Barros, H. R.; López-Gallego, F.; Liz-Marzán, L. M. Light-Driven Catalytic Regulation of Enzymes at the Interface with Plasmonic Nanomaterials. *Biochemistry* **2021**, *60* (13), 991−998.

(17) Bretschneider, J. C.; Reismann, M.; Von Plessen, G.; Simon, U. Photothermal Control of the Activity of HRP-Functionalized Gold Nanoparticles. *Small* **2009**, *5* (22), 2549−2553.
(18) Stehr, J.; Hrelescu, C.; Sperling, R. A.; Raschke, G.; Wunderlich, M.; Nichtl, A.; Heindl, D.; Kürzinger, K.; Parak, W. J.; Klar, T. A.; et al. Gold NanoStoves for Microsecond DNA Melting Analysis. *Nano Lett.* **2008**, *8* (2), 619−623.
(19) Hecht, E. *Optics*, 5th ed.; Pearson Education Limited: Harlow, U.K., 2017.
(20) Su, J.; Chen, H.; Xu, Z.; Wang, S.; Liu, X.; Wang, L.; Huang, X. Near-Infrared-Induced Contractile Proteinosome Microreactor with a Fast Control on Enzymatic Reactions. *ACS Appl. Mater. Interfaces* **2020**, *12* (37), 41079−41087.
(21) Liz-Marzan, L. M. Nanometals Formation and Color. *Mater. Today* **2004**, *7* (2), 26−31.
(22) Liz-Marzán, L. M.; Murphy, C. J.; Wang, J. Nanoplasmonics. *Chem. Soc. Rev.* **2014**, *43* (11), 3820.
(23) Baffou, G.; Quidant, R. Nanoplasmonics for Chemistry. *Chem. Soc. Rev.* **2014**, *43* (11), 3898.
(24) Takeda, Y.; Kondow, T.; Mafuné, F. Degradation of Protein in Nanoplasma Generated around Gold Nanoparticles in Solution by Laser Irradiation. *J. Phys. Chem. B* **2006**, *110* (5), 2393−2397.
(25) Slocik, J. M.; Tam, F.; Halas, N. J.; Naik, R. R. Peptide-Assembled Optically Responsive Nanoparticle Complexes. *Nano Lett.* **2007**, *7* (4), 1054−1058.
(26) Guo, S.; Li, H.; Liu, J.; Yang, Y.; Kong, W.; Qiao, S.; Huang, H.; Liu, Y.; Kang, Z. Visible-Light-Induced Effects of Au Nanoparticle on Laccase Catalytic Activity. *ACS Appl. Mater. Interfaces* **2015**, *7* (37), 20937−20944.
(27) Blankschien, M. D.; Pretzer, L. A.; Huschka, R.; Halas, N. J.; Gonzalez, R.; Wong, M. S. Light-Triggered Biocatalysis Using Thermophilic Enzyme - Gold Nanoparticle Complexes. *ACS Nano* **2013**, *7* (1), 654−663.
(28) Tadepalli, S.; Yim, J.; Madireddi, K.; Luan, J.; Naik, R. R.; Singamaneni, S. Gold Nanorod-Mediated Photothermal Enhancement of the Biocatalytic Activity of a Polymer-Encapsulated Enzyme. *Chem. Mater.* **2017**, *29* (15), 6308−6314.
(29) Tadepalli, S.; Yim, J.; Cao, S.; Wang, Z.; Naik, R. R.; Singamaneni, S. Metal−Organic Framework Encapsulation for the Preservation and Photothermal Enhancement of Enzyme Activity. *Small* **2018**, *14* (7), 1702382.
(30) Li, W.; Liu, D.; Geng, X.; Li, Z.; Gao, R. Real-Time Regulation of Catalysis by Remote-Controlled Enzyme-Conjugated Gold Nanorod Composites for Aldol Reaction-Based Applications. *Catal. Sci. Technol.* **2019**, *9* (9), 2221−2230.
(31) De Barros, H. R.; García, I.; Kuttner, C.; Zeballos, N.; Camargo, P. H. C.; De Torresi, S. I. C.; López-Gallego, F.; Liz-Marzán, L. M. Mechanistic Insights into the Light-Driven Catalysis of an Immobilized Lipase on Plasmonic Nanomaterials. *ACS Catal.* **2021**, *11* (1), 414−423.
(32) Wang, X.; Ou, G.; Zhou, K.; Wang, X.; Wang, L.; Zhang, X.; Feng, Y.; Bai, Y.; Wu, H.; Xu, Z.; et al. Targeted Heating of Enzyme Systems Based on Photothermal Materials. *ChemBioChem* **2019**, *20* (19), 2467−2473.
(33) Reyes-De-Corcuera, J. I.; Olstad, H. E.; García-Torres, R. Stability and Stabilization of Enzyme Biosensors: The Key to Successful Application and Commercialization. *Annu. Rev. Food Sci. Technol.* **2018**, *9*, 293−322.
(34) Wu, L.; Lu, X.; Niu, K.; Dhanjai; Chen, J. Tyrosinase Nanocapsule Based Nano-Biosensor for Ultrasensitive and Rapid Detection of Bisphenol A with Excellent Stability in Different Application Scenarios. *Biosens. Bioelectron.* **2020**, *165*, 112407.
(35) Guerrieri, A.; Ciriello, R.; Bianco, G.; De Gennaro, F.; Frascaro, S. Allosteric Enzyme-Based Biosensors-Kinetic Behaviours of Immobilised L-Lysine-α-Oxidase from Trichoderma Viride: PH Influence and Allosteric Properties. *Biosensors* **2020**, *10* (10), 145.
(36) Thirumalai, D.; Kim, S.; Kim, S.; Chang, S. C. Reagentless Amperometric Pyruvate Biosensor Based on a Prussian Blue- And Enzyme Nanoparticle-Modified Screen-Printed Carbon Electrode. *ACS Omega* **2020**, *5* (46), 30123−30129.
(37) Smart, A.; Crew, A.; Doran, O.; Hart, J. P. Studies towards the Development of a Novel, Screen-Printed Carbon-Based, Biosensor for the Measurement of Polyunsaturated Fatty Acids. *Appl. Sci.* **2020**, *10* (21), 7779.
(38) Milton, R. D.; Cai, R.; Abdellaoui, S.; Leech, D.; De Lacey, A. L.; Pita, M.; Minteer, S. D. Bioelectrochemical Haber-Bosch Process: An Ammonia-Producing H 2 /N 2 Fuel Cell. *Angew. Chem.* **2017**, *129* (10), 2724−2727.
(39) El Ichi-Ribault, S.; Alcaraz, J. P.; Boucher, F.; Boutaud, B.; Dalmolin, R.; Boutonnat, J.; Cinquin, P.; Zebda, A.; Martin, D. K. Remote Wireless Control of an Enzymatic Biofuel Cell Implanted in a Rabbit for 2 Months. *Electrochim. Acta* **2018**, *269*, 360−366.
(40) Shitanda, I.; Takamatsu, K.; Niiyama, A.; Mikawa, T.; Hoshi, Y.; Itagaki, M.; Tsujimura, S. High-Power Lactate/O2 Enzymatic Biofuel Cell Based on Carbon Cloth Electrodes Modified with MgO-Templated Carbon. *J. Power Sources* **2019**, *436*, 226844.
(41) Sakai, K.; Kitazumi, Y.; Shirai, O.; Takagi, K.; Kano, K. High-Power Formate/Dioxygen Biofuel Cell Based on Mediated Electron Transfer Type Bioelectrocatalysis. *ACS Catal.* **2017**, *7* (9), 5668−5673.
(42) González-Arribas, E.; Aleksejeva, O.; Bobrowski, T.; Toscano, M. D.; Gorton, L.; Schuhmann, W.; Shleev, S. Solar Biosupercapacitor. *Electrochem. Commun.* **2017**, *74*, 9−13.
(43) Bobrowski, T.; González Arribas, E.; Ludwig, R.; Toscano, M. D.; Shleev, S.; Schuhmann, W. Rechargeable, Flexible and Mediator-Free Biosupercapacitor Based on Transparent ITO Nanoparticle Modified Electrodes Acting in MM Glucose Containing Buffers. *Biosens. Bioelectron.* **2018**, *101*, 84−89.
(44) Zhao, F.; Bobrowski, T.; Ruff, A.; Hartmann, V.; Nowaczyk, M. M.; Rögner, M.; Conzuelo, F.; Schuhmann, W. A Light-Driven Nernstian Biosupercapacitor. *Electrochim. Acta* **2019**, *306*, 660−666.
(45) Giroud, F.; Sawada, K.; Taya, M.; Cosnier, S. 5,5-Dithiobis(2-Nitrobenzoic Acid) Pyrene Derivative-Carbon Nanotube Electrodes for NADH Electrooxidation and Oriented Immobilization of Multicopper Oxidases for the Development of Glucose/O2 Biofuel Cells. *Biosens. Bioelectron.* **2017**, *87*, 957−963.
(46) Shiraiwa, S.; So, K.; Sugimoto, Y.; Kitazumi, Y.; Shirai, O.; Nishikawa, K.; Higuchi, Y.; Kano, K. Reactivation of Standard [NiFe]-Hydrogenase and Bioelectrochemical Catalysis of Proton Reduction and Hydrogen Oxidation in a Mediated-Electron-Transfer System. *Bioelectrochemistry* **2018**, *123*, 156−161.
(47) Miyata, M.; Kitazumi, Y.; Shirai, O.; Kataoka, K.; Kano, K. Diffusion-Limited Biosensing of Dissolved Oxygen by Direct Electron Transfer-Type Bioelectrocatalysis of Multi-Copper Oxidases Immobilized on Porous Gold Microelectrodes. *J. Electroanal. Chem.* **2020**, *860*, 113895.
(48) Song, Y.; Chen, J.; Liu, H.; Song, Y.; Xu, F.; Tan, H.; Wang, L. Conformation, Bioactivity and Electrochemical Performance of Glucose Oxidase Immobilized on Surface of Gold Nanoparticles. *Electrochim. Acta* **2015**, *158*, 56−63.
(49) Popovtzer, R.; Neufeld, T.; Ron, E. z.; Rishpon, J.; Shacham-Diamand, Y. Electrochemical Detection of Biological Reactions Using a Novel Nano-Bio-Chip Array. *Sens. Actuators, B* **2006**, *119* (2), 664−672.
(50) Duan, H.; Cheng, Z.; Xue, Y.; Cui, Z.; Yang, M.; Wang, S. Influences of Nano-Effect on Electrochemical Thermodynamics of Metal Nanoparticles Electrodes. *J. Electroanal. Chem.* **2021**, *882*, 115037.
(51) Ronkainen, N. J.; Halsall, H. B.; Heineman, W. R. Electrochemical Biosensors. *Chem. Soc. Rev.* **2010**, *39* (5), 1747−1763.
(52) Monteiro, T.; Almeida, M. G. Electrochemical Enzyme Biosensors Revisited: Old Solutions for New Problems. *Crit. Rev. Anal. Chem.* **2019**, *49* (1), 44−66.
(53) Wang, L.; Wang, E. A Novel Hydrogen Peroxide Sensor Based on Horseradish Peroxidase Immobilized on Colloidal Au Modified ITO Electrode. *Electrochem. Commun.* **2004**, *6* (2), 225−229.

https://doi.org/10.1021/acs.bioconjchem.1c00515
Bioconjugate Chem. 2022, 33, 53−66

(54) Luz, R. A. S.; Crespilho, F. N. Gold Nanoparticle-Mediated Electron Transfer of Cytochrome c on a Self-Assembled Surface. *RSC Adv.* **2016**, *6* (67), 62585−62593.
(55) Gutiérrez-Sánchez, C.; Pita, M.; Vaz-Domínguez, C.; Shleev, S.; De Lacey, A. L. Gold Nanoparticles as Electronic Bridges for Laccase-Based Biocathodes. *J. Am. Chem. Soc.* **2012**, *134* (41), 17212−17220.
(56) Fapyane, D.; Ferapontova, E. E. Enhanced Electron Transfer between Gold Nanoparticles and Horseradish Peroxidase Reconstituted onto Alkanethiol-Modified Hemin. *Electrochem. Commun.* **2016**, *70*, 39−42.
(57) Zeng, T.; Frasca, S.; Rumschöttel, J.; Koetz, J.; Leimkühler, S.; Wollenberger, U. Role of Conductive Nanoparticles in the Direct Unmediated Bioelectrocatalysis of Immobilized Sulfite Oxidase. *Electroanalysis* **2016**, *28* (10), 2303−2310.
(58) Frasca, S.; Rojas, O.; Salewski, J.; Neumann, B.; Stiba, K.; Weidinger, I. M.; Tiersch, B.; Leimkühler, S.; Koetz, J.; Wollenberger, U. Human Sulfite Oxidase Electrochemistry on Gold Nanoparticles Modified Electrode. *Bioelectrochemistry* **2012**, *87*, 33−41.
(59) Monsalve, K.; Roger, M.; Gutierrez-Sanchez, C.; Ilbert, M.; Nitsche, S.; Byrne-Kodjabachian, D.; Marchi, V.; Lojou, E. Hydrogen Bioelectrooxidation on Gold Nanoparticle-Based Electrodes Modified by Aquifex Aeolicus Hydrogenase: Application to Hydrogen/Oxygen Enzymatic Biofuel Cells. *Bioelectrochemistry* **2015**, *106*, 47−55.
(60) Wang, H.; Johs, A.; Browning, J. F.; Tennant, D. A.; Liang, L. Electrochemical Properties of the Interaction between Cytochrome c and a Hematite Nanowire Array Electrode. *Bioelectrochemistry* **2019**, *129*, 162−169.
(61) Adachi, T.; Kitazumi, Y.; Shirai, O.; Kano, K. Recent Progress in Applications of Enzymatic Bioelectrocatalysis. *Catalysts* **2020**, *10* (12), 1413.
(62) Pereira, A. R.; Sedenho, G. C.; de Souza, J. C. P.; Crespilho, F. N. Advances in Enzyme Bioelectrochemistry. *An. Acad. Bras. Cienc.* **2018**, *90* (1), 825−857.
(63) Liu, Y.; Atanassov, P. Charge Transfer at Biotic/Abiotic Interfaces in Biological Electrocatalysis. *Curr. Opin. Electrochem.* **2020**, *19*, 175−183.
(64) Betancor, L.; Johnson, G. R.; Luckarift, H. R. Stabilized Laccases as Heterogeneous Bioelectrocatalysts. *ChemCatChem* **2013**, *5* (1), 46−60.
(65) Zhang, M.; Mullens, C.; Gorski, W. Coimmobilization of Dehydrogenases and Their Cofactors in Electrochemical Biosensors. *Anal. Chem.* **2007**, *79* (6), 2446−2450.
(66) Song, H.; Ma, C.; Liu, P.; You, C.; Lin, J.; Zhu, Z. A Hybrid CO2 Electroreduction System Mediated by Enzyme-Cofactor Conjugates Coupled with Cu Nanoparticle-Catalyzed Cofactor Regeneration. *J. CO2 Util.* **2019**, *34* (July), 568−575.
(67) Arana-Peña, S.; Carballares, D.; Morellon-Sterlling, R.; Berenguer-Murcia, Á.; Alcántara, A. R.; Rodrigues, R. C.; Fernandez-Lafuente, R. Enzyme Co-Immobilization: Always the Biocatalyst Designers' Choice···or Not? *Biotechnol. Adv.* **2021**, *51*, 107584.
(68) Lee, S. H.; Ryu, G. M.; Nam, D. H.; Kim, J. H.; Park, C. B. Silicon Nanowire Photocathodes for Light-Driven Electroenzymatic Synthesis. *ChemSusChem* **2014**, *7* (11), 3007−3011.
(69) Ali, I.; Ullah, N.; McArthur, M. A.; Coulombe, S.; Omanovic, S. Direct Electrochemical Regeneration of Enzymatic Cofactor 1,4-NADH on a Cathode Composed of Multi-Walled Carbon Nanotubes Decorated with Nickel Nanoparticles. *Can. J. Chem. Eng.* **2018**, *96* (1), 68−73.
(70) Ali, I.; Gill, A.; Omanovic, S. Direct Electrochemical Regeneration of the Enzymatic Cofactor 1,4-NADH Employing Nano-Patterned Glassy Carbon/Pt and Glassy Carbon/Ni Electrodes. *Chem. Eng. J.* **2012**, *188*, 173−180.
(71) Mazurenko, I.; Hitaishi, V. P.; Lojou, E. Recent Advances in Surface Chemistry of Electrodes to Promote Direct Enzymatic Bioelectrocatalysis. *Curr. Opin. Electrochem.* **2020**, *19*, 113−121.
(72) Kornienko, N.; Ly, K. H.; Robinson, W. E.; Heidary, N.; Zhang, J. Z.; Reisner, E. Advancing Techniques for Investigating the Enzyme−Electrode Interface. *Acc. Chem. Res.* **2019**, *52* (5), 1439−1448.
(73) Jensen, U. B.; Ferapontova, E. E.; Sutherland, D. S. Quantifying Protein Adsorption and Function at Nanostructured Materials: Enzymatic Activity of Glucose Oxidase at GLAD Structured Electrodes. *Langmuir* **2012**, *28* (30), 11106−11114.
(74) Khoa Ly, H.; Sezer, M.; Wisitruangsakul, N.; Feng, J. J.; Kranich, A.; Millo, D.; Weidinger, I. M.; Zebger, I.; Murgida, D. H.; Hildebrandt, P. Surface-Enhanced Vibrational Spectroscopy for Probing Transient Interactions of Proteins with Biomimetic Interfaces: Electric Field Effects on Structure, Dynamics and Function of Cytochrome C. *FEBS J.* **2011**, *278* (9), 1382−1390.
(75) Robinson, P. K. Enzymes: Principles and Biotechnological Applications. *Essays Biochem.* **2015**, *59*, 1−41.
(76) Muley, A. B.; Mulchandani, K. H.; Singhal, R. S. *Immobilization of Enzymes on Iron Oxide Magnetic Nanoparticles: Synthesis, Characterization, Kinetics and Thermodynamics*, 1st ed.; Elsevier Inc.: 2020; Vol. *630*, DOI: 10.1016/bs.mie.2019.10.016.
(77) Mody, V. V.; Singh, A.; Wesley, B. Basics of Magnetic Nanoparticles for Their Application in the Field of Magnetic Fluid Hyperthermia. *Eur. J. Nanomed.* **2013**, *5* (1), 11−21.
(78) Zhu, N.; Ji, H.; Yu, P.; Niu, J.; Farooq, M. U.; Akram, M. W.; Udego, I. O.; Li, H.; Niu, X. Surface Modification of Magnetic Iron Oxide Nanoparticles. *Nanomaterials* **2018**, *8* (10), 810.
(79) Zheng, M.; Zhang, S.; Ma, G.; Wang, P. Effect of Molecular Mobility on Coupled Enzymatic Reactions Involving Cofactor Regeneration Using Nanoparticle-Attached Enzymes. *J. Biotechnol.* **2011**, *154* (4), 274−280.
(80) Zheng, M.; Su, Z.; Ji, X.; Ma, G.; Wang, P.; Zhang, S. Magnetic Field Intensified Bi-Enzyme System with in Situ Cofactor Regeneration Supported by Magnetic Nanoparticles. *J. Biotechnol.* **2013**, *168* (2), 212−217.
(81) Mizuki, T.; Watanabe, N.; Nagaoka, Y.; Fukushima, T.; Morimoto, H.; Usami, R.; Maekawa, T. Activity of an Enzyme Immobilized on Superparamagnetic Particles in a Rotational Magnetic Field. *Biochem. Biophys. Res. Commun.* **2010**, *393* (4), 779−782.
(82) Xiong, R.; Zhang, W.; Zhang, Y.; Zhang, Y.; Chen, Y.; He, Y.; Fan, H. Remote and Real Time Control of an FVIO-Enzyme Hybrid Nanocatalyst Using Magnetic Stimulation. *Nanoscale* **2019**, *11* (39), 18081−18089.
(83) Suzuki, M.; Hayashi, H.; Mizuki, T.; Maekawa, T.; Morimoto, H. Efficient DNA Ligation by Selective Heating of DNA Ligase with a Radio Frequency Alternating Magnetic Field. *Biochem. Biophys. Reports* **2016**, *8* (July), 360−364.
(84) Suzuki, M.; Aki, A.; Mizuki, T.; Maekawa, T.; Usami, R.; Morimoto, H. Encouragement of Enzyme Reaction Utilizing Heat Generation from Ferromagnetic Particles Subjected to an AC Magnetic Field. *PLoS One* **2015**, *10* (5), e0127673.
(85) Armenia, I.; Grazú Bonavia, M. V.; De Matteis, L.; Ivanchenko, P.; Martra, G.; Gornati, R.; de la Fuente, J. M.; Bernardini, G. Enzyme Activation by Alternating Magnetic Field: Importance of the Bioconjugation Methodology. *J. Colloid Interface Sci.* **2019**, *537*, 615−628.
(86) Lavorato, G. C.; Das, R.; Alonso Masa, J.; Phan, M. H.; Srikanth, H. Hybrid Magnetic Nanoparticles as Efficient Nanoheaters in Biomedical Applications. *Nanoscale Adv.* **2021**, *3* (4), 867−888.
(87) Morales, I.; Archilla, D.; de la Presa, P.; Hernando, A.; Marin, P. Colossal Heating Efficiency via Eddy Currents in Amorphous Microwires with Nearly Zero Magnetostriction. *Sci. Rep.* **2020**, *10* (1), 1−14.
(88) Figuerola, A.; Di Corato, R.; Manna, L.; Pellegrino, T. From Iron Oxide Nanoparticles towards Advanced Iron-Based Inorganic Materials Designed for Biomedical Applications. *Pharmacol. Res.* **2010**, *62* (2), 126−143.
(89) Klyachko, N. L.; Sokolsky-Papkov, M.; Pothayee, N.; Efremova, M. V.; Gulin, D. A.; Pothayee, N.; Kuznetsov, A. A.; Majouga, A. G.; Riffle, J. S.; Golovin, Y. I.; et al. Changing the Enzyme Reaction Rate in Magnetic Nanosuspensions by a Non-Heating Magnetic Field. *Angew. Chem., Int. Ed.* **2012**, *51* (48), 12016−12019.

(90) Golovin, Y. I.; Gribanovskii, S. L.; Golovin, D. Y.; Klyachko, N. L.; Kabanov, A. V. Single-Domain Magnetic Nanoparticles in an Alternating Magnetic Field as Mediators of Local Deformation of the Surrounding Macromolecules. *Phys. Solid State* **2014**, *56* (7), 1342−1351.
(91) Majouga, A.; Sokolsky-Papkov, M.; Kuznetsov, A.; Lebedev, D.; Efremova, M.; Beloglazkina, E.; Rudakovskaya, P.; Veselov, M.; Zyk, N.; Golovin, Y.; Klyachko, N.; Kabanov, A. Enzyme-Functionalized Gold-Coated Magnetite Nanoparticles as Novel Hybrid Nanomaterials: Synthesis, Purification and Control of Enzyme Function by Low-Frequency Magnetic Field. *Colloids Surf., B* **2015**, *125*, 104−109.
(92) Efremova, M. V.; Veselov, M. M.; Barulin, A. V.; Gribanovsky, S. L.; Le-Deygen, I. M.; Uporov, I. V.; Kudryashova, E. V.; Sokolsky-Papkov, M.; Majouga, A. G.; Golovin, Y. I.; et al. In Situ Observation of Chymotrypsin Catalytic Activity Change Actuated by Nonheating Low-Frequency Magnetic Field. *ACS Nano* **2018**, *12* (4), 3190−3199.
(93) Vlasova, K. Y.; Vishwasrao, H.; Abakumov, M. A.; Golovin, D. Y.; Gribanovsky, S. L.; Zhigachev, A. O.; Poloznikov, A.; Majouga, A. G.; Golovin, Y. I.; Sokolsky-Papkov, M.; et al. Enzyme Release from Polyion Complex by Extremely Low Frequency Magnetic Field. *Sci. Rep.* **2020**, *10* (1), 1−9.
(94) Guo, Q.; He, Y.; Lu, H. P. Interrogating the Activities of Conformational Deformed Enzyme by Single-Molecule Fluorescence-magnetic Tweezers Microscopy. *Proc. Natl. Acad. Sci. U. S. A.* **2015**, *112* (45), 13904−13909.
(95) Christiansen, M. G.; Howe, C. M.; Bono, D. C.; Perreault, D. J.; Anikeeva, P. Practical Methods for Generating Alternating Magnetic Fields for Biomedical Research. *Rev. Sci. Instrum.* **2017**, *88* (8), 084301.
(96) Nagase, K.; Yamato, M.; Kanazawa, H.; Okano, T. Poly(N-Isopropylacrylamide)-Based Thermoresponsive Surfaces Provide New Types of Biomedical Applications. *Biomaterials* **2018**, *153*, 27−48.
(97) Jochum, F. D.; Theato, P. Temperature- and Light-Responsive Smart Polymer Materials. *Chem. Soc. Rev.* **2013**, *42* (17), 7468−7483.
(98) Doberenz, F.; Zeng, K.; Willems, C.; Zhang, K.; Groth, T. Thermoresponsive Polymers and Their Biomedical Application in Tissue Engineering-A Review. *J. Mater. Chem. B* **2020**, *8* (4), 607−628.
(99) Cao, Y.; Wang, Y. Temperature-Mediated Regulation of Enzymatic Activity. *ChemCatChem* **2016**, *8* (17), 2740−2747.
(100) Prawatborisut, M.; Jiang, S.; Oberländer, J.; Mailänder, V.; Crespy, D.; Landfester, K. Modulating Protein Corona and Materials−Cell Interactions with Temperature-Responsive Materials. *Adv. Funct. Mater.* **2021**, *2106353*, 2106353.
(101) Shakya, A. K.; Nandakumar, K. S. An Update on Smart Biocatalysts for Industrial and Biomedical Applications. *J. R. Soc., Interface* **2018**, *15* (139), 20180062.
(102) Zhang, K.; Zhu, X.; Jia, F.; Auyeung, E.; Mirkin, C. A. Temperature-Activated Nucleic Acid Nanostructures. *J. Am. Chem. Soc.* **2013**, *135* (38), 14102−14105.
(103) Yu, J.; Yang, L.; Liang, X.; Dong, T.; Qu, H.; Rong, M.; Liu, H. Aptamer and PNIPAAm Co-Conjugated Nanoparticles Regulate Activity of Enzyme with Different Temperature. *Talanta* **2016**, *159*, 47−54.
(104) Sun, H.; Zhang, Q.; Li, J.; Peng, S.; Wang, X.; Cai, R. Near-Infrared Photoactivated Nanomedicines for Photothermal Synergistic Cancer Therapy. *Nano Today* **2021**, *37*, 101073.
(105) Knecht, L. D.; Ali, N.; Wei, Y.; Hilt, J. Z.; Daunert, S. Nanoparticle-Mediated Remote Control of Enzymatic Activity. *ACS Nano* **2012**, *6* (10), 9079−9086.
(106) Chen, Y.; Gai, P.; Xue, J.; Zhang, J. R.; Zhu, J. J. An″ON-OFF″ Switchable Power Output of Enzymatic Biofuel Cell Controlled by Thermal-Sensitive Polymer. *Biosens. Bioelectron.* **2015**, *74*, 142−149.
(107) Sánchez-Iglesias, A.; Barroso, J.; Solís, D. M.; Taboada, J. M.; Obelleiro, F.; Pavlov, V.; Chuvilin, A.; Grzelczak, M. Plasmonic Substrates Comprising Gold Nanostars Efficiently Regenerate Cofactor Molecules. *J. Mater. Chem. A* **2016**, *4* (18), 7045−7052.
(108) Zhang, S.; Wang, C.; Chang, H.; Zhang, Q.; Cheng, Y. Off-on Switching of Enzyme Activity by near-Infrared Light-Induced Photothermal Phase Transition of Nanohybrids. *Sci. Adv.* **2019**, *5* (8), 1−10.
(109) Yavuz, M. S.; Cheng, Y.; Chen, J.; Cobley, C. M.; Zhang, Q.; Rycenga, M.; Xie, J.; Kim, C.; Song, K. H.; Schwartz, A. G.; et al. Gold Nanocages Covered by Smart Polymers for Controlled Release with Near-Infrared Light. *Nat. Mater.* **2009**, *8* (12), 935−939.
(110) Shi, P.; Ju, E.; Ren, J.; Qu, X. Near-Infrared Light-Encoded Orthogonally Triggered and Logical Intracellular Release Using Gold Nanocage@smart Polymer Shell. *Adv. Funct. Mater.* **2014**, *24* (6), 826−834.
(111) Kohse, S.; Neubauer, A.; Pazidis, A.; Lochbrunner, S.; Kragl, U. Photoswitching of Enzyme Activity by Laser-Induced PH-Jump. *J. Am. Chem. Soc.* **2013**, *135* (25), 9407−9411.
(112) Kohse, S.; Neubauer, A.; Lochbrunner, S.; Kragl, U. Improving the Time Resolution for Remote Control of Enzyme Activity by a Nanosecond Laser-Induced PH Jump. *ChemCatChem* **2014**, *6* (12), 3511−3517.
(113) Martin, C. J.; Rapenne, G.; Nakashima, T.; Kawai, T. Recent Progress in Development of Photoacid Generators. *J. Photochem. Photobiol., C* **2018**, *34*, 41−51.
(114) Ruiz, G.; Tripathi, K.; Okyem, S.; Driskell, J. D. PH Impacts the Orientation of Antibody Adsorbed onto Gold Nanoparticles. *Bioconjugate Chem.* **2019**, *30* (4), 1182−1191.
(115) Agarwal, P. K.; Schultz, C.; Kalivretenos, A.; Ghosh, B.; Broedel, S. E. Engineering a Hyper-Catalytic Enzyme by Photo-activated Conformation Modulation. *J. Phys. Chem. Lett.* **2012**, *3* (9), 1142−1146.
(116) Fabris, L. Gold Nanostars in Biology and Medicine: Understanding Physicochemical Properties to Broaden Applicability. *J. Phys. Chem. C* **2020**, *124*, 26540.

Recommended by ACS

Metal–Organic Framework Derived Nanozymes in Biomedicine
Dongdong Wang, Yanli Zhao, *et al.*
JUNE 29, 2020
ACCOUNTS OF CHEMICAL RESEARCH
READ

Perspectives for Single-Atom Nanozymes: Advanced Synthesis, Functional Mechanisms, and Biomedical Applications
Lihua Shen, Jiujun Zhang, *et al.*
DECEMBER 28, 2020
ANALYTICAL CHEMISTRY
READ

Gold Nanoparticle Templating Increases the Catalytic Rate of an Amylase, Maltase, and Glucokinase Multienzyme Cascade through Substrate Channeling...
Sebastián A. Díaz, Igor L. Medintz, *et al.*
DECEMBER 29, 2020
ACS CATALYSIS
READ

Nanozymes Inspired by Natural Enzymes
Ruofei Zhang, Kelong Fan, *et al.*
JUNE 24, 2021
ACCOUNTS OF MATERIALS RESEARCH
READ

Get More Suggestions >

https://doi.org/10.1021/acs.bioconjchem.1c00515
Bioconjugate Chem. 2022, 33, 53−66

3.2.2 Physicochemical insights into the LSPR-driven Enzymatic Activity of Lipase Adsorbed on Gold Nanoparticles (Attachment 5)

Author Contribution: The author participated in the data curation, managed the project, and writing the paper.

In the last years, the benefits of enzyme immobilization on nanoparticles have been extensively studied[33]. The most established systems of immobilization are the ones with lipase from *Candida sp.* (CALB), which is a widely known and robust model in studies of organic and polymeric synthesis[34]. Recently, thermal stability and catalytic activity of lipase from *Candida sp.* (CALB) supported on plasmonic NPs was evaluated in nanobioconjugates designed with AuNP[35–37].

This part of the work is a deepened perspective on the LSPR stimulus on CALB@AuNP nanohybrid. Biocatalytic data show that conversion yields of p-nitrophenyl palmitate (pNPP) hydrolysis to p-nitrophenol (pNP) are approximately doubled upon LSPR stimulus. Thermal Camera shows that the solution temperature upon AuNP LSPR stimulus (533 nm) is increased by 30 °C, whereas LSPR non-matching stimulus (808 nm) reached a 10 °C increase, which may indicate an important thermodynamical change of the catalytic activity derived from local heat generation of LSPR. Circular Dichroism (CD) and Raman investigations on the secondary structure of CALB are performed upon immobilization, changes in external temperature, and light stimulus. All three events result in significant changes in α-helix conformations, the main domain associated with protein folding. In addition, Raman modes show the importance of N-terminal groups of amino acids in general and phenylalanine (Phe) residues in the interaction between CALB and

AuNP on the nanobioconjugate, which are considerably changed over either immobilization or external stimuli. Molecular Dynamics (MD) data show that, upon temperature changes, the unfolding of CALB presents a significant exposition of the catalytic triad Ser105-Asp187-His224, which suggests one of the main mechanisms of LSPR-driven biocatalysis of CALB@AuNP. This work is a look through the complex interactions between nanomaterials and biomolecules, advocating that every system is particular on its effects upon LSPR-driven nanobiocatalysis.

RESEARCH ARTICLE

Physicochemical insights into the LSPR-driven Enzymatic Activity of Lipase Adsorbed on Gold Nanoparticles

Rafael T. P. da Silva, [a] Heloise R. de Barros, [a,b] Rafaella F. Fernandes,[a] Jhoan Toro-Mendoza,[b] Ivan Colluzza,[c,d] Marcia L. A. Temperini[a], and Susana Inés C. de Torresi*[a]

[a] R.T.P. da Silva, Dr. H. R. de Barros, Dr. R. F. Fernandes, Prof. Dr. M. L. A. Temperini and Prof. Dr. S. I. C.ordoba de Torresi
Instituto de Química
Universidade de São Paulo
Av. Prof. Lineu Prestes, 748, 05508-000, São Paulo-SP, Brasil
E-mail: storresi@iq.usp.br
[b] Dr. H. R. de Barros, Dr. J. Toro-Mendoza
CIC biomaGUNE and CIBER-BBN
Paseo de Miramón 182, 2014 Donostia – San Sebastián, Spain
[c] Dr Ivan Coluzza
Fundacion BCMaterials
Edif. Martina Casiano, Pl. 3
Parque Científico UPV/EHU
Barrio Sarriena s/n
E-48940 Leioa (SPAIN)
[d] Dr. Ivan Coluzza
Ikerbasque, Basque Foundation for Science, Plaza de Euskadi 5, Bilbao, 48009, Spain

Supporting information for this article is given via a link at the end of the document.

Abstract: The interaction of metallic nanoparticles (NP) with electromagnetic fields via localized surface plasmon resonance (LSPR) has been extensively explored to improve inorganic catalysis. However, the biocatalytic reactions upon light stimulus are still poorly understood due to the high complexity involving the interrelation of light, enzymes, and nanoparticles. In the present work, we combined the valuable outputs from circular dichroism (CD), Raman spectroscopy, and Molecular Dynamics simulations (MD) to elucidate some of the biocatalytic outcomes of LSPR-driven hydrolysis of 4-nitrophenyl palmitate (pNPP) by lipase from *Candida antarctica* (CALB) supported on gold nanoparticles (AuNP). CD and Raman results indicate crucial transformations on CALB secondary structure possibly induced by local heat generated by LSPR excitation, whereas MD indicates the exposition and stability of the catalytic triad Ser105-Asp187-His224 upon local heat and adsorption on the NP and, thus, higher catalytic yields are to be achieved. This study reveals valuable insights toward understanding the physicochemical transformations in nanobioplasmonic catalysis.

Introduction

Nanocatalysts with improved performance driven by localized surface plasmon resonance (LSPR) have been explored mainly for inorganic reactions within the last few years.[1,2] On the other hand, nanobioplasmonics is a thriving emerging topic in this field that couples metallic nanoparticles and the LSPR outcomes to enhance the performance of biocatalysts.[3–8] Responsive nanoplasmonic biocatalysts pave the way to regulate enzyme catalytic properties by non-invasive strategies.[9]

Despite the growing number of publications with studies concerning the mechanisms involved in inorganic reactions, the nano-bio interfacial effects upon LSPR excitation add complexity to the system and, thus, are still poorly understood. Moreover, the understanding of interactions between biomolecules and nanoparticles at a molecular level is a hard challenge to be faced and imperative for the understanding of nanobiocatalysis.

This study opens up the possibility to explore this mechanism through the use of a model system of lipase from *Candida antarctica* fraction B (CALB) adsorbed on gold nanoparticles (AuNPs). Among the formation of hot carriers, near-field enhancement, and heat generation as the three main LSPR outcomes,[10] the use of a non-redox enzyme as a model system focuses on the influence of heat generation on the mechanism of biocatalytic improvement upon LSPR stimulus. Three complementary techniques, namely circular dichroism (CD), Raman spectroscopy, and Molecular Dynamics Simulations (MD) were used to probe and depict the mechanism of LSPR-driven hydrolysis of 4-nitrophenyl palmitate (pNPP) by CALB.

Results and Discussion

Characterization and Catalysis

AuNPs were synthesized by Turkevich's method and CALB was immobilized onto its surface via physisorption, as previously described[11], to provide close contact between the parties. This system, CALB@AuNP, is represented by the transmission electron microscopy (TEM) micrographs in **Figure 1A.** AuNPs were spherical with an average diameter of 13 ± 2 nm. A thin layer of 1-2 nm coating AuNPs is apparent, suggesting the physisorbed CALB on the metallic surface of the nanoparticles.

Then, CALB@AuNP was used as a biocatalyst of 4-nitrophenyl palmitate (pNPP) hydrolysis to p-nitrophenol (pNP) upon irradiation of near-infrared (NIR) and green lasers at the same power density (1.4 W/cm²), and without any external irradiation by laser, a condition which we called 'dark' for comparison (**Figure 2**). The product formation was monitored by UV-Vis at 405 nm, indicating the formation of pNP.

Results of conversion in percentage for each case are represented in **Figure 1B**. In both cases, conversion upon laser irradiation showed improvements in comparison to the same reaction performed without any irradiation, which presented 11% yield to p-nitrophenol. Between the two systems with irradiation, the green laser (532 nm) achieved a slightly better conversion (20%) compared with NIR (18%). The approximate double the yield observed in the light-driven catalytic assays is attributed mainly to the heat generated by the LSPR stimulus, which was assessed by a thermal camera.

On one hand, the infrared radiant heating source that did not match AuNP LSPR (808 nm, NIR laser) resulted from a ΔT of 10 °C upon irradiation according to the thermal camera data recorded on a cuvette (**Figure 1C**). On the other hand, the laser matching the maximum LSPR band (532 nm, green laser, **Figure S1**) of AuNPs exhibited a heating ΔT of 30 °C, which indicates the heat generation driven by LSPR stimulus.

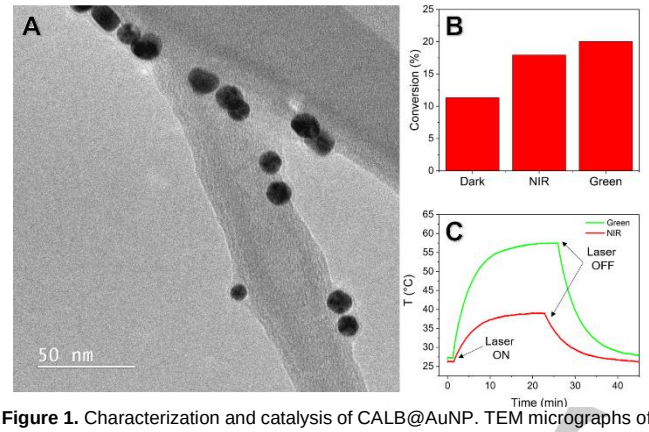


Figure 1. Characterization and catalysis of CALB@AuNP. TEM micrographs of CALB@AuNP (A). Conversion of pNPP hydrolysis catalyzed by CALB@AuNP upon different LSPR stimuli (B). Thermal camera data of a cuvette of CALB@AuNP upon green and NIR laser radiations (C).

Although thermal camera analysis is only capable of assessing the environmental temperature of the solution, it is a good indication that 532 nm as a LSPR-matching excitation wavelength is producing a local heat in the surroundings of AuNP.[12]

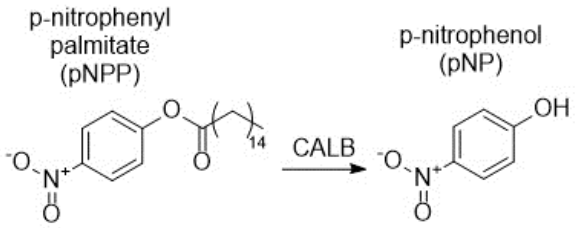


Figure 2. Scheme of hydrolysis reaction of p-nitrophenyl palmitate (pNPP) catalyzed by CALB.

Raman Spectroscopy

Deciphering the changes in the interactions at the molecular level is a challenge, in particular involving biomolecules and metallic subjects in the same system. However, a deep understanding of these interactions is imperative to the comprehension of catalytic outcomes of supported CALB and the effects promoted by LSPR in the CALB@AuNP system. With this goal, Raman spectroscopy was applied to evaluate the changes in the vibrational bands of amino acids since they provide valuable information about the conformational rearrangements of peptides and proteins.[13,14]

In general, the Raman fingerprints in the 1800-800 cm^{-1} spectral region correspond to the amide I band (~1650 cm^{-1}), amide II (~1550 cm^{-1}), amide III (α-helix, ~1320 cm^{-1}), and amide III (β-sheet, ~1240 cm^{-1}). Furthermore, other vibrational bands at 940 and 960 cm^{-1} can also be assigned to the α-helix conformation.[15]

First, we compared the spectra of free CALB to CALB@AuNP under dark conditions (**Figure 3**). Previous studies show that the secondary structure of peptides adsorbed on nanoparticles is liable to major transformations due to their high surface curvature.[16] The differences in the signals' profile at 1647-1642 cm^{-1} and 1360-1318 cm^{-1} show the main changes occurring for the amide I and amide III vibrational modes, respectively. In this regard, essential information about modifications in the secondary conformational structure of the enzymes can be provided,[17] primarily due to the signal at 1242 cm^{-1} suggesting β-sheet structure features[18] induced by the AuNPs presence.

The displacement or enlargement of both vibrational modes can indicate the adsorption of AuNPs via interactions involving these groups. Specifically, the changes from a sharp Raman band at 1647 cm^{-1} to a weaker signal at 1642 cm^{-1} and broad signals in the 1629-1512 cm^{-1} can indicate changes in the inherent secondary structure of CALB also associated with a molecular reorientation[19].

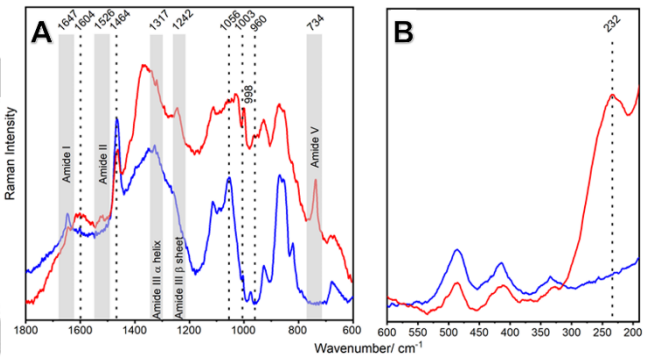


Figure 3. Raman spectra of CALB upon adsorption onto AuNPs. Free CALB (blue) and CALB@AuNP (red) in the wavenumber regions of 1800-600 cm^{-1} (A), and 600-200 cm^{-1} (B).

Notably, the Raman bands at 1604 and 1526 cm^{-1} are intrinsic for all spectra obtained in the presence of the AuNPs. The Raman signal at 1604 cm^{-1} is commonly assigned to the Tyr and Phe amino acid residues,[20] whereas the band at 1526 cm^{-1} can be assigned to the amide II vibrational mode of amino acid residues.[21] The amide II mode is primarily related to ν(CN), δ(NH), and ν(CC) vibrational modes, which are very weak in non-resonance Raman spectra being nearly undetectable.[22] Furthermore, the signal at 1465 cm^{-1} assigned to the $\delta(CH_2)$ mode was maintained in both spectra.

The assignment of the amide III vibrational mode is complex since NH bend contributes to several modes in the 1200–1400 cm^{-1} region. However, the spectral range of vibrational frequencies noticed for the secondary structures can be more evident than that for amide I and amide II. In this sense, the Raman band at 1242 cm^{-1} was assigned to the β-sheet structure,[18] which is observed well separated from the amide III modes corresponding to α-helix conformation at 1317 and 960 cm^{-1}.[18]

It is worth mentioning that the strong-intensity band observed at 1056 cm^{-1} in the CALB@AuNPs spectrum can be due to the

$\tau(NH_3^+)$ + $\varpi(CH_2)$ coupled mode, commonly observed in the Raman spectrum of Phe- adsorbed on AuNPs.[23]

The Raman band at 1003 cm^{-1} was shifted to 998 cm^{-1} for the CALB@AuNPs spectrum, indicating that the Phe residues can play a vital role in the interaction with AuNPs since the ring mode around 1002-1005 cm^{-1} is a very characteristic Raman band of phenylalanine.[21]

The spectral region below 800 cm^{-1} may be a spectral feature alternatively assigned to the amide V vibrations, –COOH group deformation as well as to the $\rho(CH_3)$ mode. Regarding this, the Raman spectrum of CALB@AuNPs reveals a prominent band at 734 cm^{-1}, tentatively assigned to the δ(NH).[24]

Finally, the Raman band at 232 cm^{-1} is characteristic of metal-N stretching vibration, reinforcing the interaction upon N-termini groups of amino acids. This intrinsic signal has also been assigned to the peptide's adsorption on AuNPs.[25]

Therefore, the Raman analyses indicate that (i) the adsorption of AuNPs was oriented by N-terminal groups of the amino acids, and (ii) changes can occur related to the secondary structure of CALB upon adsorption/interaction with AuNPs before any light stimulus.

The effects of laser irradiation on the interactions between CALB and AuNPs were analyzed. To disentangle the effect of temperature over the sample, the temperature increase with a 532 nm 1.4 W/cm² laser after the exposition of 30 min over CALB@AuNP was determined *in situ* using a thermal camera. The found temperature of 55°C was externally applied by a thermostatic bath on the sample. Spectra of laser-irradiated and externally applied temperature samples of CALB@AuNP were obtained in comparison to CALB@AuNP before any treatment (**Figure 4**).

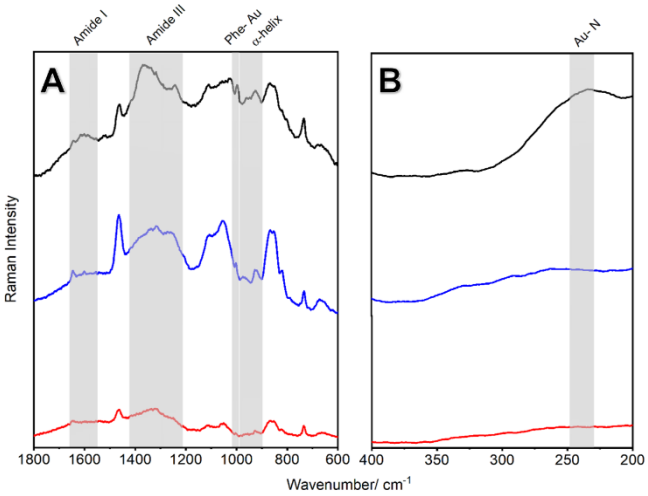


Figure 4. Raman spectra of CALB@AuNP as-prepared (black), after treatments of laser irradiation of 532 nm, 1.4 W/cm² for 30 minutes (blue) and external temperature of 55°C for 30 minutes (red), displayed in the1800-600 cm^{-1} (A) and 400-200 cm^{-1} (B) regions.

In general, the Raman intensity was significantly decreased over all the spectrum after temperature treatment. However, the regions attributed to amide I and amide III responded differently for each condition. These differences suggest conformational changes and interactions differently upon laser or temperature treatment. This result suggests that either LSPR outcomes may contribute through other mechanisms beyond temperature or that the local temperature at the AuNP surface is able to promote conformational changes uniquely.

The intrinsic signal at 998 cm^{-1} referring to Phe-Au interaction was kept with a slight shift upon temperature from 1002 cm^{-1} (after laser irradiation treatment) to 1003 cm^{-1} (use of external temperature).

Interestingly, significant conformational changes are detected in the secondary structure due to the vague α-helix vibrational attribution owing to the Raman bands at the region between 924-969 cm^{-1} referring to the vibrations of ν(C–C–N).

Finally, the Raman bands at the lower region of the spectrum referent to the Au surface were altered but not significantly differentiated upon laser and temperature conditions, which may suggest the preserved chemical environment on the NP surface after such treatments.

Then, we performed a few experiments at a temperature-controlled system by an external device to deeper understand the behavior of the CALB-Au surface interactions according to the temperature (**Figure 5**).

Notably, the temperature effect led to weaker modifications of the Raman spectra in free CALB (**Figure 5A**) in comparison to CALB@AuNPs (Erro! Fonte de referência não encontrada.**5B**).

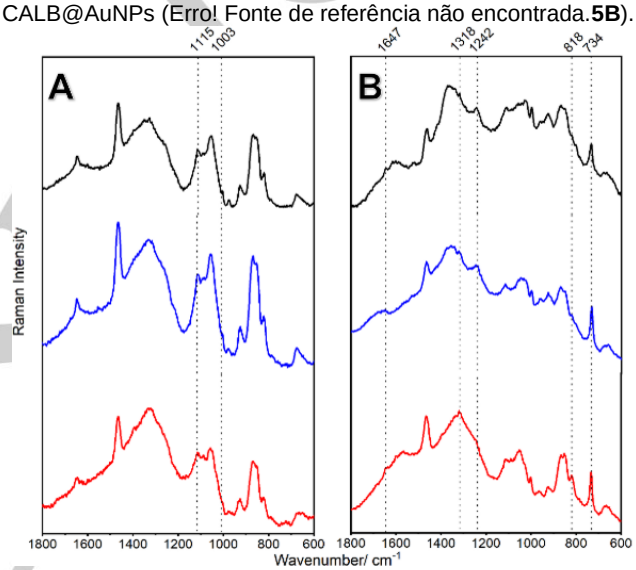


Figure 5. Raman spectra upon temperature changes. Free CALB (A) and CALB@AuNP (B) at 25°C (black), 55°C (blue), and 70°C (red).

The main changes related to CALB can be observed under 70 °C due to the absence of the Raman band at 1003 cm^{-1}. In addition, differences in the band intensities between 1115-1055 cm^{-1} are also observed.

The modification in the proportion between these two band intensities suggests conformation changes.[26] Our case indicates the structural transformation of CALB upon higher temperatures, which is a well-known behavior of enzymes in general due to denaturation.

Pronounced alterations in the Raman spectra profile were observed for the CALB@AuNPs at higher temperatures (Erro! Fonte de referência não encontrada.**5B**). These signals were broadened and unclear in the region attributed to amide I, notably at 55°C.

In the spectral region attributed to amide III (α-helix), the signal at 1318 cm^{-1} at 25°C was broadened and slightly shifted to a lower wavenumber upon higher temperatures. In contrast, the band at 1242 cm^{-1} has weakened upon higher temperatures suggesting critical changes in the secondary enzyme structure at 70 °C.

Conversely, the signal at 818 cm^{-1} becomes sharper and more defined toward higher temperatures, which can be assigned to the skeletal ν(CC) mode of amino acids.[18] The intrinsic signal for

CALB@AuNP at 734 cm^{-1} attributed to the amide V vibrational mode remained unchanged upon the analyzed temperatures.
Interestingly, the signals at the lower wavenumber region of Raman spectra attributed to stretching vibration of Au-N interaction (233 cm^{-1} at room temperature) were significantly displaced to higher wavenumbers as the temperature increased (263 and 295 cm^{-1} at 55 °C and 70 °C, respectively) (**Figure S2A and Figure S2B**).
This displacement can be attributed to the changes in the Au-N interaction stretching upon peptide's adsorption, from radial to orthogonal vibrational modes, confirming a conformation transition during adsorption at different temperatures. In contrast, no signals were evidenced in the same region for free CALB at any temperature condition analyzed.
The Raman spectroscopy could mainly identify the interaction sites of the amino acids that are closely related to the α-helix and β-sheet secondary structures. In sum, we described chemically some vital information about the interaction/adsorption of CALB onto AuNP, in which crucial modification at the secondary protein structures takes place.

Circular Dichroism

Circular dichroism (CD) was used to endorse the α-helix modifications of CALB toward temperature changes and laser incidence. Changes in the negative band at 222 nm, typically correlated to the α-helix signatures,[27] were monitored upon temperature control over time to evaluate and compare the thermal stability presented by free CALB and CALB@AuNP. **Figure 6A** shows the curves of %loss in ellipticity at 222 nm ($\theta_{222\ nm}$) for each sample. In this case, free CALB presents an inferior tolerance toward temperature changes in comparison to CALB@AuNP. This is evidenced by the more intense loss of α-helix by free CALB, in particular within the range of 50-60 °C, when denaturation occurs. Several previous studies reported an enhancement in thermal stability whenever enzymes were immobilized onto nanoparticles.[28]
In addition to Raman, which showed significant modifications in amide I and amide III (α-helix and β-sheet) modes upon CALB adsorption on AuNP and posterior thermal treatments, CD ramp temperatures indicate that the α-helix domains at CALB may be more preserved upon environmental changes whenever adsorbed onto AuNP.
The effect of the exposition to green and NIR laser source on the secondary structure changes in CALB@AuNP were evaluated by CD. To this end, CALB@AuNP was exposed for 20 minutes to each laser source at the same power density (1.4 W/cm²) (**Figure 6B**).

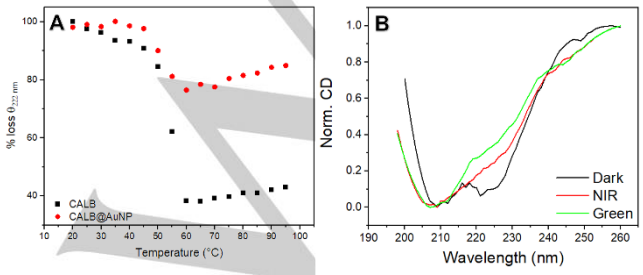


Figure 6. Circular dichroism characterization of CALB@AuNP. Response of 222 nm band in CD toward a temperature ramp for CALB (blue) and CALB@AuNP (red) (A) Spectra of CALB@AuNP (black) and CALB@AuNP after 1h of exposition to NIR (red) and green (green) lasers (1.4 W/cm²) (B).

Both conditions presented vast modifications in comparison to the CALB@AuNP sample before any laser treatment. The changes reflect the loss in the 222 nm band, mainly upon the external stimulus by the green laser source. NIR laser source achieved an intermediate loss. Interestingly, the change in conformation promoted by temperature changes represented by the loss of α-helix domains is similar to the one triggered by laser irradiation. Consequently, as the green laser corresponds to the LSPR of AuNP in the CALB@AuNP system, these findings corroborate the thermal camera results (**Figure 1C**) and point out to the influence of temperature increase driven by LSPR.

Molecular Dynamics Simulations (MD)

To unravel the unfolding determined by CD analyses for free CALB and CALB@AuNP upon temperature changes driven by LSPR stimulus, free CALB (PDB: 1TCA) in water at several temperatures were analyzed through coarse-grained molecular dynamics simulations using Large-scale Atomic/Molecular Massively Parallel Simulator (LAMMPS) and following a previously developed procedure to account for the electric and H-bond interactions between the NP and the adsorbing protein [31].
To quantify the enzymatic conformational changes in both free and adsorbed onto the AuNP conditions at different temperatures, we follow the evolution of the RMSD (root mean square displacement) and the radial distribution function of the overall structure of the enzyme. The catalytic triad formed by the residues Ser105-Asp187-His224 is also tracked during the time evolution to establish the conformation at which the activity decreases due to the separation of those residues for the denaturation of the enzyme.
The time evolution of free CALB and CALB@AuNP are presented in **Figure 7A** and **Figure 7B**, respectively. Temperatures below 4 (in LJ units) only slightly affect the whole structure of CALB in its free form and at CALB@AuNP. Temperatures above T=5 present higher shifts in RMSD, indicating denaturation independently of the presence of AuNP. Particularly at this temperature, CALB@AuNP showed a higher displacement in RMSD in comparison to free CALB. Although small, the fluctuations in the RMSD at T=4 suggest that the enzyme is close to the temperature of unfolding, reproducing the transition folded-unfolded at slightly lower temperatures observed experimentally for CALB@AUNP with CD in **Figure 6A**. The representation of CALB conformation at the surface of AuNP at different temperatures is represented in **Figure S3**. In that representation, it can be seen that while the enzyme is fully unfolded for T>5, the triad suggests a high stability and closeness to the NP.

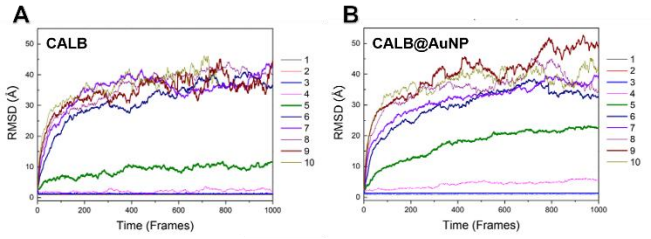


Figure 7. RMSD of CALB upon different temperatures. Free CALB (A), CALB@AuNP (B).

The denaturation tendency is reinforced by the data presented in **Figure S4**, which shows conformity between the coarse-grained simulation and the previously reported CD temperature curve at 222 nm (**Figure 6A**).[29] Although this set of data can only be indirectly compared, both CD temperature curve and RMSD tendencies exhibit a sigmoidal-type curve as a function of the temperature, indicating CALB structure stability at low temperatures and its denaturation toward higher temperatures. Noticeably, these calculations were performed by running ten different numerical experiments where different initial disposition of the enzyme were simulated in order to obtain an average final RMSD. Here, the standard deviations confirm that our estimations for single numerical experiments runs are adequate.

Interestingly, the catalytic moiety composed by the triad Ser105-Asp187-His224 of CALB is kept close to the NP at low temperatures, as demonstrated by the close to zero RMSD for T<6 in **Figure 8**.[30] However, from T=6 and above, RMSD presents higher displacements, which is an indication of conformation loss and separation among the residues within time. This result may be indicative of the triad subdomain being more stable than the rest of the structure of the enzyme. The distance among the triad residues in free CALB and CALB@AuNP are presented in **Figure 9**. Upon higher temperatures, a broader distribution of radial distance is observed up to the temperature where it is no longer possible to evaluate this distance due to denaturation because the residues are too far apart from one another.

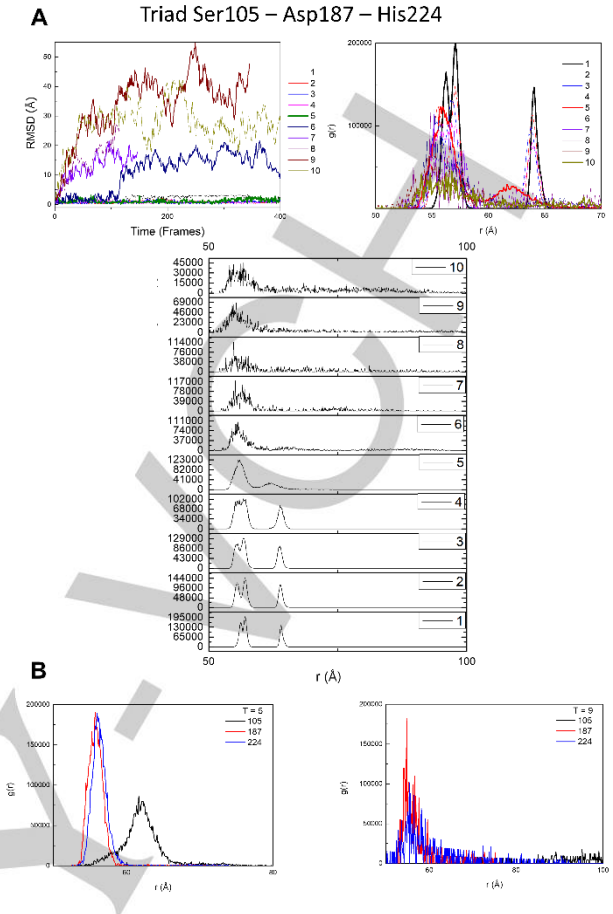


Figure 8. MD analysis for the catalytic triad Ser105-Asp187-His224. Time evolution and RMSD and radial distribution function of CALB catalytic triad Ser105-Asp187-His224 in CALB@AuNP upon different temperatures (A). Zoom in RMSD of triad residues at T = 5 and T = 9 (B).

An increase in the catalytic activity following a temperature increase can be understood in the small variations in the RMSD offering a more-exposed catalytic triad. From the calculations, the experimental data here reported can be understood in terms of three simultaneous facts: i) CALB is stable both in presence and absence of NP for temperatures <50 °C; ii) the structure of the catalytic triad is very stable in the same range; iii) the triad remains close to the surface of AuNP within same temperature range. It is important to mention that the irradiation could create temperature gradients not detected in our experiments and, thus, not accounted for in the simulations.

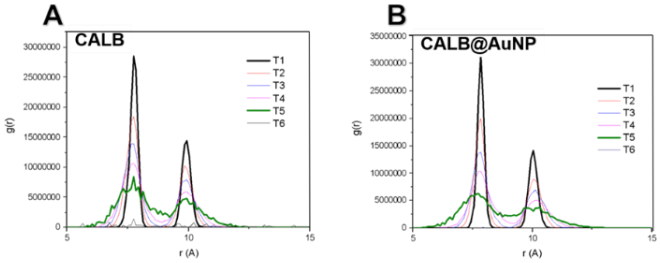


Figure 9. Radial distribution function of the triad Ser105-Asp187-His224 for temperatures <6 in CALB (A) and CALB@AuNP (B).

In summary, MD indicates the exposition and stability of the catalytic triad Ser105-Asp187-His224 upon local heat and adsorption on the AuNP. The conformation changes upon both immobilization and thermal stimulus derived from LSPR may reflect in an improvement of the catalytic activity of CALB@AuNP, as observed by the hydrolysis experimental assays.

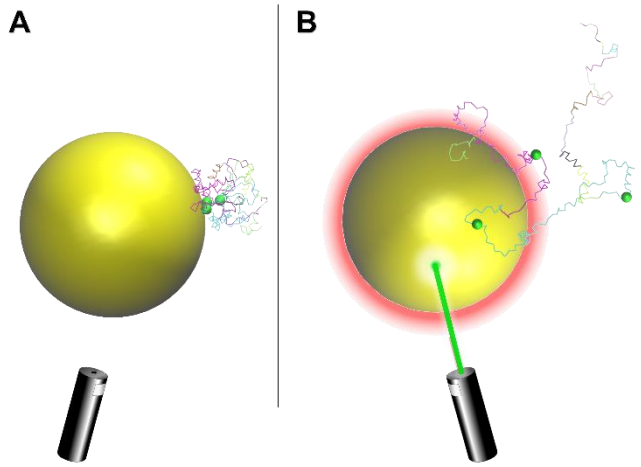


Figure 10. Schematic representation of CALB conformation immobilized on AuNP in dark conditions (A) and upon LSPR stimulation and local heat generation (B). Snapshots were taken from T=1 and T=8 of MD simulations in **Figure S3**.

Conclusion

Prominent chemical insights on the secondary structure of CALB in the system CALB@AuNP upon LSPR stimulus were obtained to investigate the LSPR-driven catalytic results. We harnessed the results from spectroscopic techniques, such as CD and Raman, and theoretical modeling via MD to decipher the changes in the interaction at the molecular level of CALB upon adsorption, thermal, and laser irradiation treatments.

These techniques converged to demonstrate that both the immobilization of CALB onto AuNPs and the heat generated by LSPR stimulus play significant roles in the original secondary structure of CALB. MD calculations were able to suggest a consequent exposition of the stable catalytic triad Ser105-Asp187-His224 upon the heat generated by LSPR and, thus, better catalytic results are to be expected.

This work is a contribution towards the understanding of the complex interactions between enzymes and nanoparticles in the particular case of CALB@AuNP and proposes a broad set of techniques to investigate them. By converging a set of data provided by different techniques, we could propose the effect of laser stimuli on the interactions at nano-bio interfaces. Moreover, this reinforces the potentialities of LSPR-driven nanobiocatalysis as a tool for high performances catalytic systems.

Acknowledgements

The authors thank Brazilian agencies CNPq (#302173/2016-1) and São Paulo Research Foundation FAPESP (2021/00675-4, 2016/21070-5, and 2018/13492-2) for financial support. R.T.P.S. acknowledges CAPES for the fellowship (88882.328241/2019-01). H.R.B. also thanks FAPESP for the fellowships granted (2019/09668-0 and 2017/20892-4). R.F.F. thanks FAPESP for the fellowship granted (2018/25422-9). We thank the support of the computing infrastructure of the i2BASQUE academic network and the ATLAS machine at the DIPC. This research was supported by the Spanish Ministerio de Economía y Competitividad (MINECO) (FIS2017-89471-R to I.C.). This research was supported by Programa Red Guipuzcoana de Ciencia, Tecnología e Información (2019-CIEN-000051-01 to I.C.). We thank Prof. Luis M. Liz-Marzán for kindly providing access to the facilities at CIC biomaGUNE. Funding is acknowledged from the Spanish State Research Agency (Project MDM-2017-0720).

Keywords: Enzyme Catalysis • LSPR-driven catalysis • Nanobioplasmonics • Nanotechnology • Secondary structure

[1] A. Zada, P. Muhammad, W. Ahmad, Z. Hussain, S. Ali, M. Khan, Q. Khan, M. Maqbool, *Adv. Funct. Mater.* **2020**, *30*, 1–29.

[2] T. P. Araujo, J. Quiroz, E. C. M. Barbosa, P. H. C. Camargo, *Curr. Opin. Colloid Interface Sci.* **2019**, *39*, 110–122.

[3] H. R. de Barros, F. López-Gallego, L. M. Liz-Marzán, *Biochemistry* **2021**, *60*, 991–998.

[4] H. R. De Barros, I. García, C. Kuttner, N. Zeballos, P. H. C. Camargo, S. I. C. De Torresi, F. López-Gallego, L. M. Liz-Marzán, *ACS Catal.* **2021**, *11*, 414–423.

[5] M. D. Blankschien, L. A. Pretzer, R. Huschka, N. J. Halas, R. Gonzalez, M. S. Wong, *ACS Nano* **2013**, *7*, 654–663.

[6] S. Guo, H. Li, J. Liu, Y. Yang, W. Kong, S. Qiao, H. Huang, Y. Liu, Z. Kang, *ACS Appl. Mater. Interfaces* **2015**, *7*, 20937–20944.

[7] S. Tadepalli, J. Yim, K. Madireddi, J. Luan, R. R. Naik, S. Singamaneni, *Chem. Mater.* **2017**, *29*, 6308–6314.

[8] W. Li, D. Liu, X. Geng, Z. Li, R. Gao, *Catal. Sci. Technol.* **2019**, *9*, 2221–2230.

[9] R. T. P. da Silva, H. Ribeiro de Barros, D. M. F. Sandrini, S. I. Córdoba de Torresi, *Bioconjug. Chem.* **2022**, *33*, 53–66.

[10] G. Baffou, R. Quidant, *Chem. Soc. Rev.* **2014**, *43*, 3898.

[11] H. R. De Barros, M. C. Santos, L. R. S. Barbosa, L. Piovan, I. C. Riegel-Vidotti, *J. Braz. Chem. Soc.* **2019**, *30*, 2231–2242.

[12] S. Lv, Y. Du, F. Wu, Y. Cai, T. Zhou, *Nanoscale Adv.* **2022**, 2608–2631.

[13] J. Kong, S. Yu, *Acta Biochim. Biophys. Sin. (Shanghai).* **2007**, *39*, 549–559.

[14] R. Tuma, *J. Raman Spectrosc.* **2005**, *36*, 307–319.

[15] P. Blanpain-Avet, A. Hédoux, Y. Guinet, L. Paccou, J. Petit, T. Six, G. Delaplace, *J. Food Eng.* **2012**, *110*, 86–94.

[16] H. S. Mandal, H. B. Kraat, *J. Am. Chem. Soc.* **2007**, *129*, 6356–6357.

[17] B. Hernández, E. López-Tobar, S. Sanchez-Cortes, Y. M. Coïc, B. Baron, A. Chenal, S. G. Kruglik, F. Pflüger, R. Cohen, M. Ghomi, *Phys. Chem. Chem. Phys.* **2016**, *18*, 24437–24450.

[18] J. A. Seo, A. Hédoux, Y. Guinet, L. Paccou, F. Affouard, A. Lerbret, M. Descamps, *J. Phys. Chem. B* **2010**, *114*, 6675–6684.

[19] J. J. Cárcamo, A. E. Aliaga, R. E. Clavijo, M. R. Brañes, M. M. Campos-Vallette, *Spectrochim. Acta - Part A Mol. Biomol. Spectrosc.* **2012**, *86*, 360–365.

[20] R. K. J., A. J. R., D. G. W. J., S. H. Eugene, *Science (80-.).* **1976**, *191*, 1176–1178.

[21] A. Rygula, K. Majzner, K. M. Marzec, A. Kaczor, M. Pilarczyk, M. Baranska, *J. Raman Spectrosc.* **2013**, *44*, 1061–1076.

[22] C. Ortiz, D. Zhang, A. E. Ribbe, Y. Xie, D. Ben-Amotz, *Biophys. Chem.* **2007**, *128*, 150–155.

[23] E. Podstawka, Y. Ozaki, L. M. Proniewicz, *Appl. Spectrosc.* **2005**, *59*, 1516–1526.

[24] F. S. Parker, in *Appl. Infrared Spectrosc. Biochem. Biol. Med.*, Springer US, Boston, MA, **1971**, pp. 165–172.

[25] E. López-Tobar, B. Hernández, J. Gómez, A. Chenal, J. V. Garcia-Ramos, M. Ghomi, S. Sanchez-Cortes, *J. Phys. Chem. C* **2015**, *119*, 8273–8279.

[26] B. S. McAvan, L. A. Bowsher, T. Powell, J. F. O'Hara, M. Spitali, R. Goodacre, A. J. Doig, *Anal. Chem.* **2020**, *92*, 10381–10389.

[27] S. M. Kelly, T. J. Jess, N. C. Price, *Biochim. Biophys. Acta-Proteins Proteomics* **2005**, *1751*, 119–139.

[28] A. Arsalan, H. Younus, *Int. J. Biol. Macromol.* **2018**, *118*, 1833–1847.

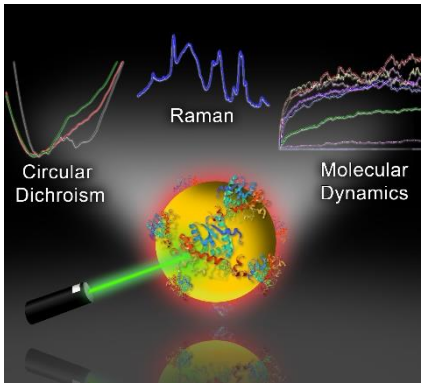
[29] G. Rabbani, E. Ahmad, M. V. Khan, M. T. Ashraf, R. Bhat, R. H. Khan, *RSC Adv.* **2015**, *5*, 20115–20131.

[30] Y. Cen, W. Singh, M. Arkin, T. S. Moody, M. Huang, J. Zhou, Q. Wu, M. T. Reetz, *Nat. Commun.* **2019**, *10*, DOI 10.1038/s41467-019-11155-3.

[31] Meesaragandla B, García I, Biedenweg D, Toro-Mendoza J, Coluzza I, Liz-Marzán L M and Delcea M, *Phys. Chem. Chem. Phys.* 2020, 22 4490–500

WILEY-VCH

Entry for the Table of Contents



Catalytic hydrolysis performed by the hybrid CALB@AuNP system upon light stimulus is discussed in terms of its structural changes of CALB. Thermal effects derived from Localized Surface Plasmon Resonance (LSPR) are assessed by circular dichroism (CD), Raman spectroscopy and Molecular Dynamics (MD). Significant changes in CALB structure are observed upon AuNP adsorption, thermal, and light treatments.

Institute and/or researcher Twitter usernames: @rafaeltrivella @HeloiseRBarros @susana_torresi @IQUSP

WILEY-VCH

Supporting Information
©Wiley-VCH 2021
69451 Weinheim, Germany

Physicochemical insights into the LSPR-driven Enzymatic Activity of Lipase Adsorbed on Gold Nanoparticles

Rafael T. P. da Silva, [a] Heloise R. de Barros, [a,b] Rafaella F. Fernandes,[a] Jhoan Toro-Mendoza,[b] Ivan Colluzza,[c,d] Marcia L. A. Temperini[a], and Susana Inés C. de Torresi*[a]

Abstract: The interaction of metallic nanoparticles (NP) with electromagnetic fields via localized surface plasmon resonance (LSPR) has been extensively explored to improve inorganic catalysis. However, the biocatalytic reactions upon light stimulus are still poorly understood due to the high complexity involving the interrelation of light, enzymes, and nanoparticles. In the present work, we combined the valuable outputs from circular dichroism (CD), Raman spectroscopy, and Molecular Dynamics simulations (MD) to elucidate some of the biocatalytic outcomes of LSPR-driven hydrolysis of 4-nitrophenyl palmitate (pNPP) by lipase from *Candida antarctica* (CALB) supported on gold nanoparticles (AuNP). CD and Raman results indicate crucial transformations on CALB secondary structure possibly induced by local heat generated by LSPR excitation, whereas MD indicates the exposition and stability of the catalytic triad Ser105-Asp187-His224 upon local heat and adsorption on the NP and, thus, higher catalytic yields are to be achieved. This study reveals valuable insights toward understanding the physicochemical transformations in nanobioplasmonic catalysis.

DOI: 10.1002/anie.2021XXXXX

Table of Contents

Table of Contents 1
Experimental Procedures 1
Results and Discussion 3
References 5
Author Contributions 5

Experimental Procedures

Materials

Sodium citrate tribasic dehydrate, tetrachloroauric (III) acid ($HAuCl_4$), phosphate buffered saline (PBS) pH 7.4, lipase from *Candida antarctica* fraction B (CALB), 4-nitrophenyl palmitate (pNPP), were purchased from Sigma-Aldrich. All chemicals were used as received. Purified Milli-Q water (Millipore, 18.2 MΩ cm) was used in the preparation of all solutions.

SUPPORTING INFORMATION

AuNP Synthesis

AuNPs were prepared through the typical Turkevich method,[1] in which to a 30 mL of H_2O, 900 µL of a 1% (w/w) solution of sodium citrate in water was heat to boiling on a heating plate with magnetic stirring and followed by the addition of 300 µL of $HAuCl_4$ 25 mmol L^{-1}. The mixture was left stirring for 15 minutes.

CALB@AuNP Synthesis

In a 32°C bath on a heat plate, 10 mL of as synthesized AuNP and 10 mL of CALB solution in PBS at pH 7.4 (0.1 mg/mL) were added in a round-bottom flask. This mixture was stirred for 2 h and preserved at 4 °C until its use.

TEM Characterization

CALB@AuNP was characterized by TEM using a JEOL JEM-1400 PLUS microscope at an acceleration voltage of 120 kV. Samples were prepared by drop casting 3 µL of the sample on a carbon-coated copper grids and left to dry.

Laser Apparatus

Experiments regarding laser irradiation were performed using two different laser sources. An NIR laser at λ = 808 nm (fiber-coupled laser diode, Lumics LU0808T040) and a green laser at λ = 532 nm (fiber-coupled laser diode, CNI MGL-FN-532) with adjustable power densities. Both laser sources illuminated the samples passing through two lenses, one to collimate and the other to expand the laser beam adjusted to illuminate a spot of 1 cm^2 of the sample in a cuvette. The power density used in the experiments was 1.4 W/cm^2.

Thermal Camera Analysis

Thermal camera analyses were performed by placing the equipment (FLIRA35) 15 cm above the cuvette. The heating and cooling curves were obtained using the ResearchIR software after discounting the blank curves performed with PBS.

pNPP Hydrolysis

Hydrolysis of pNPP was monitored through the formation of para-nitrophenol (pNP) with a UV-Vis spectrophotometer set at λ = 405 nm.[2] 120 µL of the substrate pNPP (0.5 mM) previously prepared in isopropanol was added in a quartz cuvette containing 1.83 mL of PBS buffer and 150 µL of CALB@AuNP. The conversion percentage was determined through the plateau in the kinetic curves.

CD Spectroscopy

CD spectroscopy was performed with Jasco J-815 Spectrometer, ranging from 190 to 260 nm with scanning speed of 50 nm min^{-1}, bandwidth of 1 nm, data pitch of 0.5 nm. A quartz cuvette of 1 mm was used and the temperature was controlled by a Peltier system whenever the temperature ramps were performed. Spectra were recorded by an average of 10 accumulations and the CD spectra were corrected by the water blank.

Molecular Dynamics Calculations

In a previous report, it was developed a numerical protocol where the interaction between the different residues and the surface charges of the NP are included [5]. Hence, we developed a coarse-grained representation of the protein-NP system based on the one used in our previous study.[3] The acceptor and donor state is determined from the ζ -potential using the expression from Oshima

$$\sigma_\zeta = \frac{2\varepsilon_r\varepsilon_0\kappa kT}{e}\sinh\left(\frac{e\zeta}{2kT}\right)\left[1+\frac{1}{\kappa a}\left(\frac{2}{\cosh^2\left(\frac{e\zeta}{4kT}\right)}\right)+\frac{1}{(\kappa a)^2}\left(\frac{8\mathrm{Ln}\left[\cosh\left(\frac{e\zeta}{4kT}\right)\right]}{\sinh^2\left(\frac{e\zeta}{2kT}\right)}\right)\right]^{1/2}, \qquad (1)$$

where ε_r=80.2 is the relative permittivity of water at room temperature, =8.85x10ε_0^{-12} C/Nm^2 the permittivity of vacuum, is the κ^{-1}Debye length estimated at 0.7 nm under physiological conditions, e=1.6x10^{-19} C the elementary electric charge, kT=4.11x10^{-19} J the thermal energy, and ζ potential estimated in the experiments. Here, we We then determined the protonation state of CALB using the PropKA software package.[4–6]

Molecular dynamics calculations were performed using the package LAMMPS. From the PDB file obtained from the Protein Database (code 1TCA), a first calculation for structure stability was performed. Then, an additional “atom” was added to both input and coordinates files in order to model the presence of the nanoparticle. The interactions between the different residues and the NP consisted in sigmoidal-type including repulsive and attractive forces depending on the electric charge of each surface residue and the one of the NP. The magnitude of the force interaction was studied using 60 LJ potential strength units. All the calculations were performed at constant temperature and pressure, implicit solvent, using a Langevin thermostat for 1M steps single runs under a NVE integration scheme. The results were analyzed in terms of the mean square displacement of CALB, and the radial distribution function of the indicated residues. The values of the parameters in LJ units are temperature T*, mass, and epsilon = 1, timestep = 0.002, and sigma = 4. Particles were placed in the center of a cubic box large enough to avoid periodic boundary conditions effects.

Raman Spectroscopy

Raman spectra were acquired using a Renishaw inVia Reflex fitted with a Peltier cooled CCD camera (Renishaw, 600x400 pixels) and coupled to a Leica Microscope (DM2500M). The spectra were obtained using the 785 nm laser line focused on the samples by an x20 Leica objective (NA 0.40). All Raman spectra were acquired through 2 scans with 20s accumulation time.

Results and Discussion

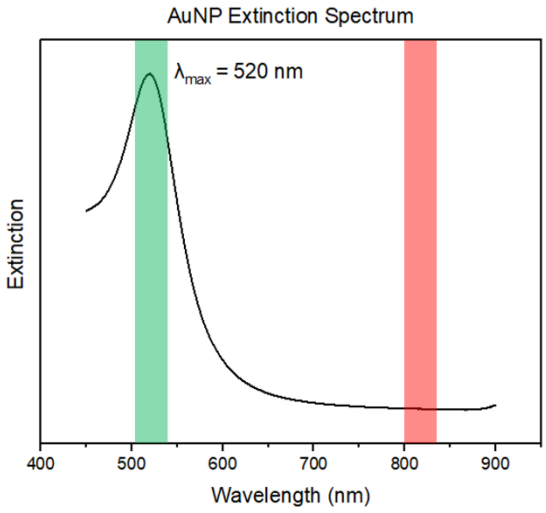


Figure S1. Extinction spectrum and LSPR band maximum indication of AuNPs synthesized by Turkevich’s method. Green and red rectangles represent the wavelength range from the lasers used in the experiments (λ = 532 nm and λ = 808 nm, respectively).

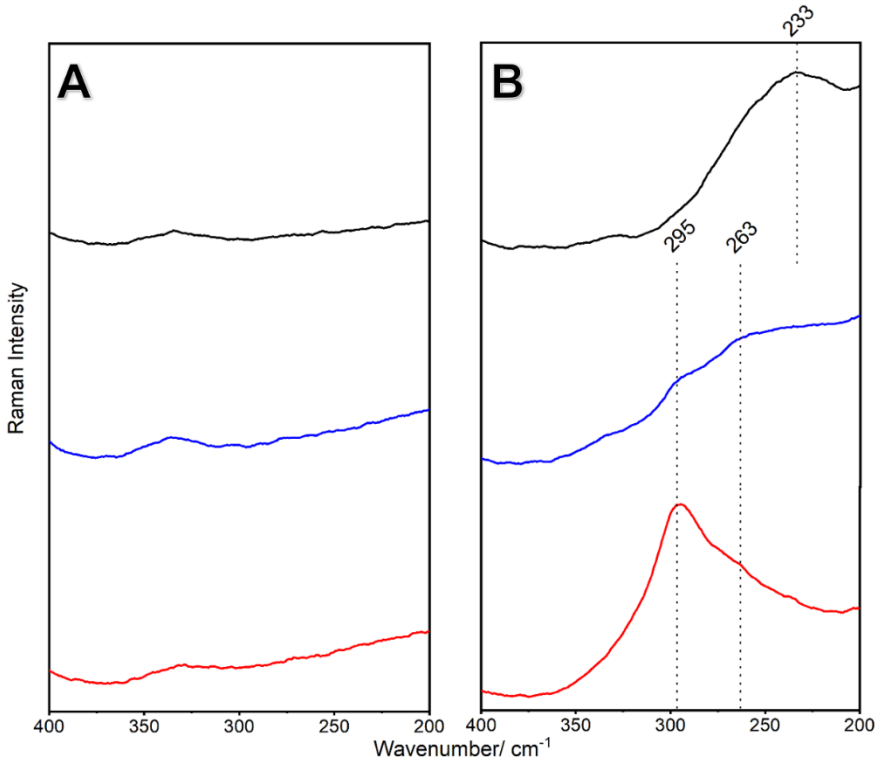


Figure S2. Lower wavenumbers (400-200 cm^{-1}) Raman spectra upon temperature changes. Free CALB (A) and CALB@AuNP (B) at 25°C (black), 55°C (blue), and 70°C (red).

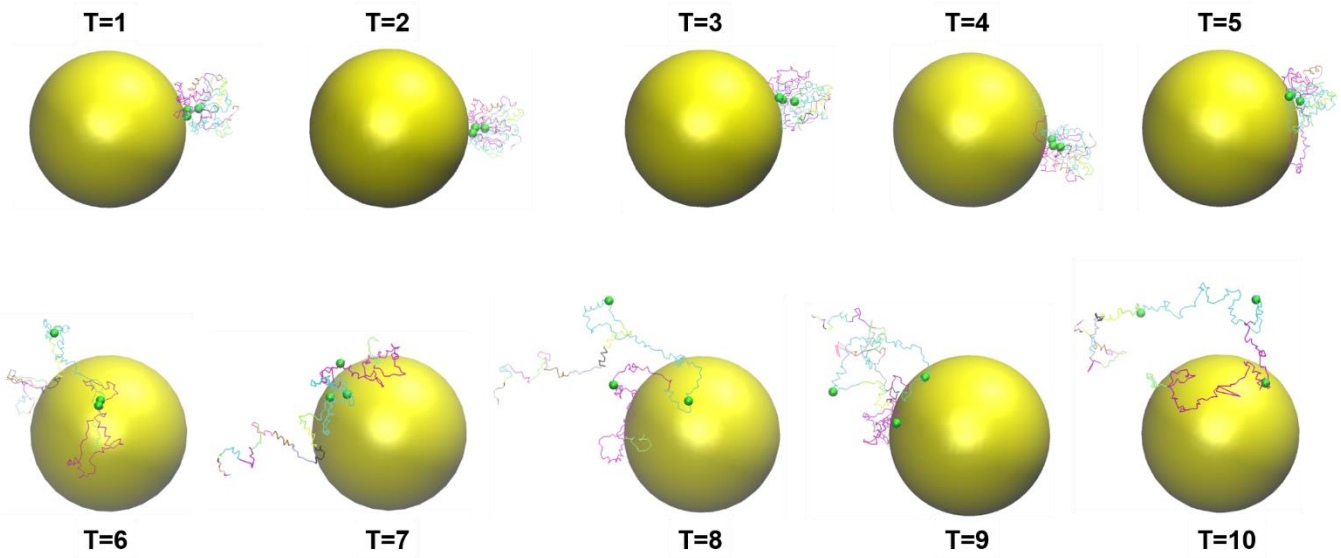


Figure S3. Representation of unfolding of CALB at CALB@AuNP upon increase of temperature. The temperature is represented in Lennard-Jones (LJ) units. The catalytic triad is represented in green spheres.

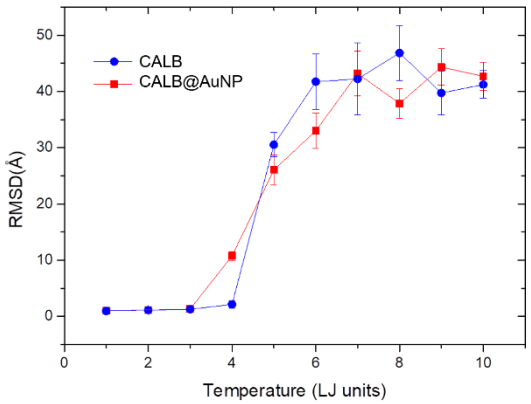


Figure S4. Comparison between the RMSD of CALB and CALB@AuNP in the coarse-grained simulations generated by LAMMPS upon different temperatures in Lennard-Jones (LJ) units.

References

[1] J. Turkevich, P. C. Stevenson, J. Hillier, *Discuss. Faraday Soc.* **1951**, *11*, 55–75.
[2] H. R. De Barros, F. López-Gallego, L. M. Liz-Marzán, *Biochemistry* **2021**, *60*, 991–998.
[3] B. Meesaragandla, I. García, D. Biedenweg, J. Toro-Mendoza, I. Coluzza, L. M. Liz-Marzán, M. Delcea, *Phys. Chem. Chem. Phys.* **2020**, *22*, 4490–4500.
[4] H. Li, A. D. Robertson, J. H. Jensen, *Proteins Struct. Funct. Bioinforma.* **2005**, *61*, 704–721.
[5] N. Powers, J. H. Jensen, *J. Biomol. NMR* **2006**, *35*, 39–51.
[6] M. N. Davies, C. P. Toseland, D. S. Moss, D. R. Flower, *BMC Biochem.* **2006**, *7*, 18.

Author Contributions

R.T.P.S. was responsible for the data curation, project administration and wrote the original draft. H.R.B. idealized and administrated the project, acquired TEM micrographs, performed catalytic and CD assays. Both R.T.P.S. and H.R.B. led the execution of this study. R.F.F. acquired Raman data. R.F.F. and M.L.A.T. analyzed Raman results. J.T.M. and I.C. acquired MD data and analyzed its results. L.M.L.M and S.I.C.T. supervised the project.

3.2.3 Cytochrome C with Peroxidase-like Activity Supported on Plasmonic AuNPs: Improved Stability and Enhanced Nanobioplasmonic Catalytic Conversion (Attachment 6)

Author Contribution: The author participated in conceiving the idea, designing the experiments, performing the assays, and writing the paper.

Cytochrome C (CytC) is a small redox macromolecule with a prosthetic heme group[38]. Its iron-containing center with variable oxidation number was vastly explored in electrochemical assays and its important peroxidase activity has been considered in organic transformations[39].

In this work, we synthesize a CytC@AuNP nanobioconjugate to aspects of CytC immobilization on AuNP not yet reported. Raman and Circular Dichroism (CD) data assessed aspects regarding secondary structure and chemical changes in structure upon immobilization on AuNP. CD shows a drastic decrease on α-helix domains, with a percentage increase on β-sheet and random coils with an increasing concentration of AuNP. Cohesively, Raman analysis reinforces these modifications and highlights the importance of tryptophan (Trp) residues on the interactions with AuNP surface. The thermal stability of the CytC@AuNP nanobioconjugate was assessed through ramp temperatures performed by CD. From the heating curve, the denaturation temperature for free CALB was 73 °C, whereas a 15 °C delayed start on the denaturation process. It was, therefore, not possible to precisely determine CytC@AuNP denaturation temperature before solvent evaporation, suggesting it had an increase of at least 15 °C. Cooling ramps performed right after the heating step show the protein refolding, which occurred only partially in free CytC, but completely in CytC@AuNP. Thus, the thermal stability of CytC was substantially changed upon immobilization on the nanobioconjugate, a fact that proves CytC@AuNP a good candidate for

nanobiocatalysis. Biocatalytic oxidation of 2,2′-azinobis-(3-ethylbenzothiazoline-6-sulfonic acid) (ABTS) to its cation radical form ($ABTS^{+\cdot}$) was performed. CytC@AuNP presented a typical Michaelis-Menten reaction progress curve, whereas free CytC at the same concentration showed a linear aspect, suggesting its activity was summarily lower and the reaction and it could not achieve the steady-state. The reaction yield of the nanobioconjugate was 68% superior compared to free CytC. LSPR-driven reaction was able to improve 12% of the catalytic yield of CytC@AuNP, although it did not affect free CytC. Although further studies must be performed to elucidate the mechanisms of LSPR catalysis on this redox molecule to carry out a redox biocatalytic reaction, we suggest that a combination of local heat and hot carrier generation may play significant roles. In this way, we were able to demonstrate the role of biomolecules immobilization on thermal stability and reaction mechanisms on nanobiocatalysis. In addition, we instigate further studies of hot carriers transfer with the use of redox proteins in LSPR-driven catalysis.

RESEARCH ARTICLE

Cytochrome C with Peroxidase-like Activity Supported on Plasmonic AuNPs: Improved Stability and Enhanced Nanobioplasmonic Catalytic Conversion

Rafael T. P. da Silva,[a] Heloise R. de Barros,[a] Rafaella F. Fernandes,[a] Marcia L. A. Temperini,[a] Susana I. Cordoba de Torresi*[a]

[a] R.T.P. da Silva, Dr. H. R. de Barros, Dr. R. F. Fernandes, Prof. Dr. M. L. A. Temperini and Prof. Dr. S. I. C. de Torresi
Instituto de Química
Universidade de São Paulo
Av. Prof. Lineu Prestes, 748, 05508-000, São Paulo-SP, Brazil
E-mail: storresi@iq.usp.br

Abstract: Metallic nanoparticles have been used to adsorb biomolecules and improve their stability under broader conditions. However, plasmon-driven catalytic reactions with metallic nanostructures are still imminent. This study focuses on the interaction of Cytochrome C (CytC) adsorbed on gold nanoparticles (AuNP), CytC@AuNP. Circular dichroism (CD) and Raman show significant differences in secondary structure, mainly in α-helix. CD ramp temperatures revealed enhanced thermal stability of CytC@AuNP, as evidenced by a refolding of the α-helix conformation of CytC and a considerable delay in denaturation temperature by approximately 15 °C. Catalytic oxidation performed with CytC@AuNP showed a typical Michaelis-Menten profile and 68% higher yields compared to CytC, which exhibited a linear profile. The same reaction performed upon plasmon stimulus comparatively increased the catalytic yield of CytC@AuNP in 12%, although it had no effect on free CytC. This study highlights the advantages of adsorbing biomolecules on nanoparticles and is an important contribution to plasmon-driven nanobiocatalysis.

Introduction

Interest in metallic nanoparticles (NPs) is steadily increasing due to the exceptional properties of these nanostructures, which make them suitable for applications in catalysis, energy conversion, biomedicine and sensing. As for the use of metallic NPs in biocatalytic transformations, the usual poor stability of macromolecules to temperature, pH, stirring and other reaction conditions has been partially circumvented by using NPs as supports.[1]

Cytochrome C (CytC) is a redox macromolecule of low molecular weight with a prosthetic heme group. Changing the oxidation state of iron confers a peroxidase-like activity to CytC, which is mainly used in biocatalytic and electrocatalytic approaches.[2–5]

More recently, the results of chemical redox reactions have been improved by plasmon-driven effects.[6] In this phenomenon, hot carriers can interact with the NPs and the substrate bound to their active surface upon localized surface plasmon resonance (LSPR) stimulus.[7] However, few studies have focused on plasmon-driven biocatalytic transformations using enzymes.[8,9]

In this sense, the present work is devoted to the physicochemical characterization of CytC adsorbed on gold NP (AuNP) surface. The CytC@AuNP system was characterized by spectrophotometry, electron microscopy, circular dichroism (CD) and Raman. In addition, catalytic assays were performed regarding the peroxidase-like activity of CytC in CytC@AuNP compared to its free CytC counterpart. Finally, both catalytic systems were stimulated with a laser whose irradiation wavelength matches the LSPR of AuNP to evaluate the effects of this plasmon-driven catalysis.

Results and Discussion

Synthesis and Characterization

AuNPs were synthesized by the Turkevich method and CytC was adsorbed on their surface, as previously described.[10] Transmission electron microscopy (TEM) micrographs using lacey carbon grids show high contrast metallic spherical nanoparticles with an average diameter of 13 ± 2 nm (**Figure 1A** and **Figure 1B**). A structure of 1-2 nm on the nanoparticles suggests a layer of adsorbed CytC and the formation of the nanobioconjugate CytC@AuNP. UV-Vis spectra confirm this result with the changes in the LSPR band by the protein corona formed with the CytC adsorption, indicated by a 8 nm shift in the UV-Vis spectrum of the naked AuNP (**Figure 1C**).[11,12] The spectrum of free CytC absorbs mainly at shorter wavelengths, below 500 nm (**Figure S1**). The bands with the highest absorption are the Soret band (405-415 nm) and the L band (< 290 nm), both related to intraporphyrin transitions of the heme group.[13]

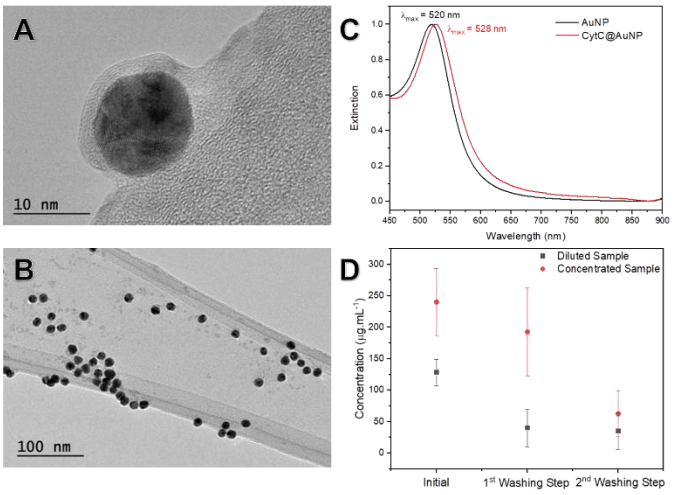


Figure 1. Characterization of CytC@AuNP. TEM micrographs using a lacey-carbon grid (A and C). UV-Vis spectra of AuNP (black) and CytC@AuNP (red), with the maximum extinction wavelengths indicated (B). CytC concentration in

CytC@AuNP determined by the Bradford assay in two consecutive washing steps (D).

To investigate the CytC effectively adsorbed on the AuNPs in the CytC@AuNP nanobioconjugates, a Bradford assay was performed. Two different CytC@AuNP samples were prepared in terms of CytC concentration, namely concentrated (0.5 mg/mL) and diluted (0.2 mg/mL). The concentration of AuNP in CytC@AuNP nanobioconjugates was kept constant in both samples. Bradford assay was carried out with the as-prepared samples in triplicates, as well as two consecutive washing steps by centrifugation and the pellet resuspension in the same original volume of phosphate-buffered saline (PBS). After two washing steps, the protein concentration of both samples converged to approximately 50 µg/mL, with no statistically significant difference. This concentration level was reached by the diluted sample in the first washing step, although a second step was required for the concentrated sample. This highlights that 50 µg/mL is the remaining protein content adorbed on the AuNPs surface, regardless of the initial concentration, which correspond to the hard corona. A third washing step was not feasible because the CytC@AuNP samples began to aggregate on the walls of the microtubes.

Circular Dichroism (CD) Spectroscopy

Circular Dichroism (CD) spectroscopy was used to evaluate the changes in the secondary structure of CytC induced by adsorption on AuNPs. For this purpose, three samples were prepared in PBS buffer with increasing concentrations of AuNP (0, 10%, and 50% by volume). The final concentration of CytC was constant for all samples.

Figure 2A shows the CD spectra in the 205-230 nm range, where most of the deviations were found. This region is of great importance because it is here that the content of α-helix domains can be determined.[14] CytC is a protein with a high content of α-helix and a heme group surrounded by three major α-helix domains (N-terminal, C-terminal, and 60s helices) that play a major role in its secondary structure.[15] Both samples with AuNP showed deviations from free CytC spectrum, which are interpreted as different ratios of secondary structure features in **Figure 2B**, obtained by DichroWeb software.

When the percentage of AuNP in the sample was increased, the α-helix domains (67%) in the sample containing 50% AuNP were drastically decreased to 31%. This lost percentage was split into β-sheet and random coils along the structure. The β-sheet domains, which previously accounted for only 4% of the total structure, reached 10% in the sample with the highest AuNP concentration. The random coils, which accounted for 28% of the original CytC structure, almost doubled their proportion to 59% in the sample with higher AuNP content.

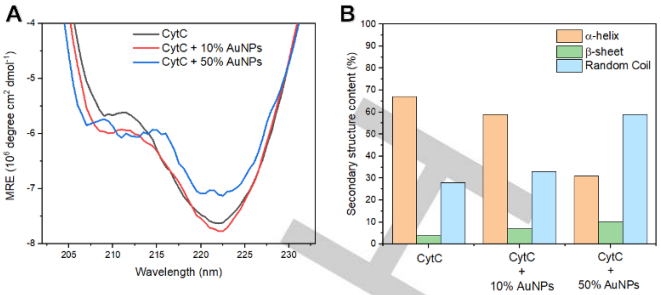


Figure 2. Circular Dichroism (CD) analyses of different ratios between CytC and AuNP in CytC@AuNP. CD Spectra obtained at room temperature (A). DichroWeb secondary structure analyses using K2D model in the wavelength range of 200-240 nm (B).[16]

It has been previously reported that the surface curvature of nanoparticles plays an importante role in the secondary structure of polypeptides.[17] The data from CD data show that the curvature of our AuNP can successfully change the secondary structure of CytC. However, the relationship between the unfolding of proteins and their catalytic activity is not direct, which means that this phenomenon can deteriorate, maintain or even improve the catalytic performance depending on the catalytic mechanisms of each particular case.[18,19] To further explore the effects of secondary structure in CytC@AuNP, we decided to study the sample containing 50% of the volume of AuNP as described in the experimental methods in our following experiments.

Raman Spectroscopy

Raman spectroscopy is an advantageous technique for its ultrasensitivity and effectiveness in identification of proteins and enzymes. The analysis of vibrational spectra of CytC using AuNPs should provide rich insights into tracing its secondary structure and conformational states before and after adsoprtion on AuNP. This study will elaborate on the CD results presented in the last section from a more specific chemical point of view.

The non-resonant Raman spectrum of CytC provided extensive vibrational information associated not only with the heme group, but also with some amino acid residues and the peptide backbone.[20]

Thus, some typical vibrational modes of heme are apparent in **Figure 3**: 1633 cm^{-1} $\nu(C_\alpha C_m)_{asym}$, 1584 cm^{-1} $\nu(C_\alpha C_m)_{asym}$, 749 cm^{-1} ν(pyr breathing), 1127 cm^{-1} ν(pyr breathing half-ring)$_{sym}$, 1168 cm^{-1} ν(pyr breathing half-ring)$_{sym}$, 1370 cm^{-1} ν(pyr breathing half-ring)$_{sym}$.[21] Moreover, some bands can be ascribed to different amino acid residues: 1560 cm^{-1} (Trp, indole ring) and 990 cm^{-1} (Trp), while the 1247 cm^{-1} mode is assigned to the amide III.[22]

In other words, the normal group vibrations of the pyrrole rings (bonds C_aN, C_aNC_a, C_aC_b) can be described as the bands at 749, 1168, and 1370 cm^{-1} and the methine bridges (bonds C_aC_m, C_aC_mH) to the bands at 1584 and 1633 cm^{-1}.

Thus, some essential information about the changes in the conformational structure of CytC induced by the presence of AuNPs was observed in the CytC@AuNP sample. First, the Raman band at 1560 cm^{-1} related to the indole ring of the Trp amino acid is slightly shifted to 1550 cm^{-1}, suggesting that the Trp residues may play an important role in the interaction with the AuNPs, since the very characteristic Raman band at 990 cm^{-1}

(ring breathing mode)[23] comes out to evidence in the CytC@AuNPs spectrum.

Moreover, the Raman signal at 1247 cm^{-1} shifted to 1243 cm^{-1} indicates a substantial change in the β-sheet structural features, in which vibrational frequencies can be observed well separated from the amide III modes corresponding to the α-helix conformation at 1314 cm^{-1}.[22] This result suggests that there are structural changes in the β-sheets when CytC is adsorbed on AuNP, in addition to the change in the percentage of secondary features displayed by CD.

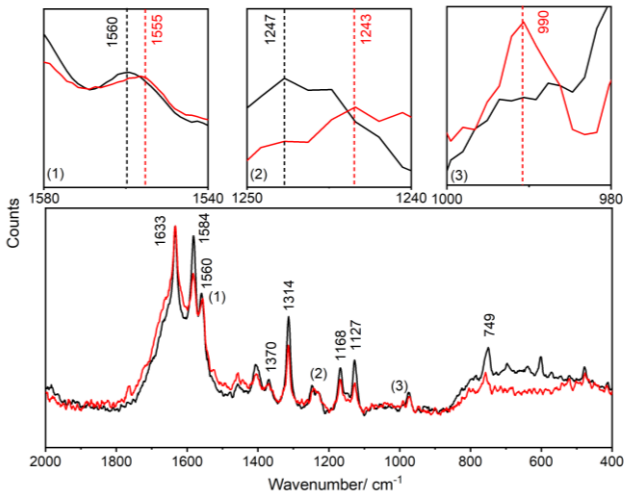


Figure 3. Raman spectrum of CytC (0.2 mg/ mL) (black) and SERS spectrum CytC@AuNPs (red) in the wavenumber range of 2000-400 cm^{-1} and the highlighted spectral regions of (1) 1580-1540 cm^{-1}, (2) 1250-1240 cm^{-1} and (3) 1000-980 cm^{-1}.

With respect to the heme-sensitive oxidation modes, we note that the prominent band corresponding to the ferrous state (ν_{15} at 749 cm^{-1})[21] was found in the CytC@AuNP spectrum at 757 cm^{-1}, which is an additional indication of the adsorption of CytC on AuNPs by pyrrole rings in the heme center, as shown in **Figure 4**.

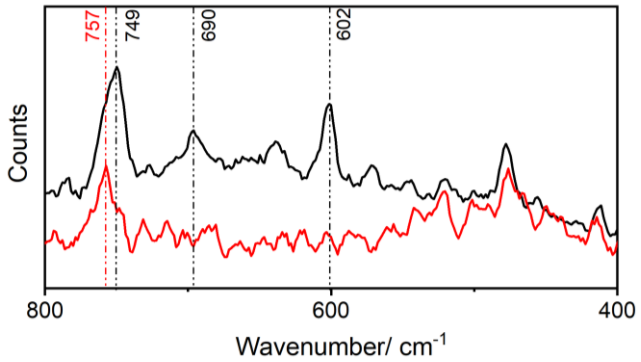


Figure 4. Raman spectrum of CytC (0.2 mg/mL) (black) and SERS spectrum CytC@AuNP (red) in the wavenumber range of 800-400 cm^{-1}.

The spectral region below 800 cm^{-1} provides information about specific changes in the pyrrole groups in the presence of AuNPs. In particular, the absence of the Raman bands at 690 cm^{-1} assigned to the ν_7 mode (ν(pyr deform)$_{sym}$)[23], and also the particular band of ferrous CytC obtained with the Q-state excitation at 602 cm^{-1} assigned to the ν_{24} mode (ν(pyr deform)$_{asym}$)[24].

Thus, Raman analysis indicates that the adsorption of CytC on AuNPs was directed by the pyrrole groups reflecting the minimal changes in the heme structure. The changes in the vibrational modes of pyrrole breathing and pyrrole deformation were detected with a slight frequency shift for some characteristic bands related to the amino acid residues. In this way, the vibrational evidence can also be related to the secondary conformational change in the adsorption of AuNPs and the interaction with the AuNP surfaces.

Thermal Stability

To evaluate the effects of the protein adsorption on CytC thermal stability, temperatures ramps (heating and cooling steps) were performed and the band at 222 nm was monitored as an indicator of α-helix loss and CytC unfolding (**Figure 5**). Temperature ramps were performed from 20 °C to 95 °C in a heating step followed by a cooling step with a sealed cuvette to prevent water evaporation.

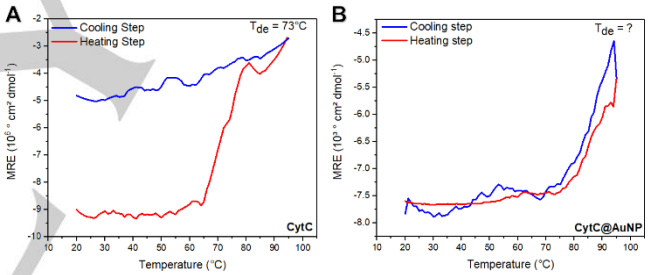


Figure 5. Temperature ramps (heating and cooling steps) acquired by CD at 222 nm and denaturation temperatures. Free CytC (A) and CytC@AuNP (B).

On one hand, free CytC (**Figure 5A**) showed a sigmoidal transition at the heating step, where the denaturation temperature (T_{de}) was determined to be at 73°C.[25] The cooling step showed a linear trend and the original α-helix content was partially recovered.

On the other hand, the CytC@AuNP bioconjugate (**Figure 5B**) did not show a sigmoidal transition, because it did not achieve fully denaturation within the temperature of analysis. Therefore, a denaturation temperature cannot be accurately determined. Interestingly, it is noticeable that the Mean Residue Ellipsity (MRE) of this sample, after some small fluctuations, only starts to increase at 80 °C, whereas it increased at 65 °C for the free CytC sample. This indicates a delayed loss of the α-helix by at least 15 °C, which shows the AuNPs improve the thermal stability of CytC. Moreover, the cooling step reveals that the system is practically reversible once the α-helix content is restored to the same initial level after the cooling ramp is completed. This behavior can be interpreted as refolding of the secondary structure of CytC when adsorbed on AuNP, and has been described previously in a heat-resistant fungus structure, ascopore[26]. **Figure 6** is a scheme representing the thermal

stability assessed by CD temperature ramps presented in **Figure 5**.

In addition to CD and Raman characterization, these findings suggest that adsorption of CytC on AuNP may cause structural changes that are advantageous in terms of thermal stability and reversibility, crucial parameters for efficient application of CytC@AuNP as a biocatalyst.

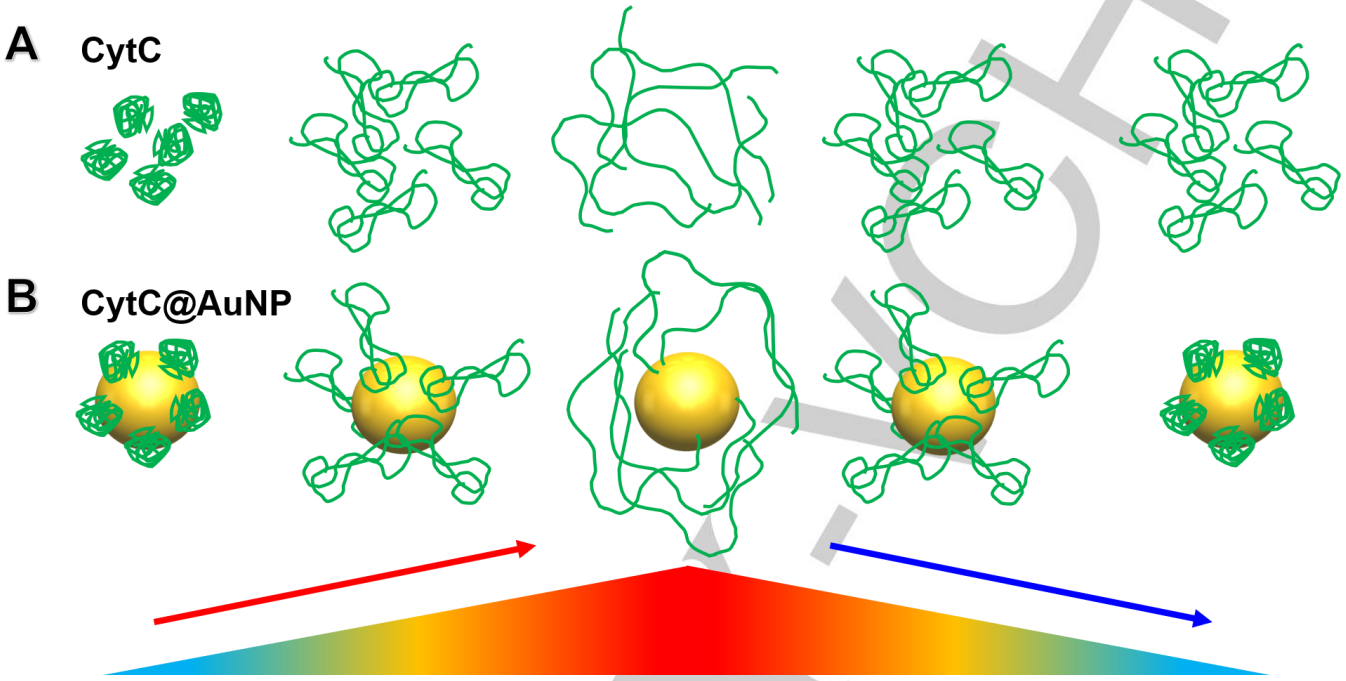


Figure 6. Scheme representing thermal stability of CytC (A) and CytC@AuNP (B) over a temperature ramp. The green coils represent macromolecules of CytC and AuNP are represented by golden spheres. At the bottom, the triangle depicts the ramp temperature performed from CD and the arrow colors are similar to the heating (red data) and cooling (blue data) curves represented in Figure 5.

Catalytic Results

CytC is usually an electron transfer protein present in the electron transport chain and an important activator of the caspase cascade in the apoptosis process.[27] However, due to its heme center containing iron ions with exchangeable oxidation state, it has been used in redox catalysis, mainly as hydrogen peroxide biosensors in electrochemistry.[28] The adsorption of CytC on AuNP was already investigated by Luz and Crespilho, who showed the advantages of this bioconjugate in electron transfer on the electrode surface compared to free CytC.[29] In heterogeneous biocatalysis, CytC was more intensively explored as a peroxidase-like catalyst between the decades 90 and 2000.[2–4] One of the standard reactions catalyzed by CytC is the oxidation of 2,2′-azinobis-(3-ethylbenzothiazoline-6-sulfonic acid) (ABTS) to its cation radical form ($ABTS^{+\cdot}$) in the presence of H_2O_2 (**Figure 7**). However, this reaction remains poorly understood in the context of adsorption on various matrices, and recent advances in nanotechnology, including LSPR-driven biocatalysis, may lead to a better understanding of the potential of CytC.

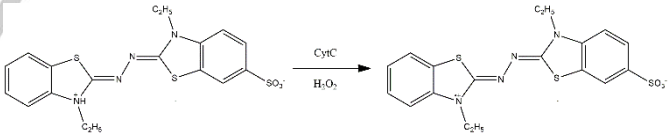


Figure 7. Schematic of biocatalytic oxidation of 2,2′-azinobis-(3-ethylbenzothiazoline-6-sulfonic acid) (ABTS) into its cation radical form ($ABTS^{+\cdot}$) in the presence of H_2O_2.

ABTS oxidation can be monitored by UV-Vis, with a decrease in the 340 nm band (consumption of ABTS) and an increase in the 410 nm band (formation of $ABTS^{+\cdot}$) (**Figure 8A**). Although it is a protein with peroxidase-like activity, CytC is inactivated in the presence of an excess of H_2O_2, which is accompanied by destruction of the heme group destruction and the alteration of the covalent features of amino acid residues.[30] This is reflected by the decrease in the Soret band at 410 nm and, thus, it happens in parallel to the formation of $ABTS^{+\cdot}$ at the same wavelength, masking the true reaction yield (**Figure S2**). Therefore, using free CytC and CytC@AuNP as catalysts for ABTS oxidation, our studies began by optimizing the concentration of H_2O_2 in the reaction. We found that a concentration of 0.1 mM was optimal to carry out the reaction and not cause any interference in the

analysis of the reaction progress (**Figure S3**). **Figure S3** also shows other blank reactions proving that ABTS oxidation is possible only in the presence of both CytC and H_2O_2. ABTS oxidation was performed in triplicates for free CytC and CytC@AuNP (**Figure 8B**).

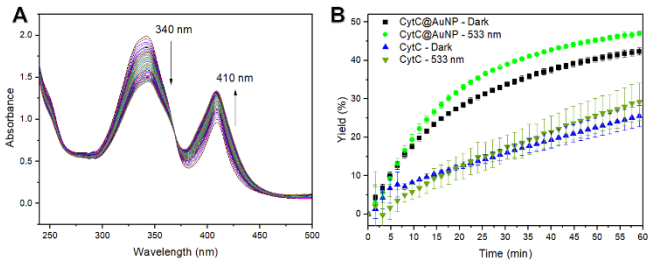


Figure 8. Catalytic results from the oxidation of ABTS. UV-Vis monitoring of the 340 and 410 nm bands (A). Catalytic curves in triplicate and dark conditions for free CytC (blue) and CytC@AuNP (black). Catalytic curves upon LSPR stimulation (533 nm) for free CytC (pink) and CytC@AuNP (red).

The reaction was followed for 60 min by monitoring the formation of $ABTS^{+\cdot}$ at 410 nm. The first difference that stands out between free CytC and CytC@AuNP is the standard deviation of the samples. CytC@AuNP behaves more reproducibly in the triplicates, while free CytC presents a large standard deviation of the data points along the progress curves.

Free CytC and CytC@AuNP show significant differences in the shape of the reaction progress curves. The first data points show the initial rate period in pre-steady-state kinetics, which is much shorter period for free CytC than for CytC@AuNP. From this point, free CytC progress curve has a linear trend, whereas CytC@AuNP has a more typical Michaelis-Menten curve shape. While CytC never reached a steady-state, CytC@AuNP kept slightly increasing the yield of $ABTS^{+\cdot}$ formation instead of reaching a plateau. This is an indication that there is a rate-limiting product dissociation or substrate rebinding that prevents the formation of a clear steady-state.

Although the same amount of enzyme was used in both samples, the curve of CytC@AuNP indicates that a supposedly larger amount of protein was used and, thus, almost all substrate was oxidized in the first 22 min of the reaction, resulting in a flattening of the curve after this point[31]. However, the curve of free CytC shows a decreased rate, with a much lower yield over time, as if the amount of enzyme added in the assay was lower and a steady-state could not be achieved. After 60 min, the yield of $ABTS^{+\cdot}$ is 42% for CytC@AuNP and 25% for free CytC, meaning a 68% increase in performance. These are indications that the bioconjugate CytC@AuNP has an improved catalytic efficiency rather than the free CytC.

As mentioned earlier, nanobioconjugates are capable of improving catalytic features of individual biomolecules.[19] This effect may be due to conformational changes of proteins, as described here by Raman and CD data, but also to the creation of microenvironments and confinement effects.

In redox biomolecules, such as CytC, electron transfer mechanisms may undergo different pathways in the presence of conducting materials such as metallic nanoparticles.[29] In this sense, plasmon-driven redox catalysis based on hot carriers generation and injection may benefit from electron transfer[32,33]. Therefore, an external laser source matching the LSPR of AuNP (533 nm) was applied in the reading intervals of the catalytic system.

Figure 8B shows the catalytic assays upon LSPR stimulus. Both curves show the same shape as before the application of the external stimulus. CytC shows no statistically significant difference between the sample under 533 nm irradiation and the sample treated in the dark. Interestingly, the yield achieved by the bioconjugate CytC@AuNP is 12% higher in LSPR than in the dark sample after 60 min reaction time, corresponding to an absolute yield increase of 5%. Contrarily, Guo et al. worked on a laccase@AuNP nanobioconjugate that had a decrease in performance upon LSPR stimulus.[34] The authors suggest that the local heat generation could have affected the conformations of the catalytic center, harming the electron transfer process. Fo our system, this indicates that: i) the heating effect of the external energy source is not sufficient to increase the reaction yield; ii) the LSPR outcomes considerably enhance catalytic yield. Mechanistically, this effect promoted by LSPR can be explained either by local heat, as already observed by other nanobioconjugate systems,[8,9] or by the formation of hot carriers that are able to interact with ABTS and promote its oxidation. As far as we know, the phenomenon of LSPR-driven hot carriers transfer to biomolecules has not yet been reported and points out to a whole new approach in nanobiocatalysis. However, further studies are still necessary to its elucidation.

Conclusion

Here we report the synthesis of CytC@AuNP nanobioconjugate. Its characterization by UV-Vis and TEM suggests the formation of a protein corona on the surface of plasmonic AuNP, which was quantified to 50 µg/mL by the Bradford assay. CD and Raman spectroscopy show significant structural changes upon adsorption to AuNP. CD shows a decreasing α-helix secondary feature upon addition of AuNP, while β-sheet and random coil percentage increase. Raman revealed the role of pyrrole groups of amino acid residues in the adsorption of CytC onto AuNP, as well as the changes of Trp indole rings and β-sheet features in CytC structure, following what was suggested by CD. These conformational changes confer a better thermal stability to CytC, as assessed by the delayed denaturation of the α-helix in the heating step and a complete recovery by refolding in the cooling step. These properties make CytC@AuNP an ideal candidate as biocatalyst and, thus, it was tested as a peroxidase-like catalyst for the oxidation of ABTS. The performance of the nanobioconjugate was remarkable compared to free CytC, with nearly twice the yield of $ABTS^{+\cdot}$ and rapid attainment of steady-state. LSPR-driven catalysis was performed with the stimulus of an external laser source matching AuNP LSPR. While this had no significant effect on free CytC, the performance of CytC@AuNP was increased by 12%. These findings highlight the importance of adsorption on nanoparticles in altering protein structure, stability and activity toward biocatalytic reactions. Moreover, it brings to light the under-explored LSPR-driven biocatalysis and the possibility of a hot carrier mechanism in a redox biomolecule in addition to the local heat effects.

Acknowledgements

The authors thank Brazilian agencies CNPq (#302173/2016-1) and São Paulo Research Foundation FAPESP (2015/26308-7, 2016/21070-5, 2018/16219-5 and 2018/13492-2) for financial support. R.T.P.S. acknowledges CAPES for the fellowship (88882.328241/2019-01). H.R.B. also thanks FAPESP for the fellowships granted (2019/09668-0 and 2017/20892-4). R.F.F. thanks FAPESP for the fellowship granted (2018/25422-9).

Keywords: Biocatalysis • Cytochromes • LSPR • Nanobioconjugate • Nanotechnology

[1] S. A. Ansari, Q. Husain, *Biotechnol. Adv.* **2012**, *30*, 512–523.

[2] N. H. Kim, M. S. Jeong, S. Y. Choi, J. H. Kang, *Bull. Korean Chem. Soc.* **2004**, *25*, 1889–1892.

[3] R. Vazquez-Duhalt, *J. Mol. Catal. - B Enzym.* **1999**, *7*, 241–249.

[4] R. Radi, L. Thomson, H. Rubbo, E. Prodanov, *Arch. Biochem. Biophys.* **1991**, *288*, 112–117.

[5] P. Thakur, J. Mannuthodikayil, G. Kalita, K. Mandal, T. N. Narayanan, *Mater. Chem. Front.* **2021**, *5*, 1295–1300.

[6] T. P. Araujo, J. Quiroz, E. C. M. Barbosa, P. H. C. Camargo, *Curr. Opin. Colloid Interface Sci.* **2019**, *39*, 110–122.

[7] G. Baffou, R. Quidant, *Chem. Soc. Rev.* **2014**, *43*, 3898.

[8] H. R. De Barros, F. López-Gallego, L. M. Liz-Marzán, *Biochemistry* **2021**, *60*, 991–998.

[9] H. R. De Barros, I. García, C. Kuttner, N. Zeballos, P. H. C. Camargo, S. I. C. De Torresi, F. López-Gallego, L. M. Liz-Marzán, *ACS Catal.* **2021**, *11*, 414–423.

[10] H. R. De Barros, M. C. Santos, L. R. S. Barbosa, L. Piovan, I. C. Riegel-Vidotti, *J. Braz. Chem. Soc.* **2019**, *30*, 2231–2242.

[11] A. P. Ault, D. I. Stark, J. L. Axson, J. N. Keeney, A. D. Maynard, I. L. Bergin, M. A. Philbert, *Environ. Sci. Nano* **2016**, *3*, 1510–1520.

[12] I. Gomes, N. C. Santos, L. M. A. Oliveira, A. Quintas, P. Eaton, E. Pereira, R. Franco, *J. Phys. Chem. C* **2008**, *112*, 16340–16347.

[13] C. Consani, O. Bräm, F. Van Mourik, A. Cannizzo, M. Chergui, *Chem. Phys.* **2012**, *396*, 108–115.

[14] S. M. Kelly, T. J. Jess, N. C. Price, *Biochim. Biophys. Acta-Proteins Proteomics* **2005**, *1751*, 119–139.

[15] S. Akiyama, S. Takahashi, K. Ishimori, I. Morishima, *Nat. Struct. Biol.* **2000**, *7*, 514–520.

[16] M. A. Andrade, P. Chacón, J. J. Merelo, F. Morán, *Protein Eng. Des. Sel.* **1993**, *6*, 383–390.

[17] H. S. Mandal, H. B. Kraat, *J. Am. Chem. Soc.* **2007**, *129*, 6356–6357.

[18] A. Seehuber, R. Dahint, *J. Phys. Chem. B* **2013**, *117*, 6980–6989.

[19] B. J. Johnson, W. R. Algar, A. P. Malanoski, M. G. Ancona, I. L. Medintz, *Nano Today* **2014**, *9*, 102–131.

[20] P. Matteini, M. De Angelis, L. Ulivi, S. Centi, R. Pini, *Nanoscale* **2015**, *7*, 3474–3480.

[21] I. Delfino, A. R. Bizzarri, S. Cannistraro, *Biophys. Chem.* **2005**, *113*, 41–51.

[22] J. A. Seo, A. Hédoux, Y. Guinet, L. Paccou, F. Affouard, A. Lerbret, M. Descamps, *J. Phys. Chem. B* **2010**, *114*, 6675–6684.

[23] A. Rygula, K. Majzner, K. M. Marzec, A. Kaczor, M. Pilarczyk, M. Baranska, *J. Raman Spectrosc.* **2013**, *44*, 1061–1076.

[24] S. Hu, T. G. Spiro, I. K. Morris, J. P. Singh, K. M. Smith, *J. Am. Chem. Soc.* **1993**, *115*, 12446–12458.

[25] S. Robic, *CBE Life Sci. Educ.* **2010**, *9*, 189–195.

[26] R. K. Singh, B. M. Blossom, D. A. Russo, B. Van Oort, R. Croce, P. E. Jensen, C. Felby, M. J. Bjerrum, *RSC Adv.* **2019**, *9*, 29734–29742.

[27] D. Alvarez-Paggi, L. Hannibal, M. A. Castro, S. Oviedo-Rouco, V. Demicheli, V. Tórtora, F. Tomasina, R. Radi, D. H. Murgida, *Chem. Rev.* **2017**, *117*, 13382–13460.

[28] Z. S. Aghamiri, M. Mohsennia, H. A. Rafiee-Pour, *Talanta* **2018**, *176*, 195–207.

[29] R. A. S. Luz, F. N. Crespilho, *RSC Adv.* **2016**, *6*, 62585–62593.

[30] N. Tomášková, P. Novák, T. Kožár, M. Petrenčáková, D. Jancura, G. Yassaghi, P. Man, E. Sedlák, *Int. J. Biol. Macromol.* **2021**, *174*, 413–423.

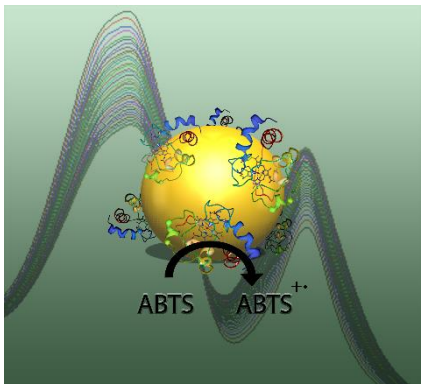
[31] F. A. Leone, *Fundamentos de Cinética Enzimática*, Appris, Curitiba, **2021**.

[32] R. T. P. da Silva, H. Ribeiro de Barros, D. M. F. Sandrini, S. I. Córdoba de Torresi, *Bioconjug. Chem.* **2022**, *33*, 53–66.

[33] R. T. P. Da Silva, M. P. De Souza Rodrigues, G. F. B. Davilla, A. M. R. P. Da Silva, A. H. B. Dourado, S. I. Córdoba De Torresi, *ACS Appl. Nano Mater.* **2021**, *4*, 12062–12072.

[34] S. Guo, H. Li, J. Liu, Y. Yang, W. Kong, S. Qiao, H. Huang, Y. Liu, Z. Kang, *ACS Appl. Mater. Interfaces* **2015**, *7*, 20937–20944.

Entry for the Table of Contents



CytC@AuNP bioconjugate promoting a biocatalytic conversion of ABTS to its cation radical species ($ABTS^{+\cdot}$). The reaction is monitored by the UV-Vis spectra depicted in the background, which is colored according to the laser color corresponding to the LSPR of AuNP.

Institute and/or researcher Twitter usernames: @rafaeltrivella @HeloiseRBarros @susana_torresi @IQUSP

WILEY-VCH

Supporting Information
©Wiley-VCH 2021
69451 Weinheim, Germany

Cytochrome C with Peroxidase-like Activity Supported on Plasmonic AuNPs: Improved Stability and Enhanced LSPR-driven Conversion

Rafael T. P. da Silva,[a] Rafaella F. Fernandes,[a] Heloise R. de Barros,[a] Marcia L. A. Temperini,[a] Susana I. Cordoba de Torresi*[a]

Abstract: Metallic nanoparticles have been used to adsorb biomolecules and improve their stability under broader conditions. However, plasmon-driven catalytic reactions with metallic nanostructures are still imminent. This study focuses on the interaction of Cytochrome C (CytC) adsorbed on gold nanoparticles (AuNP), CytC@AuNP. Circular dichroism (CD) and Raman show significant differences in secondary structure, mainly in α-helix. CD ramp temperatures revealed enhanced thermal stability of CytC@AuNP, as evidenced by a refolding of the α-helix conformation of CytC and a considerable delay in denaturation temperature by approximately 15 °C. Catalytic oxidation performed with CytC@AuNP showed a typical Michaelis-Menten profile and 68% higher yields compared to CytC, which exhibited a linear profile. The same reaction performed upon plasmon stimulus comparatively increased the catalytic yield of CytC@AuNP in 12%, although it had no effect on free CytC. This study highlights the advantages of adsorbing biomolecules on nanoparticles and is an important contribution to plasmon-driven nanobiocatalysis.

DOI: 10.1002/anie.2021XXXXX

Table of Contents

Experimental Procedures 1
Results and Discussion 3
References 4
Author Contributions 4

Experimental Procedures

Materials

Sodium citrate tribasic dehydrate, tetrachloroauric (III) acid ($HAuCl_4$), phosphate buffered saline (PBS) pH 7.4, Cytochrome C from equine heart (≥95%), Bradford reagent, Bovine Serum Albumin (BSA), and 2,2'-Azino-bis(3-ethylbenzothiazoline-6-sulfonic

acid) (ABTS) were purchased from Sigma-Aldrich. Hydrogen peroxide (H_2O_2) was purchased from Synth. All chemicals were used as received. Purified Milli-Q water (Millipore, 18.2 MΩ cm) was used in the preparation of all solutions.

AuNP Synthesis

A typical Turkevich's method was used to prepare AuNPs,[1] in which 30 mL of distilled water with 300 µL of a 1% (w/w) solution of sodium citrate in water were heated to boiling on a heating plate with magnetic stirring and followed by the addition of 300 µL of $HAuCl_4$ 25 mmol L^{-1}. The mixture was left stirring for 15 minutes.

CytC@AuNP Synthesis

In a 32°C bath on a heat plate, 10 mL of as synthesized AuNP and 10 mL of CytC solution in PBS at pH 7.4 (0.4 mg/mL) were added in a round-bottom flask. This mixture was stirred for 2 h and preserved at 4 °C until its use. The final solution concentration in terms of protein is 0.2 mg/mL, corresponding to the 50% in volume of AuNP. The sample of 10% in volume of AuNP used in CD followed the same procedures with an initial mixture of 1 mL of AuNP and 10 mL of CytC.

TEM Characterization

CytC@AuNP was characterized by TEM using a JEOL JEM-1400 PLUS microscope at an acceleration voltage of 120 kV. Samples were prepared by drop casting 3 µL of the sample on a carbon-coated copper grids and left to dry.

Protein concentration determination

Two different samples of CytC@AuNP were prepared to quantify the amount of protein prior to washing steps and after 2 consecutive washing steps. Both analyzed samples had the same amount of AuNP, but the concentrated sample was prepared with 0.5 mg/mL of protein, whereas the called diluted sample had the initial concentration of 0.2 mg/mL. Bradford assays were carried out starting with a calibration curve of standard solutions of BSA with known concentrations. For the assay, 1 mL of Bradford reagent and 100 µL of the sample were mixed for 1 minute using a vortex mixer. Their absorbance at λ = 595 nm were measured in a cuvette by a UV-Vis (Shimadzu UV-2600) spectrophotometer (Thermo-Scientific, instructions 23200). The washing steps consisted in the centrifugation (18000 rpm, 5 min) and resuspension of pellets in its original volume before the reading step at the UV-Vis.

ABTS Oxidation

Oxidation of ABTS was performed in a 3 mL cuvette and monitored with a UV-Vis spectrophotometer (Shimadzu UV-2600). A 0.3 mM solution of ABTS and 0.1 mM solution of H_2O_2 were freshly prepared in water. In the cuvette, 2 mL of the catalyst (free CytC or CytC@AuNP 0.2 mg/mL) was carefully mixed with 0.5 mL of each as-prepared solutions of H_2O_2 and ABTS. The reaction was monitored in the range of 240-500 nm and an interval of 90 s was implemented between each measurement.[2] Laser irradiation experiments were performed using a modular laser source at λ = 533 nm with 250 mW. The laser module was positioned 7 cm above the cuvette. When using the laser source, a standardized exposure time of 60 s was used between each measurement.

Circular Dichroism (CD) Spectroscopy

CD spectroscopy was performed with Jasco J-815 Spectrometer, ranging from 190 to 260 nm with scanning speed of 50 nm/min, bandwidth of 1 nm, data pitch of 0.5 nm. A quartz cuvette of 1 mm was used and the temperature was controlled by a Peltier system when the temperature ramps were performed, with a 1 °C/min rate of heating and cooling steps. Spectra were recorded by an average of 10 accumulations and the CD spectra were corrected by the water blank. To analyze secondary structure of CytC, samples with different percentage (in volume) of AuNP were prepared, as indicated in the main text. Secondary structure was evaluated by K2D in DICHROWEB.[3] Normalization of CD spectra was done by the molar residue ellipticity (MRE) the following relation:

$$MRE = {MRW\theta}/{10dC}$$

Where, θ is the ellipticity in degrees, d is the path length of the cell in centimeters, and C is the concentration of protein in g/mL. MRW is the mean residue weight and is defined as:

$$MRW = {M}/{(N-1)}$$

Where M is the molecular mass of the protein and N is the number of its amino acids. For CytC, M = 12,384 g/mol and N =104.

Raman Spectroscopy

Raman spectra were acquired using a Renishaw inVia Reflex spectrometer fitted with a Peltier cooled CCD camera and coupled to a Leica Microscope (DM2500M). The spectra were obtained using the 532 nm laser line focused on the samples by an x20 Leica objective (NA 0.40). All Raman spectra were acquired through 3 scans with 20s accumulation time.

Results and Discussion

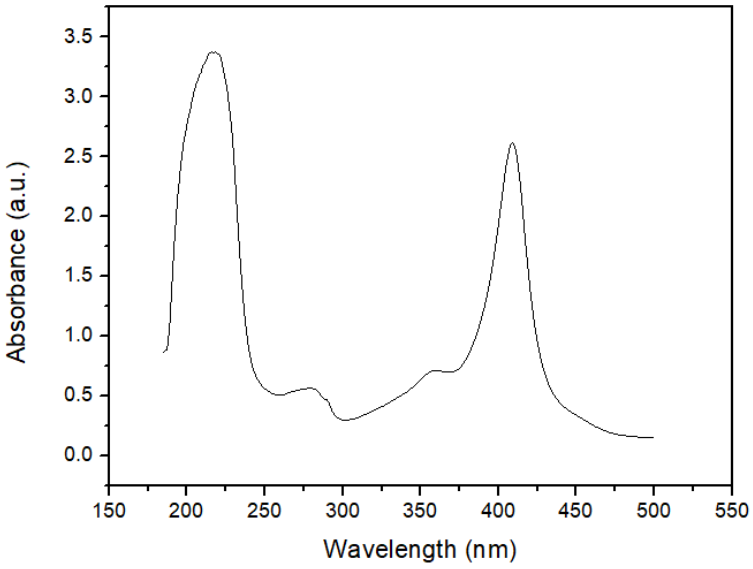


Figure S1. UV-Vis Absorption spectrum of CytC in PBS buffer.

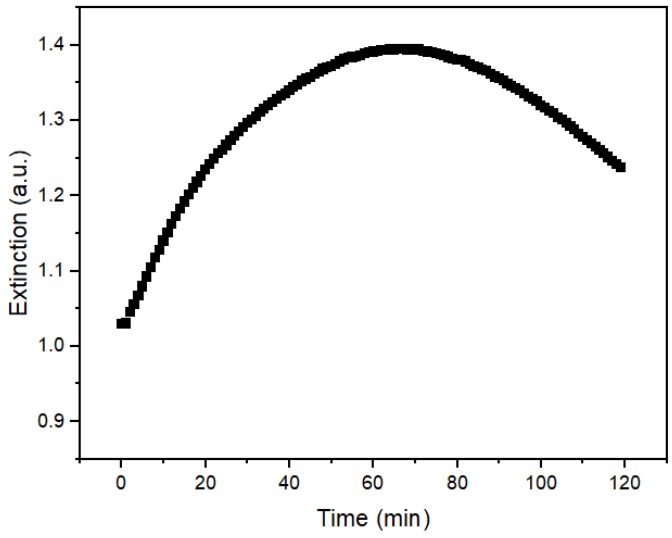


Figure S2. Extinction measurements at 410 nm of CytC@AuNP in the presence of 0.5 mL of 0.5 mM H_2O_2 in catalytic oxidation of ABTS.

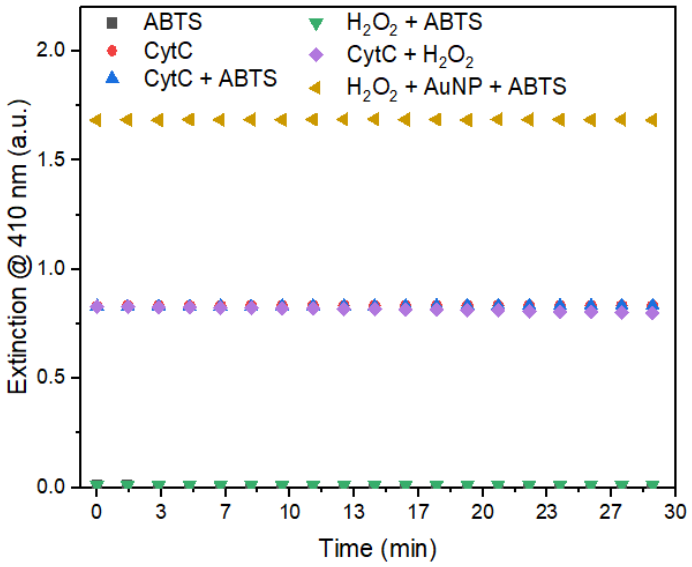


Figure S3. Extinction measurements at 410 nm of blanks in catalytic oxidation of ABTS.

References

[1] J. Turkevich, P. C. Stevenson, J. Hillier, *Discuss. Faraday Soc.* **1951**, *11*, 55–75.

[2] N. H. Kim, M. S. Jeong, S. Y. Choi, J. H. Kang, *Bull. Korean Chem. Soc.* **2004**, *25*, 1889–1892.

[3] A. J. Miles, S. G. Ramalli, B. A. Wallace, *Protein Sci.* **2022**, *31*, 37–46.

Author Contributions

R.T.P.S. was responsible for the synthesis optimization, UV-Vis and Bradford characterization, thermal stability studies, catalytic reactions, data curation, project administration and wrote the original draft. R.F.F. acquired Raman data. R.F.F. and M.L.A.T. analyzed Raman results. H.R.B. performed TEM characterization and circular dichroism characterization. S.I.C.T. supervised the project.

4. Conclusions

In this thesis, we discuss nanobiotechnology in the specific aspects of nanobiocatalysis. To this end, this topic was addressed in terms of plasmonic metallic nanoparticles and split into two different approaches: nanozymes and nanobioconjugates. Nanozymes are nanoparticles with enzyme-like properties toward catalytic reactions. In contrast, nanobioconjugates are systems in which biomolecules such as proteins are immobilized on nanostructured materials, which confer them a new set of properties for catalysis.

Concerning the nanozymes, AgNPs and AgAu nanoalloys were used as oxidase (**Attachment 1**), hydrogenase (**Attachment 2**), and peroxidase (**Attachment 3**). The three examples were able to show the efficiency of the metallic nanocatalysts in heterogeneous catalysis (**Attachment 1** and **Attachment 2**) and electrocatalysts (**Attachment 3**). In addition, AgNPs and AgAu nanoalloys show an improvement in biocatalytic efficiency upon light stimuli on LSPR, mechanistically explained by an enhanced electron transfer to the biocatalytic substrate (**Attachment 1** and **Attachment 3**). The control over the composition of AgAu bimetallic materials was studied by mechanochemical and solution-based approaches and the changes induced in the structures were characterized and evaluated in terms of biocatalytic performance (**Attachment 2** and **Attachment 3**).

Regarding the nanobioconjugates, interesting properties of stimuli-responsive systems were discussed according to the state of the art (**Attachment 4**). Then, AuNP were used as supports for the immobilization of proteins such as CALB (**Attachment 5**) and CytC (**Attachment 6**). Both systems were studied by circular dichroism and Raman spectroscopy, which indicate the enhancement of thermal stability of the biomolecules and the significant changes in secondary

structure upon immobilization and external stimuli. Biocatalytic activity was assessed through hydrolysis (**Attachment 5**) and oxidation (**Attachment 6**). Electromagnetic field was studied as an external stimulus to both systems, which especially responded with higher yields in the LSPR range. In **Attachment 5**, the main proposed mechanism for LSPR outcomes was the local heat generation, which induced a change in conformation that led to a greater exposition of the catalytic triad. In **Attachment 6**, however, the changes can be explained by both local heat generation and electron transfer mechanisms, since CytC is a redox molecule. Disentangling these two effects is yet a challenge to withstand.

Interactions between nanomaterials and biomolecules are still in dispute. The high complexity of biological matrices and substrates and their broad variety make every system unique and, thus, generalizations on the subject of interactions with nanoparticles must be guarded. On the other hand, the control over the synthesis of metallic nanomaterials is becoming more refined, and nanoparticles of multiple shapes, compositions, and sizes are currently emerging in the literature. Further development in spectroscopic and electrochemical techniques, as well as theoretical modeling, will lead to a deeper comprehension of nanomaterials and their manipulation as nanozymes and nanobioconjugates. Conclusively, the findings of this thesis are only a glimpse of nanobiocatalysis using two metals and two biomolecules out of an infinity of possibilities that can be created.

Nonetheless, this thesis brought a focused and organized discussion on nanobiocatalysis. Both approaches presented were able to demonstrate the advantages of the use of metallic nanoparticles in nanobiocatalysis and may motivate the development of new nanocatalysts inspired by biological resources. In terms of stability, either nanozymes or nanobioconjugates presented

improvements compared to isolated biomolecules regarding storage conditions and thermal treatments. Catalytically, all systems were able to perform in comparable or superior efficiencies to free enzymes. Moreover, nanozymes and nanobioconjugates were studied as smart materials on the responsiveness toward external stimuli and modulation of nanobiocatalysis, in special LSPR. This enlightens a yet prominent field of LSPR-driven nanobiocatalysis, bringing together the challenges concerning interactions of nanostructures and biological components to the ones regarding light-matter interactions. This thesis is a tool to explore and build bridges toward advances in the vast field of nanobiocatalysis.

5. References

(1) Shoseyov, O.; Levy, I. *Nanobiotechnology: Bioinspired Devices and Materials of the Future*; Springer Science & Business Media, 2008.

(2) Fornaguera, C.; Solans, C. Methods for the in Vitro Characterization of Nanomedicines—Biological Component Interaction. *Journal of Personalized Medicine*. 2017, pp 1–16. https://doi.org/10.3390/jpm7010002.

(3) Liu, H.; Dai, E.; Xiao, R.; Zhou, Z.; Zhang, M.; Bai, Z.; Shao, Y.; Qi, K.; Tu, J.; Wang, C.; Wang, S. Development of a SERS-Based Lateral Flow Immunoassay for Rapid and Ultra-Sensitive Detection of Anti-SARS-CoV-2 IgM/IgG in Clinical Samples. *Sensors Actuators B Chem.* **2021**, *329*, 129196. https://doi.org/10.1016/j.snb.2020.129196.

(4) Sannegowda, L. K. Metal Nanoparticles for Electrochemical Sensing Applications. *Handb. Nanomater. Sens. Appl.* **2021**, 589–629. https://doi.org/10.1016/B978-0-12-820783-3.00001-4.

(5) Liu, Y.; Crawford, B. M.; Vo-Dinh, T. Gold Nanoparticles-Mediated Photothermal Therapy and Immunotherapy. *Immunotherapy* **2018**, *10* (13), 1175–1188. https://doi.org/10.2217/imt-2018-0029.

(6) Sonström, P.; Bäumer, M. Supported Colloidal Nanoparticles in Heterogeneous Gas Phase Catalysis: On the Way to Tailored Catalysts. *Phys. Chem. Chem. Phys.* **2011**, *13* (43), 19270–19284. https://doi.org/10.1039/C1CP22048A.

(7) Phan, H. T.; Haes, A. J. What Does Nanoparticle Stability Mean? HHS Public Access. *J Phys Chem C Nanomater Interfaces* **2019**, *123* (27), 16495–16507. https://doi.org/10.1021/acs.jpcc.9b00913.What.

(8) Cuenya, B. R. Synthesis and Catalytic Properties of Metal Nanoparticles: Size, Shape, Support, Composition, and Oxidation State Effects. *Thin Solid Films* **2010**, *518* (12), 3127–3150. https://doi.org/10.1016/j.tsf.2010.01.018.

(9) Sharma, G.; Kumar, A.; Sharma, S.; Naushad, M.; Prakash Dwivedi, R.; ALOthman, Z. A.; Mola, G. T. Novel Development of Nanoparticles to Bimetallic Nanoparticles and Their Composites: A Review. *J. King Saud Univ. - Sci.* **2019**, *31* (2), 257–269. https://doi.org/10.1016/j.jksus.2017.06.012.

(10) Pinel, S.; Thomas, N.; Boura, C.; Barberi-Heyob, M. Approaches to Physical Stimulation of Metallic Nanoparticles for Glioblastoma Treatment. *Adv. Drug Deliv. Rev.* **2019**, *138*, 344–357. https://doi.org/10.1016/j.addr.2018.10.013.

(11) Baffou, G.; Quidant, R. Nanoplasmonics for Chemistry. *Chem. Soc. Rev.* **2014**, *43* (11), 3898. https://doi.org/10.1039/c3cs60364d.

(12) Catalysis, N. On Advances and Challenges in Biocatalysis. *Nat. Catal.* **2018**, *1* (9), 635–636. https://doi.org/10.1038/s41929-018-0157-7.

(13) Selvamani, T.; Gangadharan, D.; Anandan, S. Synthetic Strategies of Nanobioconjugates for Bioelectrochemical Applications. *Bioelectrochemical Interface Eng.* **2019**, 411–430. https://doi.org/10.1002/9781119611103.ch21.

(14) Liu, D. M.; Dong, C. Recent Advances in Nano-Carrier Immobilized Enzymes and Their Applications. *Process Biochem.* **2020**, *92* (February), 464–475. https://doi.org/10.1016/j.procbio.2020.02.005.

(15) Assfalg, M. Protein Adsorption and Conformational Changes. *Molecules* **2021**, *26* (23). https://doi.org/10.3390/molecules26237079.

(16) Ballesteros, C. A. S.; Mercante, L. A.; Alvarenga, A. D.; Facure, M. H. M.; Schneider, R.; Correa, D. S. Recent Trends in Nanozymes Design: From Materials and Structures to Environmental Applications. *Mater. Chem. Front.* **2021**, *5* (20), 7419–7451. https://doi.org/10.1039/d1qm00947h.

(17) Liang, M.; Yan, X. Nanozymes: From New Concepts, Mechanisms, and Standards to Applications. *Acc. Chem. Res.* **2019**, *52* (8), 2190–2200. https://doi.org/10.1021/acs.accounts.9b00140.

(18) Wu, J.; Wang, X.; Wang, Q.; Lou, Z.; Li, S.; Zhu, Y.; Qin, L.; Wei, H. Nanomaterials with Enzyme-like Characteristics (Nanozymes): Next-Generation Artificial Enzymes (II). *Chem. Soc. Rev.* **2019**, *48* (4), 1004–1076. https://doi.org/10.1039/c8cs00457a.

(19) OMS. Global Action Plan on Antimicrobial Resistance. *World Heal. Organ.* **2017**, 1–28.

(20) Xu, L.; Wang, Y. Y.; Huang, J.; Chen, C. Y.; Wang, Z. X.; Xie, H. Silver Nanoparticles: Synthesis, Medical Applications and Biosafety. *Theranostics* **2020**, *10* (20), 8996–9031. https://doi.org/10.7150/thno.45413.

(21) Pulit-Prociak, J.; Banach, M. Silver Nanoparticles - A Material of the Future...? *Open Chem.* **2016**, *14* (1), 76–91. https://doi.org/10.1515/chem-2016-0005.

(22) McShan, D.; Ray, P. C.; Yu, H. Molecular Toxicity Mechanism of Nanosilver. *J. Food Drug Anal.* **2014**, *22* (1), 116–127. https://doi.org/10.1016/j.jfda.2014.01.010.

(23) Cabral, J.; AG, R. Blue Light Disinfection in Hospital Infection Control: Advantages, Drawbacks, and Pitfalls. *Antibiotics* **2019**, *8* (2), 58. https://doi.org/10.3390/antibiotics8020058.

(24) Gomollón-Bel, F. IUPAC Top Ten Emerging Technologies in Chemistry 2021. *Chem. Int.* **2021**, *43* (4), 13–20. https://doi.org/10.1515/ci-2021-0404.

(25) de Oliveira, P. F. M.; Torresi, R. M.; Emmerling, F.; Camargo, P. H. C. Challenges and Opportunities in the Bottom-up Mechanochemical Synthesis of Noble Metal Nanoparticles. *J. Mater. Chem. A* **2020**, *8* (32), 16114–16141. https://doi.org/10.1039/D0TA05183G.

(26) De Oliveira, P. F. M.; Quiroz, J.; De Oliveira, D. C.; Camargo, P. H. C. A Mechano-Colloidal Approach for the Controlled Synthesis of Metal Nanoparticles. *Chem. Commun.*

2019, *55* (95), 14267–14270. https://doi.org/10.1039/c9cc06199a.

(27) Gilroy, K. D.; Ruditskiy, A.; Peng, H. C.; Qin, D.; Xia, Y. Bimetallic Nanocrystals: Syntheses, Properties, and Applications. *Chem. Rev.* **2016**, *116* (18), 10414–10472. https://doi.org/10.1021/acs.chemrev.6b00211.

(28) Sha, J.; Paul, S.; Dumeignil, F.; Wojcieszak, R. Au-Based Bimetallic Catalysts: How the Synergy between Two Metals Affects Their Catalytic Activity. *RSC Adv.* **2019**, *9* (51), 29888–29901. https://doi.org/10.1039/c9ra06001d.

(29) Naseem, K.; Begum, R.; Farooqi, Z. H. Catalytic Reduction of 2-Nitroaniline: A Review. *Environ. Sci. Pollut. Res.* **2017**, *24* (7), 6446–6460. https://doi.org/10.1007/s11356-016-8317-2.

(30) Mahmudunnabi, R. G.; Farhana, F. Z.; Kashaninejad, N.; Firoz, S. H.; Shim, Y. B.; Shiddiky, M. J. A. Nanozyme-Based Electrochemical Biosensors for Disease Biomarker Detection. *Analyst* **2020**, *145* (13), 4398–4420. https://doi.org/10.1039/d0an00558d.

(31) Jiang, D.; Ni, D.; Rosenkrans, Z. T.; Huang, P.; Yan, X.; Cai, W. Nanozyme: New Horizons for Responsive Biomedical Applications. *Chem. Soc. Rev.* **2019**, *48* (14), 3683–3704. https://doi.org/10.1039/C8CS00718G.

(32) Russo, L.; Merkoçi, F.; Patarroyo, J.; Piella, J.; Merkoçi, A.; Bastús, N. G.; Puntes, V. Time- and Size-Resolved Plasmonic Evolution with Nm Resolution of Galvanic Replacement Reaction in AuAg Nanoshells Synthesis. *Chem. Mater.* **2018**, *30* (15), 5098–5107. https://doi.org/10.1021/acs.chemmater.8b01488.

(33) Ansari, S. A.; Husain, Q. Potential Applications of Enzymes Immobilized on/in Nano Materials: A Review. *Biotechnol. Adv.* **2012**, *30* (3), 512–523. https://doi.org/10.1016/j.biotechadv.2011.09.005.

(34) Lu, Y.; Lv, Q.; Liu, B.; Liu, J. Immobilized Candida Antarctica Lipase B Catalyzed Synthesis of Biodegradable Polymers for Biomedical Applications. *Biomater. Sci.* **2019**, *7* (12), 4963–4983. https://doi.org/10.1039/c9bm00716d.

(35) De Barros, H. R.; García, I.; Kuttner, C.; Zeballos, N.; Camargo, P. H. C.; De Torresi, S. I. C.; López-Gallego, F.; Liz-Marzán, L. M. Mechanistic Insights into the Light-Driven Catalysis of an Immobilized Lipase on Plasmonic Nanomaterials. *ACS Catal.* **2021**, *11* (1), 414–423. https://doi.org/10.1021/acscatal.0c04919.

(36) De Barros, H. R.; Santos, M. C.; Barbosa, L. R. S.; Piovan, L.; Riegel-Vidotti, I. C. Physicochemical Study of the Interaction between Gold Nanoparticles and Lipase from Candida Sp. (CALB): Insights into the Nano-Bio Interface. *J. Braz. Chem. Soc.* **2019**, *30* (10), 2231–2242. https://doi.org/10.21577/0103-5053.20190127.

(37) de Barros, H. R.; Tanaka, L. Y.; da Silva, R. T. P.; Santiago-Arcos, J.; de Torresi, S. I. C.; López-Gallego, F. Assembly of Nano-Biocatalyst for the Tandem Hydrolysis and Reduction of p-Nitrophenol Esters. *Part. Part. Syst. Charact.* **2021**, *38* (10), 1–8. https://doi.org/10.1002/ppsc.202100136.

(38) Alvarez-Paggi, D.; Hannibal, L.; Castro, M. A.; Oviedo-Rouco, S.; Demicheli, V.; Tórtora, V.; Tomasina, F.; Radi, R.; Murgida, D. H. Multifunctional Cytochrome c: Learning New Tricks from an Old Dog. *Chem. Rev.* **2017**, *117* (21), 13382–13460. https://doi.org/10.1021/acs.chemrev.7b00257.

(39) Kim, N. H.; Jeong, M. S.; Choi, S. Y.; Kang, J. H. Peroxidase Activity of Cytochrome C. *Bull. Korean Chem. Soc.* **2004**, *25* (12), 1889–1892. https://doi.org/10.5012/bkcs.2004.25.12.1889.

6. Appendix

Copyright of Attachment 1



Copyright of Attachment 2

Creative Commons License Deed

Attribution 4.0 International (CC BY 4.0)

This is a human-readable summary of (and not a substitute for) the license.

You are free to:

Share — copy and redistribute the material in any medium or format

Adapt — remix, transform, and build upon the material

for any purpose, even commercially.

The licensor cannot revoke these freedoms as long as you follow the license terms.

Under the following terms:

Attribution — You must give appropriate credit, provide a link to the license, and indicate if changes were made. You may do so in any reasonable manner, but not in any way that suggests the licensor endorses you or your use.

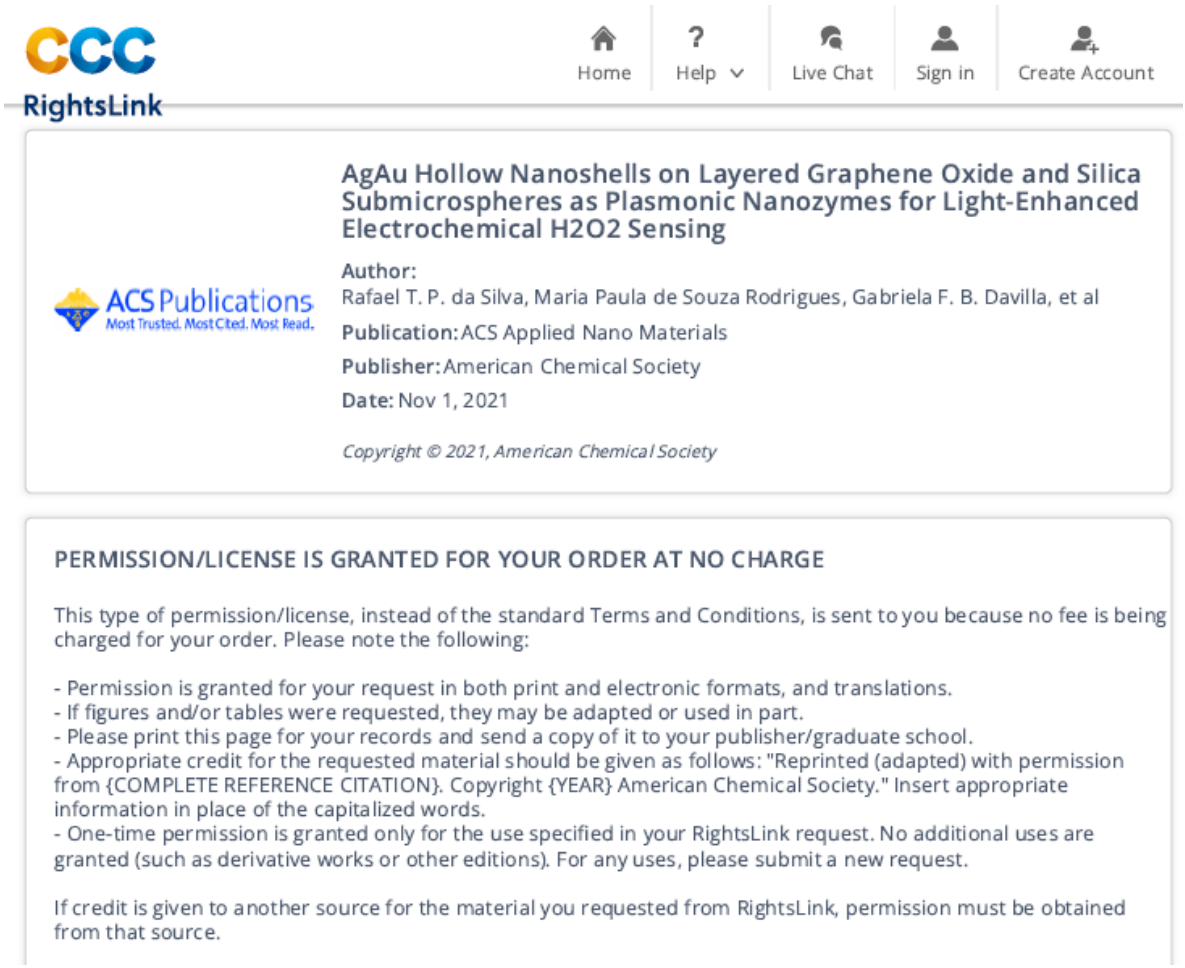
No additional restrictions — You may not apply legal terms or technological measures that legally restrict others from doing anything the license permits.

Notices:

You do not have to comply with the license for elements of the material in the public domain or where your use is permitted by an applicable exception or limitation.

No warranties are given. The license may not give you all of the permissions necessary for your intended use. For example, other rights such as publicity, privacy, or moral rights may limit how you use the material.

Copyright of Attachment 3



CCC RightsLink

Home | Help | Live Chat | Sign in | Create Account

AgAu Hollow Nanoshells on Layered Graphene Oxide and Silica Submicrospheres as Plasmonic Nanozymes for Light-Enhanced Electrochemical H2O2 Sensing

ACS Publications
Most Trusted. Most Cited. Most Read.

Author:
Rafael T. P. da Silva, Maria Paula de Souza Rodrigues, Gabriela F. B. Davilla, et al

Publication: ACS Applied Nano Materials

Publisher: American Chemical Society

Date: Nov 1, 2021

Copyright © 2021, American Chemical Society

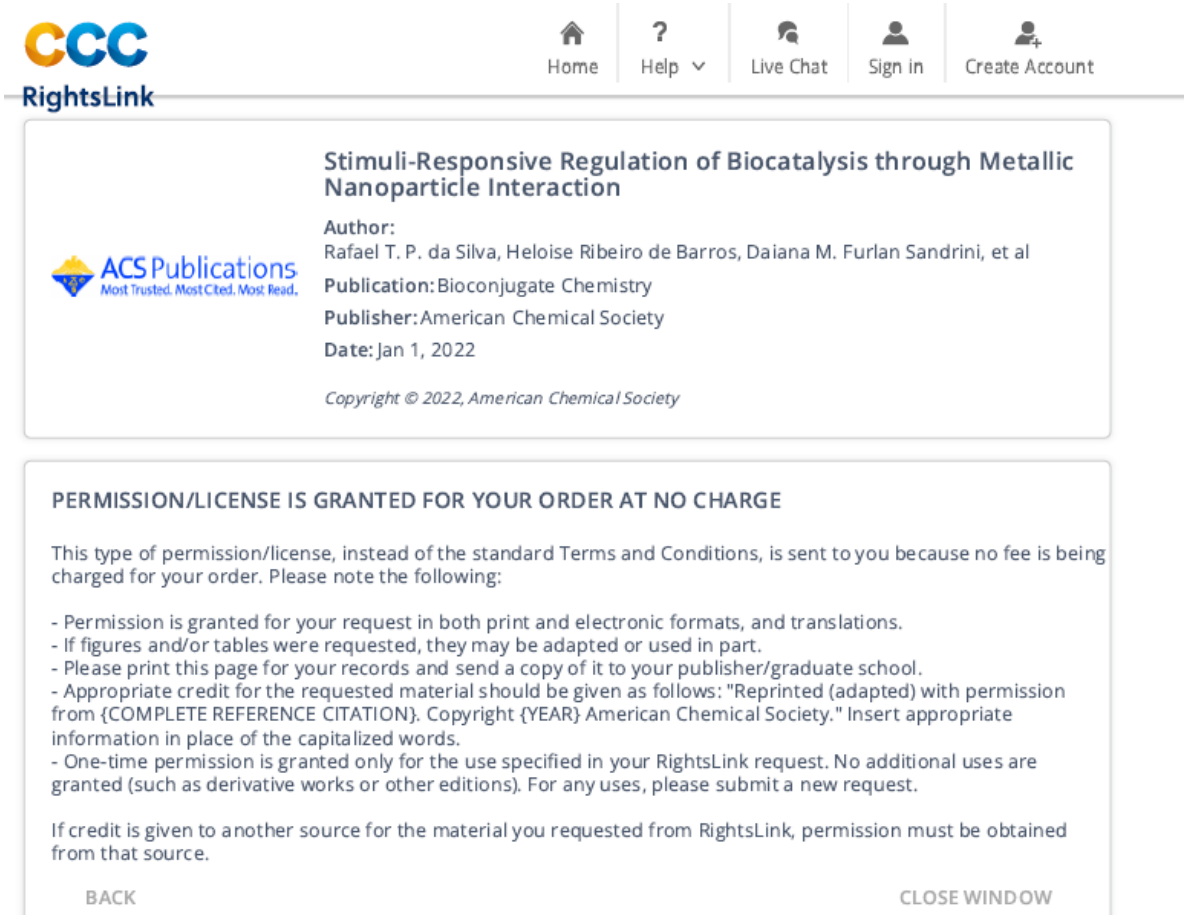
PERMISSION/LICENSE IS GRANTED FOR YOUR ORDER AT NO CHARGE

This type of permission/license, instead of the standard Terms and Conditions, is sent to you because no fee is being charged for your order. Please note the following:

- Permission is granted for your request in both print and electronic formats, and translations.
- If figures and/or tables were requested, they may be adapted or used in part.
- Please print this page for your records and send a copy of it to your publisher/graduate school.
- Appropriate credit for the requested material should be given as follows: "Reprinted (adapted) with permission from {COMPLETE REFERENCE CITATION}. Copyright {YEAR} American Chemical Society." Insert appropriate information in place of the capitalized words.
- One-time permission is granted only for the use specified in your RightsLink request. No additional uses are granted (such as derivative works or other editions). For any uses, please submit a new request.

If credit is given to another source for the material you requested from RightsLink, permission must be obtained from that source.

Copyright of Attachment 4



CCC RightsLink

Home | Help | Live Chat | Sign in | Create Account

Stimuli-Responsive Regulation of Biocatalysis through Metallic Nanoparticle Interaction

ACS Publications
Most Trusted. Most Cited. Most Read.

Author:
Rafael T. P. da Silva, Heloise Ribeiro de Barros, Daiana M. Furlan Sandrini, et al

Publication: Bioconjugate Chemistry

Publisher: American Chemical Society

Date: Jan 1, 2022

Copyright © 2022, American Chemical Society

PERMISSION/LICENSE IS GRANTED FOR YOUR ORDER AT NO CHARGE

This type of permission/license, instead of the standard Terms and Conditions, is sent to you because no fee is being charged for your order. Please note the following:

- Permission is granted for your request in both print and electronic formats, and translations.
- If figures and/or tables were requested, they may be adapted or used in part.
- Please print this page for your records and send a copy of it to your publisher/graduate school.
- Appropriate credit for the requested material should be given as follows: "Reprinted (adapted) with permission from {COMPLETE REFERENCE CITATION}. Copyright {YEAR} American Chemical Society." Insert appropriate information in place of the capitalized words.
- One-time permission is granted only for the use specified in your RightsLink request. No additional uses are granted (such as derivative works or other editions). For any uses, please submit a new request.

If credit is given to another source for the material you requested from RightsLink, permission must be obtained from that source.

BACK CLOSE WINDOW

Submission Certificate of Attachment 5

Angewandte <em@editorialmanager.com> 15:12 (há 27 minutos)
para Rafael

inglês › português Traduzir mensagem Desativar para: inglês ×

Manuscript number: 202211447
Title: "Physicochemical insights into the LSPR-driven Enzymatic Activity of Lipase Adsorbed on Gold Nanoparticles"

Dear Mr da Silva,

This is to inform you that the above-mentioned Research Article has just been submitted to Angewandte Chemie by Prof. Susana Ines Cordoba de Torresi including Rafael T. P. da Silva; Heloise R. de Barros; Rafaella F. Fernandes; Jhoan Toro-Mendoza; Ivan Colluzza; Marcia L. A. Temperini; Susana Ines Cordoba de Torresi and you are listed as a co-author. Please contact the submitting corresponding author for status updates.

This journal offers a number of license options; information about this is available here:
https://authorservices.wiley.com/author-resources/Journal-Authors/licensing/index.html
The submitting author has confirmed that all co-authors have the necessary rights to grant in the submission, including in light of each co-author's funder policies. If any author's funder has a policy that restricts which kinds of license they can sign, for example if the funder is a member of Coalition S, please make sure the submitting author is aware.

Yours sincerely,
Editorial Office Staff

Submission Certificate of Attachment 6

ChemCatChem em@editorialmanager.com por usp.br seg., 1 de ago. 15:38 (há 22 horas)
para Rafael

inglês > português Traduzir mensagem Desativar para: inglês

Manuscript number: cctc.202200972
Title: "Cytochrome C with Peroxidase-like Activity Supported on Plasmonic AuNPs: Improved Stability and Enhanced Nanobioplasmonic Catalytic Conversion"

Dear Ms da Silva,

This is to inform you that the above-mentioned Research Article has just been submitted to ChemCatChem by Prof. Susana Ines Cordoba de Torresi including Rafael T. P. da Silva; Heloise R. de Barros; Rafaella F. Fernandes; Marcia L.A. Temperini; Susana Ines Cordoba de Torresi and you are listed as a co-author. Please contact the submitting corresponding author for status updates.

This journal offers a number of license options; information about this is available here:
https://authorservices.wiley.com/author-resources/Journal-Authors/licensing/index.html
The submitting author has confirmed that all co-authors have the necessary rights to grant in the submission, including in light of each co-author's funder policies. If any author's funder has a policy that restricts which kinds of license they can sign, for example if the funder is a member of Coalition S, please make sure the submitting author is aware.

Yours sincerely,
Editorial Office Staff

7. Curriculum Vitae

Rafael Trivella Pacheco da Silva

e-mail: rafaeltrivella@gmail.com

Academic

- **Bachelor Degree in Chemistry** – Universidade de São Paulo, Instituto de Química. São Paulo – SP, Brazil – Obtained in July 2014.
- **Master Degree in Chemistry –** Universität Siegen, Department Chemie und Biologie. Siegen, Germany – Obtained in November 2017
- **PhD in Chemistry** – Universidade de São Paulo, Instituto de Química. São Paulo, Brazil – Started in March, 2018. Conclusion planned to September 2022 – Grant: Coordenação de Aperfeiçoamento de Pessoal de Nível Superior (CAPES) – Advisor: Prof. Dr. Pedro H. C. Camargo and Prof. Dr. Susana Inés Córdoba de Torresi (from 2019).
- **Specialization in Didactic-Pedagogical Training for Distance Learning Courses –** Universidade Virtual do Estado de São Paulo (UNIVESP) – Obtained in July 2021.
- **Bachelor and Teaching Degrees in Biology –** Universidade de São Paulo, Instituto de Biociências – SP, Brazil – Conclusion planned to December 2022.

Publications

1. Anderson G. M. da Silva, Thenner S. Rodrigues, Alexandra Macedo, Rafael T. P. da Silva, and Pedro H. C. Camargo. An undergraduate level experiment on the synthesis of Au nanoparticles and their size-dependent optical and catalytic properties. *Quim. Nova.*, **2015**, 37(10), p. 1716-1720. DOI: 10.5935/0100-4042.20140235
2. Fernanda de F. Ventura, Rafael T. P. da Silva, Cassius V. Stevani. História do fungo bioluminescente Flor-de-Coco (*Neonothopanus gardneri*) e efeitos das condições de cultura sobre a emissão de luz. *Rev. Virtual de Química*. **2015**, 7(1), p. 41-55. DOI: 10.5935/1984-6835.20150003.

3. Rafael T. P. da Silva, Marcos V. Petri, Estela Y. Valencia, Pedro H. C. Camargo, Susana I. Cordoba de Torresi, and Beny Spira. Visible light plasmon excitation of silver nanoparticles against antibiotic-resistant *Pseudomonas aeruginosa*. *Photodiagnosis Photodyn. Ther.,* **2020**, 31, p. 101908-13555. DOI: 10.1016/j.pdpdt.2020.101908

4. Heloise R. de Barros, Livia Y. Tanaka, Rafael T. P. da Silva, Javier Santiago-Arcos, Susana I. Cordoba de Torresi, and Fernando Lópes-Gallego. Assembly of Nano-Biocatalyst for the Tandem Hydrolysis and Reduction of p-Nitrophenol Esters. *Part. Part. Syst. Charact.* **2021**, 38(10), 2100136. DOI: 10.1002/ppsc.202100136

5. Associação de Pós-Graduação Helenira Preta Rezende USP Capital, Associação de Pós-Graduação USP Ribeirão Preto, Associação de Pós-Graduação USP São Carlos, Associação de Pós-Graduação ESALQ USP. Relatório da comunidade pós-graduanda da Universidade de São Paulo frente à pandemia de Covid-19 em 2020. *OSF Registries.* **2021**. DOI: 10.17605/OSF.IO/7GHV6

6. Rafael T. P. da Silva, Maria P. S. Rodrigues, Gabriela F. D. Davilla, Adriano M. R. P. da Silva, André H. B. Dourado, and Susana I. Cordoba de Torresi. AgAu Hollow Nanoshells on Layered Graphene Oxide and Silica Submicrospheres as Plasmonic Nanozymes for Light-Enhanced Electrochemical H_2O_2 Sensing. *ACS Appl. Nano Mater.,* **2021**, 4, 12062-12072. DOI: 10.1021/acsanm.1c02611

7. Rafael T. P. da Silva, Heloise R. de Barros, Daiana M. F. Sandrini, and Susana I. Cordoba de Torresi. Stimuli-Responsive Regulation of Biocatalysis through Metallic Nanoparticle Interaction. *Bioconjugate Chem.* **2022**, 33, 53-56. DOI: 10.1021/acs.bioconjchem.1c00515 . **Cover Art**.

8. Rafael T. P. da Silva, Susana I. Cordoba de Torresi, and Paulo F. M. de Oliveira. Mechanochemical Strategies for the Preparation of SiO2-Supported AgAu Nanoalloy Catalysts. *Front. Chem.* **2022**, 10:836597. DOI: 10.3389/fchem.2022.836597

9. Heloise R. de Barros, Vitor M. Miguel, Rafael N. P. Colombo, Rafael T. P da Silva, Susana I. Cordoba de Torresi (**2022**). Plasmonics in Bioanalysis: SPR, SERS, and Nanozymes. In Frank N. Crespilho (Ed.). *Advances in Bioelectrochemistry Volume 5: Emerging Techniques and Materials, Biodevice Design and Reactions*. Switzerland: Springer Cham.

10. **Rafael T. P. da Silva**, Heloise R. de Barros, Rafaella F. Fernandes, Marcia L. A. Temperini, and Susana I. Cordoba de Torresi. Cytochrome C with Peroxidase-like Activity Supported on Plasmonic AuNPs: Improved Stability and Enhanced Nanobioplasmonic Catalytic Conversion. **Submitted**. *ChemCatChem.* **2022**
11. **Rafael T. P. da Silva**, Heloise R. de Barros, Rafaella F. Fernandes, Jhoan Toro-Mendoza, Ivan Colluzza, Marcia L. A. Temperini, and Susana I. Cordoba de Torresi. Physicochemical insights into the LSPR-driven Enzymatic Activity of Lipase Adsorbed on Gold Nanoparticles. **Submitted**. *Angew. Chem.* **2022**

Participation in Conferences

- **35ª Reunião Anual da Sociedade Brasileira de Química (RASBQ)**, 2012 – Águas de Lindoia, SP – Brazil. Da Silva, R. T. P.; Camargo, P. H. C.. *"Investigando a Reação Galvânica entre Nanopartículas de Ag e $AuCl_4^-$ na Presença de Citrato: Síntese de Nanodendritos de Ag-Au"*.
- **36ª Reunião Anual da Sociedade Brasileira de Química (RASBQ)**, 2013 – Águas de Lindoia, SP – Brazil. Poster Presentation: da Silva, R. T. P.; Wendler, A. M.; dos Santos, A. A.; Camargo, P. H. C.. *Nanomateriais de prata-paládio: efeito da composição e estrutura sobre a atividade catalítica frente a reação de acoplamento Suzuki*.
- **2º Simpósio Nacional de Nanobiotecnologia (SNNB)**, 2018 **–** São Bernardo, SP – Brazil. Poster Presentation: da Silva, R. T. P.; Petri, M. V.; Valencia, E. Y. M.; Camargo, P. H. C.; Torresi, S. I. C.; Spira, B. *Aumento da Atividade Antimicrobiana de Nanopartículas de Prata por Indução Plasmônica.*
- **Applied Nanotechnology and Nanoscience International Conference (ANNIC),** 2021 – Online. Oral Presentation: da Silva, R. T. P.; Rodrigues, M. P. S.; Davilla, G. F. D.; da Silva, A. M. R. P.; Torresi, S. I. C. *Light-enhanced H_2O_2 Sensing by Supported AgAu Bimetallic Nanoshells as Plasmonic Nanozymes.*
- **18th International Conference on Electroanalysis (ESEAC)**, 2022 – Vilnius, Lithuania. Poster Presentation: da Silva, R. T. P.; Rodrigues, M. P. S.; Davilla, G. F. D.; da Silva, A. M. R. P.; Torresi, S. I. C. *AgAu Hollow Nanoshells on Layered Graphene Oxide and Silica Submicrospheres as*

Plasmonic Nanozymes for Light-Enhanced Electrochemical H_2O_2 Sensing. **Certificate Best Poster Award: First Prize.**

Working Experience

- **February/2018 – January/2022:** Coordinator and English teacher for women resising in favela (VOICE – Inglês para Elas), São Paulo, SP - Brazil.
- **July/2019 – December/2020:** Teaching Assistant for Distance Learning Courses – Final Papers for Engineers, Calculus I, Statistics. UNIVESP, São Paulo, SP, Brazil.
- **June/2018 – November/2018:** Teaching Assistant of Inorganic Chemistry I. *Supervisor:* Prof. Vera R. L. Constantino. Instituto de Química da Universidade de São Paulo, São Paulo, SP - Brazil.
- **February/2018 – June/2018:** Teaching Assistant of General Chemistry to Physics. *Supervisor:* Prof. Marcia L. A. Temperini. Instituto de Química da Universidade de São Paulo, São Paulo, SP – Brazil.
- **July/2016 – July/2017:** Project Researcher – Batchpur – Luminescent Nanomaterials as Sensors for Waste Water Treatment. SHK contract – Siegen - Germany.
- **July/2014 – September/2015 –** R&D Technician - DOW Brasil Sudeste – Polyglycols, Surfactants and Fluids, São Paulo, SP – Brazil.
- **July/2013 – July/2014 –** Internship at DOW Brasil Sudeste – Laboratory Research in Polyglycols, Surfactants and Fluids (PS&F), São Paulo, SP – Brazil.
- **January/2012 – December/2012 –** Alphabetization Teacher for adults (EJA Program) – Colégio Friburgo, São Paulo, SP – Brazil.